Investigating the impact of amyloid plaques on surrounding tissue with particular focus on microglia

Jack Isaac Wood

UCL

Thesis submitted for the degree of Doctor of Philosophy

May 2025

Declaration

I, Jack Isaac Wood confirm that the work presented in this thesis is my own. Where information has been derived from other sources, I confirm that this has been indicated in the thesis.

ACKNOWLEDGEMENTS

I want to express my gratitude to Prof. Frances Edwards for your invaluable guidance and mentorship throughout my PhD, as well as during my Master's project, literature review, and time as a research assistant. I am particularly thankful for the trust you placed in me, which allowed me to shape the direction of my project as well as supervise and guide other student projects within the lab.

I would like to thank Prof. Jörg Hanrieder for your supervision, guidance, and care throughout every stage of my PhD. Our many discussions, whether in the lab, at conferences around the world, in restaurants, or at the pub, strengthened my love for science. I am especially grateful for the times spent in the lab in Gothenburg. You have built a team that not only reflects your dedication to producing amazing research but also adopts your friendliness and kindness.

I would like to thank Dr. Damian Cummings. Your natural ability to teach and explain complex concepts with clarity and insight, greatly supported me throughout my PhD. You have been the cornerstone of the Edwards Lab and have supported the success of every lab member, both past and present.

I would also like to give a massive thanks to the Edwards Lab as a whole. Over the past six years, I've had the pleasure of meeting so many incredible people and collecting countless memories that I will always cherish. Sneha, in particular, you've made doing a PhD genuinely enjoyable. From heated scientific discussions to hilarious nonsensical chatter, your advice, our many post-work drinks, our general frolicking around London and our conference adventures around the world have all made coming to the lab something to look forward to. Thank you also to Barbara, Brendan, Prishaa, and Aziz for your incredible friendship and support both in the lab and but also beyond. Thank you to Kari, Katie, and Diana for giving me such a warm introduction to lab life and for filling the lab with great discussions and laughter. I would also like to thank Tashu and Shenyi for showing me the ropes and helping me find my feet when I first joined the lab. Thank you to Georgia, Eugenia, Ridwaan, Lydia, and RongPing for putting up with my supervision, you were all perfect students, and I look forward to keeping in touch.

Thank you also to Sri, Junyue, Maciej, Alicja, Durgha, and all the other members of the Hanrieder Lab. It was a pleasure getting to know you all, and I'm grateful for the fun times we shared in Gothenburg, Norway, Cyprus, and Krakow.

I would also like to thank my friends and family. Your genuine curiosity, encouragement, and support meant everything. Thanks to my housemates George and Finley for your constant friendship and encouragement throughout my PhD. Thank you particularly to my mum, dad, and brother who have been a constant source of belief throughout my life.

Lastly, I would like to thank Molly, you have been my foundation of support throughout this PhD (and way beyond). There is no failed experiment big enough to overcome the love and care I get to go home to every day; I will always be grateful for this.

UCL Research Paper Declaration Form: referencing the doctoral candidate's own published work(s)

1. **For a research manuscript that has already been published** (if not yet published, please skip to section 2)**:**

   (a) **What is the title of the manuscript?**
   Plaque contact and unimpaired Trem2 is required for the microglial response to amyloid pathology

   (b) **Please include a link to or doi for the work:**
   https://doi.org/10.1016/j.celrep.2022.111686

   (c) **Where was the work published?**
   Cell Reports

   (d) **Who published the work?**
   Jack Wood (1st Author), Frances Edwards (Last Author), Cell Press (Publisher)

   (e) **When was the work published?**
   22 November 2022

   (f) **List the manuscript's authors in the order they appear on the publication:**

   Jack I. Wood, Eugenia Wong, Ridwaan Joghee, Aya Balbaa, Karina S. Vitanova, Katie M. Stringer, Alison Vanshoiack, Stefan-Laural J. Phelan, Francesca Launchbury, Sneha Desai, Takshashila Tripathi, Jörg Hanrieder, Damian M. Cummings, John Hardy, Frances A. Edwards

   (g) **Was the work peer reviewed?**
   Yes

   (h) **Have you retained the copyright?**
   Yes

   (i) **Was an earlier form of the manuscript uploaded to a preprint server (e.g. medRxiv)? If 'Yes', please give a link or doi**
   https://doi.org/10.1101/2022.01.26.477873

   If 'No', please seek permission from the relevant publisher and check the box next to the below statement:

   ☐ *I acknowledge permission of the publisher named under 1d to include in this thesis portions of the publication named as included in 1c.*

2. **For a research manuscript prepared for publication but that has not yet been published** (if already published, please skip to section 3)**:**

   (a) **What is the current title of the manuscript?**
   Isotope Encoded chemical Imaging Identifies Amyloid Plaque Age Dependent Structural Maturation, Synaptic Loss, and Increased Toxicity

   (b) **Has the manuscript been uploaded to a preprint server e.g. medRxiv'?**

   If 'Yes', please please give a link or doi:

   https://doi.org/10.1101/2024.10.08.617019

   (c) **Where is the work intended to be published?**
   Nature Communications

   (d) **List the manuscript's authors in the intended authorship order**
   Jack I Wood, Maciej Dulewicz, Junyue Ge, Katie Stringer, Alicja Szadziewska, Sneha Desai, Srinivas Koutarapu, Haady B Hajar, Kaj Blenno, Henrik Zetterberg, Damian M Cummings, Jeffrey N Savas, Frances A Edwards, Jörg Hanrieder

   (e) **Stage of publication:**
   Responding to reviewer comments

3. **For multi-authored work, please give a statement of contribution covering all authors** (if single-author, please skip to section 4)**:**

   For Wood et al 2022, Cell Reports:

   Conceptualization: F.A.E. and J.I.W. Methodology: F.A.E., D.M.C., J.I.W., A.V., and R.J. Investigation: J.I.W., E.W., R.J., K.S.V., S.D., A.B., S.-L.J.P., F.L., and K.S. Visualization: F.A.E., J.I.W., and D.M.C. Supervision: D.M.C., F.A.E., and T.T. Writing – original draft: F.A.E. and J.I.W. Writing – review & editing: J.I.W., J. Hardy, D.M.C., and F.A.E. (all authors). Funding: F.A.E., D.M.C., J. Hardy, and J. Hanrieder.

   For Wood et al 2024, bioRxiv:

   Conceptualization: JH, JIW, FAE. Methodology: JIW, KS, JG, SK, AS, SD, JH. Investigation: JIW, MD, KS, JG, SK, AS, HBH, JH. Visualization: JIW, MD, KS, JG, SK. Funding acquisition: JH, FAE, JNS. Supervision: JH, FAE, DMC. Writing – original draft: JIW, JH. Writing – review & editing: JIW, MD, KB, HZ, DMC, JNS, FAE, JH.

4. **In which chapter(s) of your thesis can this material be found?**Wood et al., 2022: Chapter 3. Wood et al., 2024: Chapter 5.

e-Signatures confirming that the information above is accurate (this form should be co-signed by the supervisor/ senior author unless this is not appropriate, e.g. if the paper was a single-author work)**:**

Candidate: Jack Isaac Wood

Date: 20/05/25

[redacted]

Wood et al., 2022, Cell Reports

Supervisor/Senior Author signature (where appropriate)**:** Frances A. Edwards

Date: 22nd May 2025

[redacted]

Wood et al., 2024, bioRxiv

Supervisor/Senior Author signature (where appropriate)**:** Jörg Hanrieder

Date: 26th May 2025

[redacted]

ABSTRACT

The deposition of Aβ plaques is widely considered the initiating event in the pathogenesis of Alzheimer's disease (AD). This is followed by a substantial temporal delay before the onset of neurofibrillary tangle formation and cognitive decline. The reasons for this delay and the mechanisms by which Aβ plaques lead to tangle formation remain poorly understood. It is, therefore, critical to better understand the impact of Aβ plaques on surrounding brain tissue. This thesis addresses this by investigating both the immune response to plaques, characterised by the clustering and activation of microglial cells and the local toxicity induced by plaques, including synapse loss and the formation of dystrophic neurites.

Using microglia-enriched spatial transcriptomics, I show that microglial contact with plaques is a modulator of microglial gene expression in both the NLF mouse model of AD and human AD brain tissue. Furthermore, I show that introducing the microglial-specific, AD-associated *Trem2*^{R47H} risk mutation into NLF mice disrupts a gene module normally upregulated in response to plaque contact, involved in phagosomal, lysosomal, and lipid-processing pathways. This loss of microglial function associated with *Trem2*^{R47H} also results in an increase of very small plaques.

I demonstrate that plaque toxicity is influenced by both the age of a plaque and its structural morphology. To assess plaque age, I used a ^{15}N-enriched heavy isotope diet to label newly deposited plaques, followed by spatial transcriptomics to assess surrounding gene expression. These early-deposited plaques were associated with a greater loss of synapse-related genes and an upregulation of genes involved in metabolism. Structural plaque types were classified using a combined staining approach, revealing an increase in diffuse plaques relative to more compact plaques as a mouse ages. Notably, the most aggregated plaque type showed substantial toxicity and synapse loss, whereas diffuse plaques exhibited no evidence of local synapse loss.

IMPACT STATEMENT

Alzheimer's disease is the most common cause of dementia worldwide, accounting for approximately 60–70% of cases. The global burden of dementia is increasing, with the number of people affected estimated to double by 2050 (World Alzheimer Report, 2024). Understanding the pathogenesis of Alzheimer's disease is, therefore, critical for the development of effective therapeutics. However, the complexity of the disease is highlighted by the high failure rate of clinical trials, with 98% of Alzheimer's disease-targeting drugs failing to progress beyond Phase III as of 2022 (Kim et al., 2022).

Key findings from this thesis contribute important insights into the pathogenesis of Alzheimer's disease. Microglial contact with amyloid plaques was found to regulate gene expression in both mouse models and human AD tissue. These findings provide valuable insights into spatially resolved microglial activity and suggest that future therapeutic strategies, such as TREM2-activating drugs, should potentially target plaque-associated regions. This response was disrupted by the *Trem2*^{R47H} mutation, a known Alzheimer's disease risk variant. This disruption highlights key disease mechanisms linked to genetic risk and identifies a module of genes involved in phagocytic, lysosomal, and lipid-associated pathways. This gene network may offer promising targets for therapeutic intervention. The findings on plaque heterogeneity are also significant. The observed decline in synapse-associated gene expression with increasing plaque age may help explain the lag between early Aβ deposition and the onset of cognitive decline and tau pathology. Moreover, the characterisation of structural plaque types supports current Aβ immunotherapy strategies by confirming that pathogenic Aβ species are likely those that are highly aggregated or found in compact, cored plaques.

The findings presented in this thesis have been widely disseminated across conferences and publications. The results on plaque-associated microglial gene expression were first shared as an online presentation at the Society for Neuroscience conference 2021 and later as a poster at the ADPD Conference 2022. This data was subsequently published in Cell Reports (Wood et al., 2022). Findings on plaque heterogeneity were initially presented as a poster at ADPD 2023 and later at the UCL Neuroscience Symposium 2023. This work is currently available as a preprint on bioRxiv (Wood et al., 2024), and we are currently addressing reviewer comments for its publication in Nature Communications. I have delivered talks on both projects together at the Translation Omics 2023 conference, the departmental seminar series NPP Shorts 2023, and the largest neuroscience conference in Eastern Europe, Neuronus 2024. Most recently, data from the human tissue spatial transcriptomic study was presented as a poster at ADPD 2025. A further poster on this

project has also been shortlisted for a prize at the upcoming UCL Neuroscience Symposium 2025. A manuscript based on these findings will be prepared for publication. In addition to the direct findings, methods developed during this thesis have been applied to other research. The protein analysis towards plaque approach contributed to Koutarapu et al. (2025) (published in Nature Communications), while the plaque categorisation method was used in the preprint Desai et al. (2024).

TABLE OF CONTENTS

LIST OF FIGURES

Chapter 1

Chapter 3

Chapter 4

Chapter 5

Chapter 6

LIST OF TABLES

Chapter 4

Chapter 2

ABBREVIATIONS

Only frequently referenced genes and proteins included

aCSF	Artificial Cerebrospinal Fluid
AD	Alzheimer's Disease
AICD	Amyloid Precursor Protein Intracellular Domain
AOI	Area of Interest
APOE / *APOE* / *Apoe*	Apolipoprotein E
APP / *APP* / *App*	Amyloid Precursor Protein
Aβ	Amyloid-β
AβpE3–42	Pyroglutamate-modified Amyloid-β
BACE1 / *BACE1*	Beta-site APP-cleaving Enzyme 1
BP	Biological Process
C1q / *C1qa/b/c*	Complement Component 1Q
CC	Cellular Component
CNS	Central Nervous System
CSF	Cerebrospinal Fluid
CTS/S/D/B... / *Cts*/*s*/*d*/*b...*	Cathepsin S/D/B...
CU-AP	Cognitively Unimpaired–Amyloid Positive
DAA	Disease-Associated Astrocytes
DAM	Disease-Associated Microglia
EOAD	Early-Onset Alzheimer's Disease
FDA	Food and Drug Administration
FDR	False Discovery Rate
fEPSP	Field Excitatory Postsynaptic Potential
FFPE	Formalin-Fixed Paraffin-Embedded
FTD	Frontotemporal Dementia
GWAS	Genome-Wide Association Study
HK	Housekeeping
HOMER1	Homer Scaffold Protein 1
IHC	Immunohistochemistry
iSILK	Imaging Stable Isotope Labelling Kinetics
KEGG	Kyoto Encyclopedia of Genes and Genomes
LAMP1	Lysosome-Associated Membrane Protein 1
LCO	Luminescent Conjugated Oligothiophene
LOAD	Late-Onset Alzheimer's Disease
LPS	Lipopolysaccharide
LTP	Long-Term Potentiation
MAC	Membrane Attack Complex
MALDI-MSI	Matrix-Assisted Laser Desorption Ionisation–Mass Spectrometry Imaging
MAPT	Microtubule Associated Protein Tau
MF	Molecular Function
MHC	Major Histocompatibility Complex
MRI	Magnetic Resonance Imaging
NFT	Neurofibrillary Tangle
NPC	Niemann-Pick disease type C

NPC2 / *Npc2*	NPC Intracellular Cholesterol Transporter 2
NPTX2 / *Nptx2*	Neuronal Pentraxin 2
NSS	Normal Splice Site
PCA	Principal Component Analysis
PGRN / *Grn*	Progranulin / Granulin
PIGs	Plaque-Induced Genes
PLEK / *Plek*	Pleckstrin
PSEN1 / *PSEN1*	Presenilin-1
PtdSer	Phosphatidylserine
Q3	Quartile 3
qFTAA / hFTAA	Quadro- / Hepta-formylthiophene Acetic Acid
qPCR	Quantitative Polymerase Chain Reaction
RNA-seq	RNA Sequencing
ROI	Region of Interest
SILK	Stable Isotope Labelling Kinetics
SLM	Stratum Lacunosum-Moleculare
SM	Stratum Moleculare
SNP	Single Nucleotide Polymorphism
SO	Stratum Oriens
SP	Stratum Pyramidale
sTREM2	Soluble TREM2
TMM	Trimmed Mean of M-values
TREM2 / *TREM2* / *Trem2*	Triggering Receptor Expressed on Myeloid cells 2
WT	Wild Type

CHAPTER 1

LITERATURE REVIEW

1.1 Alzheimer's Disease

Over the past decade, dementia has been the leading cause of death in the UK, with Alzheimer's disease (AD) accounting for approximately 60–70% of cases (Alzheimer's Society Report 2023/24). The financial burden is equally startling, with the annual cost of care for an individual with severe dementia being £80,500, placing an immense strain on families and the healthcare system (Alzheimer's Society Report 2023/24). In contrast to conditions like heart disease, where advances in treatments have significantly reduced mortality, deaths from AD continue to rise. Over the past 20 years, AD-related mortality has increased by 141% (Alzheimer's Association Report 2024). This lack of effective treatments or a cure has contributed to the widespread misconception that AD is a normal part of ageing, with 80% of Americans holding this view (World Alzheimer Report 2024).

Clinically, AD progresses from a prodromal state of mild cognitive impairment and gradually worsens over several years through increasing dementia severity (Long and Holtzman, 2019). This clinical progression is driven by underlying pathological changes that begin long before the presentation of symptoms. The two hallmark pathologies of AD are extracellular plaques, primarily made up of aggregated amyloid-β (Aβ) peptide and neurofibrillary tangles (NFTs), formed of intracellular aggregates of hyperphosphorylated tau protein. Aβ plaques can be deposited decades before the development of any clinical diagnosis, with plaque burden shown to correlate poorly with cognitive decline (Figure 1.1; Josephs et al., 2008; Morris et al., 2014). In contrast, NFTs develop post-Aβ plaque development and have been shown to correlate much better with cognitive decline (Long and Holtzman, 2019). The progression of Aβ plaque and NFT pathology is paralleled by a loss of neuronal tissue, with MRI studies revealing significant brain atrophy that correlates with worsening cognitive function (Fox et al., 1999; Fox and Schott, 2004). The temporal sequence of pathologies beginning with Aβ deposition, followed by tau pathology, and eventual symptomatic AD has driven investigations into the causal mechanisms linking these stages (Figure 1.1). Key questions remain: how does Aβ pathology trigger tau pathology, and why does Aβ accumulation alone not lead to cognitive decline? Despite these uncertainties, Aβ plaques being the initiating step in the pathological cascade has led to the development of the amyloid hypothesis, which posits that Aβ accumulation is the primary driver of AD pathogenesis (Hardy and Higgins, 1992).

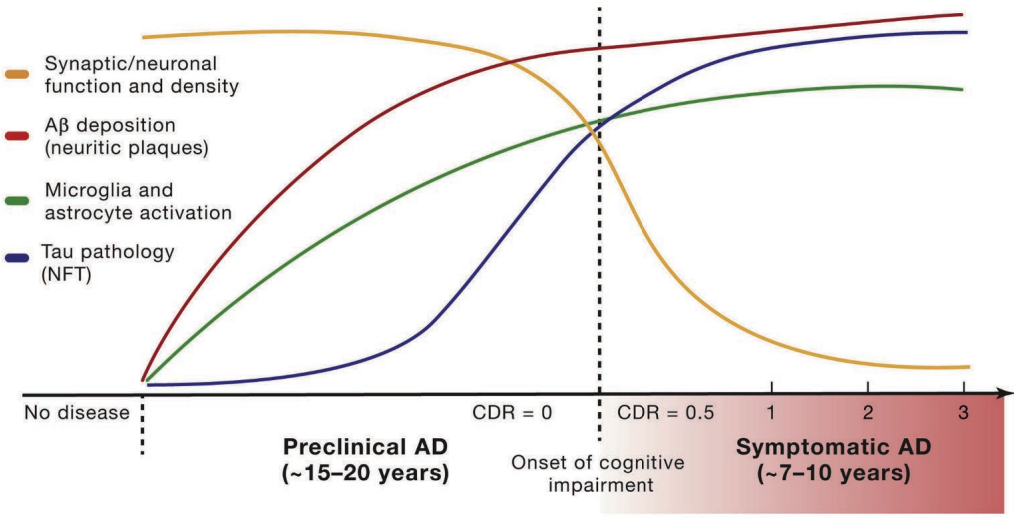

Figure 1.1 Development of AD-associated pathological changes from preclinical to symptomatic AD
The pathological hallmarks of AD begin with the deposition of Aβ as plaques, potentially decades before clinical symptoms. This is followed by an immune response involving microglia and astrocytes, which are visualised surrounding and interacting with plaques. Tau pathology, seen as neurofibrillary tangles (NFTs), emerges after a significant temporal delay from initial Aβ deposition. As pathology progresses, neuronal viability declines, leading to loss of neuronal matter. Both NFT burden and neuronal loss correlate well with cognitive decline, and thus symptomatic AD begins to develop. Diagram taken from Long and Holtzman (2019).

The importance of Aβ in AD is highlighted by populations of people carrying autosomal-dominant mutations in genes directly involved in Aβ production. These include mutations in the amyloid precursor protein (*APP*) gene or in genes encoding proteins that regulate APP metabolism (*PSEN1* and *PSEN2*)(Levy et al., 1990; Sherrington et al., 1995). These mutations lead to an increased production or altered processing of Aβ species, ultimately resulting in Aβ plaque deposition and an early onset of AD (EOAD). In these cases, the development of clinical symptoms typically emerges between the ages of 45 and 60 (Campion et al., 1999). Similarly, individuals with Down syndrome, who carry a third copy of chromosome 21 containing the *APP* gene, exhibit APP overexpression and develop AD pathology early in life, with an average clinical onset of around 52 years of age (Wisch et al., 2024). Although EOAD cases demonstrate a clear link between Aβ and AD pathogenesis, they only account for approximately 5% of all AD cases (Zhu et al., 2015). The most common form of AD, known as late-onset AD (LOAD), is diagnosed at much older ages, with a mean clinical diagnosis age of 81 (Nedelec et al., 2022). Although LOAD is not determined by single mutations like EOAD, genetic variants still contribute to the risk of LOAD diagnosis (Bellenguez et al., 2022). While a risk variant in *APP* (rs2154481) has been linked to LOAD, most associated genes have broader roles, including functions in lysosomal activity, lipid metabolism, endocytosis, and immune responses. These genes are expressed across

various brain cell types, some are expressed specifically in microglia, neurons, or astrocytes, and others are more ubiquitously expressed (Bellenguez et al., 2022). Despite this genetic component, ageing remains the greatest risk factor for LOAD (Guerreiro and Bras, 2015). Thus, AD reflects a complex interplay of multiple cellular processes across multiple cell types.

1.2 Aβ Plaques

1.2.1 From ‘peculiar substance’ to Aβ plaques

Alois Alzheimer first described AD in 1907, reporting on a woman whose brain exhibited ‘dense bundles’ of neurons and a ‘peculiar substance’ (Alzheimer, 1907). These features are now known as neurofibrillary tangles and Aβ plaques, the defining histological hallmarks of AD (Hyman et al., 2012). However, the precise structure of these plaques, then referred to as ‘senile plaques’ due to their prevalence in the ageing brain and association with cognitive decline, remained unclear for next 60 years, until x-ray diffraction studies revealed that they were organised as β-pleated sheets (Eanes and Glenner, 1968). The main molecular component of plaques was later identified through studies involving denaturation and fractionation of cerebral amyloid deposits from AD brain tissue. These investigations revealed a ~4 kDa peptide with a unique amino acid sequence that showed no homology to any previously known proteins (Allsop et al., 1983; Glenner et al., 1984). This peptide was initially termed the amyloid 4 monomer, ‘amyloid’ due to the characteristic amyloid staining properties observed in plaques and ‘4’ due to the ~4 kDa size of the monomer. The peptide is now known as Aβ (Masters et al., 1985b). Subsequent studies using antibodies raised against Aβ confirmed the presence of the monomeric peptide within senile plaques (Masters et al., 1985a). However, the unusually small size of Aβ led to the hypothesis that it was derived from a larger precursor protein. Researchers thus reverse-translated the Aβ amino acid sequence to design a DNA probe used to screen a human brain DNA library. This approach led to the isolation of a full-length 695-residue protein, initially termed the A4 precursor, and later renamed the Aβ precursor protein (APP) (Kang et al., 1987).

1.2.2 APP processing

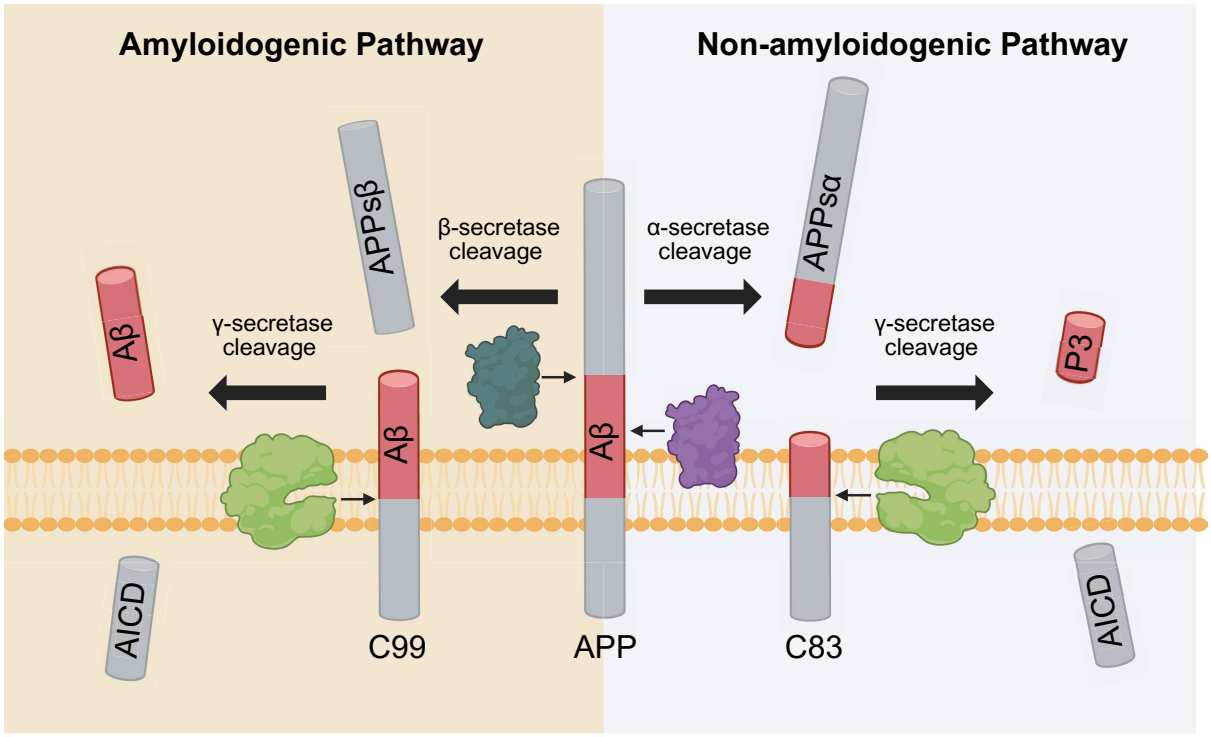

Figure 1.2 APP processing via the amyloidogenic and non-amyloidogenic pathway
Steps are described below. Original diagram, Biorender.

APP can be processed via one of two pathways: the non-amyloidogenic pathway or the amyloidogenic pathway. The pathway taken depends on the initial cleavage of APP, by α-secretase for the non-amyloidogenic pathway, or by β-secretase for the amyloidogenic pathway. Initial α- and β-secretase cleavage releases the ectodomain of APP as a soluble non-membrane-bound APPsα and APPsβ fragments into the external domain, respectively. The remaining membrane-bound fragments, C83 after α-secretase cleavage and C99 after β-secretase cleavage, are subsequently cleaved by γ-secretase at a common intramembrane site. For both C83 and C99 fragments, this γ-secretase cleavage releases the amyloid precursor protein intracellular domain (AICD) into the internal space. In the α-secretase-initiated non-amyloidogenic pathway, cleavage of the C83 fragment also releases a small P3 fragment into the external space. In contrast, in the amyloidogenic pathway, cleavage of the C99 fragment by γ-secretase releases the Aβ peptide (Mattson et al., 1993; Zhang et al., 2011).

BACE1 is the primary enzyme responsible for the β-secretase cleavage of APP (Vassar et al., 1999). Although other enzymes, such as BACE2 and cathepsin-B, have been proposed as the β-secretase, studies in BACE1-knockout mice show a dramatic reduction in Aβ levels and a lack of plaque formation in mouse models of AD (Hook et al., 2009; Luo et al., 2001; Ohno et al., 2007). The cleavage of APP by BACE1 is considered the rate-limiting step in Aβ

production rather than the cleavage by γ-secretase. Therefore, BACE1 activity levels are closely linked to the extent of Aβ generation and are thought to be a major determinant of Aβ burden (Hampel et al., 2021). Interestingly, it has been shown that BACE1 activity is increased by oxidative damage, inflammation, and ageing, suggesting that Aβ-driven amyloidogenesis is actively promoted under these conditions (Bao and Shen, 2023; Hampel et al., 2021; Ito et al., 2023). While no mutations in *BACE1* itself have been identified that influence AD risk, several *APP* mutations have been shown to alter BACE1-mediated cleavage and thereby modulate disease susceptibility (Hampel et al., 2021). Notably, a double nucleotide substitution in APP, known as the Swedish mutation (KM670/671NL), is located adjacent to the β-secretase cleavage site and significantly increases BACE1 processing of APP. This mutation leads to elevated Aβ production and is a deterministic cause of early-onset familial AD (Mullan et al., 1992). In contrast, the A673T mutation in *APP*, also situated near the β-secretase site, reduces cleavage efficiency by BACE1 and lowers Aβ production. Carriers of the A673T variant have an approximate five-fold lower risk of developing AD (Jonsson et al., 2012).

A shift away from Aβ production can be achieved by promoting the non-amyloidogenic pathway through the action of the metalloprotease ADAM10, which has been identified as the main α-secretase (Kuhn et al., 2010; Lammich et al., 1999). A few rare mutations in *ADAM10* have been found to reduce its cleavage activity, thereby diverting APP processing toward the amyloidogenic pathway and increasing the risk of AD (Kim et al., 2009). Consistent with this, knockout models of *Adam10* exhibit increased Aβ production and tau phosphorylation (Epis et al., 2010), while its overexpression reduces plaque burden in AD mouse models (Postina et al., 2004). Furthermore, cholesterol levels appear to modulate α-secretase activity, with elevated cholesterol promoting Aβ generation through direct binding to APP (Bodovitz and Klein, 1996; Cole et al., 2005; van der Kant et al., 2019).

γ-Secretase is a multi-subunit intramembrane protease complex responsible for the final cleavage in the APP processing pathway. It is composed of presenilin, nicastrin, APH-1, and PEN-2 (Kimberly et al., 2003). Initial cleavage of the C99 fragment, as well as releasing AICD, produces either Aβ49 or Aβ48, both of which go through subsequent γ-secretase-mediated tripeptide trimming, Aβ49->46->43->40->37 and Aβ48->45->42->38. The relative abundance of these Aβ species varies, with Aβ40 being the most predominant, accounting for approximately 80–90% of total Aβ, and Aβ42 contributing around 5–10% (Murphy and LeVine, 2010). Aβ42 contains two additional hydrophobic amino acids compared to Aβ40, which increases its propensity to aggregate and form insoluble Aβ plaques (De Felice et al., 2008; Kim and Hecht, 2005). However, as the disease progresses, many of the minority Aβ

species can also be found accumulating within Aβ plaques (Michno et al., 2020). The increased amyloidogenic properties of Aβ42 are further highlighted by the strong association between AD and mutations in the presenilin subunits of the γ-secretase complex, many of which are determinative for familial AD. These mutations act by shifting C99 processing to favour the production of Aβ42 over Aβ40, thereby promoting plaque deposition. The PSEN1 subunit of γ-secretase is particularly mutation-prone, with over 300 mutations having been reported, many of which are associated with an increased risk of AD (alzforum.org/mutations/psen-1). The other γ-secretase subunit, PSEN2, is similarly affected, with 91 reported mutations, several of which also increase AD risk (www.alzforum.org/mutations/psen-2).

1.2.3 Physiological role of Aβ

The discovery of Aβ's involvement in AD pathogenesis motivated investigations into its potential physiological functions. Early studies suggested a synaptic role for Aβ, as exogenous application of Aβ40 to hippocampal slices enhanced long-term potentiation (Wu et al., 1995). Similar LTP-enhancing effects were observed with low concentrations of Aβ42 (Puzzo et al., 2008). This role appeared to be endogenous, as blocking Aβ with specific antibodies reduced LTP in wild-type mice that do not overexpress Aβ (Puzzo et al., 2011). Additional studies have highlighted a presynaptic role of Aβ. Here, inhibiting Aβ degradation led to an increased probability of neurotransmitter release, shown through elevated synaptic vesicle turnover and increased miniature excitatory post-synaptic current frequency, without changes in synapse number (Abramov et al., 2009). A similar effect is observed in young, pre-plaque AD mouse models, whereby Aβ levels are increased but not yet deposited into plaques, leading to an increased probability of glutamate release (Cummings et al., 2015).

Aside from synaptic involvement, at low concentrations, Aβ appears to have a protective physiological role by acting as an antioxidant. It binds metal ions and inhibits lipoprotein oxidation, thereby reducing oxidative stress (Kontush et al., 2001; Zou et al., 2002). In neuronal cultures, Aβ monomers protect against cell death caused by antioxidant depletion or metal ion-induced oxidative damage. Notably, this protective effect is specific to monomeric Aβ, as oligomeric or aggregated forms do not show these protective effects (Plant et al., 2003; Zou et al., 2002). Furthermore, at higher concentrations, such as those present in Aβ plaques, Aβ can shift from an antioxidant to a pro-oxidant, contributing to oxidative damage (Kontush et al., 2001). Aβ has also been shown to have antimicrobial properties as it can bind to and inhibit the growth of a range of bacterial strains (Soscia et al., 2010). This role may be physiologically relevant, as nasal application of chlamydia bacteria induced an Aβ response and led to a surprising deposition of extracellular Aβ

plaques in WT mice (Little et al., 2004). Furthermore, in a separate study looking into AD comorbidities, in 90% of tested AD brain tissue, there was evidence of chlamydia DNA (Balin et al., 1998). The role of Aβ in fighting infection may also help explain the common presence of herpesvirus DNA within Aβ plaques and the increased risk of AD associated with herpes infections (Araya et al., 2025; Wozniak et al., 2009).

1.2.4 Aβ targeting therapies for AD

The discovery of the Aβ peptide, the identification of AD-associated mutations influencing Aβ production, and the development of the amyloid cascade hypothesis convincingly placed Aβ at the centre of AD pathogenesis. Targeting Aβ itself was therefore investigated as a treatment option for AD. A seminal breakthrough came from a study showing that immunising young transgenic AD mouse models with Aβ42 inhibited subsequent plaque formation at older ages (Schenk et al., 1999). This finding demonstrated that priming the immune system to recognise Aβ as a harmful antigen could induce a response capable of clearing or preventing its accumulation. Subsequent studies showed that Aβ immunisation not only reduced plaque burden but also ameliorated associated behavioural deficits (Janus et al., 2000; Morgan et al., 2000) and later showed to attenuate Aβ plaque-exaggerated tau pathology in transgenic mouse models harbouring frontotemporal dementia (FTD) determinate mutations (3xTg-AD mice: expressing AD associated *APP* KM670/671NL, *PSEN1* M146V, and FTD associated *MAPT* P301L) (Oddo et al., 2004). These findings were translated into human clinical trials of Aβ42 immunisation, which successfully induced the development of anti-Aβ42 antibodies and led to a corresponding reduction in Aβ plaque pathology (Lee et al., 2005; Nicoll et al., 2003). Moreover, immunisation was associated with decreased levels of phosphorylated tau, however, it did not affect tau aggregates (Boche et al., 2010). Despite these neuropathological improvements, there was no observed cognitive benefit, and approximately 6% of immunised participants developed meningoencephalitis, likely due to T-cell–mediated inflammation (Boche et al., 2010; Nicoll et al., 2003; Vellas et al., 2009). The trial was therefore terminated.

Recent clinical trials have shifted away from strategies that aim to induce endogenous antibody production and instead directly administer exogenous antibodies. Moreover, rather than targeting Aβ42, these antibodies are designed to selectively target more pathogenic forms of Aβ and hence avoid interrupting the physiological role of Aβ. Currently, three Aβ-targeting immunotherapies have received FDA approval for the treatment of AD: aducanumab, lecanemab, and donanemab. All three have been shown to enhance Aβ plaque clearance, reduce tau pathology to varying degrees, and slow cognitive decline. Aducanumab targets a conformational epitope present on aggregated Aβ species, including

both oligomers and fibrils, enabling it to bind a range of pathogenic Aβ aggregates (Budd Haeberlein et al., 2022; Sevigny et al., 2016). Lecanemab, in contrast, is selective for soluble Aβ protofibrils, intermediate structures thought to precede the formation of insoluble plaques (Logovinsky et al., 2016; Swanson et al., 2021; van Dyck et al., 2023). Donanemab takes a more targeted approach by binding to pyroglutamate-modified Aβ, a particularly aggregation-prone and neurotoxic form of Aβ that is abundant in mature plaques (Lowe et al., 2021; Sims et al., 2023). The effectiveness of Aβ immunotherapies highlights the importance of Aβ in AD and demonstrates a link between Aβ plaques and cognitive decline.

1.3 Mouse models of AD

One of the major limitations of AD research is the unsuccessful replication of the disease into mouse models. Although the presence of both Aβ plaques and tau tangles is necessary for an AD neuropathological diagnosis (DeTure and Dickson, 2019), mouse models of AD only exhibit Aβ plaques. The timeline of AD progression, however, presents a period before the onset of cognitive impairment whereby only Aβ plaques are present without tau tangles (Long and Holtzman, 2019). Therefore, current AD mouse models likely represent this early preclinical stage of the disease. Although not modelling the full extent of AD, this period is extremely valuable for research into the initial staging of AD, the interaction of plaque pathology with responding glia, and the possible progression towards tau pathology. Studies that have attempted to recapitulate tau tangles in AD models are frequently used; however, they rely on the introduction of tau mutations commonly associated with FTD such as *P301S/L* (Lewis et al., 2001). These mice, therefore, model a hybrid of AD and FTD and thus cannot be labelled as AD models.

To precipitate Aβ plaques in AD mouse models, familial deterministic mutations in APP are introduced. Until recently, this has relied on the random insertion of these mutations into the mouse genome. This technique is known as transgenesis. Although effective in producing Aβ pathology, the technique creates further problems not associated with AD. Firstly, the mutated *APP* will be randomly inserted into unknown segments of the mouse genome, rendering their functions incompetent (Kitazawa et al., 2012; Sasaguri et al., 2017). Secondly, the insert is not usually under the control of the endogenous mouse promoter, therefore, the expression of APP will not fully match the cell-type specificity or the expression level. Thirdly, as multiple *APP*-containing plasmids are injected, recombination will recruit a high *APP* copy number whilst also maintaining the expression of endogenous non-mutated mouse *App*. This results in an overexpression of APP that will not only lead to the desired increase in the Aβ peptide but will also include the other metabolites of APP that are not seen at such high levels in AD. These models always carry the risk of false-positive data; results are thought to be associated

with AD but are instead due to artefacts of transgenesis (Jankowsky and Zheng, 2017; Saito et al., 2016).

Over the past few years, Knock-in techniques that avoid the problems of transgenesis have risen to prominence. The *App*$^{NL\text{-}F/NL\text{-}F}$ (NLF) knock-in mouse introduces a targeted replacement of the murine Aβ with a humanised Aβ sequence with two flanking familial AD mutations (Saito et al., 2014). The Swedish mutation, NL (KM670/671NL), increases the production of both Aβ42 and Aβ40 peptides, whilst the Beyreuther/Iberian mutation, F (I716F), increases the ratio of Aβ42 to Aβ40. This overproduction of Aβ species, particularly Aβ42, will result in its aggregation and the formation of Aβ plaques (Figure 1.3A). This plaque pathology in the NLF model slowly develops from middle age at 9 months through to older age at 24 months (Figure 1.3B and 1.3C). In contrast, the more commonly used knock-in model, *App*$^{NL\text{-}G\text{-}F/NL\text{-}G\text{-}F}$ (NLGF), harbours an additional mutation within the Aβ exon itself (Arctic mutation: E693G), which increases the aggregability of Aβ. Plaque pathology in this model is seen as early as 2 months (Figure 1.3B; Benitez et al., 2021).

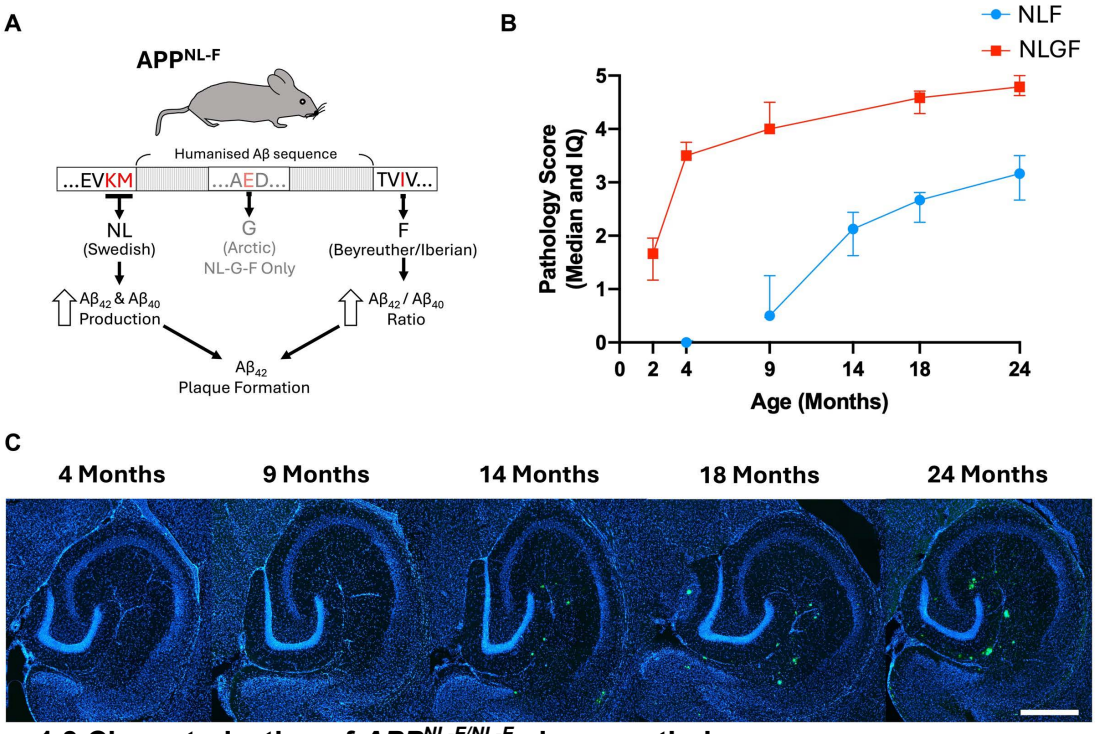

Figure 1.3 Characterisation of *APP*$^{NL\text{-}F/NL\text{-}F}$ plaque pathology
(A) *APP*$^{NL\text{-}F/NL\text{-}F}$ (NLF) mouse model of AD showing the humanised Aβ sequence with flanking regions with both NL Swedish and F Beyreuther/Iberian mutations that ultimately lead to plaque formation. Figure edited from Saito et al., 2014. (B) Pathology scoring using a visual assessment scale showing plaque deposition beginning in NLF mice around 9 months and increasing onwards. A much more aggressive model of AD, the NLGF model, shows rapid plaque deposition even as young as 2 months of age. (C) Images of plaque (Amytracker, Green) and nuclei (DAPI, blue) stained hippocampi from NLF mice across five ages. Scale bar: 500 µm. Figure 1.3A original Diagram. Figure 1.3B and 1.3C, adapted from Benitez et al. (2021).

1.4 Plaque heterogeneity

1.4.1 Plaque type classification

The initial classification of Aβ plaque types, based on plaque 'fibro-architecture' morphologies from electron microscopy images, proposed three plaque types thought to represent the evolution of a plaque: non-cored plaques, cored plaques, and compact (or 'burnt-out') plaques (Armstrong, 1998; Wiśniewski and Terry, 1973). Initially, non-cored plaques were thought to appear first, with Aβ gradually aggregating over time to form a central core, giving rise to cored plaques. Eventually, at the end stage of maturation, Aβ was believed to condense into a single 'compact-only' plaque composed solely of the dense core, which was considered non-toxic and not associated with surrounding neuronal dystrophy, hence the plaques impact on surrounding tissue had 'burnt-out' (Armstrong, 1998; Ikeda et al., 1990; Wiśniewski and Terry, 1973). Advances in fluorescent staining combined with high-resolution confocal microscopy improved the signal-to-noise and enabled three-dimensional plaque imaging. These studies revealed that previously defined 'compact-only' plaques were consistently surrounded by a halo of fibrillar Aβ. Furthermore, many plaques were observed to exhibit a scattered, unstructured morphology composed of diffuse Aβ, whilst others presented with a strand-like fibrillar structure. As a result, plaque classification was updated to diffuse, fibrillar, and cored plaques (Figure 1.4; Dickson and Vickers, 2001). These categories have largely persisted with a few additions, including coarse grain plaques, bird-nest plaques, and cotton wool plaques, all of which are defined through morphological features (Boon et al., 2020). Since these plaque types are typically associated with genetically determined Aβ pathology, the traditional classifications of diffuse, fibrillar, and cored plaques remain applicable in the context of late-onset AD. However, within these broad categories, numerous subtypes have been identified based on more detailed morphological characteristics, the presence of various surrounding proteins, and the specific composition of Aβ species contributing to the plaques (Thal et al., 2006). Nonetheless, the overarching categories of diffuse, fibrillar, and cored plaques continue to be the most widely referenced.

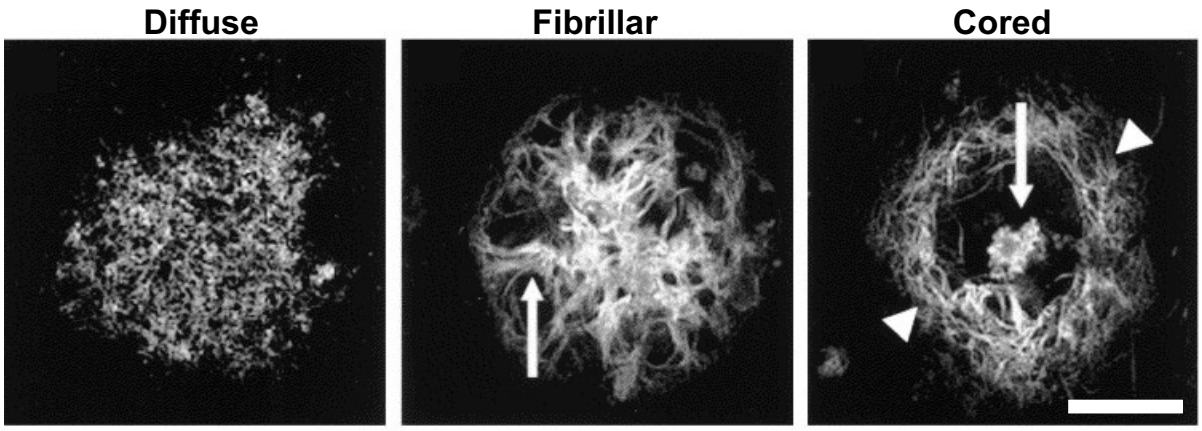

Figure 1.4 Diffuse, fibrillar and cored plaque types in human AD brain tissue
Thioflavin S-stained human AD brain tissue revealed three distinct plaque types. Diffuse plaques show a lack of fibril morphology, with a scattered appearance. Fibrillar plaques show more organised Aβ fibrils emanating from the plaque centre (arrow). Cored plaques show a central core (arrow) with a halo of surrounding Aβ fibrils (triangles). Scale bar: 50 μm. Figure adapted from Dickson and Vickers (2001).

Plaque type classification has historically been performed through morphological analysis of high-resolution images. However, the use of structure-specific dyes such as Congo Red, Thioflavin, and X-34 has made this process easier as these dyes selectively bind to fibrillar Aβ. The propensity of these dyes to bind amyloid fibrils varies, with Congo Red and its derivatives, such as X-34, tending to bind more tightly aggregated amyloid compared to Thioflavin (Maiti et al., 2019). Nonetheless, diffuse plaques lacking the tightly fibrillised Aβ appear mostly negative for such dyes (Rozemuller et al., 1989; Yamaguchi et al., 1988). Thus, when combined with a global Aβ immuno-stain, this approach enables the distinction between diffuse and fibrillised plaques, which has been invaluable in assessing the impact of plaque types on surrounding tissue (Gotkiewicz et al., 2025; Serrano-Pozo et al., 2011b; Spires et al., 2005). This method, however, lacks morphological categorisation and therefore overlooks the distinction between fibrillar and cored plaques.

Morphological categorisation of Aβ plaque types is accurate but time-consuming, typically requiring the expertise of a pathologist, and is therefore not suited for high-throughput analysis. In contrast, classification using amyloid-binding dyes is significantly faster but lacks the resolution to capture the full spectrum of plaque diversity. Recent advances in machine learning have enabled the categorisation of tens of thousands of plaques using Aβ immunohistochemical or amyloid dye-stained images (Amin et al., 2023; Koutarapu et al., 2025; Tang et al., 2019). This high-throughput approach not only facilitates rapid and accurate classification but also identifies subtle morphological features relevant to plaque type that may have been previously overlooked by pathologists (Amin et al., 2023).

1.4.2 Structure-specific dyes: the development of qFTAA and hFTAA

Dyes traditionally used to stain the amyloid fibrils of Aβ plaques, such as Congo Red and Thioflavin, feature chains of aromatic rings that form a planar structure. Interestingly, naturally occurring compounds with similar aromatic configurations, such as curcumin, a polyphenol derived from turmeric, also exhibit an affinity for amyloid fibrils and produce fluorescence upon binding (Condello et al., 2015; Maiti et al., 2021). These structures lie parallel to the long axis of amyloid fibrils and interact with hydrophobic pockets along the beta pleated structure; this non-covalent interaction enhances the fluorescence of the dye (Frieg et al., 2020).

The conformational specificity of these dyes for β-pleated sheets can be leveraged to develop derivatives that target specific structural polymorphisms within amyloid fibrils. The thiophene aromatic ring in Thioflavin has been shown to be critical for amyloid binding, as even monomeric thiophene derivatives interact with amyloid structures (Aslund et al., 2007). However, polymerising these thiophene units enhances the interaction with β-sheet structures, resulting in stronger spectral changes and specificity. For example, trimeric through to heptameric thiophene chains exhibited particularly strong specificity for amyloid fibrils compared to native, non-fibrillised proteins (Aslund et al., 2007; Aslund et al., 2009). These structures were named luminescent conjugated oligothiophenes (LCOs) and were subsequently used as dyes for fibrillised insulin (Aslund et al., 2007), tau tangles (Klingstedt et al., 2011), protein inclusion bodies (Klingstedt et al., 2013), prion aggregates (Sigurdson et al., 2007), and Aβ aggregates (Hammarstrom et al., 2010).

A change in the thiophene chain length of LCOs also appears to alter the dye's propensity to bind to different Aβ aggregation states. Two LCOs at opposite ends of their ability to detect distinct Aβ aggregation states are quadro-formylthiophene acetic acid (qFTAA) and hepta-formylthiophene acetic acid (hFTAA) (Klingstedt et al., 2011). qFTAA tends to bind more tightly packed β-pleated sheets, while hFTAA is more promiscuous and can bind to both tightly and moderately aggregated fibrils (Nystrom et al., 2013). The exact mechanism behind their structural binding specificities is unknown, but is likely related to the difference in rotational freedom in the chain of thiophenes (Klingstedt et al., 2011). Due to their unique spectral properties, these two dyes can be used in tandem. qFTAA exhibits a blue-shifted emission (max 500 nm), whereas hFTAA exhibits a red-shifted emission (max 580 nm). Therefore, their differences in binding abilities and spectral separation allow for a detailed study of aggregation dynamics. For example, their combined use has revealed a tendency for increased aggregation with chronological age in transgenic mouse models of AD (Nystrom et al., 2013), distinct structural Aβ plaque polymorphisms between familial and

sporadic AD in human tissue samples (Rasmussen et al., 2017), and structural differences between plaques in various AD mouse models (Parvin et al., 2024).

The commercialisation of LCOs offers a range of dyes marketed under the name Amytracker™, each featuring a unique structure corresponding to distinct excitation and emission spectra (Pretorius et al., 2018).

1.4.3 Plaque development

Initial work on plaque categorisations assumed that plaques evolve over time from early diffuse deposits to increasingly aggregated forms, resulting in a spectrum of plaque types that reflect different stages of maturation. This is supported by infrared imaging experiments, which are not reliant on antibodies and structural dyes, that showed a spectrum of increasing β-sheet content from diffuse through to cored plaques (Rohr et al., 2020).

Evidence of temporal plaque maturation dynamics is found in individuals who were cognitively unimpaired but amyloid positive at the time of death (CU-AP individuals). These brain samples were particularly abundant in diffuse plaques (Dickson et al., 1992; Murray and Dickson, 2014; Serrano-Pozo et al., 2011a). This finding can be interpreted in two ways: either these individuals were resilient to the clinical manifestations of AD due to an unexplained propensity to form diffuse plaques, or they represent individuals with pre-clinical AD, with diffuse plaques marking initial plaque deposition. One finding that supports the latter hypothesis is that individuals with Down syndrome develop diffuse plaque pathology first, as early as 12 years of age, with more compact plaques detected in older individuals (Lemere et al., 1996). Regional staging of Aβ plaque pathology has shown that newly affected brain regions present diffuse Aβ plaques before developing cored plaques (Thal et al., 2006). However, although diffuse plaques may appear first in the disease, this does not necessarily indicate that they evolve into cored plaques, as cored plaques may emerge independently at later stages. For instance, in individuals carrying familial AD mutations in PSEN1, diffuse-like Congo Red-negative plaques have been observed to persist for up to 30 years without progressing into other classical plaque types (Miki et al., 2019).

Determining whether plaque types evolve independently or represent sequential stages of maturation requires tracking the development of individual plaques over time, rather than relying solely on static assessments. Numerous studies have used *in vivo* cranial window imaging to track Aβ plaque development over time. The first study using this technique suggested that cored plaques appear rapidly *de novo* and grow to near-final size within days, with little subsequent growth implying a rapid and stable formation (Meyer-Luehmann

et al., 2008). However, follow-up studies using the same method reported a much slower and more gradual process with growth occurring over the course of weeks to months, with growth rates decreasing as plaques enlarge (Burgold et al., 2011; Hefendehl et al., 2011; Yan et al., 2009). The discrepancy between these findings is thought to stem from the binding dynamics of the injected dyes occurring over days rather than *de novo* plaque appearance. The findings also suggested that as overall plaque burden increases, the rate of new plaque formation declines, possibly because soluble Aβ is increasingly sequestered by existing plaques, preventing the precipitation of new plaques (Hefendehl et al., 2011). In support of this, a 'time-stamp' labelling technique combining early *in vivo* labelling followed by postmortem labelling confirmed that, in mouse models of AD, plaques continue to grow over several months, with the most rapid growth occurring early in the life of a plaque (Condello et al., 2011). However, due to the biological activity of Aβ specific antibodies, all aforementioned *in vivo* studies relied on amyloid-binding structural dyes. Therefore, it remains unclear whether these fibrillised plaques formed spontaneously or developed from pre-existing diffuse, dye-negative plaques. A novel method to 'time-stamp' label Aβ plaque development, whilst overcoming the reliance on amyloid fibril dyes, involves feeding AD mouse models a diet enriched in the stable ^{15}N isotope of nitrogen during different periods in the ageing (Michno et al., 2021). Here, the enrichment of ^{15}N detected through mass spectrometry imaging could delineate how far from the feeding period a specific plaque was deposited, thus delineating plaque development through age. This study found that plaques begin to deposit as initial dense cores rather than a development from diffuse plaques (Michno et al., 2021). However, this was performed in the NLGF model (harbouring the Arctic mutation), whereby Aβ has a much greater propensity to aggregate (Lord et al., 2011). Thus, whether this result can be translated to non-Arctic mutation AD models or humans is unknown.

A novel approach to studying the evolution of plaque formation involves inoculating total brain extracts into the brains of AD mouse models using tissue derived from human AD brain samples or another AD mouse model. Surprisingly, in initial experiments, inoculation typically induced diffuse plaques, with very few plaques stained positive for Congo Red (Meyer-Luehmann et al., 2006). A subsequent study expanded on this by testing brain extracts from various AD mouse models, each characterised by distinct predominant plaque types (Xu et al., 2022). The results showed that inoculation with extracts from mice with diffuse plaques tended to induce diffuse pathology, while extracts from mice with cored plaques tended to induce cored pathology. Remarkably, the plaque type introduced via inoculation often dominated the host mouse's genetic tendency; for example, mice genetically predisposed to develop cored plaques primarily developed diffuse plaques when injected with diffuse plaque

homogenate (Xu et al., 2022). This indicates a critical role of the initial Aβ seed and suggests that distinct plaque types may develop independently, driven by the nature of the original Aβ seed.

1.4.4 Different plaque types associated with different Aβ species

The idea that the initial Aβ seed predetermines plaque type aligns with observations that specific familial AD mutations in mouse models consistently lead to the development of particular plaque types. For example, mouse models that produce predominantly Aβ42 develop primarily diffuse plaques, whereas models producing high quantities of Aβ40 are abundant in cored plaques (Xu et al., 2020). Furthermore, the non-canonical plaque types found in early onset AD patients, such as coarse grain, bird-nest, and cotton wool plaques, are all predominantly composed of Aβ40 (Boon et al., 2020; Ichimata et al., 2022; Willumsen et al., 2022).

Early investigations into Aβ species composition across plaque types used C-terminal-specific antibodies to differentiate between Aβ40 and Aβ42. These studies revealed that diffuse plaques are mainly composed of Aβ42, while cored plaques are enriched in Aβ40 (Iwatsubo et al., 1994). More recent advances using mass spectrometry imaging, which bypasses the need for antibody-based detection, have consistently confirmed these findings. These studies show that Aβ40 is concentrated in the cores of cored plaques, with diffuse deposits containing Aβ42 and lacking Aβ40 (Koutarapu et al., 2025; Michno et al., 2019; Michno et al., 2020). Moreover, truncated forms of Aβ, such as Aβ1-38 and Aβ1-39, are also seen enriched in cored plaques (Michno et al., 2020). The early appearance of diffuse plaques aligns with the higher aggregation propensity of Aβ42 (Lemere et al., 1996). However, it remains unclear why the most compact and aggregated plaque types are predominantly associated with Aβ40 and truncated forms of Aβ, despite their inherently lower tendency to aggregate. One possible explanation is the presence of pyroglutamated Aβ42 (AβpE3–42), a modified form of Aβ42 produced through enzymatic truncation. AβpE3–42 is found highly enriched in cored plaques, and subsequent experiments have revealed that this species has higher levels of hydrophobicity and an increased tendency to aggregate compared to other Aβ species (Bayer, 2022; Michno et al., 2019). This suggests that the deposition of Aβ40 and truncated Aβ forms may follow the initial seeding of cored plaques by AβpE3–42. Interestingly, donanemab and lecanemab, the two currently available Aβ-targeting therapies for AD, show high affinity for pyroglutamated Aβ, with donanemab specifically raised against Aβ3pE-42 (Fertan et al., 2024).

1.4.5 Impact of different plaque types on surrounding tissue

The accumulation of plaques decades before the onset of clinical AD, alongside the weak correlation between overall plaque burden and cognitive decline, suggests that plaque toxicity may be relatively low or insufficient on its own to produce cognitive impairment (Josephs et al., 2008; Morris et al., 2014). However, the observation that diffuse plaques tend to appear earlier than cored plaques and are abundant in CU-AP individuals indicates that diffuse plaques may be responsible for the lack of Aβ plaque-induced clinical phenotypes. This hypothesis is consistent with studies showing that a higher propensity for Aβ aggregation and the presence of dense cored plaques are associated with increased progression of clinical dementia (Liu et al., 2022; Murray and Dickson, 2014; Rijal Upadhaya et al., 2014; Serrano-Pozo et al., 2016).

Understanding the clinical phenotypes associated with distinct plaque types requires evaluating their effects on the surrounding tissue microenvironment. Plaques associated with surrounding neuronal injury are commonly referred to as neuritic plaques. Historically, this term described plaques encircled by swollen, dystrophic neurites exhibiting signs of autophagic stress (Cataldo and Nixon, 1990). However, the standardised criteria for postmortem neuropathological assessment have broadened this definition to include plaques surrounded by markers of neuronal toxicity such as ubiquitin, neurofilament proteins, and hyperphosphorylated tau (Hyman et al., 2012; Mirra et al., 1991). Notably, this criterion explicitly states that diffuse plaques should not be included in the neuritic plaque count, thereby implicitly assuming that diffuse plaques do not contribute to AD-associated neuritic damage. In contrast, when delineating neuritic plaques across plaque types through co-staining with neurofilament proteins and phosphorylated tau, approximately 20% of diffuse plaques show surrounding dystrophic neurites (Dickson and Vickers, 2001). However, it remains evident that cored plaques are more strongly associated with toxicity, as around 80% exhibited associated dystrophic neurites. This suggests that while plaque morphology is a key factor in determining toxicity, it may not be the only determinant.

A loss of dendritic spines is consistently observed around fibrillised Aβ plaques defined by structural amyloid dyes (Spires et al., 2005; Spires-Jones et al., 2007; Tsai et al., 2004). This includes an *in vivo* observation showing that the loss of dendritic spines proceeds the *de novo* formation of dye-positive plaques, suggesting that the formation of a fibrillised core may be key to inducing synapse loss (Bittner et al., 2012). This is supported by within plaque analysis, revealing that synaptic density is significantly more reduced at the core of cored plaques compared to the surrounding halo of oligomeric Aβ (Koffie et al., 2009). However,

although investigations specifically examining diffuse plaques are limited, some early evidence has suggested these plaques are not associated with presynaptic loss (Masliah et al., 1990).

Microglial clustering around Aβ plaques is a hallmark neuropathological feature of AD. However, most studies demonstrating this phenomenon have relied on structural amyloid-binding dyes that selectively label fibrillar plaques, with relatively few studies having directly compared different plaque types (Condello et al., 2015; Haga et al., 1989; Itagaki et al., 1989). Early evidence using Congo Red staining showed that microglia consistently cluster and activate around fibrillar plaques, whereas diffuse, Congo Red-negative plaques showed minimal microglial activation (Stalder et al., 1999). Similarly, in an investigation of the non-canonical plaque types of EOAD tissue, the highly aggregated coarse-grained plaques were associated with increased microglial density compared to the more diffuse cotton wool plaques (Boon et al., 2020). More recent studies have employed combined staining approaches using: Aβ immunohistochemistry to label diffuse plaques; Thioflavin to detect fibrillar plaques; and DAPI to identify cored plaques. DAPI's ability to bind highly aggregated Aβ fibrils in plaque cores has only recently been demonstrated (Mabrouk et al., 2022). While the exact mechanism is unclear, its planar aromatic structure resembles Thioflavin, suggesting a potential interaction with β-sheet-rich fibrils distinct from its classical DNA-binding role (Mabrouk et al., 2022). This revealed that while cored plaques were associated with greater numbers of plaque-contacting microglia, diffuse plaques also showed some microglial engagement. Notably, however, microglia near cored plaques displayed thickened processes indicative of activation and potential phagocytic function, whereas those near diffuse plaques maintained thin, homeostatic-like morphology (Gotkiewicz et al., 2025).

In addition to neuritic dystrophy, synapse loss, and microglial activation, several other pathological changes have been shown to be more prominent around fibrillated plaques compared to diffuse plaques. These include elevated levels of reactive oxygen species (McLellan et al., 2003), increased mitochondrial loss and disrupted membrane potential (Xie et al., 2013), enhanced astrogliosis (Boon et al., 2020; Tsering et al., 2025), and upregulated complement system activity (Lue and Rogers, 2010; Snyder et al., 1994). Taken together, the lower toxicity of diffuse plaques, their earlier emergence relative to cored plaques, the preserved cognition in CU-AP individuals, the lack of synapse loss at diffuse plaques, and the strong association between cored plaques and cognitive impairment collectively suggest that diffuse plaques may be less strongly associated with neurodegeneration and clinical symptoms compared to the more aggregated cored plaques.

1.5 Microglia

1.5.1 Microglia during development

Microglia originate from the yolk sac during embryonic development and infiltrate the brain around embryonic day 9 (Ginhoux et al., 2010; Kierdorf et al., 2013). Once established in the central nervous system, microglia serve as the resident phagocytes and regulate a range of key developmental processes. These include synaptic pruning (Hoshiko et al., 2012; Paolicelli et al., 2011; Schafer et al., 2012), mediating neuronal death and engulfment (Frade and Barde, 1998; Marin-Teva et al., 2004; Sierra et al., 2010; Wakselman et al., 2008), supporting axonal growth and fasciculation (Squarzoni et al., 2014), and promoting myelination (McNamara et al., 2023). Disruption of microglial developmental roles, through deletion of key migratory and phagocytic receptors such as CX3CR1, leads to delayed synaptic pruning, increased synaptic density, and behavioural phenotypes reminiscent of autism (Hoshiko et al., 2012; Zhan et al., 2014). The modulation of these microglial processes is thought to be partially driven by the detection of neuronal activity. Here, microglia have shown preferential pruning of inactive synapses during the first postnatal week, being more likely to engulf synapses from neurons that have been pharmacologically silenced (Schafer et al., 2012). Recent studies have also shown that microglial calcium activity correlates with neuronal activity, increasing in response to both hyper- and hypo-excitation (Logiacco et al., 2021; Umpierre et al., 2020). This bidirectional sensitivity is believed to be mediated by astrocytes, which detect extracellular glutamate and subsequently release GABA and ATP to influence microglial responses (Logiacco et al., 2021). Importantly, microglial sensitivity to neuronal activity persists into adulthood, with microglia preferentially contacting active dendritic spines and promoting the frequency of neuronal calcium transients (Hristovska et al., 2022).

1.5.2 Microglia in response to pathogens

Under homeostatic conditions, microglia are distributed in a grid-like, non-overlapping pattern and continuously survey their microenvironment using long, ramified processes (Davalos et al., 2005; Nimmerjahn et al., 2005). Upon detection of a pathogen or injury, microglia respond by migrating to the affected area, where they undergo a multitude of changes, including morphological adaptation, proliferation, release of inflammatory cytokines, secretion of messenger molecules to recruit additional immune cells, phagocytosis of debris or pathogens, and interactions with other surrounding cells (Borst et al., 2021). Collectively, these responses constitute the primary innate immune response of the CNS. Early mechanistic studies investigating microglial immune responses often relied on non-physiological models such as laser-induced tissue damage or exposure to a bacterial

endotoxin (lipopolysaccharide, LPS). In response to laser ablation, microglia react quickly, extending their processes toward the lesion site, forming a containment barrier within approximately 30 minutes, demonstrating a quick targeted response to physical damage (Davalos et al., 2005; Nimmerjahn et al., 2005). LPS injection, in contrast, triggers a broad inflammatory response characterised by increased expression of pro-inflammatory cytokines, chemokines, and upregulation of receptors involved in antigen recognition and presentation (Olson and Miller, 2004; Qin et al., 2007). Furthermore, the sensitivity of this response is age-dependent, with older mice displaying heightened inflammatory activation (Henry et al., 2009). Gene expression analysis has also shown that microglia adapt to LPS exposure by entering distinct transcriptional states (Sousa et al., 2018). In AD, similar to the response to laser ablation and LPS, microglia encounter both focal pathology and sustained toxicity from Aβ plaques.

1.5.3 Microglia in AD

Microglia, as the innate immune cells of the CNS, exhibit a wide range of immunological responses to Aβ pathology. Even in the first description of AD, Alois Alzheimer noted the presence of numerous glial fibres and cells (Alzheimer, 1907). As imaging and staining technologies advanced, so did the phenotypic characterisation of microglia in AD. This included the observation of microglial clustering around Aβ plaques (Condello et al., 2015; Itagaki et al., 1989), their chemotaxis toward plaques (Lue et al., 2001; Takahashi et al., 2005), an ameboid morphology (Davalos et al., 2005; Davies et al., 2017), and their potential involvement in the engulfment of plaques, synapses, and neuronal debris (Frackowiak et al., 1992; Huang et al., 2021; Takahashi et al., 2005). Together, this suggested that microglia may be protecting surrounding tissue from Aβ plaque-induced toxicity whilst simultaneously attempting to phagocytose the plaque and associated damage. The following sections will provide an in-depth review of the literature surrounding advancements in understanding the role of microglia in AD.

1.5.4 Microglial genetic studies in AD

The first genetic evidence implicating microglia (and/or astrocytes in this case) in AD came with the identification of the APOE4 allele, which was found to be significantly more prevalent in individuals with AD (Strittmatter et al., 1993). The development of genome-wide association studies (GWAS) using SNP genotyping technologies enabled the discovery of additional risk loci in microglia-associated genes, including *ABCA1*, *CTSS*, *CR1*, and *PICALM*, alongside the confirmation of *APOE* as a major risk gene (Grupe et al., 2007; Harold et al., 2009; Hollingworth et al., 2011). A further major advancement came with the identification of rare variants in the microglial-specific triggering receptor expressed on

myeloid cells 2 (*TREM2*) gene. One such variant, *TREM2*^{R47H}, was initially known in homozygosity to cause Nasu-Hakola disease, a rare early-onset dementia; however, in heterozygosity, it was shown to increase the risk of developing late-onset AD by approximately 3- to 5-fold (Guerreiro et al., 2013; Jonsson et al., 2013). As genotyping platforms improved and larger, more diverse cohorts were analysed, recent GWAS have identified over 75 genetic loci associated with AD risk, over 20% of which are highly expressed in microglia over other cell types, including *TREM2* (Bellenguez et al., 2022; Wightman et al., 2021). These genetic findings support an essential role for microglia in AD, with the roles of such genes supporting the pathological observations of microglia clustering around Aβ plaques.

To build on these genetic discoveries, analysing microglial gene expression changes became necessary for understanding the downstream effects of AD risk variants and for uncovering additional genes and pathways involved in disease progression. While targeted approaches like qPCR enabled hypothesis-driven validation of risk genes, such as confirming elevated APOE expression in AD tissue (Yamada et al., 1995), the advent of microarray-based transcriptomic profiling allowed for unbiased, genome-wide analysis using thousands of mRNA-specific probes (conception paper: Fodor et al., 1991). Early microarray studies on human brain tissue revealed upregulation of immune signalling genes, including cytokines and chemokines. Here, their altered expression pointed to a significant microglial inflammatory component in AD pathogenesis (Weeraratna et al., 2007; Xu et al., 2006). Later microarray studies in AD mouse models confirmed widespread microglial gene expression changes, identifying a module of immune-associated genes that correlated almost perfectly with increasing Aβ plaque pathology (Matarin et al., 2015). Importantly, *Trem2* emerged as a central hub gene within this module, identifying its central role in controlling microglial transcriptional responses to Aβ plaques. The second advance in transcriptomic profiling was the development of bulk RNA sequencing (conception: Mortazavi et al., 2008), which enabled genome-wide expression analysis without reliance on predefined probe sets. Using this approach, further studies identified gene networks associated with the microglial innate immune response, again placing *Trem2* at the centre. These networks also included complement pathway components, lysosomal genes, and multiple AD risk genes implicated in GWAS (Humphries et al., 2015; Salih et al., 2019).

The third major advancement in transcriptomic techniques was the development of single-cell RNA sequencing (conception papers: Islam et al., 2011; Tang et al., 2009), which enabled the isolation and individual sequencing of microglia. A seminal study by Keren-Shaul et al. (2017) demonstrated that microglia within the same tissue could be clustered

into heterogeneous subpopulations based on transcriptional similarities. This approach distinguished homeostatic microglia from a novel subtype termed disease-associated microglia (DAM), which exhibited a gene expression profile resembling a microglial immune response to Aβ pathology. Importantly, analysis of DAM in *Trem2*-knockout mice revealed that in the absence of *Trem2*, microglia fail to upregulate genes involved in phagocytosis, lipid metabolism, and inflammation suppression, highlighting *Trem2*'s critical role in promoting a phagocytic anti-inflammatory microglial response to Aβ plaques. Subsequent studies have consistently confirmed the existence of diverse microglial states in AD and the pivotal role of *Trem2*-dependent transcriptional states (Olah et al., 2020; Sun et al., 2023). Moreover, a similar *TREM2*-dependent gene signature was observed in microglia that had internalised Aβ (Grubman et al., 2021).

Although it is widely assumed that DAM microglia and related transcriptomic states are present in microglia surrounding Aβ plaques, this could not be confirmed without spatially resolved gene expression. The fourth transcriptomic advancement was the advent of spatial transcriptomics (conception paper: Stahl et al., 2016), which enabled the analysis of gene expression in defined regions of slide-loaded tissue sections. This technique led to the discovery of plaque-induced genes (PIGs), which showed an increase in immune-associated gene expression as plaque density increased within predefined regions (Chen et al., 2020). These findings were the first to establish a spatial relationship between the accumulation of Aβ plaque pathology and the enrichment of immune-related genes, including *Trem2*, in whole transcriptome analysis.

1.5.5 Microglial phagocytosis of plaques in AD

Following the discovery that microglia cluster around Aβ plaques, it was hypothesised, given their known phagocytic function, that microglia might directly ingest plaque-associated Aβ. This prompted a series of *in vitro* studies investigating the mechanisms underlying Aβ uptake. Early work using primary microglia cultured from dog brain demonstrated that microglia could indeed engulf plaque-associated Aβ (Frackowiak et al., 1992). Subsequent studies in cultured murine microglia identified key receptor systems involved in this process. Scavenger receptors such as CD36, CD14, and CD47 were shown to mediate uptake of aggregated Aβ42, with phagocytosis being blocked by specific antagonists (Bamberger et al., 2003; Koenigsknecht and Landreth, 2004; Paresce et al., 1996). Toll-like receptors (TLRs), particularly TLR2 and TLR4, were also implicated in regulating microglial activation and Aβ uptake (Reed-Geaghan et al., 2009; Tahara et al., 2006), while liver X receptors (LXRs) emerged as modulators of this phagocytic function under inflammatory conditions (Terwel et al., 2011; Zelcer et al., 2007). Translation of these findings into mouse models

with genetic deletion or pharmacological modulation of scavenger receptors, TLRs, and LXRs significantly altered Aβ plaque burden in mouse models, highlighting the importance of receptor-mediated microglial activity in Aβ clearance (Tahara et al., 2006; Terwel et al., 2011; Zelcer et al., 2007). Of note, inflammation was found to modulate microglial uptake of Aβ, with heightened levels of inflammatory cytokines reducing phagocytosis. However, treatment with anti-inflammatory agents such as ibuprofen helped to restore microglial phagocytic function, suggesting that an anti-inflammatory microglial phenotype may promote more effective plaque clearance (Heneka et al., 2005; Koenigsknecht-Talboo and Landreth, 2005; Zelcer et al., 2007).

Since these studies, Aβ has been frequently observed within microglia surrounding plaques in both human AD postmortem tissue and in the brains of AD mouse models (Condello et al., 2015; D'Andrea et al., 2004). However, even from the earliest observations of this accumulation, the continued presence and growth of plaques has suggested that microglia are ultimately ineffective at clearing Aβ pathology (Itagaki et al., 1989). Several mechanisms may underlie this inefficacy. First, numerous studies have shown that once Aβ is internalised, microglia often struggle to degrade it, leading to impaired autophagic processes, lysosomal enlargement, and the onset of cellular senescence (Baik et al., 2016; Cho et al., 2014; Frackowiak et al., 1992; Halle et al., 2008; Paresce et al., 1997). Second, under chronic immune conditions such as those present in AD, and with ageing, microglia exhibit reduced phagocytic capacity (Floden and Combs, 2006). Notably, experiments have shown that microglia from young or wild-type mice can restore phagocytic function and facilitate plaque clearance when transplanted into AD mouse models (Daria et al., 2017; Hellwig et al., 2015). A third explanation is that microglia may not adequately recognise Aβ as a pathogenic target. This is supported by findings from Aβ immunotherapy studies, where plaque clearance is significantly enhanced once Aβ is sufficiently opsonised with antibodies (Bard et al., 2000; Halle et al., 2015; Schenk et al., 1999). This process has been shown to depend on the engagement of microglial Fc receptors binding to the Fc region of antibodies, stimulating phagocytosis and degradation. These findings suggest that Fc receptor activation could provide a critical stimulus for efficient microglial uptake and clearance of Aβ and is the current hypothesis for the mechanism of action for the FDA-approved immunotherapies (Gogesch et al., 2021).

1.5.6 Microglial phagocytosis of synapses in AD

A consistent feature of AD pathology is the local loss of synapses within and surrounding Aβ plaques (Bittner et al., 2012; Spires et al., 2004). Two main mechanisms have been proposed to explain this: either neurites are sterically displaced by the plaques, or microglia

actively phagocytose synapses that have been damaged by plaque-associated toxicity. Furthermore, the persistent presence of plaques, despite reports of microglial internalisation of Aβ, raises the hypothesis that microglia clustered around plaques may be primarily engaged in the removal of damaged synapses (Edwards, 2019). This role is also consistent with the known role of microglia in controlling network connectivity through developmental synaptic pruning (Paolicelli et al., 2011; Schafer et al., 2012). Despite this theoretical hypothesis, direct evidence of plaque-induced microglial internalisation of synaptic elements around plaques remains limited. Most studies demonstrating synaptic phagocytosis by microglia have involved the injection of oligomeric Aβ, either in cell culture or into wild-type mice, where an increase in microglial synapse engulfment has been observed (De Schepper et al., 2023; Hong and Stevens, 2016). Similarly, in young NLF mice, which have elevated levels of oligomeric Aβ but no plaques, the internalisation of synaptic material within microglia is increased (Rueda-Carrasco et al., 2023). However, confirmation of increased microglial synapse engulfment around plaques has only recently been shown in a study of postmortem human tissue (Tzioras et al., 2023). The scarcity of direct evidence may in part be due to the rapid degradation of synaptic elements within microglia, making them difficult to detect. As such, much of the current understanding of microglial synapse phagocytosis remains indirect, from studies that manipulate microglial recognition towards ‘eat me’ signals that guide phagocytosis.

1.5.7 Trem2 and microglial phagocytosis in AD

Early *in vitro* studies demonstrated that *Trem2* expression modulates microglial phagocytosis of apoptotic neurons in a dose-dependent manner, with knockdown impairing and overexpression enhancing uptake (Takahashi et al., 2005). This has since been consistently replicated, with studies showing reduced engulfment of apoptotic neurons by *Trem2*-deficient microglia (Hsieh et al., 2009; Kawabori et al., 2015). Similarly, microglia harbouring loss-of-function *Trem2* mutations, such as *T66M* and *W50C*, exhibited reduced uptake of apoptotic cells (Garcia-Reitboeck et al., 2018). This *Trem2*-dependent phagocytosis has been shown to be substrate dependent, as *Trem2* knockout microglia showed no impairment in the phagocytosis of E. coli, zymosan, or fluorescent beads (Garcia-Reitboeck et al., 2018; Hsieh et al., 2009). Similarly, phagocytosis of Aβ appears to be dependent on the presence of ligands other than Aβ alone. It was initially reported that there were no significant difference in the microglial uptake of Aβ between WT and *Trem2* knockout microglia in culture (Wang et al., 2015). However, a subsequent *in vivo* study by the same group showed that *Trem2* knockout microglia contained less fibrillar Aβ in the vicinity of plaques, suggesting that Aβ uptake may depend on the presence of *Trem2* ligands within the plaque environment (Wang et al., 2016). Translating these findings to cell culture, it was shown that Aβ uptake

was unaffected by *Trem2* expression in the absence of ligands. However, with the addition of LDL or CLU, Aβ uptake increased in wild-type microglia and was significantly reduced in *Trem2*-knockout microglia, establishing a ligand-dependent effect of TREM2-mediated Aβ phagocytosis (Yeh et al., 2016). Although most studies focus on TREM2's role in Aβ phagocytosis rather than synapses, Meilandt et al. (2020) found that dendritic spine density near plaques declined with decreasing *Trem2* gene dosage (WT > heterozygote > KO), suggesting that functional *Trem2* may actually inhibit microglial synapse elimination near Aβ plaque deposits.

The observation that reduced *Trem2* gene dosage impairs microglial phagocytosis has led to the hypothesis that this may result in increased Aβ plaque load due to diminished clearance. However, findings across these studies have been mixed. Some reported the expected increase in plaque accumulation in *Trem2*-deficient mice (Wang et al., 2015), while others observed either no significant change (Yuan et al., 2016) or even a decrease in plaque burden (Jay et al., 2015). Similarly, in mice expressing the AD-associated $Trem2^{R47H}$ variant, no change in total plaque load was detected (Cheng-Hathaway et al., 2018). These discrepancies may reflect differences in the age at which the animals were assessed. For example, Meilandt et al. (2020) demonstrated that *Trem2* knockout led to increased plaque burden at early ages, but reduced plaque load at later ages. These results suggest a complicated interaction between *Trem2* activity and age that may not purely be driven by changes in phagocytosis.

TREM2 enhances phagocytosis through various downstream signalling pathways activated upon ligand engagement, primarily via its adaptor protein DNAX-activating protein of 12 kDa (DAP12). DAP12 contains immunoreceptor tyrosine-based activation motifs (ITAMs) that initiate downstream signalling cascades. A key mechanism underlying phagocytic regulation is the activation of the ERK pathway, which promotes F-actin polymerisation and cytoskeletal remodelling, facilitating the membrane dynamics required for effective engulfment (Takahashi et al., 2005). This ERK phosphorylation is likely mediated by SYK activation downstream of the adaptor protein DAP12 (Hamerman et al., 2006; Kim et al., 2017). Supporting this, SYK knockout mice exhibit impaired cytoskeletal organisation and fail to form phagocytic cups (Wang et al., 2022). Moreover, TREM2–DAP12 signalling activates the PI3K–AKT pathway, which supports microglial survival and metabolic function (Ulland et al., 2017). This pathway also promotes the expression of transcription factors such as C/EBPα. Increased levels of C/EBPα then upregulate scavenger receptors like CD36, enhancing phagocytic capacity through an indirect, transcriptionally mediated mechanism (Kim et al., 2017). Thus, TREM2 regulates phagocytosis by not only promoting

immediate cytoskeletal changes but also increasing the expression of receptors associated with phagocytosis.

1.5.8 The complement system in AD

The phagocytosis of synapses, Aβ plaques, and other cellular debris often relies on opsonisation, a process in which surface tagging with specific 'eat me' signals allow microglia to recognise a target for phagocytosis. An exogenous example is the previously mentioned Aβ targeting antibodies, enabling microglia to recognise plaques as pathogenic. Endogenous opsonisation is often performed by the complement system. This is highlighted by developmental studies showing that complement inhibition impairs microglial synapse elimination, resulting in an aberrant increase in synaptic density (Schafer et al., 2012; Stevens et al., 2007). Genetic evidence further supports this role, whereby variants in the complement component *C4* have been linked to increased complement-mediated synaptic pruning and a heightened risk of developing schizophrenia (Sekar et al., 2016).

In human postmortem AD brains, early studies have shown a significant increase in complement protein C1q tagging at both Aβ plaques and tau tangles (Afagh et al., 1996; Ishii and Haga, 1984; Webster et al., 1997). Furthermore, GWAS studies have also found variants in the complement receptor 1 (*CR1*) and the complement-activated serine protease (*C1S*) genes that increase the risk of developing AD (Bellenguez et al., 2022; Jiwaji et al., 2022). Moreover, complement proteins consistently appear in AD-associated genetic studies, including spatial transcriptomics analysis revealing increased complement expression with increasing plaque density (Chen et al., 2020). Together, these findings point to a potential role for complement in AD.

The complement system is a complex cascade of proteins produced and secreted by various cell types in the brain (Nimmo et al., 2024). However, it appears microglia are the primary source of C1q, as microglia-specific deletion of the C1q subunit encoding *C1QA* gene nearly abolishes C1q expression (Fonseca et al., 2017). C1q initiates the classical complement cascade, which functions to clear damaged structures, through the following steps (Figure 1.5):

1. C1q protein, released by microglia, binds and tags damaged synapses or plaques, subsequently recruiting C1r and C1s proteases and activating their proteolytic function, forming the C1 complex,
2. The C1 complex cleaves extracellular C4 into C4a and C4b, and C2 into C2a and C2b. C4a and C2b are released, while C2a remains bound to membrane-associated C4b, forming the C4b2a complex, also known as the C3 convertase,

3. C3 convertase cleaves C3 into C3a and C3b,
4. C3b is then processed by the extracellular protease Factor I into iC3b,
5. iC3b remains on the synapse or plaque and acts as an opsonin, attracting microglia via their C3 receptors.

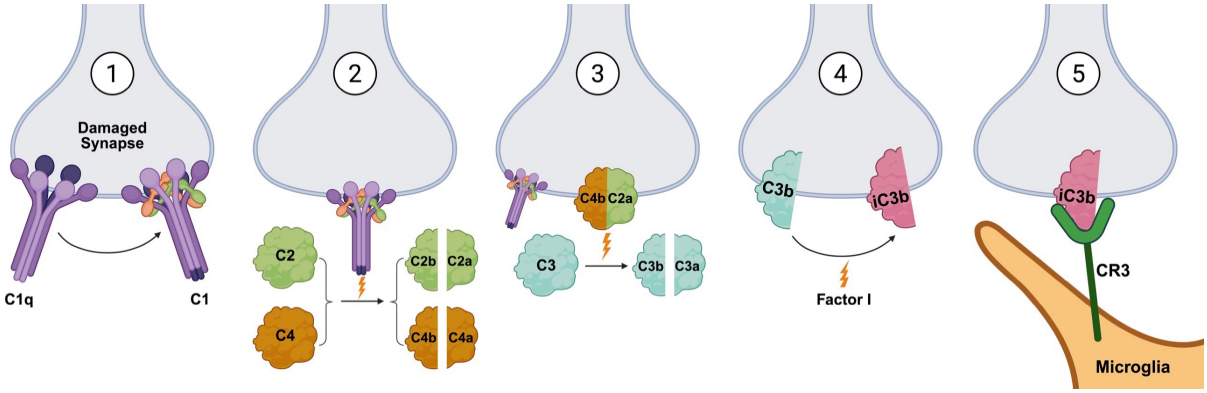

Figure 1.5 Proposed complement cascade involvement in damaged synapse removal
Steps described above. Original diagram, Biorender.

At this point, microglia can phagocytose the opsonised target. However, the presence of the membrane attack complex (MAC) components around plaques in AD postmortem tissue (Webster et al., 1997) and associated with synapses in AD mouse models (Carpanini et al., 2022; Zelek et al., 2024) suggests that the process may cascade further:

6. Some C3b molecules may stick next to the existing C4b2a complex, forming the C5 convertase,
7. The C5 convertase cleaves C5 into C5a and C5b. C5b initiates the assembly of the membrane attack complex through binding C6, C7, C8 and C9, forming the MAC.

The MAC is a non-selective pore that forms in the plasma membrane, disrupting osmotic balance and triggering cell death pathways. An additional proposed mechanism is that MAC precursors, such as C5b6-7, could be generated at plaques and diffuse towards and attach to nearby synapses in a ‘bystander’ mechanism, leading to local MAC formation (Carpanini et al., 2022).

Experimental manipulation of the complement system in mouse models of AD has provided compelling evidence for the importance of this pathway. A seminal study demonstrated that microglial synaptic engulfment induced by oligomeric Aβ depends on the complement receptor CR3, with its deletion inhibiting microglial synapse uptake (Hong et al., 2016). Furthermore, global knockout or pharmacological inhibition of C3 in AD mouse models resulted in increased plaque burden, reduced microglial activation, preserved synaptic density, and improved cognitive performance, suggesting that C3 plays a role in both plaque and synaptic phagocytosis in AD (Shi et al., 2017; Wyss-Coray et al., 2002). More recent

work has highlighted the importance of the MAC, the terminal step in the complement cascade, in AD-associated synapse elimination. Components of the MAC have been detected in synaptic fractions of AD mouse brains (Carpanini et al., 2022). Additionally, global knockout of MAC components C6 or C7, as well as pharmacological inhibition of C7, prevented MAC formation, rescued plaque-associated synapse loss, and rescued behavioural deficits (Carpanini et al., 2022; Zelek et al., 2024). Although many studies have concluded that the complement system contributes to disease progression in AD by promoting synapse loss, it may also serve a protective role by eliminating plaque-associated damage before it spreads through the affected neuron and disrupts broader neural networks (Edwards, 2019).

1.5.9 Trem2 and the complement system in AD

Increased complement and Trem2 activity have been observed both at Aβ plaques (Afagh et al., 1996; Jay et al., 2015) and during brain development (Filipello et al., 2018; Schafer et al., 2012), where they play similar roles in mediating microglial phagocytosis. These overlapping functions suggest a potential interaction between the two proteins. Supporting this, *Trem2* knockout mice exhibit reduced expression of complement genes and decreased neuronal loss with ageing, implying that functional *Trem2* may facilitate complement-mediated phagocytosis (Linnartz-Gerlach et al., 2019). More direct evidence of an interaction comes from recent findings showing that C1q binds to TREM2, suggesting that C1q may recruit microglia for synaptic engulfment independently of C3 receptor signalling (Greven et al., 2025; Monroe and Lewcock, 2023). Moreover, complexes of C1q and TREM2 have been identified in both human AD brain tissue and mouse models (Zhong et al., 2023). However, recent findings suggest that the binding of C1q to TREM2 appears to inhibit complement-mediated synaptic engulfment (Monroe and Lewcock, 2023; Zhong et al., 2023). Supporting this, in a tauopathy mouse model, *Trem2* haploinsufficiency led to elevated levels of complement-mediated synapse loss. Furthermore, administration of a synthetic TREM2 protein in both a tauopathy and amyloid mouse model reduced synaptic engulfment and increased synaptic density (Zhong et al., 2023). This mechanism may also explain the gene dosage effect observed by Meilandt et al. (2020), in which reduced TREM2 expression was associated with increased plaque-induced synapse loss.

1.5.10 Phosphatidylserine as an ‘eat me’ signal

The recognition of cellular damage is thought to rely on specific damage signals that mark targets for microglial phagocytosis, commonly referred to as ‘eat me’ signals. Among the various proposed markers, the externalisation of phosphatidylserine (PtdSer) is the most widely referenced (Birge et al., 2016; Nagata et al., 2016).

Under homeostatic conditions, scramblases continuously flip PtdSer bidirectionally across the plasma membrane, while flippases actively transport PtdSer unidirectionally from the outer to the inner leaflet. Together, their coordinated activity maintains a net asymmetry of PtdSer predominantly facing the inner membrane leaflet. However, under conditions of cellular damage, flippase activity is inhibited via caspase-dependent cleavage and disrupts this balance, leading to an increased externalisation of PtdSer (Nagata et al., 2020). PtdSer externalisation can thus be seen covering plasma membranes of apoptotic neurons (Paidassi et al., 2008; Sapar et al., 2018). Moreover, synaptic pruning during development also appears dependent on the externalisation of PtdSer (Scott-Hewitt et al., 2020). C1q, among other proteins including TAM receptors, has shown an affinity to bind PtdSer, and loss of C1q leads to an increased number of synapses due to the lack of C1q-dependent removal (Paidassi et al., 2008; Scott-Hewitt et al., 2020). Furthermore, imaging and extraction of C1q-tagged synaptosomes are positive for both PtdSer and caspase-3 activity (Andoh et al., 2025; Gyorffy et al., 2018; Scott-Hewitt et al., 2020). Pharmacological and genetic manipulation of the PtdSer externalisation pathway has been shown to influence the removal of apoptotic cells and synapses in a microglia-dependent manner (Asano et al., 2004; Krahling et al., 1999; Park et al., 2021; Scott-Hewitt et al., 2020).

Although these findings suggest an important role for PtdSer in mediating microglial phagocytosis in AD, the findings are limited. In AD mouse models, Aβ plaques have been shown to be coated with PtdSer (Huang et al., 2021). In this study, the authors hypothesised that PtdSer regulates TAM receptor-mediated Aβ phagocytosis. However, this was not directly tested (Huang et al., 2021). Furthermore, an addition of PtdSer to microglial cultures has been shown to enhance the uptake of oligomeric Aβ (Park et al., 2024). At synapses specifically, Aβ-induced hyperactivity has been shown to trigger PtdSer externalisation and promote microglial engulfment (Rueda-Carrasco et al., 2023). This could suggest that near plaques, Aβ-driven synaptic hyperactivity may lead to local synapse loss via PtdSer-mediated pruning. Moreover, the microglial phagocytosis of neurons harbouring tau pathology occurs through a PtdSer-dependent mechanism, as blocking PtdSer recognition significantly inhibits this process (Brelstaff et al., 2018). Despite this growing evidence, microglial-mediated synapse and Aβ phagocytosis via C1q recognition of PtdSer around plaques remain uncharacterised.

1.5.11 Trem2 and phosphatidylserine

TREM2 has been shown to be essential for microglial synapse elimination during development, as demonstrated by an increased synaptic density and neuronal excitability in

Trem2-knockout mice (Filipello et al., 2018). This synaptic pruning appears to rely on the recognition of externalised PtdSer, as blocking its detection had no additional effect on synapse elimination in *Trem2*-knockout microglia. This suggests that PtdSer is a key mediator of TREM2-dependent engulfment (Scott-Hewitt et al., 2020). Consistent with this, AD mouse models harbouring the *Trem2*^{R47H} mutation exhibit an accumulation of externalised PtdSer at synapses, possibly reflecting an inability to recognise these synapses for engulfment (Rueda-Carrasco et al., 2023). Recent studies have shown that microglia preferentially cluster around PtdSer-rich Aβ plaques, with corresponding increases in both microglial density and TREM2 expression (Park et al., 2024). Furthermore, human AD brains with the *TREM2*^{R47H} variant show elevated levels of synaptic caspase activity, which is known to drive PtdSer externalisation, supporting the mechanism in which defective TREM2 function leads to impaired clearance of damaged synapses (Rueda-Carrasco et al., 2023).

1.5.12 Microglial regulation of plaque structure and seeding

The limited evidence of microglial phagocytic activity around Aβ plaques prompted investigations into alternative functions. Using a combined staining approach, through pairing a structural amyloid dye with an Aβ42-specific antibody, Condello et al. (2015) observed that regions of plaques not encapsulated by microglia developed ‘hotspots’ of Aβ42. These hotspots appeared to diffuse outward from the plaque core and were associated with increased neuritic dystrophy. This suggested a protective, barrier-like role for microglia, where they contain Aβ spillage to limit local damage. Supporting this, Aβ-targeting immunotherapy enhanced microglial coverage of plaques and reduced Aβ42 leakage (Condello et al., 2015). Subsequent studies expanded on this concept, proposing that plaque-associated microglia were actively compacting plaques. Therefore, the Aβ42 hotspots may not be leakage from the core but rather regions of uncompacted Aβ (Wang et al., 2016; Yuan et al., 2016). This interpretation is supported by microglial depletion studies, which demonstrate that in the absence of microglia, plaques are more diffuse and less structurally compact (Casali et al., 2020; Kiani Shabestari et al., 2022; Spangenberg et al., 2019). Interestingly, however, in these microglial studies, not only were the plaques more diffuse, but there was a reduction in the total number of plaques, suggesting that the seeding of plaques, as well as compaction, is a possible role of microglia.

This apparent microglial-dependent plaque seeding aligns with early Aβ phagocytosis studies, which showed that while microglia readily ingest Aβ, they struggle to degrade it, ultimately releasing it back into the extracellular space (Paresce et al., 1996). This intracellular accumulation leads to enlarged lysosomes packed with Aβ, whereby the acidic environment provides favourable conditions for Aβ aggregation (Friedrich et al., 2010; Su

and Chang, 2001). This Aβ-induced autophagic stress was shown to ultimately result in microglial cell death and the spillage of the intra-lysosomal Aβ aggregates into the surrounding tissue, potentially seeding plaques (Baik et al., 2016).

While these findings suggest a dysfunction in microglial autophagy, a of Aβ by microglia and direct it to lysosomes for subsequent aggregation, rather than degradation (Huang et al., 2021). Knockout of TAM receptors results in a reduction of cored plaques, supporting the idea that microglia actively contribute to plaque maturation. The authors propose that this may represent a protective mechanism in which toxic oligomers are sequestered, similar to the proposed barrier function in preventing toxic Aβ42 hotspots (Condello et al., 2015; Lemke and Huang, 2022).

An interesting candidate for the catalysis of this process is APOE, which has also been shown to aggregate within microglial lysosomes and colocalise with Aβ aggregates and extracellular Aβ plaques (Kaji et al., 2024; Spangenberg et al., 2019). Injection of these APOE aggregates into AD mouse models significantly increases plaque formation, supporting a potential role for APOE in seeding Aβ pathology (Kaji et al., 2024). Consistent with this, targeting aggregated APOE with specific antibodies has been shown to reduce Aβ plaque burden (Liao et al., 2018). Moreover, although APOE3 is the most prevalent allele in the general population, APOE4, the most common genetic risk factor for late-onset AD, exhibited greater Aβ seeding capacity (Kaji et al., 2024). These findings suggest that Aβ seeding by microglia and catalysed by APOE aggregation may represent a key mechanism of plaque formation and highlight APOE aggregates as a promising therapeutic target. Other co-aggregating factors have also been proposed, including apoptosis-associated speck-like protein (ASC) specks released by microglia following Aβ-induced inflammasome activation. Once released into the extracellular space, ASC specks bind Aβ and act as cross-seeding agents, accelerating its aggregation and promoting plaque formation. Like APOE, injection of ASC specks enhances Aβ plaque seeding, while anti-ASC antibodies reduce plaque load (Venegas et al., 2017).

1.5.13 Trem2 in the microglial regulation of plaque structure

The migration and accumulation of microglia around Aβ plaques depend critically on TREM2 signalling. Both complete deletion of *Trem2* and *Trem2* haploinsufficiency result in a reduced number of plaque-associated microglia and impaired engagement of microglial processes with plaques. In these models, plaques appear more diffuse and less compact (Meilandt et al., 2020; Wang et al., 2016; Yuan et al., 2016). Similarly, in AD human brain tissue from patients harbouring the *TREM2*^{R47H} variant, microglia coverage around plaques was

significantly reduced with a consequential increase in surrounding neuritic dystrophy (Meilandt et al., 2020; Yuan et al., 2016).

1.5.14 Microglia and lipid homeostasis

Many genes harbouring mutations that increase the risk of developing AD enrich ontology terms involved in lipid metabolism, including *LPL*, *ABCA1*, and *APOE* (Bellenguez et al., 2022; Kunkle et al., 2019). In addition to genetic factors, obesity also increases the risk of developing AD (Qu et al., 2020). Metabolomic analyses of postmortem human brains further support a role for lipid dysregulation in AD, revealing elevated levels of unsaturated fatty acids and increased catabolism and storage of cholesterol correlate with Aβ plaque burden (He et al., 2025; Snowden et al., 2017; Varma et al., 2021). Direct lipid analysis in AD has lagged behind that of proteins and RNA, largely due to the lack of standard molecular biology techniques in resolving lipid species. However, recent advances in chemical imaging technologies, particularly MALDI-MSI, have enabled the spatial mapping of lipids, which have shown localised alterations in lipid composition at Aβ plaques, with recent studies identifying plaque-induced changes to 40 distinct lipid species (Ge et al., 2023; Kiskis et al., 2015; Michno et al., 2024). In addition, there is growing evidence that lipids can directly influence plaque formation. Similar to APOE and ASC specks in plaque nucleation, cholesterol in plasma membranes has been shown to catalyse Aβ42 aggregation, suggesting that plaque seeds may initially form at the membrane surface (Banerjee et al., 2021; Habchi et al., 2018).

In the brain, astrocytes and microglia are the main cell types involved in maintaining lipid homeostasis, with microglia increasingly recognised for roles in lipid sensing, uptake, storage, and clearance, particularly under conditions of neuroinflammation (Paasila et al., 2021). For example, in obesity, microglia respond to saturated fatty acids by adopting a pro-inflammatory phenotype and accumulating intracellular lipids (Folick et al., 2022). In an AD context, single-cell transcriptomic studies of microglia from both human AD patients and mouse models of AD have shown an upregulation of genes involved in lipid-associated pathways such as *Apoe*, *Cst7*, *Trem2*, and *Lpl* (Grubman et al., 2021; Keren-Shaul et al., 2017). Interestingly, recent studies suggest that semaglutide, a GLP-1 receptor agonist originally developed for obesity and type 2 diabetes, may exert neuroprotective effects in AD by promoting anti-inflammatory microglial and astrocytic phenotypes (Folick et al., 2022; Zheng et al., 2024).

Across ageing, obesity, neuroinflammatory diseases, and surrounding plaques in AD, microglia accumulate lipids in internal membrane-bound organelles named lipid droplets

(Arbaizar-Rovirosa et al., 2023; Folick et al., 2022; Marschallinger et al., 2020). Lipid droplets form when intracellular lipid levels exceed metabolic demand, leading to the sequestration of neutral lipids, such as triacylglycerols and cholesteryl esters, within a phospholipid monolayer. They function as energy reserves whereby their merging with lysosomes triggers lipophagy, a process that breaks down stored lipids into free fatty acids, which are then used to fuel ATP production (Liu and Czaja, 2013; Olzmann and Carvalho, 2019). Although one might expect that increased energy reserves would be beneficial, microglia laden with lipid droplets exhibit impaired phagocytic capacity, elevated oxidative stress, a heightened pro-inflammatory profile, and features of cellular senescence (Marschallinger et al., 2020; Prakash et al., 2024). Genetic or pharmacological inhibition of lipid droplet formation increases the phagocytic ability of microglia and reduces overall plaque load in mouse models of AD (Prakash et al., 2024; Wu et al., 2025). It is thought that reducing lipid droplet accumulation improves phagocytic function because excessive lipid droplets compete with phagocytosed material for lysosomal degradation. Therefore, by limiting lipid droplet formation, lysosomal degradation of Aβ is restored, enabling more effective clearance (Wu et al., 2025). However, others have proposed that autophagic dysfunction may precede and drive lipid droplet accumulation, rather than result from it (Xu et al., 2021). Notably, in microglial cultures, the induction of microglial lipid droplet accumulation by fibrillised Aβ is only observed in microglia harbouring the *APOE4* AD risk allele (Haney et al., 2024).

1.5.15 Trem2 in microglial lipid homeostasis

In transcriptomics studies, the observed upregulation of lipid-associated genes in disease-associated microglia has been shown to be mediated by *Trem2* expression (Keren-Shaul et al., 2017). This is perhaps unsurprising, given that TREM2 is a lipid-sensing receptor activated by ligands such as phospholipids (Wang et al., 2015; Yeh et al., 2016). In the vicinity of Aβ plaques, where both lipid accumulation and microglial clustering occur, TREM2-driven lipid signalling is amplified, contributing to microglial activation. Supporting this, a study of microglial responses to demyelination found that the metabolism and sequestration of cholesterol into lipid droplets were TREM2-dependent, with *Trem2*-knockout microglia failing to form lipid droplets in response to myelin debris (Gouna et al., 2021). Similarly, in AD mouse models, microglia carrying the $Trem2^{R47H}$ risk variant exhibited reduced lipid droplet accumulation around plaques (Claes et al., 2021), likely due to the impaired lipid-binding capacity of the $TREM2^{R47H}$ receptor (Atagi et al., 2015; Wang et al., 2015; Yeh et al., 2016). However, in contrast, Nugent et al. (2020) reported that *Trem2*-knockout mice exhibited heightened lipid droplet accumulation following demyelination, which was attributed to impaired expression of key cholesterol transport and metabolism

genes, including *Npc2*, *Apoe*, and *Apoc1*. These incongruous findings likely reflect differences in disease models, lipid species, or stages of microglial activation, but collectively they indicate a central role of TREM2 in regulating lipid metabolism with emerging evidence implicating it in AD pathogenesis.

1.5.16 Microglial interaction with tau pathology

As with Aβ pathology, tauopathies, including some forms of FTD, and mouse models of FTD exhibit enhanced microgliosis (Woollacott et al., 2020; Yoshiyama et al., 2007). In human AD tissue, microglia are frequently found interacting with and surrounding tau tangles (Bolos et al., 2016). *In vitro* studies further demonstrate that microglia can internalise and degrade hyperphosphorylated tau and tau aggregates derived from both FTD mouse models and human FTD brain tissue (Bolos et al., 2016; Luo et al., 2015). This process is enhanced by the application of anti-tau antibodies, which facilitate tau uptake, similar to the anti-Aβ antibodies, through Fc receptor–mediated opsonisation (Luo et al., 2015). The ability of microglia to phagocytose tau is impaired by genetic knockout of the phagocytic receptor CX3CR1 (Bolos et al., 2017). Notably, deletion of CX3CR1 in WT mice expressing humanised tau results in increased tau hyperphosphorylation, indicating that microglial phagocytic ability plays a regulatory role in limiting tau pathology (Maphis et al., 2015). Moreover, transferring microglia that lack the CX3CR1 receptor from older mice with humanised tau into the brains of young wild-type mice was enough to promote tau hyperphosphorylation in the areas surrounding these microglia. This suggests that either previously phagocytosed hyperphosphorylated tau is being exocytosed or that these microglia actively promote tau hyperphosphorylation (Maphis et al., 2015).

1.5.17 Trem2 in the microglial interaction with tau pathology

In FTD models, *Trem2*-knockout reduces microgliosis but does not alter tau pathology, suggesting that TREM2-driven inflammation may not influence tau accumulation in the absence of Aβ plaque pathology (Leyns et al., 2017). In contrast, *Trem2*-knockout AD models exhibit significantly increased tau hyperphosphorylation following injection of homogenised human AD tau aggregates, compared to mice expressing *Trem2*. This suggests that TREM2 plays a critical role in restricting the spread of tau pathology (Leyns et al., 2019). Additional findings revealed increased tau phosphorylation in peri-plaque regions of *Trem2*-knockout mice, supporting the idea that TREM2-mediated microglial responses may contain plaque-induced tau propagation. Importantly, in human AD brains carrying $TREM2^{R47H}$ or $TREM2^{R62H}$ AD risk variants, tau pathology surrounding Aβ plaques was significantly increased (Leyns et al., 2019). Together, these results highlight a possible link

between Aβ plaque pathology, TREM2-dependent microglial activity, and tau propagation in AD.

1.6 Summary and present study

Although introduced over a decade ago, knock-in mouse models of AD remain the most faithful to human AD compared to transgenic models, which often rely on APP overexpression and develop Aβ plaques independent of old age (Saito et al., 2014). Throughout this project, I therefore employed the use of the NLF knock-in model of AD at 18 months of age, an age that captures the progression of Aβ plaques into old age following their initial deposition in the hippocampus at around 9 months (Figure 1.3; Benitez et al., 2021). NLF mice were selected over NLGF mice as they express the non-mutated Aβ peptide found in LOAD, resulting in a broad range of plaque types, whereas NLGF mice carry the Arctic mutation, which increases Aβ aggregation and skews pathology toward highly compact plaques (Lord et al., 2011; Saito et al., 2014). Furthermore, NLGF mice shown early onset plaque formation seen from as early as 2 months, timing that does not reflect LOAD (Benitez et al., 2021; Saito et al., 2014). I further examined microglial involvement in Aβ plaque pathology by investigating the impact of the *Trem2*^{R47H} risk mutation, which impairs microglial function. This was achieved using wild-type (WT) and NLF mice carrying the *Trem2*^{R47H} mutation in homozygosity, generating *Trem2*$^{R47H/R47H}$ (Trem2^{R47H}) and NLFx*Trem2*$^{R47H/R47H}$ (NLFTrem2^{R47H}) mice, respectively.

There is strong evidence that microglia are highly responsive to Aβ plaque pathology. Imaging studies consistently show microglia clustering around and interacting with Aβ plaques, while genetic analyses implicate them in key functions related to lysosomal activity, lipid metabolism, and phagocytosis. Numerous studies have demonstrated that plaque-associated microglia actively engage in these roles, particularly in the phagocytosis of Aβ and synapses. This project aims to build on these findings by providing a more direct investigation of the roles of plaque-associated microglia using the recent advance of spatial transcriptomics to characterise their gene expression profiles in NLF mice. This was also studied in NLFTrem2^{R47H} mice to develop an understanding of the importance of functional Trem2 in the microglial response to Aβ pathology. Furthermore, the historical lack of translation from pre-clinical mouse studies to clinical human trials emphasises the need for studies to translate their findings to human AD tissue. Therefore, in this project, I aimed to also confirm the microglial spatial transcriptomics findings from mouse to human tissue.

Plaque heterogeneity, defined by both structural morphology and age-related maturation, is a key variable in understanding the differential impact of Aβ plaques on surrounding tissue.

These studies may help to explain key gaps in the amyloid cascade hypothesis, such as the temporal disconnect between initial plaque deposition and the onset of cognitive decline. Structural studies have revealed that cored plaques tend to be more neurotoxic than diffuse plaques, which are considered relatively inert. However, these findings are limited by low-throughput approaches and a lack of reliable staining methods to detect diffuse plaques. To address this, I aim to develop a higher-throughput method for assessing the impact of plaque morphology on the surrounding tissue microenvironment. Temporal tracking of plaque maturation has also recently been explored using ^{15}N metabolic labelling through diet, which enables a non-invasive method to track temporal Aβ deposition without reliance on structural dyes (Michno et al., 2021). In this project, I apply this approach to investigate how the age and structural characteristics of plaques influence the surrounding tissue.

The primary aim of this study is to advance our understanding of the relationship between Aβ plaques and their impact on the surrounding tissue microenvironment.

CHAPTER 2

MATERIALS AND METHODS

2.1 Mice

The mice used in this study were group-housed (2-5) with same sex littermates with an *ad libitum* supply of food and water, under a 12-hr light/dark photoperiod, at a controlled temperature and humidity. Experiments were performed in accordance with the UK Animal Scientific Procedures Act, 1986 and following local ethical review. Scientific procedures were performed under the home office project licence: PPL70/89999 (2016-2021) and PPL8988901 (2021-2026).

Homozygous $App^{NL\text{-}F/NL\text{-}F}$ (NLF) knock-in mice were developed by the Saido group at the RIKEN Centre for Brain Science, Japan (Saito et al., 2014), and were a gift to the Edwards Lab. $Trem2^{R47H/R47H}$ ($Trem2^{R47H}$) knock-in mice were developed by and subsequently purchased from the Jackson Laboratory. Both models were developed on a C57BL/6J (WT) background. NLF mice were crossed with $Trem2^{R47H}$ mice to generate homozygous $App^{NL\text{-}F/NL\text{-}F}Trem2^{R47H/R47H}$ mice ($NLFTrem2^{R47H}$). C57BL/6J (WT) mice were purchased from Charles River. Throughout this thesis, equal numbers of male and female mice were used in each experimental group. However, sex differences were not analysed, as the research questions were not sex-specific and thus the study was not sufficiently powered to support valid statistical comparisons between males and females.

2.2 Mouse tissue extraction

Mice were decapitated, and the brain was rapidly extracted on ice and bisected in the sagittal plane. One hemisphere was drop-fixed in 10% formalin at 4°C overnight, then transferred to a 30% sucrose, 0.02% sodium azide in phosphate-buffered saline (PBS) solution for long-term storage at 4°C. For RNA extraction, the other hemisphere was dissected into the hippocampus, cortex, midbrain, cerebellum, olfactory bulb, and brainstem. The dissected tissues were snap-frozen on dry ice and stored at -80°C. For the stable isotope labelled mice, the other hemisphere was snap-frozen whole on dry ice and stored at -80°C. For field electrophysiology, tissue processing followed the protocol described below (see - Field Electrophysiology – Slice Preparation).

2.3 Mouse tissue immunohistochemistry

2.3.1 Tissue sectioning: free-floating sections

Formalin-fixed hemispheres were orientated to the long axis of the hippocampus and loaded onto a dry-ice-frozen stage of a frozen sledge microtome. For each mouse, a total of 36 serial sections containing transverse ventral-medial hippocampus were cut at 30 µm. Sections were collected into 0.02% sodium azide in 0.1 M PBS in 24-well plates and stored at 4°C.

2.3.2 Free-floating histology

Free-floating 30 µm sections underwent antigen retrieval in 10 mM pH 9 Tris-EDTA buffer for 30 min at 80°C. The tissues were then permeabilised three times in 0.3% Triton X-100 in PBS (PBST) for 10 min. Non-specific binding was blocked in appropriate blocking solution (10% donkey serum, 3% Goat serum, or 2% Fish gelatine, in PBST) for 1 hr, followed by incubation with the appropriate primary antibodies (see key resources table, appendix) in blocking solution at 4°C overnight. Sections were washed three times in PBST for 10 min, followed by incubation with appropriate secondary antibodies (see key resources table, appendix) in blocking solution for 2 hrs in the dark at room temperature (RT). Finally, nuclei were counterstained with 4′,6-diamidino-2-phenylindole (DAPI) for 5 min at RT. For various experiments (see key resources table, appendix), plaques were then dye-labelled (Amytracker520, qFTAA and/or hFTAA) for 30 min at RT. Free-floating sections were mounted onto superfrost plus slides and coverslipped using Fluoromount-G mounting medium.

2.3.3 Widefield microscopy

Fluorescent widefield photomicrographs of whole cross-section hippocampal regions were acquired using an EVOS® FL Auto Cell Imaging Microscope with a 20X objective. Imaging was performed under constant light intensity, gain, and exposure settings. The system was equipped with four fluorescence channels:

DAPI: Ex 357/44 nm, Em 447/60 nm
GFP: Ex 482/25 nm, Em 524/24 nm
TxRed: Ex 585/29 nm, Em 628/32 nm
Cy5: Ex 628/40 nm, Em 692/40 nm

For each animal, 2–3 hippocampal sections were imaged. The use of widefield microscopy is indicated in the corresponding figure legends.

2.3.4 Confocal microscopy

Fluorescent confocal photomicrographs were acquired using a Zeiss LSM 880. All images presented and analysed were taken on a 20X air objective. For each imaging experiment, the following parameters were optimised and then maintained: laser intensity, master gain, digital offset, pixel sampling rate, digital zoom, wavelength emission collection range, imaging speed (pixel exposure), pixel averaging, scanning direction, pinhole diameter, and track switching method.

Laser intensity, master gain, and digital offset were adjusted in range indicator mode to prevent under- and over-saturation while achieving a normal distribution of pixel intensities. Pixel sampling was determined according to the Nyquist theorem, calculated using the 'optimise' setting in the LSM 880 Zen Black software. Imaging speed and pixel averaging were adjusted to maximise signal accuracy while minimising fluorophore bleaching. Digital zoom, scanning direction, and track switching method were primarily adjusted to balance image acquisition time with accurate channel-to-channel correlation. The wavelength emission collection range was optimised to reduce spectral bleed-through while ensuring maximal signal collection from the corresponding fluorophores. Whole hippocampal images were acquired using tile scanning mode. For z-stack imaging, the pinhole diameter was set to 1 Airy unit based on the longest emission wavelength. However, to reduce acquisition time, the stack step size was set to 3 µm. Digital gain was not used in any imaging experiment.

For linear unmixing of qFTAA and hFTAA emissions, whole hippocampal images were acquired using online fingerprinting mode. This hyperspectral imaging technique relied on reference emission spectra obtained from tissues stained separately with either qFTAA or hFTAA, which remained constant throughout the experiment. Imaging of all secondary antibody fluorophores, Amytracker520, and DAPI was performed under channel mode.

For each animal, 2–3 whole hippocampal sections were imaged. The use of confocal microscopy is indicated in the corresponding figure legends.

2.3.5 Histological analysis

For all protein towards plaque analysis, a mean plaque value was first calculated from all plaques in the hippocampal region. An animal mean was then determined by averaging the plaque means across 2–3 hippocampal regions per animal. All histological analysis was performed in FIJI. The measured regions of interest (ROIs) were created as described below:

Creating ROIs for protein intensity towards Amytracker520 defined plaques (Figures: 3.3, 3.6, 3.8, and 3.9)

ROI creation was carried out using Edwards Lab-written semi-automated macros within FIJI as described below and in Wood et al. (2022). The macros are published and available at: *https://doi.org/10.5281/zenodo.5847431.*

1. *Plaque thresholding macro*

Although plaque detection using dyes is a rigid staining method, differences in background signal can vary greatly. Therefore, the Edwards Lab developed this macro to tackle the signal-to-noise variability of these dyes.

A hippocampal ROI was manually drawn to restrict all subsequent analyses to the hippocampus. Next, the image was processed through a range of threshold values. For each threshold, the Analyse Particles function was applied to detect particles >10 μm^2, as smaller particles were considered background noise. The total particle area was then plotted against the threshold value. The resulting data formed an exponential decay curve, where the plateau values indicated thresholds that captured the 'real' signal, as further increases in threshold resulted in minimal changes to the captured signal. The final 40% of plotted data (plateau) were plotted, with a one-phase decay line; the lowest threshold value to fit this model ±2 (allowing for minor manual editing) was chosen as the threshold value.

2. *Plaque concentric circles macro*

For each plaque within the selected hippocampal region, concentric circles were drawn outwards with increasing 10 µm radii from the plaque, reaching a final circle with a radius of the average plaque radius plus 100 µm. As most plaques in the plaque ROIs were not more than 100 µm apart, data are shown up to 50 µm from the plaque edge.

3. *Concentric circles macro for controls*

For images from WT and $Trem2^{R47H}$ mice, ten randomly placed circles, each with a 20 µm radius, were positioned within the hippocampus. To imitate the plaque measurements, circles were drawn outwards with increments of 10 µm radii, reaching a distance of 100 µm from the inner circle.

4. *Protein intensity macro*

Fluorescence intensity within the regions identified as microglia (AU/pixel) was calculated for plaque regions and radiating concentric rings using FIJI's 'measure' function.

Creating ROIs for protein intensity towards Aβ-, qFTAA-, and hFTAA-defined plaques (Figures: 5.5, 5.6, 5.7, 5.8 and 5.9)

Aβ-defined plaques were less structurally spherical than Amytracker-defined plaques. Therefore, instead of using concentric circular rings, Aβ-defined plaque ROIs were shaped to radiate outward following the plaque's contour. Macros for this analysis were self-written.

1. *hFTAA thresholding macro*

Z-stacked images were first projected onto a single plane using the standard deviation projection method. Thresholding was performed as above, see ‘plaque thresholding macro’.

2. *Plaque merging*

Small areas of hFTAA positivity were often surrounded by larger areas of hFTAA positivity; these were presumed to belong to a single plaque and were therefore merged into a single plaque ROI. To achieve this, thresholded particles from Macro 1 were expanded by 2.5 μm, ensuring that any particles <5 μm apart were incorporated into the same expanded ROI. These overlapping particles were then merged and saved as hFTAA-positive ROIs.

3. *qFTAA thresholding*

The signal-to-noise ratio of qFTAA was significantly higher than that of hFTAA and Amytracker520, with background signal approaching zero and real signal nearing saturation. Therefore, a single threshold value was selected and consistently applied across all images within an experimental batch to identify qFTAA-positive particles.

4. *Labelling hFTAA particles as qFTAA + or -*

The area within qFTAA particles was set to a pixel value of 255, all regions outside of these areas were set to a value of 0. The hFTAA particles from Macro 2 were loaded onto this edited image. Any hFTAA particle that contained pixels with values at 255 were labelled as hFTAA and qFTAA positive, whereas particles containing pixel values of only 0 were labelled as hFTAA positive but qFTAA negative.

5. *Aβ thresholding*

Similarly to qFTAA, the Aβ staining background was consistent across images. Therefore, a single auto threshold method (depending on the experiment, either otsu or triangle methods) was applied to the Aβ-stained images. The thresholded particles were added as ROIs.

6. *Aβ plaque merging*

Similarly to Macro 2, any Aβ particles within 5 μm of each other were considered as the same plaque.

7. *Removing overlapping data.*

To prevent the overlapping of concentric shapes generated in Macro 8, a cropping limit was applied. Each Aβ-defined ROI was expanded by 30 μm. Regions where two or more 30 μm expansions overlapped were removed from the expanded ROIs, ensuring a final 30 μm ROI set without overlaps. This ensured no data duplication in the final analysis.

8. *Creating concentric rings*

From each Aβ-defined plaque ROI, concentric rings of 10 μm thickness were generated, radiating outward up to a 30 μm limit. This created ROIs for analysis at the following distances: Plaque edge–10 μm (10 μm label), 10 μm–20 μm (20 μm label), 20 μm–30 μm (30 μm label).

9. *Removing the overlap of concentric rings*

The cropping limit ROIs generated in Macro 7 were applied to the concentric rings generated in Macro 8. The rings were then cropped accordingly to ensure no overlap.

10. *Trimming ROIs to within the hippocampal area*

The manually defined hippocampal ROI generated in Macro 1 was used to crop the concentric ring ROIs, thereby restricting all subsequent measurements to the hippocampal region.

11. *Final Labelling*

The labelled ROIs created in Macro 4 define regions positive for hFTAA and qFTAA. These regions were loaded into the Aβ-defined plaque ROIs. Depending on the overlap, ROIs were thus labelled as Aβ+hFTAA+qFTAA+ (Aβ+h+q+), Aβ+hFTAA+qFTAA- (Aβ+h+q-), or Aβ+hFTAA-qFTAA- (Aβ+h-q-). The resulting ROIs are a set of Aβ-defined plaques, with radiating 10 μm concentric rings up to 30 μm, with no overlap, and labelled as to their hFTAA and qFTAA positivity.

12. *Protein intensity measurement*

The final ROI set created in Macro 11 is overlapped onto the appropriate fluorescence image, and the fluorescence intensity is measured through FIJI's 'measure' function and normalised to ROI area and averaged for each plaque type.

2.4 Mouse RNA extraction and quantification

2.4.1 RNA extraction

Frozen hippocampal tissue was homogenised in QIAzol RNA lysis reagent using a Polytron PT 3000 homogeniser at 7500 rpm for 30 s. Chloroform was added for phase separation and centrifuged at 12000 g for 15 min. RNA was extracted, and DNA was digested using the miRNeasy Mini Kit according to the manufacturer's instructions. RNA quality and concentration were assessed using spectrophotometry by measuring A_{260}/A_{280} ratios. Total RNA extract was stored at -80°C.

2.4.2 Reverse transcription

RNA was diluted to 2 µg in 7.5 µl of RNase-free water. The samples were first thermocycled at 37°C for 15 min with RNaseOUT™ and amplification grade DNaseI to prevent RNase activity and remove contaminating DNA. The reverse-transcription protocol was performed using the High-Capacity cDNA Reverse Transcription kit according to the manufacturer's instructions. The resulting cDNA was subsequently diluted in 60 µl of RNase-free water to form a cDNA stock, which was subsequently stored at -20°C.

2.4.3 RT-qPCR

cDNA samples were tested in triplicate in a 20 µl reaction volume in skirted 96-well plates. Each 20 µl reaction contained 10 µl of SsoAdvanced™ Universal SYBR® Green Supermix, 0.5 µl of both forward and reverse 10 mM primers, 7.5 µl of nuclease-free water, and 1.5 µl of diluted cDNA. For Actg1 measurements, the cDNA stock was diluted 1:100 in RNase-free water. For Aif1 and Trem2 measurements, the cDNA stock was diluted 1:10 in RNase-free water. Plates were cycled in the CFX96TM Real-Time System as follows: 3 min at 95°C followed by 40 cycles of [30 s at 95°C, 30 s at 58°C, and 30 s at 72°C] finishing with 5 min at 72°C. All reactions were tested for a single peak to reflect a single PCR product. The raw Ct values were averaged over their triplicates, with results being expressed as $2^{-(\text{mean Ct value for the gene of interest} - \text{mean Ct value for the control gene})}$.

2.4.4 Bulk hippocampal RNA sequencing

RNA was processed by Eurofins Genomics (Eurofins Genomics Europe Sequencing GmbH, Germany) for RNA sequencing using the NextSeq 2000 RNA sequencer.

2.5 Field electrophysiology

2.5.1 aCSF preparation

A base artificial cerebrospinal fluid (aCSF) solution was prepared in Milli-Q purified water (18.2 MΩ·cm) with the following composition: 125 mM NaCl, 26 mM $NaHCO_2$, 20 mM D-glucose, 2.4 mM KCl, and 1.4 mM NaH_2PO_2. From this base solution, four aCSF variants were prepared by adding different concentrations of $MgCl_2$ and $CaCl_2$:

- 3 mM $MgCl_2$, 0.5 mM $CaCl_2$,
- 1 mM $MgCl_2$, 0.5 mM $CaCl_2$,
- 1 mM $MgCl_2$, 1 mM $CaCl_2$,
- 1 mM $MgCl_2$, 2 mM $CaCl_2$.

The final solutions achieved a pH of 7.4 and an osmolarity of ~315 mOsm/L. aCSF solutions are stored at 4°C for no longer than 5 days.

2.5.2 Slice preparation

Slice preparation followed standard protocols (Cummings et al., 2015). Following decapitation (see Mouse Tissue Extraction), the fresh hemisphere was immediately submerged in ice-cold slicing solution of artificial cerebrospinal fluid (aCSF) containing 3 mM $MgCl_2$ and 0.5 mM $CaCl_2$. The tissue was then transferred to a vibratome chamber, secured to the wax stage using superglue, and submerged in the same ice-cold slicing solution. Transverse slices (300 µm thick) were cut along the long axis of the hippocampus.

Given the logistical and ethical importance of maximising tissue yield from aged animals, each brain was used for multiple downstream applications, including acute slice electrophysiology, fixed tissue histology, and frozen molecular analyses. This approach reduces the number of animals required, optimises resource use, and enables within-subject correlations across different experimental modalities. Both whole-cell patch clamp and field potential recordings were successfully obtained from these mice.

Based on prior experience and established protocols (Edwards, 1995; Edwards and Konnerth, 1992), rapid removal of the brain and immersion in ice-cold slicing solution within one minute of decapitation is critical to preserve slice quality, particularly for patch-clamp recordings. Immediate cooling suppresses cellular metabolism and ion channel activity, reducing energy demand and improving neuronal viability. To further improve slice quality in aged animals, the slicing solution contains low Ca^{2+} (0.5 mM) and high Mg^{2+} (3 mM) concentrations. High magnesium blocks NMDA receptors and competes with calcium at voltage-gated calcium channels, while low calcium reduces synaptic release probability. Together, these conditions suppress synaptic transmission and glutamatergic activity,

helping to prevent excitotoxic damage and lower metabolic burden during slicing. While this approach may not be optimal for all immunohistochemical applications, we found that rapidly immersing one hemisphere in paraformaldehyde yielded tissue of sufficient quality for histological analysis.

Each slice was dissected into a region of hippocampus and entorhinal cortex before sequentially incubating in aCSF solutions bubbled with 95% O_2 and 5% CO_2 at 35°C, maintained by a water bath:

1. Base aCSF + 1 mM $MgCl_2$, 0.5 mM $CaCl_2$ for 5 min,
2. Base aCSF + 1 mM $MgCl_2$, 1 mM $CaCl_2$ for 5 min,
3. Base aCSF + 1 mM $MgCl_2$, 2 mM $CaCl_2$ for 5 min,

The gradual increase in calcium concentration, presence of oxygen, and increased temperature aim to slowly restore cellular metabolism and neurotransmitter release without causing excitotoxic damage.

2.5.3 Slice recording setup

Field potential recordings followed standard protocol (Cummings et al., 2015). The slices were moved to a flow chamber where 1 mM $MgCl_2$, 2 mM $CaCl_2$ aCSF bubbled with 95% O_2 and 5% CO_2 was heated to 30±1°C and perfused through the chamber at a rate of ~2 mL/min with a peristaltic pump. The slices rested at the base of the flow chamber and were held in place by a platinum harp with nylon strings running across. Slices were left to recover in this setup for at least 1 hr.

Recording and stimulating electrodes made of borosilicate glass capillaries (1.5 mm outer and 0.86 mm inner diameter) were pulled with the Narishige PC-1000 puller to a tip resistance of ~2 MΩ and filled with $1Mg^{2+}$, $2Ca^{2+}$ aCSF. Silver/silver chloride wire was run through the glass electrodes to convert Ionic current to electronic current.

The electrodes, controlled with micromanipulators, were placed 150-300 µm apart in the *stratum radiatum* of the CA1 hippocampal subfield. This region harbours the Schaffer collateral axonal projections from the CA3 subfield and the apical dendrites of the CA1 pyramidal cells. The stimulating electrodes aim to stimulate a synchronous synaptic input from the Schaffer collateral axons to the CA1 apical dendrites. As Na^+ and Ca^{2+} ions flow into the dendrites through AMPA and NMDA receptors, a localised extracellular negativity (sink) forms due to the loss of positive charge. Current will therefore flow into the extracellular sink from neighbouring regions, known as the source (source of charge). This flow of current, from source to sink, is detected by the recording electrode.

The stimulating electrode was directly connected to the output of a Grass SD8 stimulator and paired with a silver/silver chloride reference electrode submerged in the flow chamber. Stimulation voltage and duration were manually controlled on the stimulator, while stimulus delivery was triggered in the WinWCP software.

The recording electrode was mounted onto an Axon HS-2 headstage (1x gain) and paired with a silver/silver chloride reference electrode submerged in the flow chamber. The voltage difference between the recording and reference electrodes was initially filtered at 30 kHz using an Axoclamp 1B amplifier, then amplified 100x and filtered at 2 kHz using a Brownlee Precision 440 amplifier, followed by 50 Hz filtering with a Hum Bug. Voltage was sampled at 20 kHz using a Digidata 1322A digitizer, which fed data into WinWCP software where voltage was rescaled back down to 1x for visualisation of the field excitatory postsynaptic potential (fEPSP).

2.5.4 Experimental protocols

Stimulation frequency was predefined in the experimental protocols within WinWCP. Stimulus intensity and duration were manually controlled on the stimulator. Basal synaptic transmission was assessed using Input-Output and Paired-Pulse experimental protocols. For the Input-Output protocol, stimulus intensity was increased in 10 V increments from 10 V to 50 V, applied at 0.1 Hz for 1 min, resulting in six responses per stimulation intensity. For all remaining experimental protocols, stimulus intensity was set to ~40% of the intensity required to produce a population spike. For the Paired-Pulse protocol, stimulation was delivered in pairs, with the inter-stimulus interval incrementally adjusted to 25 ms, 50 ms, 100 ms, and 200 ms. Paired stimuli were applied at 0.1 Hz for 1 min per inter-stimulus interval, resulting in six paired responses per interval.

The long-term potentiation experimental protocol was first preceded by a baseline recording consisting of ≥14 min of 0.1Hz stimulation with an inter-stimulus interval of 50 ms. LTP conditioning consisted of three trains of 20 stimuli at 100 Hz (tetanus stimulation), with a 1.5 s inter-train interval. Following this, responses were stimulated for 60 min at 0.1 Hz with an inter-stimulus interval of 50 ms.

2.5.5 Analysis

All field recording analysis was performed on WinWCP software. Experimental recordings were analysed blind to the experimental group and only unblinded once the analysis was complete. Any responses that were interrupted by significant noise interference were excluded from further analysis. For basal inter-stimulus interval and paired-pulse analysis,

responses were averaged in groups of six to obtain a 1-minute average. For LTP analysis, responses were averaged in groups of twelve to obtain a 2-minute average. All responses were quantified by calculating the slope of the fEPSP, measured from just after the initial downward deflection to ~60% of the negative peak amplitude. Paired-pulse ratios (PPR) were calculated by dividing the fEPSP slope of the second response by that of the first response. fEPSP slope and PPRs as a percentage of baseline were determined by dividing the values for each 2-minute period by the mean value of the baseline period multiplied by 100. Slices were excluded from LTP analysis if the 2-minute averaged baseline fEPSP slope deviated by more than ±10% from the overall baseline mean. For each mouse, 1–2 slices were recorded. If two slices were used, the individual slice averages were further averaged to generate a single mouse average.

2.6 Human microglial GeoMx

2.6.1 Tissues, MTA, and ethics

Use of FFPE human brain tissue for this project was approved by the UCL ethics committee, Ethics ID: 26399.001. Transfer of FFPE human brain tissue was approved by the Netherlands Brain Bank under the Material Transfer Act, Project 1612. The storage of FFPE human brain tissue was at the UCL dementia research institute, HTA licence: 12198. The case summary of all tissues used for this project is found in Table 4.1.

Clinical AD diagnosis was initially based on the criteria established by McKhann et al. (1984) and later updated by Dubois et al. (2007) for probable AD. The Netherlands Brain Bank performed the final confirmation of AD by histopathological assessment. Whole brain tissue was fixed in formalin for 4 weeks before individual regions were dissected and embedded in paraffin. All samples for this project were hippocampal; however, due to the availability of hippocampal regions, the sampled regions ranged from the posterior, mid, and anterior hippocampus.

2.6.2 Tissue sectioning

Performed by IQPath, UCL. FFPE blocks containing human hippocampus were sectioned at 8 µm using a rotary microtome. Each section was then cut into 10 mm × 10 mm squares. Three of these tissue squares were mounted per SuperFrost Plus slide within the designated GeoMx scan area.

2.6.3 Slide preparation

Slide preparation followed the ‘GeoMx Slide Preparation’ protocol with minor adjustments for optimisation. To adhere the tissue sections and melt the paraffin embedding, slides were

baked at 60°C for 1 hr, then cooled for 30 min at RT. Paraffin was removed by immersing slides in xylene three times for 5 min at RT, followed by two washes in 100% ethanol for 5 min each. Sections were then rehydrated in 95% ethanol for 5 min, followed by 0.1 M PBS for 1 min at RT. For antigen retrieval, slides were first heated in DEPC-treated water for 10 s at 100°C using a slide steamer, followed by incubation in 10 mM Tris, 1 mM EDTA (Tris-EDTA solution) for 35 min at 100°C, also maintained by a slide steamer. To cool the slides, they were transferred to 0.1 M PBS for 5 min at RT. RNA retrieval was performed using minimal protein digestion with 0.5 µg/ml proteinase K in 0.1 M PBS for 15 min at 37°C in a water bath, followed by a 0.1 M PBS wash for 5 min at RT. For morphology preservation, sections were fixed in 4% formaldehyde for 5 min at RT, then fixation was quenched using 0.1 M glycine and 0.1 M Tris in DEPC-treated water for two washes of 5 min each at RT. Slides were then washed in 0.1 M PBS for 5 min at RT.

2.6.4 Probe hybridisation

Following slide preparation, the slides were transferred to a humidity chamber, and a hydrophobic barrier was drawn around the slide edges. Sections were then immersed in a hybridisation probe mix (per slide: 225 µl Buffer R, 25 µl GeoMx Whole Transcriptome Probe Mix, and 25 µl DEPC-treated water) and incubated overnight at 37°C in a hybridisation oven. Non-hybridised, weakly hybridised, and non-specifically bound probes were removed using a 50% formamide, 2XSSC solution (prepared by mixing equal volumes of 50% formamide and 4XSSC) twice for 25 min at 37°C in a water bath. Formamide was removed in a 2XSSC wash twice for 2 min at RT.

2.6.5 Immunohistochemistry

Following probe hybridisation, sections were blocked for non-specific binding in Buffer W for 30 min at RT. Sections were then incubated with primary antibodies (rabbit anti-IBA1, 1:300; see key resources table, appendix) diluted in Buffer W for 4 hrs at RT. After primary antibody incubation, sections were washed in 2XSSC solution three times for 5 min at RT. Next, sections were incubated with secondary antibodies (goat anti-rabbit 594, 1:500) diluted in Buffer W for 2 hrs at RT, followed by three washes in 2XSSC solution for 5 min each at RT. To stain plaques, sections were incubated with Amytracker520 dye (1:1000 in 0.1 M PBS) for 30 min at RT, then washed twice in 2XSSC solution for 5 min at RT. Slides are then left in 2XSCC solution overnight at 4°C.

2.6.6 ROI/AOI selection and barcode collection

One section from each human hippocampus was analysed, with 3–4 technical replicates per ROI type per section collected. Due to the four-slide limit of the GeoMx DSP machine,

tissues were processed in three batches of four slides each, with each slide containing three sections (12 tissues per batch). The GeoMx DSP machine collects one area of interest per well of a 96-well plate. ROIs and AOIs were defined based on the morphological stains.

Regions of interest (ROIs):
1. A region drawn around an area of heavy plaque load in which all microglia would fall within 50 µm of a plaque. This was only performed in plaque-bearing tissue.
2. A region drawn which did not contain plaques and with borders >100 µm from any visible plaque. This was performed on all tissues.

Areas of interest (AOIs):
- Plaque Contacting Microglia: co-localisation of Amytracker520 and IBA1 in ROI 1.
- Periplaque Microglia: IBA1 signal in ROI 1 not colocalised with Amytracker520.
- Away Microglia: all IBA1 signal in ROI 2.

2.6.7 Library preparation

RNA probe-associated DNA oligomer tags were released by illuminating the chosen AOIs under ultraviolet laser exposure and aspirated into a microtiter plate, whereby each well contains the DNA oligomer tags of a single AOI. The aspirates were dried for 1 hr at 60°C in a thermocycler. Collections were then rehydrated in 10 µl of RNase-free water. A PCR plate was prepared, with each well containing: 4 µl of the corresponding well from the GeoMx DSP rehydrated collection plate, 4 µl of the corresponding well from the Seq Code primer plate, 2 µl of GeoMx master mix. The plates were thermocycled as follows: 30 min at 37°C, 20 min at 50°C, 3 min at 95°C, 18 cycles of [15 s at 95°C, 60 s at 65°C, 60 s at 68°C], 5 min at 68°C, ending at 4°C. Since all barcodes from an area of interest now contain a well-specific sequence due to the Seq Code primer plate, 4 µl from each well of the PCR plate was pooled into a single Eppendorf tube. To remove impurities, the PCR product was DNA purified using two cycles of AMPure XP bead purification. Each cycle included: addition of AMPure XP beads for 5 min, pellet formation on a magnetic stand, supernatant removal, two washes with 80% ethanol (discarding ethanol each time), and resuspension in elution buffer. The amount of AMPure XP beads and elution buffer was adjusted based on reaction size, as specified in the manufacturer's instructions.

2.6.8 TapeStation barcode detection

A D1000 TapeStation system was employed to confirm the successful collection and preparation of GeoMx DNA oligomer barcodes. Here, 1 µl of D1000 ladder and 1 µl of the

sample were diluted in 3 µl of sample buffer before loading into the D1000 Tapestation. A peak at 170bp confirmed the presence of barcodes.

2.6.9 RNA sequencing

RNA sequencing of the barcodes was performed by UCL Genomics using the Illumina NextSeq 2000.

2.6.10 GeoMx NGS pipeline

FASTQ files from the sequencing run were converted to .DCC files using the GeoMx NGS graphical user interface. This process utilised configuration files from the GeoMx DSP, which contained information on well IDs for each collected area and well-specific sequences from the Seq Code primer plate. These data were used to deconvolve the FASTQ files into .DCC files, which contain deduplicated counts for each area of interest.

2.6.11 Probe quality control

DCCs containing barcode counts were translated to gene symbols with the human probe assay metadata PKC files. Counts were also matched to their associated AOIs with the sample annotation file provided from the GeoMx collection run. AOIs that did not meet a minimum number of 1000 reads per AOI, ≥80% of reads in an AOI successfully trimmed, ≥80% of reads in an AOI successfully stitched, ≥75% of reads in an AOI aligned to the reference, and ≥50% sequencing saturation were removed from further analysis.

2.6.12 Analysis

All analysis was performed in RStudio. A DESeq2 matrix was created with a design that accounted for variability between samples, with the experimental condition set as AOI type. Although including sample information in the DESeq2 design should account for batch differences, separation in PCA plots persisted. Therefore, the ComBat_seq function from the SVA package was used to adjust the raw counts for batch effects before proceeding with the DESeq2 pipeline. The large DESeq matrix was subset into three AOI comparisons: plaque microglia vs away microglia, plaque microglia vs periplaque microglia, and periplaque microglia vs away microglia. P-values were adjusted for multiple comparisons using the Benjamini-Hochberg false discovery rate (FDR). Significant genes were then subset into categories based on the direction and significance of their expression across the three microglial areas (Figure 4.2B):

- Plaque Response: genes that were significantly upregulated or downregulated in the plaque region compared to away or periplaque, with away and periplaque regions not significantly differing.

- Graded Response: genes in this category show a consistent direction of change across all three regions. Plaque microglia are always significant compared to away microglia. Periplaque microglia follow the direction of change from away to plaque, but their expression can be either significantly different or not significantly different from both plaque and away regions.
- Plaque and Periplaque Response: genes that were significantly upregulated or downregulated in both the plaque and periplaque regions compared to the away region, with plaque and periplaque regions not significantly differing.
- Periplaque Only Response: genes that showed significant upregulation or downregulation in the periplaque region, with the away and plaque regions not significantly differing.

These categories were subdivided into whether the response was upregulated or downregulated compared to away regions (Figure 4.2B). The ggplot2 library was used to create the volcano plots. Enrichment analysis for each category was performed using the ClusterProfiler package to compute enrichment statistics for Biological Process (BP), Cellular Component (CC), Molecular Function (MF), Reactome pathway and KEGG pathway databases.

2.7 Mouse microglial GeoMx -

2.7.1 Tissue sectioning

A tissue block containing mid to dorsal hippocampus was dissected out of the remaining un-sectioned formalin-fixed tissue from the frozen sledge microtome (as described above, Mouse Tissue Sectioning: Free floating Section). Performed by IQPath, UCL: The remaining tissue containing the hippocampus was paraffin-embedded, sectioned at 8 µm using a rotary microtome, and directly mounted onto SuperFrost Plus slides. A total of eight hippocampi, from eight individual mice, were mounted per slide onto the GeoMx scan area.

2.7.2 Slide preparation

The sections were processed by the Nanostring Technology Access Program (Seattle, WA, USA). Epitope retrieval and staining were performed using the Leica Bond Autostainer. The slide preparation steps followed the human GeoMx protocol outlined above, with the following modifications:

- Slides were baked at 60°C for 30 min.
- Heat-induced epitope retrieval was performed using 0.1 µg/ml proteinase K at 37°C for 20 min.
- Sections were stained for GFAP, Aβ40/42, and TMEM119 using the following antibodies: mouse anti-GFAP Alexa Fluor 488, mouse anti-Aβ40/42 Alexa Fluor 594,

and rabbit anti-TMEM119, with goat anti-rabbit Alexa Fluor 647 as the secondary antibody. Nuclei were counterstained with SYTO 83 in Buffer W for 1 hour at RT (see key resources table, appendix).

2.7.3 ROI/AOI selection and barcode collection

One section from each mouse hippocampus was analysed, with 1-3 technical replicates per ROI type per section collected. The GeoMx DSP machine collects one AOI per well of a 96-well plate. ROIs were defined based on the morphological stains:

Regions of Interest:
1. Plaque-associated ROI: Defined around regions with a high plaque load, ensuring that all included tissue was within approximately 30 µm of a plaque. This analysis was performed exclusively in plaque-bearing tissue (NLF and NLFTrem2^{R47H} mice).
2. Non-plaque-associated ROI: Defined in regions free of plaques, with boundaries set at least >100 µm away from any visible plaque. This analysis was performed across all tissue samples.

Areas of Interest, Microglia:
- Plaque Contacting Microglia: co-localisation of TMEM119 and Aβ42 in ROI 1.
- Periplaque Microglia: TMEM119 signal in ROI 1 not colocalised with Aβ42.
- Away Microglia: all TMEM119 signal in ROI 2.

Areas of Interest, Astrocytes:
- Plaque Associated Astrocytes: All GFAP signal in ROI 1.
- Away Astrocytes: All GFAP signal in ROI 2.

The astrocytic AOIs are not a main focus of this thesis, but are used to compare GeoMx to bulk RNA sequencing counts in Figure 3.10 (see - Mouse Microglial GeoMx vs Bulk RNAseq).

A limitation of the GeoMx platform during ROI segmentation was the inability to define regions exactly 30 µm from thresholded plaques. Instead, ROIs were manually drawn using scale bars for guidance, and care was taken to ensure that no ROI extended beyond 30 µm from the edge of a plaque. All ROIs were double-checked to confirm adherence to this constraint.

2.7.4 Library preparation, sequencing, and FASTQ conversion

As described in the Human Tissue GeoMx section.

2.7.5 Quality control and counts

Deduplicated counts were normalised to housekeeping genes by dividing the count for each gene by the mean of the *Actb* and *Actg1* counts within an AOI, then multiplied by the mean count for *Actb* and *Actg1* across all AOIs. Where this fell below 15 the ROI was discarded. Where >1 AOI was collected from a section for the same category in the same tissue (plaque, periplaque, or away), the data were averaged, giving n=1 per section/mouse.

2.7.6 Data accessibility

The 18-month spatial transcriptomic data was converted into an easy-to-use online platform through the R-based shiny-app package and can be found here - https://jackwood.shinyapps.io/MALDIGeoMx/. The aesthetic template for Mouseac was borrowed from previous Edwards Lab Shiny Apps. All graphical and statistical code is original.

2.7.7 Mouse microglial GeoMx vs bulk RNAseq

Bulk hippocampal RNA sequencing counts were normalised to the average counts of *Actg* and *Actb* housekeeping genes. Microglial GeoMx counts were similarly normalised, as described above (see - Quality Control and Counts section). Disease-associated microglial (DAM) genes were defined as those significantly altered in single-cell RNA sequencing of 5XFAD mouse brains, transitioning from homeostatic to DAM clusters (Table S3 of Keren-Shaul et al. (2017)). Similarly, disease-associated astrocytic (DAA) genes were defined as those significantly altered in single-nucleus RNA sequencing of 5XFAD mouse hippocampus, comparing homeostatic astrocytes to the DAA cluster (Cluster 1 vs. 4, Table S3 of Habib et al. (2020)). Synaptic hub genes were defined as the top 50 downregulated synaptic hub genes, identified through network analysis of microarray data, comparing human AD and non-AD prefrontal cortex (Figure 1E of Williams et al. (2021)). For heatmaps, fold change in bulk RNA sequencing compared WT to NLF hippocampus for all gene sets, while GeoMx counts compared plaque-contacting versus away microglia for DAM genes and plaque versus away astrocytes for DAA and synaptic hub genes. Heatmaps were generated from fold change calculations using the ComplexHeatmap R package, with the colour scale defined using the Circlize R package. Principal Components Analysis was performed using the prcomp function from base R, and the first principal component was extracted and visualised using the ggplot2 package.

2.8 SILK guided MALDI-MSI & GeoMx

2.8.1 Mouse feeding paradigm

The iSILK experiments were enabled by a pulse chase feeding paradigm consisting of standard chow naturally abundant in the ^{14}N isotope and a Spirulina-based chow enriched in the heavier ^{15}N isotope at a 1:3 ratio with standard chow. The pulse period of ^{15}N enriched diet was fed to 6-month-old NLF mice for 4 months (Pulse: 6- and 10-months). This was followed by an 8-month chase period (10-18months) on standard ^{14}N diet until decapitation at the experimental end point of 18 months (Fig. 3A). The pulse period of 6-10 months was chosen as this is the period in which plaques begin to appear in the hippocampus of NLF mice (Benitez et al., 2021; Saito et al., 2014).

2.8.2 Tissue sectioning

Snap frozen hemispheres were mounted onto a Cryostat using frozen OCT compound, 10 µm sagittal sections were thaw mounted directly onto SuperFrost plus slides for GeoMx spatial transcriptomics or Indium tin oxide coated slides for MALDI imaging and stored at -80°C. Neighbouring sections were collected and mirror-mounted on alternating slides to ensure adjacent sections were used in both MALDI imaging and spatial transcriptomics.

2.8.3 MALDI slide preparation

The sections were initially fixed in 100% ethanol for 60 s followed by 70% ethanol for 30 s. Lipids were removed in Carnoy's solution (6:3:1 ethanol/chloroform/acetic acid) for 110 s with a subsequent wash in 100% ethanol for 15 s, 0.2% trifluoroacetic acid in water, and 100% ethanol for 15 s. The tissues then underwent peptide retrieval using formic acid vapour exposure by inverse mounting of the glass slide in a glass Petri dish for 20 min. To facilitate peptide ionisation and desorption, a matrix (15 mg/ml 2,5-dihydroxyacetophenone (DHAP), in 70% acetonitrile, 2% acetic acid, 2% TFA) was applied using a TM sprayer and recrystallised in 5% methanol vapour at 85°C for 3 min.

2.8.4 MALDI data acquisition

MALDI-MSI was performed with a rapifleX TissueTyper MALDI-time-of-flight (TOF/TOF) instrument (Bruker Daltonics) equipped with the scanning Smartbeam 3D laser. The laser fired 200 shots per pixel with 90% attenuator setting (3% global offset, range 20%) at a laser repetition frequency of 10000Hz. The pixel size was set to 10 µm (laser diameter 5 µm, focus: small, setting: single)). A mass range of 1500-5500Da was analysed in linear positive mode (mass resolution: $m/\Delta m = 500$ at m/z 4515) due to higher sensitivity towards larger mass species, ensuring sensitive peptide detection at high spatial resolution. For accurate detection of Aβ, the system was calibrated to synthetic Aβ (Aβ1-38, -39, -40, -42, -43, -44, -

45, -46, -47 and -48) and peptide molecular weight standard I (Bruker Daltonics). The total ion current normalisation for each ROI was executed using FlexImaging 5.0 software. For an unbiased, quantitative comparison of label incorporation into Aβ, curve analytics were performed on the Aβ1-42 mass peak (m/z=4515) of a plaque-ROI sum spectrum. To estimate the degree of label incorporation, the width of the Aβ1-42 peaks caused by the ^{15}N label was analysed. Due to the comparably low mass resolution in linear mode, relative label content was estimated by analysing the full width at half maximum (FWHM, (15 Nitrogen Index)) of the curve fitted to the low resolved Aβ1-42 isotopologue pattern.

2.8.5 GeoMx collection

The sections were processed by the NanoString Technology Access Program (Seattle, WA, USA). Slide preparation, probe hybridisation, library preparation, and file processing were performed as described in the Mouse Microglia GeoMx section. However, due to the use of fresh frozen tissue, the tissue was first fixed in 10% formalin overnight, and the slide baking and xylene deparaffinisation steps were omitted.

ROI selection

MALDI-MSI was performed on adjacent sections to those sent for spatial transcriptomics analysis. During ROI selection, the MALDI-MSI image was used as an overlay; plaques that presented over both the MALDI image and the DSP fluorescent image were selected. ROIs were placed over the plaques at 3X the plaque diameter. As this analysis was not cell-type specific and the whole ROI was analysed, no AOIs existed within these ROIs.

2.8.6 GeoMx count normalisation

Unlike the microglial analysis, MALDI-MSI paired with spatial transcriptomics was not cell-type specific and analysed the whole transcriptome using Q3 normalisation in a non-hypothesis-driven investigation.

2.8.7 Analysis

Base R was used to apply Pearson correlation between the Nitrogen Index of an AOI extracted from the MALDI-MSI data, against the Q3 normalised expression counts for each gene extracted from the GeoMx data. Enrichment analysis of significantly correlated genes was performed in R using the ClusterProfiler package to compute enrichment statistics for Biological Process (BP), Cellular Component (CC), Molecular Function (MF), and KEGG databases. Reactome pathway enrichment was analysed using the ReactomePA package. All enrichment statistics were corrected for multiple comparisons using the Benjamini-Hochberg false discovery rate (FDR) method. For each database, the 15 most significantly

enriched terms were reported. Notably, for KEGG and Reactome databases, significant term enrichment was observed only for negatively correlated genes.

2.8.8 Data accessibility

The SILK-guided MALDI MSI with GeoMx data revealing correlation statistics between gene expression and plaque age was converted into an easy-to-use online platform through the R-based shiny-app package and can be found here- https://hanriederlab.shinyapps.io/PlaqueAgeTranscriptomics/. The aesthetic template for Mouseac was borrowed from previous Edwards Lab Shiny Apps. All graphical and statistical code is original.

2.9 Statistics

All statistical analyses were performed using GraphPad Prism (versions 9 and 10) or R. Main effects and interactions are also reported in the figure legends. Post hoc analysis was typically conducted only when a significant interaction was detected. However, in cases where relevant comparisons were possible, post hoc analysis was performed even in the absence of an interaction, as noted in the figure legends. When multiple comparisons were made, Sidak, Tukey, or Benjamini-Hochberg post hoc corrections were applied to adjust p-values. Asterix (*) symbols denote significance within genotype, dagger (†) symbols denote significance between genotypes. Sample sizes are indicated in the figure legends. All analyses were conducted blind to the experimental group. Any data point >±2 standard deviations from the mean was classed as an outlier and excluded from statistical analysis. Sample sizes for each experiment were guided by power analysis or prior published data. For field electrophysiology, group sizes were determined using power calculations ($\alpha = 0.05$, power = 0.8) based on effect sizes estimated from previous patch-clamp recordings in the Edwards lab (Benitez et al., 2021). For SILK experiments, sample size estimates were based on a prior study by the Hanrieder lab (Michno et al., 2021), which demonstrated that n = 3 was sufficient to detect significant 15N enrichment in plaque centres relative to peripheries. qPCR sample sizes were based on power calculations using standard deviations from previous Trem2 qPCR data in NLF mice (Benitez et al., 2021) and an estimated 60% effect size from Xiang et al., 2018, indicating that n = 3 per group would provide 80% power at $\alpha = 0.05$. Sample sizes for immunohistochemical experiments were similarly determined based on effect sizes estimated from pilot experiments, using $\alpha = 0.05$ and power = 0.8. For GeoMx spatial transcriptomics, no gold-standard method currently exists for power analysis, as tools such as RNASeqPower are designed for bulk or single-cell RNA-seq datasets with substantially larger library sizes. The mouse GeoMx experiments were exploratory, with sample sizes (n = 5 per group) based on manufacturer (Nanostring)

recommendations. Post hoc power analysis using the NLF dataset showed that, for genes with a twofold change, n = 6 per group provided 80% power (α = 0.05). For highly responsive genes such as Trem2 (~3-fold change), power exceeded 0.95. For human GeoMx studies, no prior example using paired analysis provided a reliable effect size for pre-study estimation. Given the increased variability expected in human tissue, due to factors such as sample quality, age, sex, and genotype, we conservatively assumed a substantially larger standard deviation than in mouse. Based on this, a sample size of approximately n = 18 per group was estimated to maintain comparable power.

CHAPTER 3

THE PLAQUE MICROGLIA RELATIONSHIP

3.1 Introduction

Together, observations from imaging studies and genetic analyses have highlighted multiple roles for microglia in AD, including phagocytosis, lipid metabolism, and the protection of surrounding tissue from Aβ plaque-induced damage (Condello et al., 2015; Keren-Shaul et al., 2017; Wu et al., 2025; Yuan et al., 2016). Furthermore, both approaches agree on the importance of *Trem2* in modulating microglial responses around plaques. In imaging experiments, *Trem2* deficiency is associated with reduced microglial plaque engagement, impaired phagocytic function, and dysregulated lipid metabolism (Claes et al., 2021; Takahashi et al., 2005; Wang et al., 2016). Genetically, microglia in AD mouse models lacking *Trem2* fail to transition into a disease-associated state characterised by anti-inflammatory signalling, lipid regulation, and phagocytic function (Keren-Shaul et al., 2017). However, until recently, it remained unclear how such microglial activation states and the regulatory influence of hub genes such as *Trem2* varied spatially in relation to Aβ plaque pathology. The advent of spatial transcriptomics has addressed this gap by enabling gene expression profiling in spatially resolved tissue regions. This approach led to the identification of plaque-induced genes (PIGs), a set of immune-related transcripts whose expression increases with increasing plaque density (Chen et al., 2020). Despite this advance, the study did not resolve which cell types expressed PIGs, how PIG expression differed with microglial distance to plaques, or whether PIG expression depended on regulatory factors such as *Trem2* expression.

In Chapter 3, I describe experiments that aimed to investigate how the PIGs change in expression within microglia at differing distances from Aβ plaques. I took advantage of the novel GeoMx spatial transcriptomics technique that allows the collection of gene expression data from selected ROIs at a cell-enriched resolution. This directly ties the phenotypic role of microglia observed from imaging experiments with the microglial genetic changes associated with Aβ plaque pathology in the NLF knock-in mouse model of AD. Additionally, I aimed to assess the role of TREM2 in controlling these genes by introducing the AD-associated risk factor mutation $Trem2^{R47H}$. This approach will provide insight into dysregulated genes linked to the mutation, which in turn are associated with an increased risk of AD. These genes could represent important targets for developing AD therapeutics. To validate the results from the spatial transcriptomic experiment, I then aimed to assess the

translation of these genes at the protein level, examining protein expression at varying distances from Aβ plaques for a set of selected genes.

The added spatial resolution of this experiment aims to capture gene expression changes in NLF mice, which has previously posed a challenge due to a low plaque density even at older ages (Benitez et al., 2021; Saito et al., 2014). However, the spatial resolution of this technique overcomes that challenge, enabling the analysis of Aβ plaque-associated gene expression whilst avoiding confounding factors resulting from APP overexpression, changes in Aβ exon sequence, or the impact of severe plaque load at young ages. To confirm the benefits of using GeoMx spatial transcriptomics on NLF mice, this chapter compares its results with those from bulk RNA sequencing of whole hippocampal RNA samples previously carried out in the Edwards lab.

Besides the gain of toxic function due to oligomerisation and aggregation observed in AD, Aβ is hypothesised to act as a positive regulator of presynaptic vesicle release probability (Abramov et al., 2009). This is also evidenced in the early pre-plaque stages of AD mouse models that have overexpressed levels of Aβ, again showing an increased probability of release and an increase in long-term potentiation (Cummings et al., 2015; Medawar et al., 2019). However, as plaques begin to form and toxicity takes effect, the initial increase in LTP shifts to a decrease (Medawar et al., 2019). The effects of Aβ plaque pathology on synaptic transmission in NLF mice over age have already been established in the Edwards lab (Benitez et al., 2021). However, the effect of the *Trem2*^{R47H} mutation on synaptic transmission and its interaction with Aβ plaque pathology remains untested. The proposed *Trem2*-dependent roles of microglia, including synaptic elimination, and the aimed investigation of *Trem2*-dependent and plaque-dependent gene expression, suggest that synaptic transmission may be affected. Therefore, in Chapter 3, I also aim to evaluate possible emergent effects of the *Trem2*^{R47H} mutation on plaque pathology and synaptic transmission. To this end, I present recordings of field excitatory postsynaptic potentials (fEPSPs) from the tri-synaptic perforant pathway of the hippocampus, a region critical for learning and memory, where I assessed both short- and long-term forms of synaptic plasticity.

The spatial transcriptomic results on NLF mice with and without the *Trem2*^{R47H} mutation, alongside the validation of TREM2 protein towards plaque presented in this chapter, have already been published in Cell Reports (Wood et al., 2022).

3.2 Spatial transcriptomic targeting of microglia based on plaque association

To target microglia in the spatial transcriptomics analysis, tissues were stained with antibodies against the microglial-specific protein TMEM119, alongside astrocytic-specific GFAP, and plaque-specific Aβ40/Aβ42 (Figure 3.1A and 3.1B). SYTO83 dye was also used to counterstain nuclei to guide region selection, ensuring that cell body layers were avoided to minimise contamination from neuronal RNA. At 18 months old, the NLF mouse model of AD has a substantial plaque load, with most plaques localised around the stratum lacunosum moleculare (SLM) of the CA1-3 hippocampal subfields and the stratum moleculare of the dentate gyrus. The GeoMx spatial transcriptomics technique requires regions of interest to be manually drawn for expression data collection, with each ROI constrained to ≤660 μm in the X-plane and ≤785 μm in the Y-plane. The uneven distribution of plaques within the hippocampus of NLF mice provides a strategic advantage, enabling the selection of plaque-enriched ROIs (Plaque ROIs) and plaque-free ROIs (Away ROIs) for microglial transcriptomic analysis (Figure 3.1C).

To push the resolution of this technique, the ROIs were further subdivided into three microglial areas of interest (AOIs):

1. Plaque microglial AOI: TMEM119 signal directly contacting Aβ40/Aβ42 signal (Figure 3.2Di),
2. Periplaque microglial AOI: TMEM119 signal neighbouring Aβ40/Aβ42 signal but not in direct contact (<30 μm from the edge of a plaque, Figure 3.1Dii),
3. Away microglial AOI: TMEM119 signal located in the plaque-free ROIs (>100 μm from the edge of a plaque, Figure 3.1Cii).

Using this paradigm, RNA expression could be analysed in microglia contacting plaques, microglia in peri-plaque regions, and microglia that are away from plaques. Astrocyte expression data (GFAP+ signal) was also extracted from Plaque ROIs and Away ROIs, however, this is not a main focus of this thesis. To ensure maximal microglial enrichment with little contamination from astrocytes, the astrocyte expression data was collected before the microglial collection. Although this led to a collection of transcripts enriched for microglia, some non-microglial signal was still detected due to the presence of synapses and fine neuronal- and astrocytic processes running above and below the TMEM119 signal.

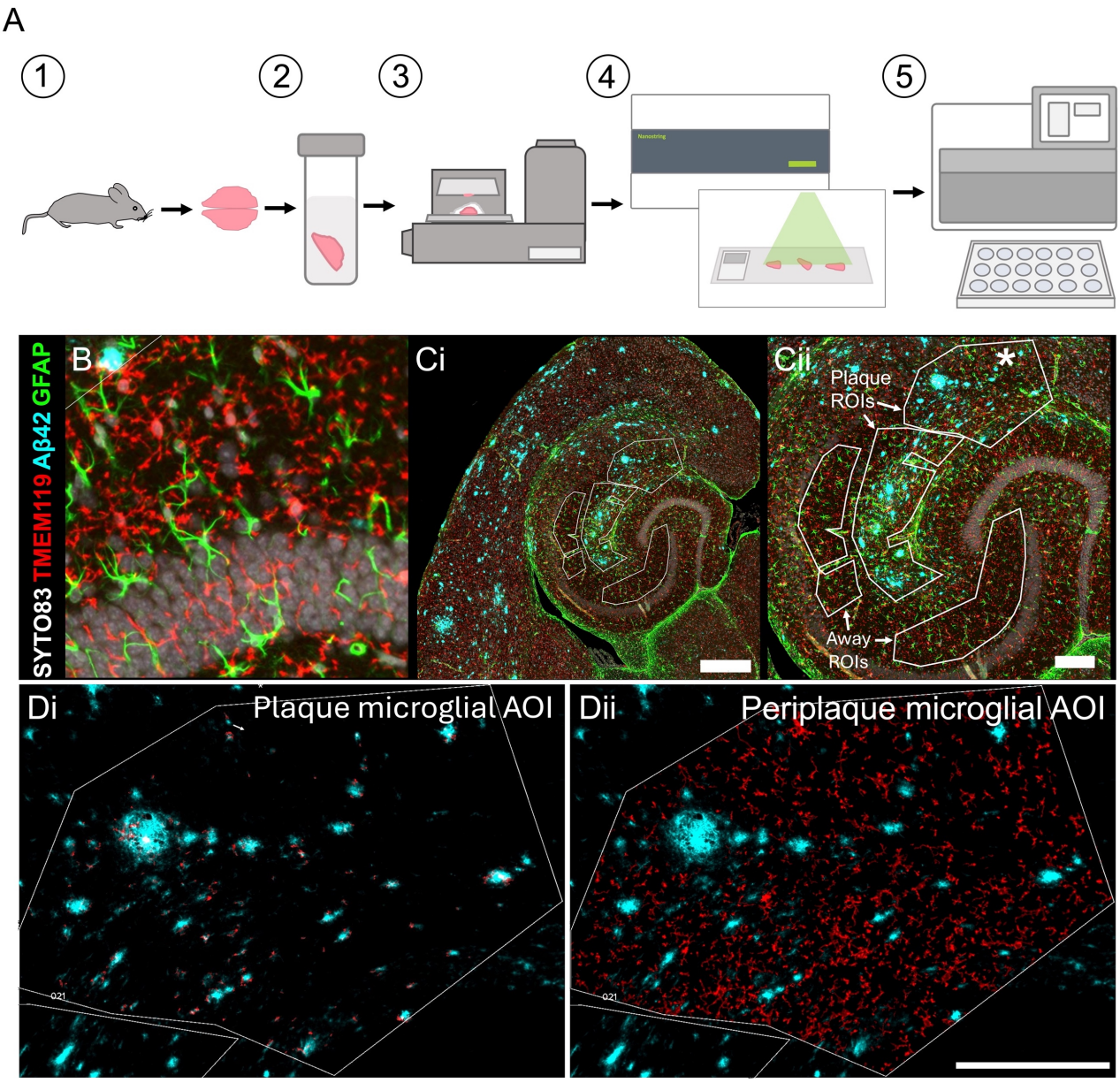

Figure 3.1 Workflow and ROI selection for microglia-enriched spatial transcriptomics
(A) Spatial Transcriptomics workflow, 1. Dissection, 2. PFA Fixation, 3. Microtome Sectioning, 4. Spatial Transcriptomics Probe Collection, to 5. Library Preparation and RNA Sequencing. (B) Example staining: 8 µm thick sections were labelled with antibodies against Aβ40/42 (Aβ plaques, Cyan), TMEM119 (microglia, Red), GFAP (astrocytes, Green), along with SYTO83 dye (nuclei, white). (C) Regions of Interest (ROIs) were drawn directly onto the hippocampal images (Ci) to capture regions with high plaque load, Plaque ROI, and regions with no plaque load, Away ROI. Scale bar: 500 µm. (Cii) Zoomed image with labelled ROIs. * indicates the ROI outlined in D. Scale bar: 200 µm. (D) The plaque ROI is divided into both TMEM119 colocalised with Aβ, Plaque microglial AOI (Di) and TMEM119 not colocalised with Aβ, Periplaque microglial AOI (Dii). Scale bar: 100 µm. B-D are also presented in Wood et al. (2022).

TMEM119 is widely recognised as a homeostatic microglial gene, and its expression has been reported to decrease under inflammatory conditions, including in plaque-bearing mouse models of Alzheimer's disease (Keren-Shaul et al., 2017; Krasemann et al., 2017;

Vankriekelsvenne et al., 2022; Zhou et al., 2020). Nevertheless, TMEM119 has previously shown strong concordance with established microglial markers such as IBA1 and Cx3cr1 (Bennett et al., 2016), and has been demonstrated to be microglia-specific, distinguishing resident microglia from infiltrating macrophages (Satoh et al., 2016).

In the present study, I independently assessed the reliability of TMEM119 as a microglial marker in our spatial transcriptomics dataset. I found that TMEM119 expression did not significantly decrease in plaque-associated regions and exhibited a high degree of spatial overlap with IBA1 immunoreactivity (Figure 3.2A and 3.2B). These findings validate the use of TMEM119 as a reliable and context-appropriate marker for microglia in our experimental model.

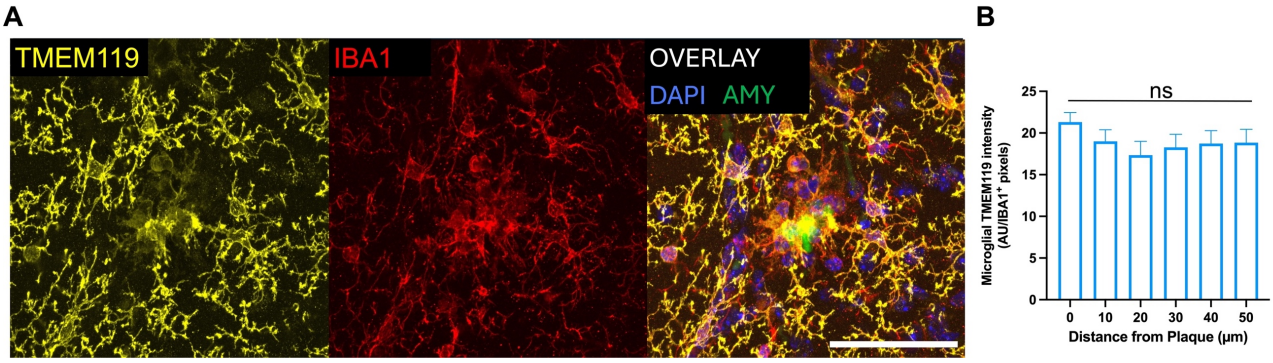

Figure 3.2 TMEM119 expression remains unchanged near plaques
(A) Confocal image of TMEM119 in an NLF mouse, TMEM119 (microglia, yellow), Amytracker (Aβ plaque, green), with IBA1 (microglia, red). Scale bar: 50 µm. (B) Quantification of TMEM119 protein measured by fluorescence intensity from widefield microscopy within IBA1$^+$ microglial pixels at varying distances from plaque. Statistical analysis: (B) one-way repeated measures ANOVA testing for main effect of distance from plaque, shown on the graph. NLF n = 6. Data plotted as mean + SEM. Figure also presented in the supplementary of Wood et al. (2022).

Given the simplicity of the following analysis, focused on a small subset of genes, and the controlled genetic background of the mice, RNA counts were normalised using housekeeping genes *Actb* and *Actg1*. To verify this HK normalisation method, counts were correlated against Q3- and TMM-weighted normalisation methods frequently used for whole transcriptome analysis; in each case, there was a very high correlation ($r>0.95$; $p<0.0001$).

3.3 Reduction in Trem2 expression due to the *Trem2^{R47H}* mutation

It has previously been reported that in young Jackson Laboratory mice harbouring the *Trem2^{R47H}* mutation, there is a 50% reduction in *Trem2* expression compared to WT mice due to a mis-splicing event (Liu et al., 2020; Xiang et al., 2018). This is an artefact of murine transcription rather than an impact of the *Trem2^{R47H}* mutation itself that is seen in humans.

However, these investigations were performed in young mice, so the extent of the mis-splicing event in older mice is unknown.

This study was initially designed to investigate the combined effect of Trem2 loss of function and reduced expression. As a first step, I therefore assessed the extent of *Trem2* downregulation attributable to the *R47H* mutation. Extracting microglial gene expression data using the spatial transcriptomics collection from the away ROIs of WT and Trem2^{R47H} mice showed a mean reduction of 20% which did not reach statistical significance (P=0.24, Figure 3.3A). However, when investigating Trem2 expression using qPCR, similar to previous studies, there was a significant reduction of 63% in Trem2^{R47H} mice compared to WT (Figure 3.3B). To see if this reflected at the protein level, immunohistochemistry towards TREM2 was analysed in whole hippocampal sections of NLF and Trem2^{R47H} mice. Similar to the spatial transcriptomics result, this revealed a 24% reduction of TREM2 protein in Trem2^{R47H} mice compared to NLF (Figure 3.3Ci). I thus tested whether TREM2 levels depended on the hippocampal region. However, for each tested region, TREM2 levels in Trem2^{R47H} mice were consistently ~24% lower than in WT mice (Figure 3.3Cii). The SP, SLM + SM, and SO were the only regions where this difference was significant. Although spatial transcriptomic and immunohistochemical analysis were harmonious, there remained a disagreement between the large difference in *Trem2* expression seen in previous literature and our qPCR analysis. However, it must be stated that the differences seen in mice harbouring the *Trem2^{R47H}* mutation in this thesis are likely due to a combination of decreased *Trem2* expression and the effects of the mutation.

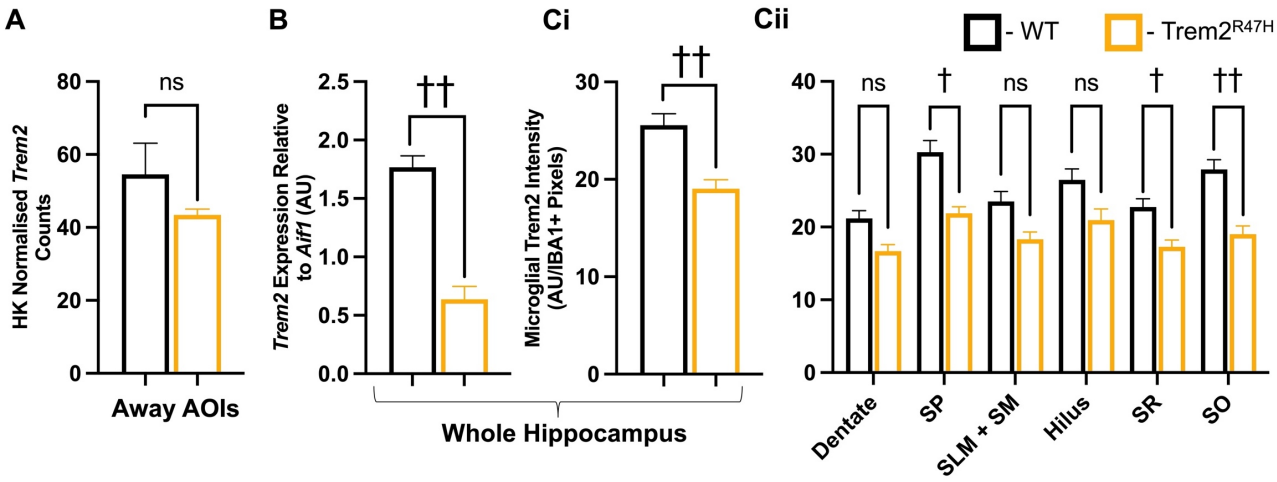

Figure 3.3 Quantification of *Trem2* RNA and protein in WT and Trem2^{R47H} hippocampus
(A) *Trem2* expression determined by microglial enriched spatial transcriptomics normalised to housekeeping genes. (B) *Trem2* expression determined by RTqPCR normalised to Aif1 expression. (C) TREM2 fluorescence intensity within IBA1+ pixels determined by immunohistochemistry in (Ci) the whole hippocampus and (Cii) various hippocampal regions

(Main effects: region P<0.0001; genotype P<0.01; interaction P<0.001). Statistical analysis: (A, B, & Ci) Main effect of genotype measured through T-test. (Cii) Two-way ANOVA followed by Sidak correction for multiple comparisons, shown on the graph. ††P<0.01; †P<0.05. The † symbol represents differences between genotypes. Spatial transcriptomics experiments n=4, RT-qPCR experiments n=3, and immunohistochemistry experiments n=6 (both WT and $Trem2^{R47H}$). Data plotted as mean + SEM.

3.4 Plaque-induced genes are dependent on microglial relation to plaque

Using the enhanced spatial resolution of this method, I aimed to investigate the expression of plaque-induced genes (PIGs), recently identified by Chen et al. (2020). These genes are defined by their increased expression with increasing plaque area within a given tissue region in 18-month-old NLGF mice. This current analysis aims to assess how the expression of these PIG genes varies based on the spatial relationship between microglia and plaques. Of the 55 tested PIGs, 38 were significantly upregulated in relation to plaque; these significant genes were further subdivided into three categories. Group 1, Plaque Response, consisted of 23 of the 38 significant PIGs (Figure 3.4A). These genes are only upregulated in microglia directly contacting plaques, with no detected upregulation in the periplaque compared to away regions. This group consisted of the microglial hub gene *Trem2*, its associated signalling partner *Tyrobp*, all three sub-units of the *C1q* complement protein, and genes involved in lysosomal and degradative processes. Group 2, Graded Response, held 11 of 38 significant PIGs (Figure 3.4B). The expression of these genes gradually increased towards plaque, with the plaque region showing significantly higher expression than the away region, but the periplaque region not differing significantly from either or differing significantly from both. Genes of note in this category included the microglial proliferation receptor *Csf1r*, immune messenger *B2m*, and the astrocytic marker *Gfap*. Finally, group 3, Plaque and Periplaque Response, contained 4 out of 38 significantly upregulated PIGs (Figure 3.4C). These genes were equally elevated in both the plaque and periplaque regions, compared to the away AOIs. Notably, this category includes two genes that harbour variants associated with an increased risk of AD, *Apoe* and *Clu* (Bellenguez et al., 2022).

Interestingly, not all significant PIG genes are known to be microglial. For each of the three groups, Figure 3.4D indicates the microglial and astrocytic cell-specificity. This was determined as an expression >2-fold compared to all other tested cell types in two previously published single-cell RNA sequencing studies (Ximerakis et al., 2019; Zhang et al., 2014). As expected, the majority of genes in groups 1 and 2 were highly microglial-specific, with the exception of *Cd9* and *Gfap,* respectively. However, *Cd9* has previously been associated with microglia in a disease-activated state (Keren-Shaul et al., 2017). Surprisingly, all genes in group 3 were astrocyte-specific. Although the GFAP signal had been removed, residual astrocytic processes were likely still present. This may be due to either GFAP-negative

astrocytic structures, such as astrocytic endfeet or astrocytic states not well captured by GFAP staining, running parallel to the collected TMEM119 signal (Escartin et al., 2021). Additionally, the low resolution of the GeoMx widefield image may have failed to capture fine GFAP-positive astrocytic processes.

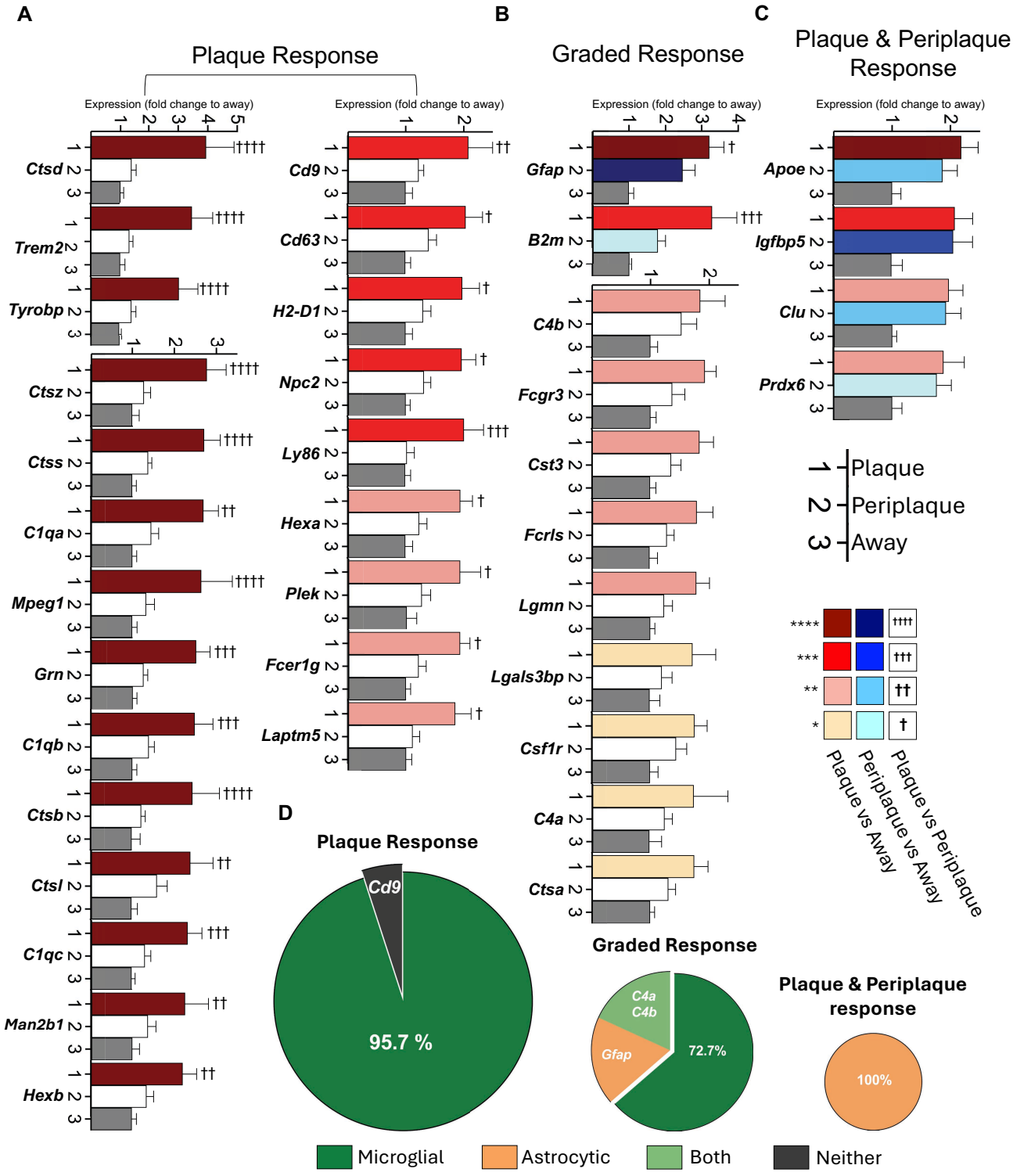

Figure 3.4 Expression of PIGs depends on relation to plaque
Expression of 38 of 55 tested PIGs showed a significant main effect of relation to plaque in a two-way repeated measures ANOVA revealing a significant Gene × Relation to Plaque

interaction, P<0.01. (A) 23 of 38 significant genes had increased expression only when the microglia were in direct contact with plaques. (B) 11 genes showed a graded response whereby expression gradually increases from away through to plaque regions. (C) 4 genes showed equal upregulation in plaque and periplaque regions, both significantly higher than away regions. (D) Pie charts representing the percentage of genes in each category that are microglial (green), astrocytic (orange), both (light green), or neither (grey). Genes were considered cell-specific if the expression is >2 fold greater than other cell types based on single-cell RNA-seq data from WT mice whole brain (Ximerakis et al., 2019) or cortex (Zhang et al., 2014). n=6 mice. Statistical difference as indicated ****/†††† P<0.0001; ***/††† P<0.001; **/†† P<0.01; */† P<0.05. The dagger symbol and bar colours represent significance from a Tukey post hoc correction for multiple comparisons. All data plotted as mean + SEM. Figure also presented in Wood et al. (2022).

3.5 *Trem2* expression is plaque and *Trem2*^{R47H} dependent

3.5.1 Bulk tissue analysis of *Trem2* found minimal expression change in NLFs

A predominant finding in the spatial transcriptomic analysis was the 2.6-fold increase in Trem2 expression with microglial contact with plaques compared to away regions (Group 1, Figure 3.4A). This result is not reflected in RNAseq or qPCR analysis of Trem2 expression of bulk hippocampus that revealed only a 1.5-fold and 1.6-fold increase, respectively (Figure 3.5Ai and 3.5Bi). Moreover, even this small difference is likely due to the increase of overall microglial number as normalising against the microglial marker Aif1 resulted in no significant change (Figure 3.5Aii, P=0.11 and 3.5Bii, P=0.12). Thus, in analysing less severe AD models such as the NLF, changes occurring due to AD pathology can often get diluted by non-plaque-associated tissue. Similarly, in bulk analysis, microglial changes are diluted by the lack of cell-type enrichment.

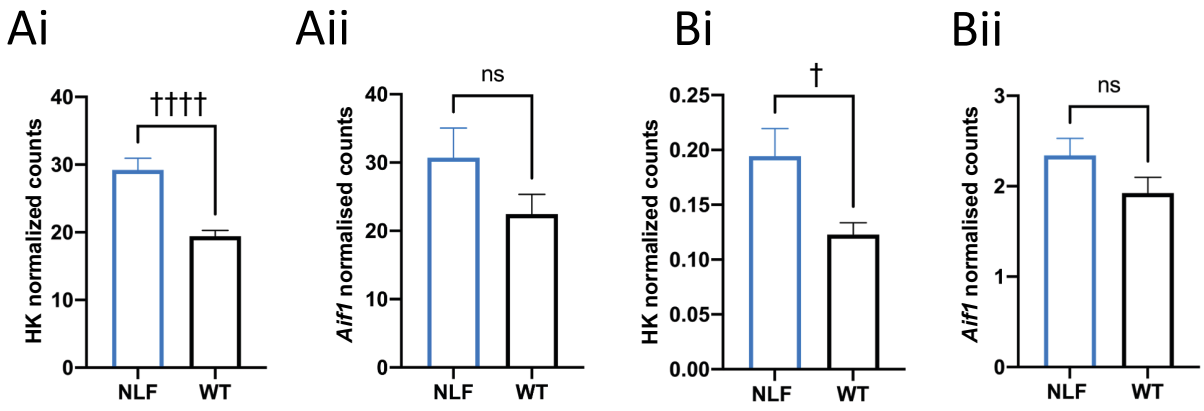

Figure 3.5 NLF bulk Trem2 hippocampal analysis showed a small change in expression

(A) *Trem2* expression in bulk hippocampal tissue measured by bulk RNA sequencing normalized to the average of (Ai) *Actg1*/*Actb* and (Aii) *Aif1*. (B) *Trem2* expression in bulk hippocampal tissue measured by RT-qPCR normalized to *Actg1* (Bi) and *Aif1* (Bii).

Statistical analysis: main effect of genotype measured through T-test, shown on graphs. ††††P<0.0001; † P<0.05. †-between genotype significance. Bulk RNA sequencing experiments: NLF n=9, WT n=12. RT-qPCR experiments NLF n=10; WT n=12. Data plotted as mean + SEM.

3.5.2 Changes in *Trem2* expression are validated by protein levels

The increase in microglial *Trem2* expression due to plaque contact suggests an important role of *Trem2* in the microglial/plaque relationship. To investigate the impact of TREM2 at plaque, I assessed the effect of decreased TREM2 efficacy by introducing the AD risk mutation *Trem2*$^{R47H/R47H}$ into NLF mice (NLFTrem2^{R47H}). Initially, I compared microglial-enriched *Trem2* expression between NLF and NLFTrem2^{R47H} mice. Strikingly, the previously observed upregulation of Trem2 expression at plaque was completely absent in NLFTrem2^{R47H} mice, showing no increase compared to periplaque and away regions (P=0.88, Figure 3.6A).

To assess whether this finding was translated to the protein level, immunohistochemistry towards TREM2 was assessed in relation to distance from plaque. Although finding a TREM2 antibody has previously been difficult, this antibody shows high specificity, with signal being completely lost in Trem2 knock-outs and reduced at heterozygosity (Cheng-Hathaway et al., 2018; Huang et al., 2021; Jadhav et al., 2020). The fluorescence intensity of the TREM2 signal within IBA1+ areas was taken as the measure of protein quantity; this was normalised per pixel to ensure no influence of microglial density changes (Figure 3.6B and 3.6C). In NLF mice, the large 2.6-fold increase in *Trem2* gene expression at plaque was similarly mirrored by a 3-fold increase in TREM2 protein at plaque. This significant increase remained at 10 μm but fell back to WT levels 20 μm from plaque. Remarkably, in NLFTrem2^{R47H} mice, although there was no increase in *Trem2* expression, TREM2 protein at plaque still increased by 1.6-fold. This, however, quickly returned to WT levels 20 μm from plaque. This increase required little, if any, change in *Trem2* RNA, suggesting either increased translation or decreased clearance.

Importantly, the increase in TREM2 protein at plaque was significantly lower in NLFTrem2^{R47H} than in NLF mice.

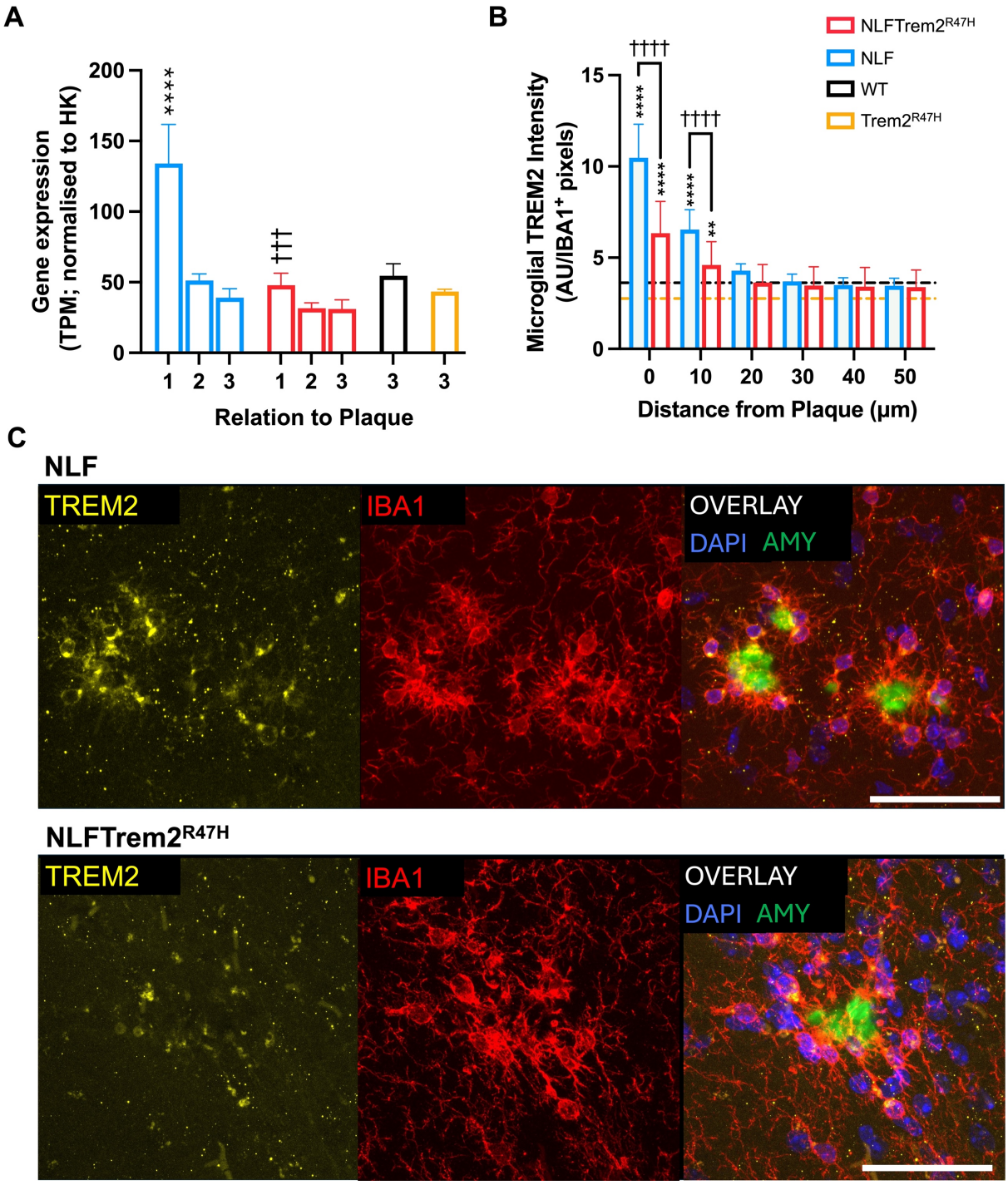

Figure 3.6 Plaque-induced increase in TREM2 protein expression is dependent on *Trem2* genotype

(A) *Trem2* expression measured by GeoMx in (1) plaque microglia, (2) periplaque microglia, and (3) away microglia (main effects: relation to plaque $P<0.01$; genotype $P<0.01$; interaction $P=0.053$). (B) Quantification of TREM2 protein measured by fluorescence intensity from widefield microscopy within IBA1$^+$ microglial pixels at varying distances from the plaque (main effects: distance to plaque $P<0.0001$; genotype $P>0.1$; interaction $P>0.1$). Note there is no significant difference between WT and Trem2^{R47H} genotypes. (C) Confocal images of TREM2 staining in NLF and NLFTrem2^{R47H} mice, TREM2 (yellow), IBA1 (microglia, red), Amytracker (Aβ plaque, green). Scale bar: 50 µm. Statistical analysis: (A & B) Two-way repeated measures ANOVA between NLF and NLFTrem2^{R47H} mice, followed by

Tukey's correction for multiple comparisons, results shown on graphs. (B) Within genotype statistical comparisons are made against the 50 µm distance from the plaque. ****/††††P<0.0001; ***/†††P<0.001; **P<0.01; *P<0.05. *-within genotype significance, †-between genotype significance. Spatial transcriptomic experiments: NLF n=6, NLFTrem2^{R47H} n=4. Immunohistochemistry experiments: NLF n=11, NLFTrem2^{R47H} n=12, with lines plotting Trem2^{R47H} and WT averages from n=12 for both genotypes. Data plotted as mean + SEM. A & B adapted from figures also presented in Wood et al. (2022).

3.6 Trem2 acts a hub gene

3.6.1 PIGs involved in lysosomal and degradative processes depend on *Trem2* genotype

As *Trem2* has repeatedly been reported as a microglial hub gene (Cheng-Hathaway et al., 2018; Keren-Shaul et al., 2017; Matarin et al., 2015; Salih et al., 2019), I investigated how the decreased efficacy and drop-off in *Trem2* expression at plaque in NLFTrem2^{R47H} mice affected the expression of the significant plaque-induced genes reported in Figure 3.4. Interestingly, in 9 of the 38 significant genes (*C1qa*, *C1qc*, *Ctsz*, *Ctss*, *Ctsd*, *Ctsb, Grn*, *Plek, Npc2*), the plaque-induced increase in expression was significantly decreased with the introduction of the *Trem2^{R47H}* mutation (Figure 3.7). Furthermore, all nine of these genes fell into the plaque response category, similar to *Trem2*, being only upregulated with microglial contact with plaque. Therefore, PIGs that were significantly upregulated in periplaque regions compared to away were not affected by the *Trem2^{R47H}* mutation. These *Trem2* genotype-dependent genes are classically associated with the complement system (*C1qa* & *C1qc*), lysosome (*Ctsz*, *Ctss*, *Ctsd*, *Ctsb, Grn*, *Npc2*) and phagocytosis (*Plek*).

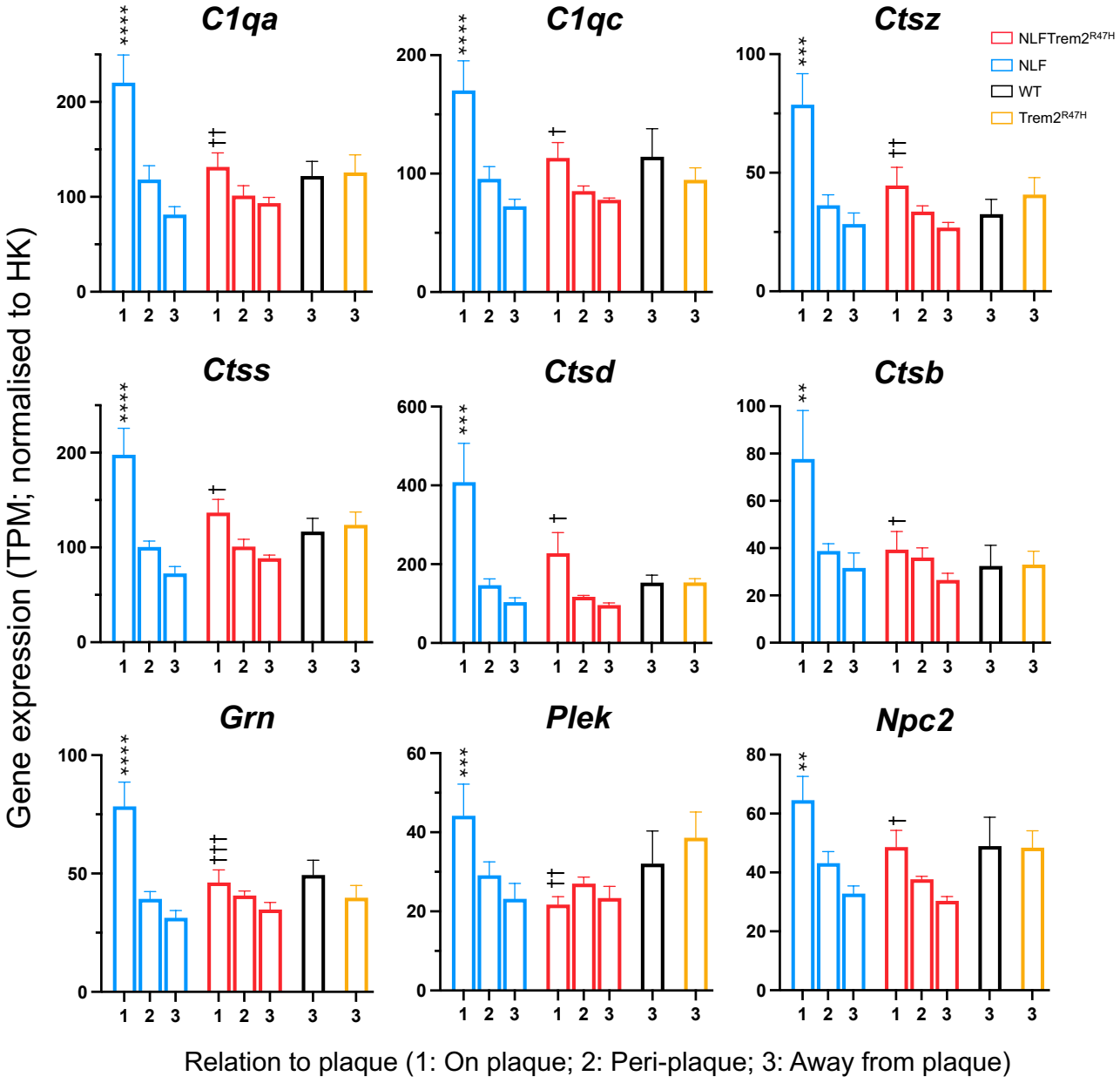

Figure 3.7 Upregulation of 9 PIGs at plaque is dependent on *Trem2* genotype
Gene expression of 9 PIGs was shown to be significantly *Trem2*^{R47H}-dependent. Two-way repeated measures ANOVA (NLF vs NLFTrem2^{R47H}: relation to plaque x genotype) with Tukeys correction for multiple comparisons performed regardless of interaction statistic. ****P<0.0001; ***P<0.001; **P<0.01, within genotype compared to column 3 (away); †††P<0.001; ††P<0.01; †P<0.05, between genotypes compared to NLF on-plaque. NLF, n=6; NLFTrem2^{R47H}, WT and Trem2^{R47H}, n=4 per genotype. Data plotted as mean + SEM.

3.6.2 Trem2 in lipid homeostasis

Many of these *Trem2*-dependent genes, particularly *Grn* and *Npc2*, play critical roles in lipid homeostasis (Evers et al., 2017). Several AD risk genes are also involved in cholesterol and lipid regulation, including *GRN,* but also *CLU*, *APOE*, *ABCA1*, and *SORT1* (Bellenguez et al., 2022).

Trem2 is frequently implicated in lipid regulation, acting as a receptor activated by various lipid species found in plaques, as well as apolipoproteins APOE and CLU (Atagi et al., 2015; Wang et al., 2015; Yeh et al., 2016). Deletion of *Trem2* has also been shown to alter a network of lipid-associated genes, including *Npc2* and *Apoe*, in an in vitro model of demyelination (Nugent et al., 2020). To investigate the role of *Trem2* in lipid homeostasis and to validate the spatial transcriptomics findings, I focused on NPC2 and APOE expression.

Npc2 encodes the intracellular cholesterol transporter NPC2, first identified through loss-of-function mutations that cause Niemann-Pick disease type C2 (Naureckiene et al., 2000). This disorder results from impaired cholesterol export from lysosomes, leading to intracellular cholesterol accumulation. In this study, *Npc2* was found to increase in expression only in microglia contacting plaques and was further found to be dependent on *Trem2* genotype (Figure 3.4A, 3.7, and 3.8A). To validate this finding, NPC2 was measured at the protein level using immunohistochemistry. Here, NPC2 was found to be significantly increased (~2-fold) at plaques compared to 50 µm away (Figure 3.8B and 3.8C). This increase remained significant at 10 µm away from the plaque. Surprisingly, despite the 25% decrease in RNA expression (Figure 3.8A), the *Trem2*^{R47H} mutation had no significant impact on NPC2 protein level.

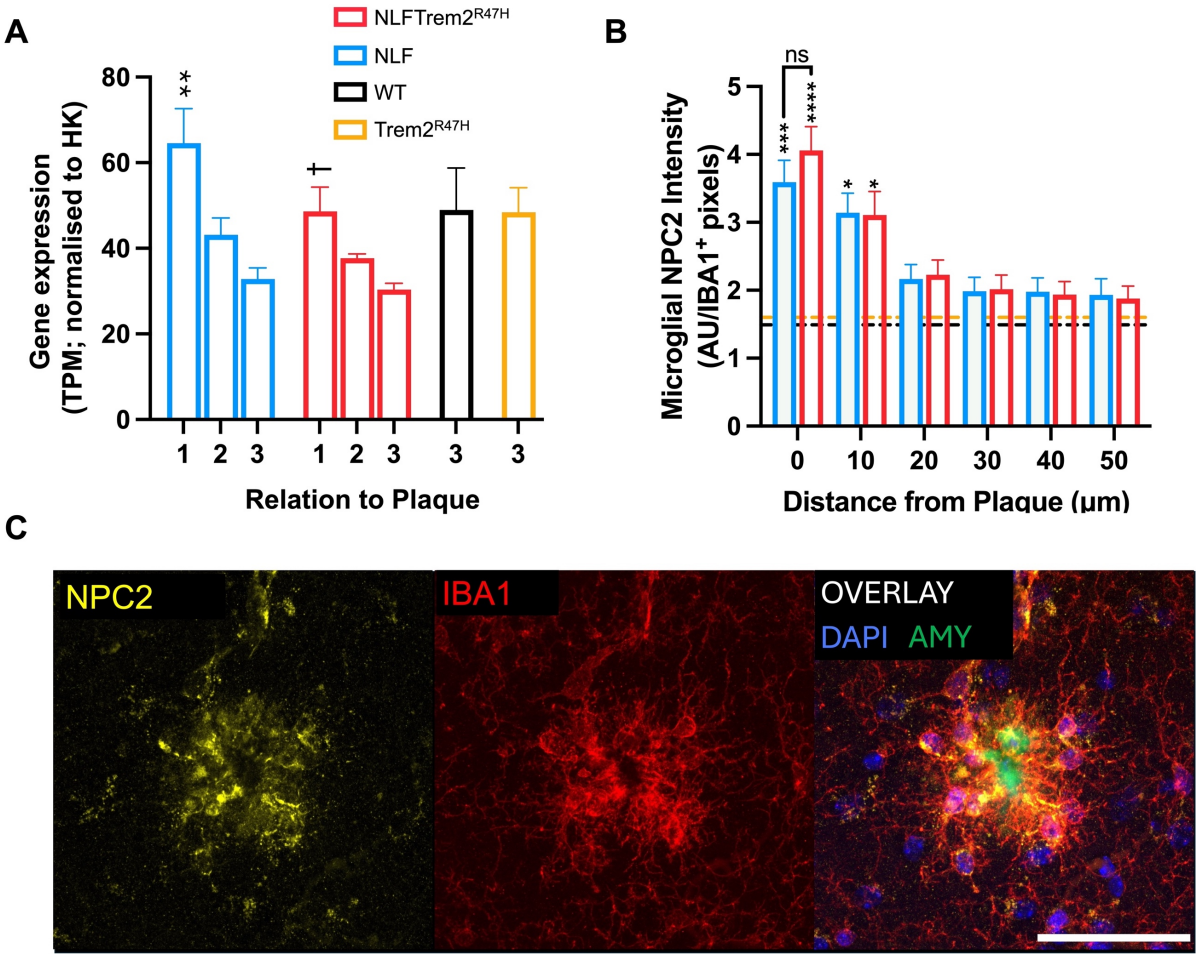

Figure 3.8 Plaque-induced increase in NPC2 protein expression is not dependent on *Trem2* genotype

(A) *Npc2* expression measured by GeoMx in (1) plaque microglia, (2) periplaque microglia, and (3) away microglia (main effects: relation to plaque P<0.01; genotype P<0.05; interaction P>0.1). (B) Quantification of NPC2 protein measured by fluorescence intensity from widefield microscopy within IBA1+ microglial pixels at varying distances from the plaque (main effects: distance to plaque P<0.0001; genotype P>0.1; interaction P>0.1). Note there is no significant difference between WT and Trem2^{R47H} genotypes. (C) Confocal microscope images of images of NPC2 staining in NLF mice, NPC2 (yellow), IBA1 (microglia, red), Amytracker (Aβ plaques, green). Scale bar: 50 µm. Statistical analysis: (A & B) Two-way repeated measures ANOVA between NLF and NLFTrem2^{R47H} mice, followed by Tukey's correction for multiple comparisons, results shown on graphs. (B) Within genotype statistical comparisons are made against the 50 µm distance from the plaque. ****P<0.0001; **P<0.01; */†P<0.05. *-within genotype significance, †- between genotype significance. Spatial transcriptomic experiments: NLF n=6; NLFTrem2^{R47H} n=4. Immunohistochemistry experiments: NLF, n=4; NLFTrem2^{R47H}, n=4, with lines plotting Trem2^{R47H} and WT averages from n=4 for both genotypes. Data plotted as mean + SEM.

Despite the lack of *Trem2* genotype dependency of *Apoe* expression in the spatial transcriptomics analysis (Figure 3.9A), *Apoe* and *Trem2* are frequently reported to interact in response to AD pathology and share similar roles, including the control of the plaque microglia response (Ulrich et al., 2018). Like *Npc2*, *Apoe* is involved in lipid homeostasis, acting as an apolipoprotein to facilitate the intracellular transport of lipids. To assess the dependence of APOE protein expression on *Trem2* genotype, I performed an immunohistochemistry experiment targeting APOE. In both NLF and NLFTrem2^{R47H} mice, APOE expression was significantly increased on plaque (Figure 3.9B and 3.9C). Interestingly, APOE expression, specifically on plaques, was significantly higher in NLF mice compared to NLFTrem2^{R47H} mice, showing approximately a 10-fold increase in NLF and a 5-fold increase in NLFTrem2^{R47H}.

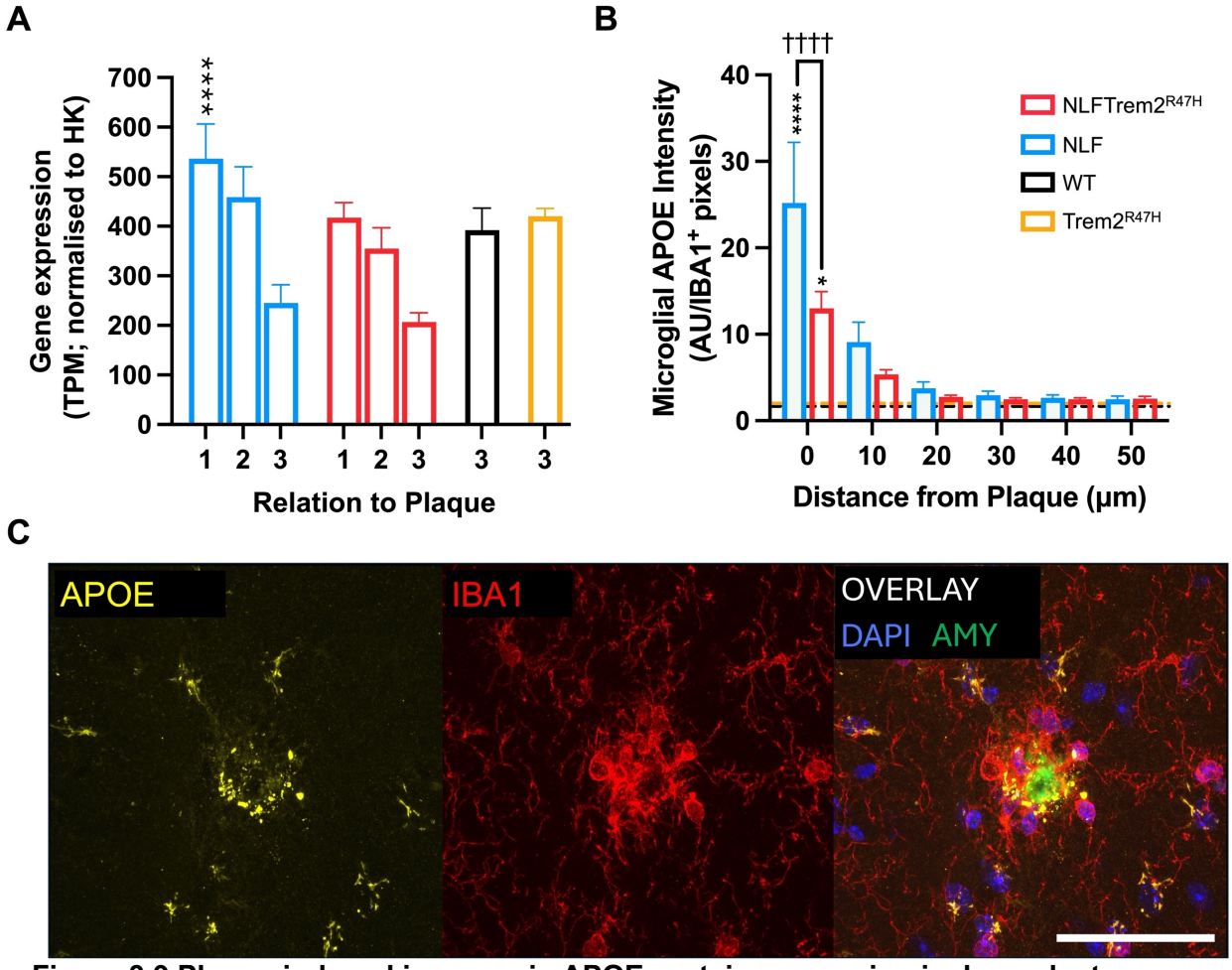

Figure 3.9 Plaque-induced increase in APOE protein expression is dependent on *Trem2* genotype

(A) *Apoe* expression measured by GeoMx in (1) plaque microglia, (2) periplaque microglia, and (3) away microglia. (Main effects: relation to plaque P<0.0001; genotype P>0.1; interaction P>0.1) (B) Quantification of APOE protein measured by fluorescence intensity from widefield microscopy within IBA1^{+} microglial pixels at varying distances from the plaque (Main effects: relation to plaque P<0.0001; genotype P<0.05; interaction P<0.05). Note there is no significant difference between WT and Trem2^{R47H} genotypes. (C) Confocal images of

APOE staining in NLF and NLFTrem2^{R47H} mice, APOE (yellow), IBA1 (microglia, red), Amytracker (Aβ plaques, green). Scale bar: 50 μm. Statistical analysis: (A & B) Two-way repeated measures ANOVA between NLF and NLFTrem2^{R47H} mice followed by Tukeys correction for multiple comparisons, shown on the graphs. (B) Within genotype statistical comparisons are made against the 50 μm distance from the plaque. ****/††††P<0.0001; **P<0.01; *P<0.05. *-within genotype significance, †- between genotype significance. Spatial transcriptomic experiments: NLF n=6; NLFTrem2^{R47H} n=4. Immunohistochemistry experiments: NLF, n=7; NLFTrem2^{R47H}, n=9, with lines plotting Trem2^{R47H} and WT averages from n=9 and n=8, respectively. Data plotted as mean + SEM.

3.7 Detection of Aβ plaque-induced changes in GeoMx and bulk RNA sequencing

The detection of AD-associated changes in gene expression has historically relied on the use of RNA sequencing techniques that analyse tissue irrespective of the spatial distribution of pathology. The identification of plaque-specific changes in gene expression (Figure 3.4) suggests that the effectiveness of whole-tissue RNA sequencing in detecting AD-associated expression changes may depend on the proportion of plaque-associated tissue analysed. Although the NLF model more accurately reflects AD compared to other existing models, even at advanced ages, NLF mice exhibit lower pathology severity compared to more aggressive models (Benitez et al., 2021).

To assess the importance of spatial resolution in studying AD-associated gene expression changes, data from GeoMx (18-month-old NLF: plaque vs. away AOIs) were compared to bulk hippocampal RNA sequencing counts (NLF & WT). Using these techniques, disease-associated microglia (DAM, Keren-Shaul et al., 2017), disease-associated astrocytes (DAA, Habib et al., 2020), and synaptic hub (Williams et al., 2021) gene sets were analysed. For consistency, counts from GeoMx and bulk RNA sequencing were both normalised to housekeeping genes *Actg1* and *Actb*.

Heatmaps of fold change revealed more pronounced changes across all three gene sets in GeoMx analysis compared to bulk RNA sequencing (Figure 3.10Ai, Figure 3.10Aii). Furthermore, to evaluate the ability of these techniques to detect gene set-level changes, principal component analysis (PCA) was used to assess the separation of plaque vs. away AOIs (GeoMx), NLF vs. WT (bulk RNA sequencing), and NLF over age (bulk RNA sequencing). For DAM, DAA and Synaptic Hub gene sets, GeoMx provided a more distinct separation than bulk RNA sequencing (Figure 3.10A, 3.10B and 3.10C).

Altogether, this indicates that the presence of DAM microglia, DAA astrocytes, and synaptic loss are not homogenous throughout the hippocampus but are specific to Aβ plaque pathology.

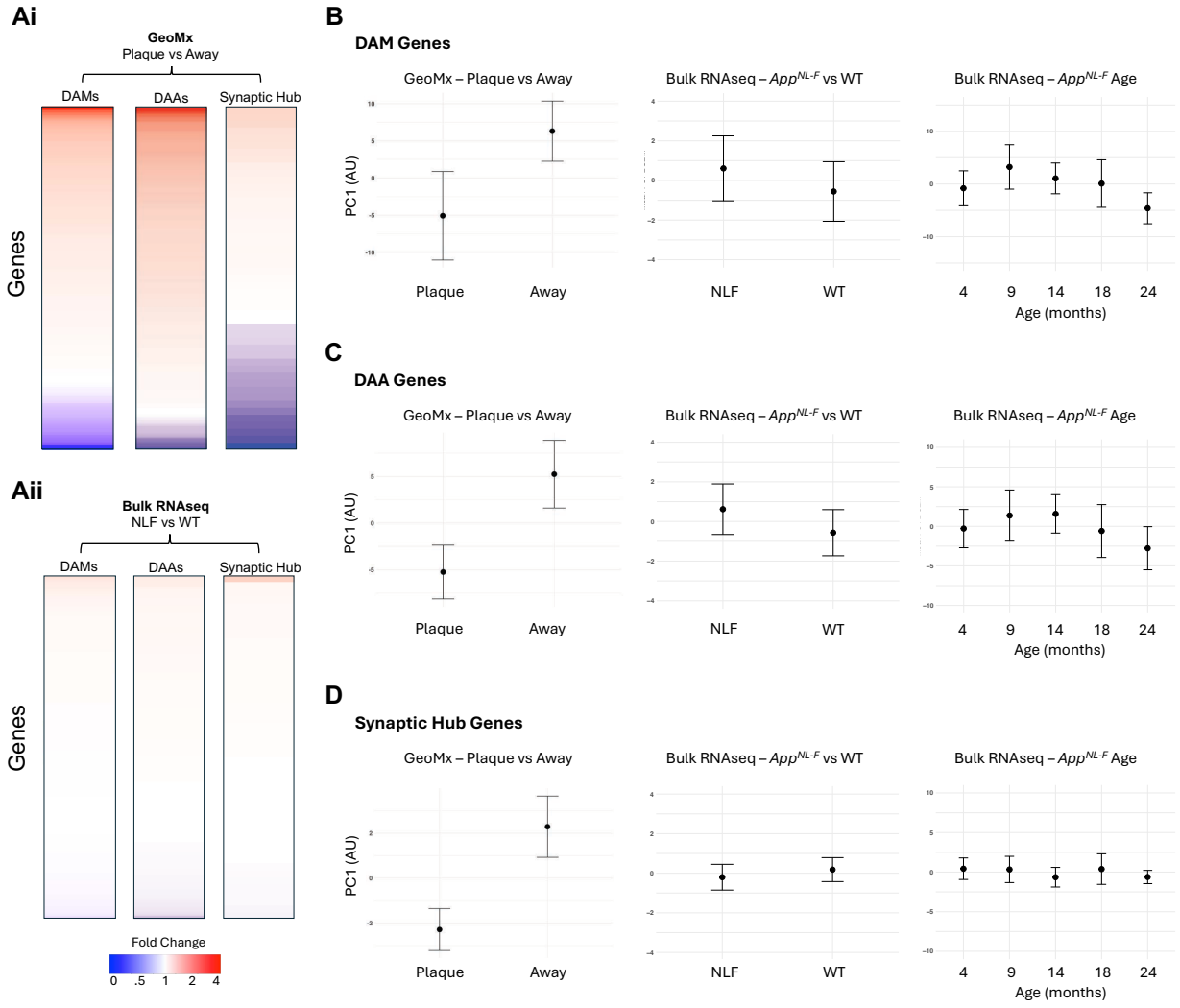

Figure 3.10 Detection of amyloid plaque-induced changes in GeoMx and bulk RNA sequencing

(A) Heatmaps showing fold change in gene expression for disease-associated microglial genes (DAMs, Keren-Shaul et al., 2017), disease-associated astrocytic genes (DAAs, Habib et al., 2020), and synaptic hub genes (Williams et al., 2021) in (Ai) GeoMx spatial transcriptomics, comparing Plaque vs. Away regions; (Aii) bulk RNA sequencing, comparing NLF vs. WT hippocampal tissue. (B-D) Principal component analysis (PCA) of DAM (B), DAA (C), and synaptic hub genes (D) in three conditions: GeoMx Plaque vs. Away, bulk RNA sequencing NLF vs. WT, and bulk RNA sequencing NLF across ageing. GeoMx DAM gene analysis was performed using the TMEM119 collection, while GeoMx DAA and synaptic hub gene analysis was performed using the GFAP collection. Bulk RNA sequencing was conducted on whole hippocampal tissue. GeoMx: NLF, n=6. Bulk RNA sequencing: WT 18m, n=11; NLF 18m, n=9; NLF 24m, n=9; NLF 14m, n=11; NLF 9m, n=12; NLF 4m, n=12. Data plotted as mean ± SEM.

3.8 Impact of *Trem2* genotype on pathology and synaptic transmission

3.8.1 The *Trem2*^{R47H} mutation increases the density of small plaques

The dependency of phagocytosis and lysosomal degradation gene expression on functioning Trem2 (Figure 3.7), along with the consistent finding of the Trem2 dependence of microglial phagocytosis (Jiang et al., 2017; Liu et al., 2020; Takahashi et al., 2005), suggests a potential effect on Aβ plaque load. To investigate this, I assessed hippocampal plaque load in 18-month-old NLF and NLFTrem2^{R47H} mice. Using Amytracker520 to stain aggregated deposits (Figure 3.11A), I found no change in either plaque coverage (Figure 3.11B) or plaque density (Figure 3.11C) between NLF and NLFTrem2^{R47H} mice. To probe this further, I investigated whether there was any potential change in plaques of certain sizes. Interestingly, I found that NLFTrem2^{R47H} mice have a higher density of small plaques (< 100 μm^2) compared to NLF mice (Figure 3.11D).

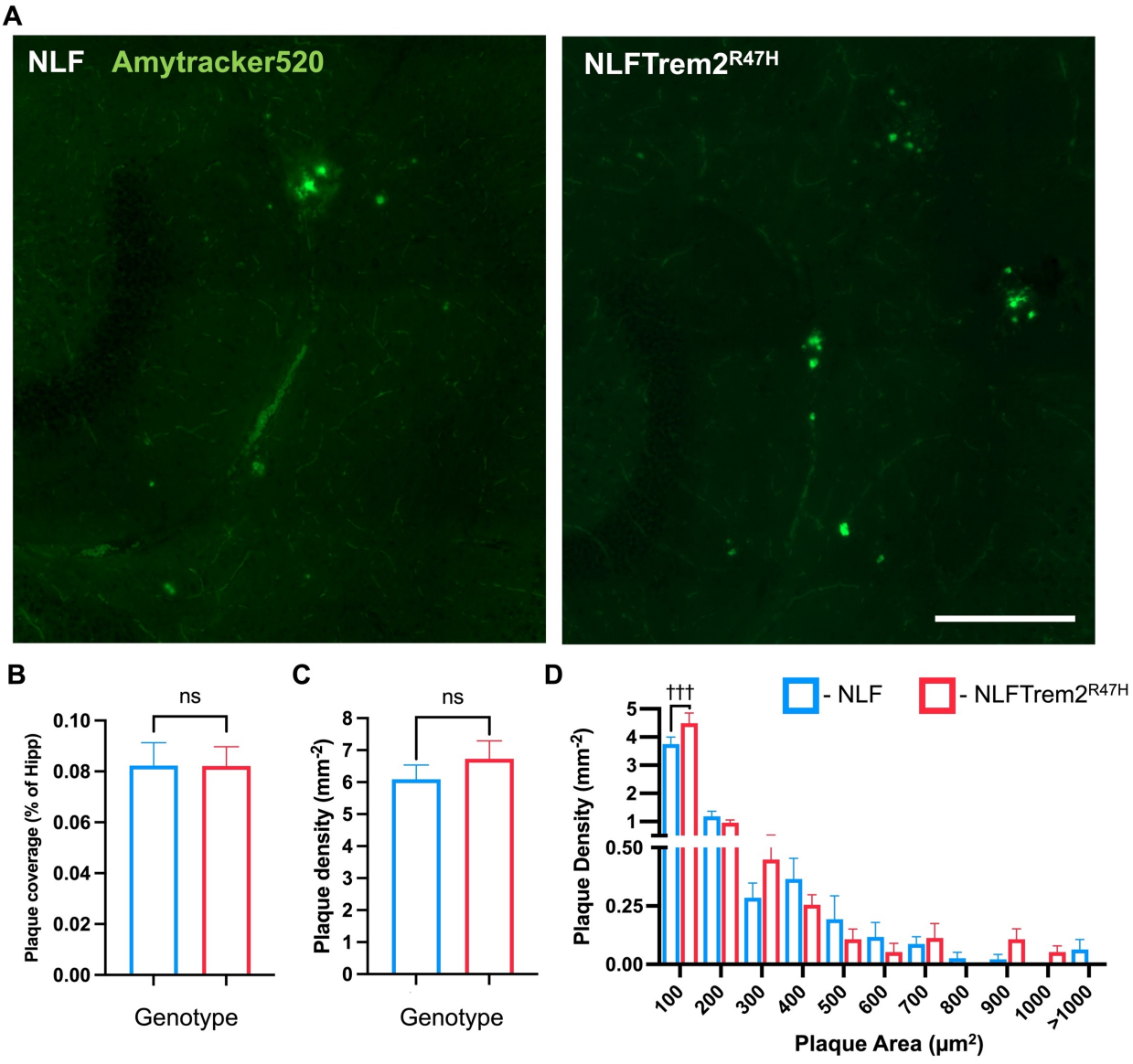

Figure 3.11 The *Trem2*^{R47H} mutation increases the density of small plaques
(A) Widefield hippocampal images of Amytacker (Aβ plaques, green) staining in NLF and NLFTrem2^{R47H} mice. Scale bar: 200 μm. (B) Amytracker defined plaque area coverage of the hippocampus between 18-month-old NLF and NLFTrem2^{R47H} mice. (C) Amytracker defined plaque density in the hippocampus between 18-month-old NLF and NLFTrem2^{R47H} mice. (D) Histogram showing the relationship between plaque area and plaque density at defined sizes in 18-month-old NLF and NLFTrem2^{R47H} mice (main effects: plaque size P<0.001; genotype P>0.1; interaction P<0.01). Statistical Analysis: (B & C) main effect of genotype measured through T-test, shown on graphs. (D) Two-way repeated measures ANOVA between NLF and NLFTrem2^{R47H} mice, followed by Tukey's correction for multiple comparisons, results shown on graph. †††P<0.001. †- between genotype significance. NLF, n=7; NLFTrem2^{R47H}, n=9.

3.8.2 *App* and *Trem2* genotypes show a trend toward interaction in basal and LTP-driven changes in field postsynaptic potentials

Microglia, the brain's primary phagocyte, regulate neuronal circuitry by removing synapses during development, throughout life, and in response to synaptic damage (Cornell et al., 2022; Hong et al., 2016; Paolicelli et al., 2011). *Trem2*, a key hub gene in the regulation of phagocytosis, plays a crucial role in these developmental processes, with its dysfunction leading to altered synaptic density and increased synaptic excitability (Filipello et al., 2018). Furthermore, microglia detect and eliminate damaged synapses caused by Aβ-induced toxicity in a *Trem2*-dependent manner(Rueda-Carrasco et al., 2023). Given that a loss of neuronal matter and synapses are a major correlate of cognitive decline (Fox et al., 1999; Sze et al., 1997), the above finding of plaque- and *Trem2*-dependent regulation of phagocytosis and lysosomal degradation genes (Figure 3.7), along with increased plaque pathology in NLF mice harbouring the *Trem2*^{R47H} mutation (Figure 3.11), suggests that synaptic activity may be disrupted.

To assess disruptions in synaptic transmission in response to both plaque pathology (due to the NL and F mutations in *App*) and the *Trem2*^{R47H} mutation, I measured short- and long-term plasticity in field excitatory postsynaptic potentials (fEPSPs) within the Schaffer collateral-CA1 connection of the hippocampal tri-synaptic pathway.

I first examined presynaptic mechanisms of short-term plasticity by measuring the fEPSP slope before and after paired-pulse stimulation. The ratio of the second fEPSP slope to the first reflects the probability of glutamate release from the presynaptic terminal. This is because the greater the number of vesicles released during the first stimulation, the fewer remain available for release during the second stimulation (Clements et al., 1992). Presynaptic terminals with a low release probability suggest that calcium levels are insufficient to release vesicles, possibly due to calcium buffering (Blatow et al., 2003;

Timofeeva and Volynski, 2015). Paired-pulse facilitation, where the second fEPSP slope is steeper than the first, typically occurs because residual presynaptic calcium from the first response pre-saturates calcium buffers, with some calcium also remaining bound to vesicle release proteins. This enhances vesicle release during the second calcium influx, leading to a greater postsynaptic fEPSP slope (Katz and Miledi, 1968). Interestingly, at paired pulse interstimulus intervals of 25 ms and 50 ms, *App* and *Trem2* genotypes showed a trend toward interaction (Figure 3.12A, 3.12Bi and 3.12Bii; $P < 0.05$, $P = 0.08$, respectively). Due to a significant interaction at 25 ms, post hoc analysis revealed that NLF mice harbouring the *Trem2*^{R47H} mutation exhibited a significantly higher paired-pulse ratio compared to both NLF and Trem2^{R47H} mice, indicating a lower probability of release (Figure 3.12Bi).

To assess the impact of *App* and *Trem2* genotypes on a correlate of learning and memory, I measured long-term plasticity by analysing fEPSP slopes before and after long-term potentiation (LTP) conditioning (Figure 3.12Ci, Bliss and Lømo, 1973). During LTP induction, bursts of activity depolarise the postsynaptic membrane, enabling NMDA receptor activation and calcium influx. Here, LTP was conditioned using tetanic stimulation following a stable baseline response. Early LTP was assessed by averaging and baseline normalising the fEPSP slope 51–60 minutes post-conditioning (Figure 3.12Cii). This phase of LTP is primarily maintained postsynaptically through calcium-activated, calmodulin-dependent kinases, which enhance AMPA receptor conductivity and promote the insertion of AMPA receptors. Similar to the findings of short-term plasticity, the fEPSP slope post-LTP conditioning showed a trend toward an interaction between *App* and *Trem2* genotypes (Figure 3.12Cii, $P = 0.06$). Notably, the effect of the *Trem2*^{R47H} mutation was opposite in mice with WT *App* to mice with NLF mutations.

Although LTP induction is primarily postsynaptic, it can also have presynaptic effects. To assess the locus of LTP expression, paired-pulse ratios were measured throughout the LTP conditioning experiment and averaged over the 51–60 minute post-LTP period (Figure 3.12D). Again, post-LTP paired pulse ratios showed a trend toward an interaction between App and Trem2 genotypes (Figure 3.12Dii, $P = 0.06$). The increase in probability of release indicated by the reduced paired pulse ratios in NLF and Trem2^{R47H} compared to WT could suggest a presynaptic component of their LTP expression. However, in NLFTrem2^{R47H} mice, this was not seen.

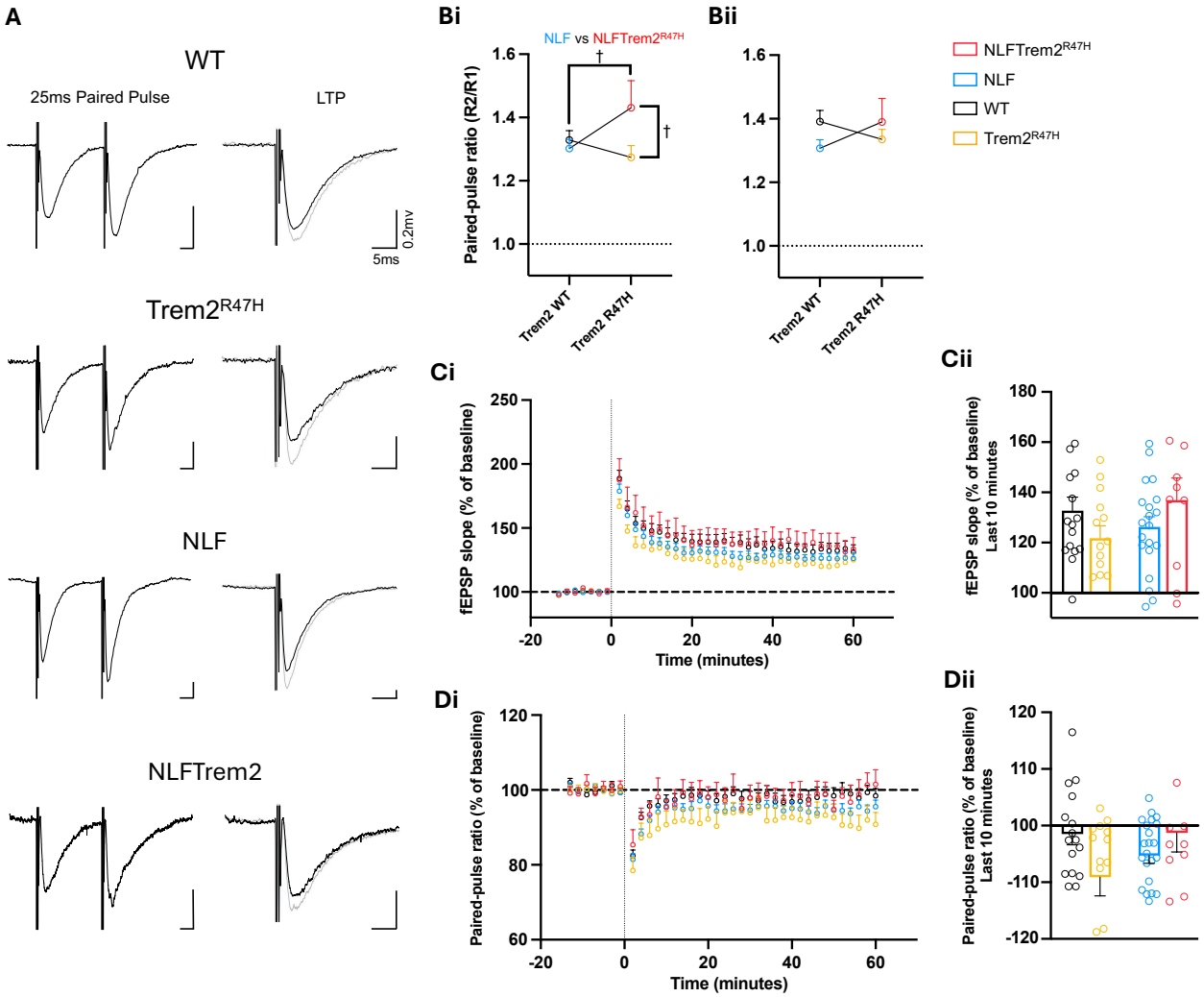

Figure 3.12 *App* and *Trem2* genotypes show a trend toward interaction in basal and LTP-driven changes in field postsynaptic potentials

(A) Representative traces from WT, Trem2^{R47H}, NLF, and NLFTrem2^{R47H} field excitatory postsynaptic potentials (fEPSPs) recorded during a 25 ms inter-stimulus interval and pre/post (black/grey) long-term potentiation conditioning. (B) Basal paired-pulse ratios at different inter-stimulus intervals: (Bi) 25 ms (main effects: *App* genotype P>0.1; *Trem2* genotype P>0.1; interaction P<0.05). (Bii) 50 ms (main effects: *App* genotype P>0.1; *Trem2* genotype P>0.1; interaction P=0.08). (C) Tetanus-induced changes in field excitatory postsynaptic potential (fEPSP) slope: (Ci) Time course of fEPSP slope measured before (baseline) and after tetanus (time 0, grey line), normalised to baseline. (Cii) Mean fEPSP slope over the last 10 minutes of the LTP paradigm recording (time 51–60 min, main effects: *App* genotype P>0.1; *Trem2* genotype P>0.1; interaction P=0.06). (D) Tetanus-induced changes in paired-pulse ratio (50 ms inter-stimulus interval): (Di) Time course of paired-pulse ratios measured before (baseline) and after tetanus (time 0, grey line), normalised to baseline. (Dii) Mean paired-pulse ratio over the last 10 minutes of the LTP recording (time 51–60 min, main effects: *App* genotype P>0.1; *Trem2* genotype P>0.1; interaction P=0.06). Statistical analysis: all analyses were performed using a two-way ANOVA between *App* and *Trem2* genotypes. Post hoc analysis was performed in cases of significant interaction using Fisher's LSD test, shown on graph. †P<0.05. †-between genotype significance. Basal paired-pulse experiments: NLF n=25, NLFTrem2^{R47H} n=13, WT n=20, Trem2^{R47H} n=23. LTP experiments: NLF, n=20; NLFTrem2^{R47H}, n=10; WT, n=16; Trem2^{R47H}, n=14. Data plotted as mean + or - SEM.

3.9 Chapter summary

This chapter investigated whether direct microglial contact with Aβ plaques is required to regulate the expression of plaque-induced genes (PIGs). The findings demonstrate that PIGs can be categorised based on their spatial expression patterns relative to plaques. However, the majority of significantly upregulated PIGs exhibited increased expression only in microglia in direct contact with plaques. Furthermore, introducing the *Trem2*^{R47H} mutation confirmed the role of TREM2 as a key controller of immune-related gene expression. The plaque specificity of *Trem2* expression was also mirrored by the plaque specificity of the genes under the regulation of functioning *Trem2*. Here, I found that 9 genes, involved mainly in phagocytosis and lysosomal degradation, lost their plaque-specific upregulation due to the introduction of the *Trem2*^{R47H} mutation. The loss of these genes could be essential in understanding the risk of AD associated with the *Trem2*^{R47H} mutation. Protein analysis of lipid-associated genes *Npc2* and *Apoe* did not mirror their associated gene expression results. However, in both cases, protein analysis still showed plaque-specific increases and a dependency on *Trem2* in the case of APOE expression.

The findings of this chapter provide a clear analysis of the benefits of using GeoMx spatial transcriptomics to assess pathology-associated changes in gene expression. I demonstrated the limitations of techniques such as bulk RNA sequencing and PCR in resolving the extent of Aβ plaque-induced *Trem2* expression in NLF mice. Additionally, I presented a direct comparison between bulk RNA sequencing and GeoMx spatial transcriptomics in assessing changes in known microglial and astrocytic activation states, as well as synaptic-associated genes. GeoMx revealed a greater magnitude of detectable Aβ plaque-associated changes compared to bulk RNA sequencing.

This chapter also confirmed that Jackson Laboratory mice harbouring the *Trem2*^{R47H} mutation had a ~63% reduction in *Trem2* expression. However, at the protein level, this amounted to a ~24% reduction assessed using the semi-quantitative analysis of histochemical images. This does not, however, falsify the findings on *Trem2* dependency but rather presents a combined effect from the loss of TREM2 function and loss of *Trem2* expression.

Finally, I showed that the emergent effects of the *Trem2*^{R47H} mutation resulted in an increase in the density of small plaques within the hippocampus, perhaps due to the associated dysregulation of immune-related gene expression. A more complicated result was presented when analysing the effects of Aβ plaque pathology and the *Trem2*^{R47H} mutation on synaptic transmission. Overall, there is a consistent trend towards interaction between *App* and

Trem2 genotypes in both short- and long-term plasticity, whereby the effect of the *Trem2*^{R47H} mutation was opposite in mice with WT *App* to mice with NLF mutations.

CHAPTER 4

PLAQUE-INDUCED MICROGLIAL GENE EXPRESSION IN HUMAN AD TISSUE

4.1 Introduction

The effort to develop better mouse models of AD, such as the NLF model, is driven by the historical lack of translation from mouse models to human clinical trials (Drummond and Wisniewski, 2017). The previous chapter presented evidence of Aβ plaque-induced changes in microglial gene expression, including the observation that direct microglial contact with plaques is required for the upregulation of many AD-associated genes. These findings may have important implications for AD drug discovery efforts targeting specific microglial pathways. Moreover, the accompanying gene expression database may serve as a valuable resource for researchers looking to investigate genes of interest, either to support ongoing work or to inform future studies. Ensuring that such findings, like all results generated in AD mouse models, are translatable to human AD is therefore of critical importance.

Numerous studies have explored microglial gene expression in the human AD brain. Notably, several have reported a lack of the classic disease-associated microglia (DAM) signature, originally identified in 5XFAD mice, in microglia responding to Aβ pathology in human AD (Mathys et al., 2019; Srinivasan et al., 2020). Despite this, shared transcriptional changes across studies include the upregulation of genes involved in phagocytosis, lipid metabolism, and cytokine signalling (Mathys et al., 2019; Olah et al., 2020; Srinivasan et al., 2020). Although these earlier studies lacked spatial resolution with respect to Aβ plaques, a recent study employed laser capture microdissection followed by bulk RNA sequencing of plaque regions, revealing an upregulation of plaque-binding proteins such as *TREM2*, Toll-like receptors, and complement components, as well as significant enrichment of the DAM signature (Das et al., 2024). While these findings highlight potential differences in the microglial response to Aβ plaque pathology between mouse and human microglia, they also suggest the importance of analysing microglia with a spatial relation to plaques. Furthermore, similar to mouse research, there is a lack of studies showing the importance of microglia plaque contact to regulate the expression of AD-associated genes.

Chapter 4 investigates Aβ plaque-induced changes in microglial gene expression in human AD brain samples. The experimental design closely parallels that of the mouse study and specifically aims to determine whether direct microglial contact with plaques is necessary for the regulation of AD-associated genes. While pairing by plaque proximity helped control variability in the mouse study, this design is particularly valuable in the human context,

where samples often differ substantially in postmortem delay, age at death, genetic background, and other confounding factors (Olney et al., 2025; Tomita et al., 2004; Zhu et al., 2017). This approach enhances statistical power by enabling within-sample comparisons and allows for robust analysis despite smaller sample sizes compared to other research utilising human tissue

4.2 Microglial plaque contact is necessary for AD-associated gene expression in human AD

4.2.1 Human microglial spatial transcriptomics design

The observation that many AD-associated microglial genes only increase in expression upon microglial-plaque contact may be an artefact of using AD mouse models. To assess the translatability of this finding, GeoMx spatial transcriptomics was performed on postmortem human hippocampal tissue. Antibodies against IBA1 were used to label microglia, and the beta-sheet dye Amytracker520 was applied to detect plaques (Figure 4.1Ai). Since tau tangles also exhibit beta-sheet morphology, Amytracker520 stained both plaques and tau tangles. However, these pathologies are often regionally separated, therefore, areas of tangle positivity were avoided to enrich for plaque-associated effects. The ROI selection paradigm mimicked that of the mouse experiment (Figure 3.1). ROIs were drawn in regions enriched with plaques (Plaque ROIs) and regions free of plaques (Away ROIs) (Figure 4.1Aii). The ROIs were further subdivided into:

-Plaque microglial AOI: IBA1 signal directly contacting Amytracker520 signal (Figure 4.1B),

- Periplaque microglial AOI: IBA1 signal neighbouring Amytracker520 signal but not in direct contact (Figure 4.1D),

- Away microglial AOI: IBA1 signal located in the plaque-free, Away ROIs (Figure 4.1C).

This direct translation of the mouse experiment to human tissue again enabled the assessment of microglial expression in regions away from plaques, in periplaque areas, and in direct contact with plaques.

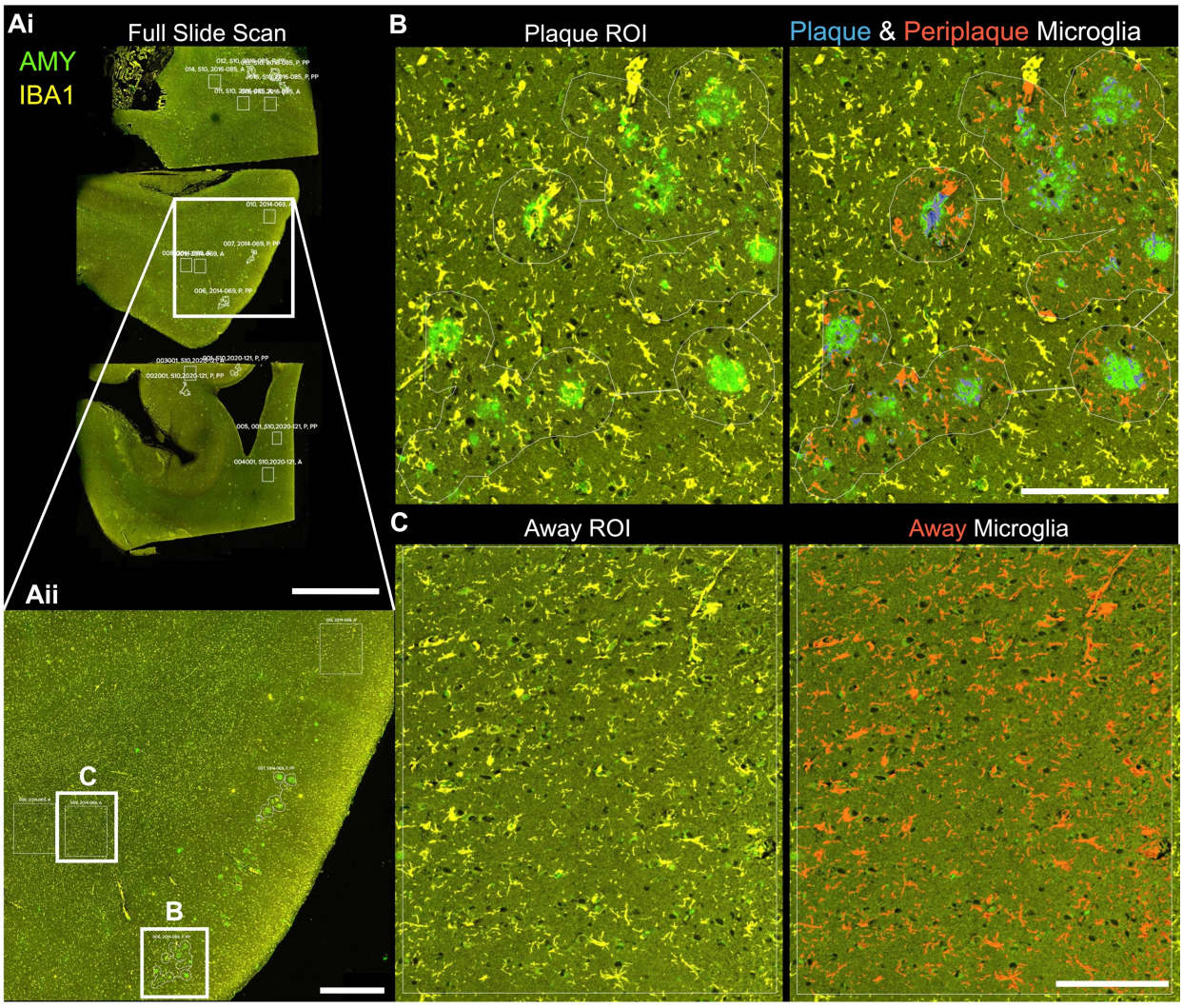

Figure 4.1 ROI selection for microglia-enriched spatial transcriptomics on human tissue

Representative staining and region of interest (ROI) selection for spatial transcriptomics analysis. 8 µm-thick sections were labelled for microglia (IBA1 antibody, yellow) and Aβ plaques (Amytracker, green).(Ai) Full-slide scan showing three hippocampal sections. Scale bar: 5000 µm. (Aii) Zoomed-in image of the highlighted region in (Ai). Scale bar: 1000 µm. (B) Example of a plaque ROI. The right panel highlights the areas collected for 'plaque' (blue) and 'periplaque' (red) microglial region of interest. Scale bar: 200 µm. (C) Example of an 'away' microglia ROI. The right panel shows the area collected for 'away' microglia (red). Scale bar: 200 µm.

Unlike mouse models, in human AD tissue, factors affecting inter-sample variation, such as genetics, environment, age at death, postmortem delay, cannot be controlled. To minimise inter-sample variation while preserving RNA integrity, FFPE hippocampal tissues were selected with a postmortem delay of ≤6 hours and a year of death within the last decade. Samples were also matched by *APOE* status and sex (Table 4.1). Due to limited tissue availability, the age at death varied widely, with a range of 33 years (Table 4.1). However, a key advantage of spatial transcriptomics in overcoming inter-sample variability is its ability to

pair collection areas, allowing gene expression changes in microglia to be analysed within the same sample.

Clinical Diagnosis	*APOE* Status	Age (Years)	Sex	Year of Death	Postmortem Delay (hrs:min)	Brain Weight (g)	Braak Stage
Alzheimer's disease	43	94	m	2015	04:15	945	4
Alzheimer's disease	33	78	f	2016	04:55	1130	6
Alzheimer's disease	33	94	m	2016	04:15	870	5
Alzheimer's disease	33	96	f	2016	04:15	940	5
Alzheimer's disease	33	87	m	2016	05:30	1045	5
Alzheimer's disease	33	73	f	2017	04:10	970	6
Alzheimer's disease	33	96	m	2017	04:25	1095	5
Alzheimer's disease	43	81	f	2017	05:30	1015	6
Alzheimer's disease	43	87	f	2017	03:25	1193	4
Alzheimer's disease	33	86	m	2017	04:50	1295	4
Alzheimer's disease	43	76	m	2018	04:40	1300	6
Alzheimer's disease	43	86	m	2018	03:45	1406	4
Alzheimer's disease	43	68	m	2018	04:30	1163	6
Alzheimer's disease	43	97	m	2018	05:10	1120	5
Alzheimer's disease	33	94	f	2019	04:35	1136	4
Alzheimer's disease	33	95	m	2020	06:05	1245	5
Alzheimer's disease	43	106	f	2020	04:50	1100	4
Alzheimer's disease	43	83	f	2021	04:30	1155	4
Alzheimer's disease	33	88	f	2021	05:55	1040	5
Alzheimer's disease	43	73	f	2021	05:15	1055	6

Table 4.1 Summary of human hippocampal sample characteristics

4.2.2 Pairwise regional comparisons reveal plaque-dependent gene expression patterns

GeoMx counts were normalised using the DESeq2 pipeline, which applies AOI-specific scaling factors to account for the variability in human tissue. Three pairwise comparisons were made and statistically accounted for: Plaque microglia vs Away microglia (Figure 4.2Ai), Plaque microglia vs Periplaque microglia (Figure 4.2Aii), and Periplaque microglia vs Away microglia (Figure 4.2Aiii).

As in the spatial transcriptomics of the mouse models (Figure 3.4), the expression pattern across the three regions enabled the categorisation of each gene into:

- Plaque Response: genes that change expression exclusively in microglia directly contacting plaques.
- Graded Response: genes that exhibit a gradual change in expression from away to periplaque microglia, and further from periplaque to plaque microglia.
- Periplaque Response: genes that change expression specifically in microglia within the periplaque region.
- Plaque and Periplaque Response: genes that change expression from away to periplaque and away to plaque microglia, but do not significantly differ between periplaque and plaque microglia.

Each category was further subdivided based on the direction of change, identifying genes that were upregulated or downregulated relative to microglia in away regions (Figure 4.2B).

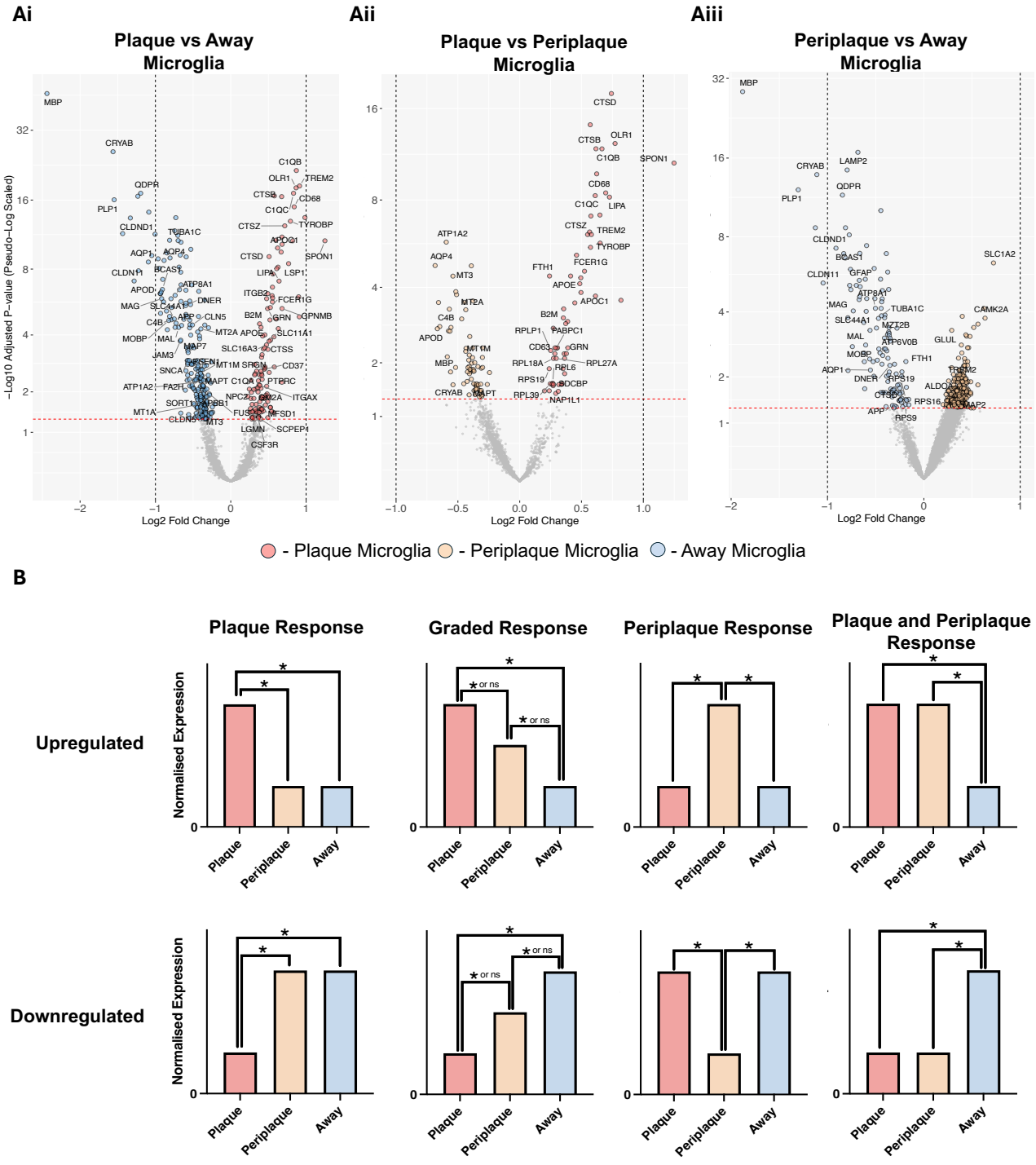

Figure 4.2 Microglial plaque contact is necessary for AD associated gene expression in human AD

(A) Volcano plots showing DESeq2-normalised differential expression analyses for microglia in (Ai) Plaque vs Away, (Aii) Plaque vs Periplaque, and (Aiii) Periplaque vs Away regions. (B) Representative categories illustrating different gene expression responses to plaques, with example graphs for each category. P values were adjusted for multiple comparisons using Benjamini-Hochberg false discovery rate (FDR) method.

4.2.3 Expression of PIGs in relation to plaque in human AD tissue

I first investigated the translation of the PIG genes from the NLF experiment to the human tissue. Among the total of 55 PIGs identified by Chen et al. (2020), 19 showed a significant increase in plaque microglia compared to away microglia. Of these 19 PIGs, 18 overlapped with the 38 significant PIGs identified in the NLF spatial transcriptomic experiment (Figure 3.4). Notably, only *CTSH* was significantly identified in the human data but not in the NLF data. All of the 18 overlapping genes fell into either the plaque response category or the graded response category (Figure 4.3).

Among the genes categorised under plaque response (Figure 4.3A), *B2M* and *APOE* were the only two that exhibited altered expression patterns in relation to plaques when compared to the NLF experiment. Specifically, B2M was previously classified in the graded response category, while APOE fell under the plaque and periplaque response category (Figure 3.4). Additionally, many genes that were previously classified under the plaque response category in the NLF experiment, such as *TREM2*, *CTSS*, *HEXA*, *NPC2*, *LY86*, and *C1QA*, are classified under the graded response category (Figure 4.3B).

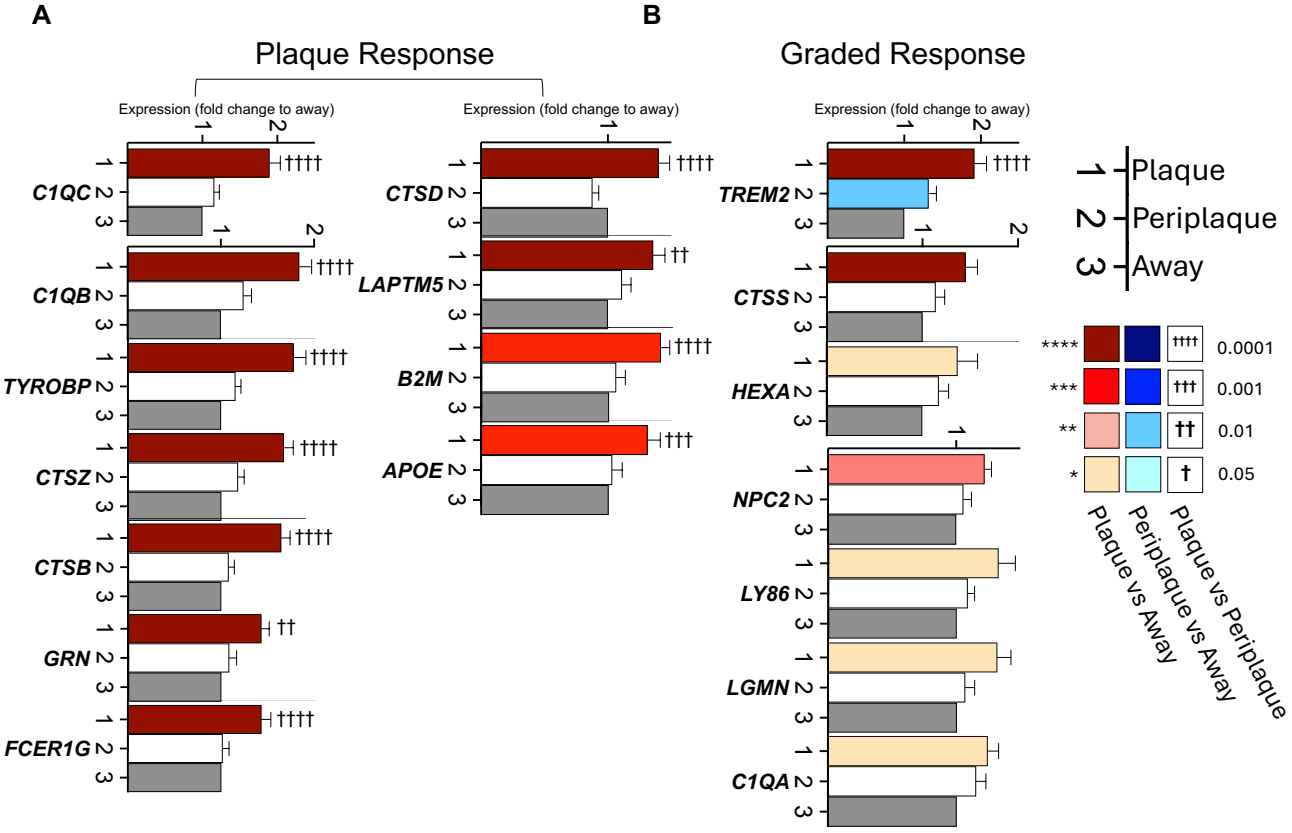

Figure 4.3 Expression of PIGs in relation to plaque in human AD tissue
Expression of 18 of 38 significant PIGs from the NLF spatial transcriptomic experiment showed a significant increase in expression in plaque contacting microglia compared to away in human AD tissue. (A) 11 of 18 significant genes had increased expression only when the microglia were in direct contact with plaques. (B) 7 genes showed a graded response whereby expression gradually increases from away through to plaque regions.

Statistical difference as indicated ****/†††† P<0.0001; ***/††† P<0.001; **/†† P<0.01; */† P<0.05. Statistical significance extracted from Deseq2 whole transcriptomic analysis with Benjamini Hochberg post hoc correction for multiple comparisons. All data plotted as mean + SEM.

4.2.4 Genes upregulated exclusively by plaque contact are involved in lipid metabolism and immune response

To gain a better understanding of the roles played by the significantly changing genes in each category from the whole transcriptome analysis, I conducted further analysis to assess their enrichment within several databases: biological process (BP), molecular function (MF), cellular compartment (CC), KEGG pathways, and Reactome pathways.

A total of 49 genes were classified in the upregulated plaque response category, displaying increased expression specifically in microglia that were in direct contact with plaques. Ontology analysis of these genes revealed that a significant portion of the associated ontology terms were related to lipid metabolism (Figure 4.4). Key enriched ontology terms included: neutral lipid metabolic process (BP), protein lipid complex binding (MF), very-low-density lipoprotein particle (CC), and cholesterol metabolism (KEGG). The genes contributing to these terms include apolipoproteins *APOE* and *APOC1*, lipid binding protein encoding *GPIHBP1*, and lysosomal lipase *LIPA*.

In addition to lipid-related functions, immune response genes were also enriched in the plaque response category. These included: regulation of immune effector processes (BP), synapse pruning (BP), complement activation and triggering (BP & Reactome), DAP12 signalling (Reactome), and lysosomal lumen (CC). Here, contributing genes include complement factors *C1QB* and *C1QC*, the TREM2 signalling partner *TYROBP*, microglial lysosomal and activation-associated genes *GRN*, *CD68* and *LAPTM5*.

Finally, several genes were linked to cellular damage and neurodegeneration, indicated by the neuron death (BP) and antioxidant activity (MF) ontologies. Example genes here are *SORL1,* involved in endosomal trafficking and APP processing, necrosis factor *TNFRSF1B*, and antioxidant *GPX1*.

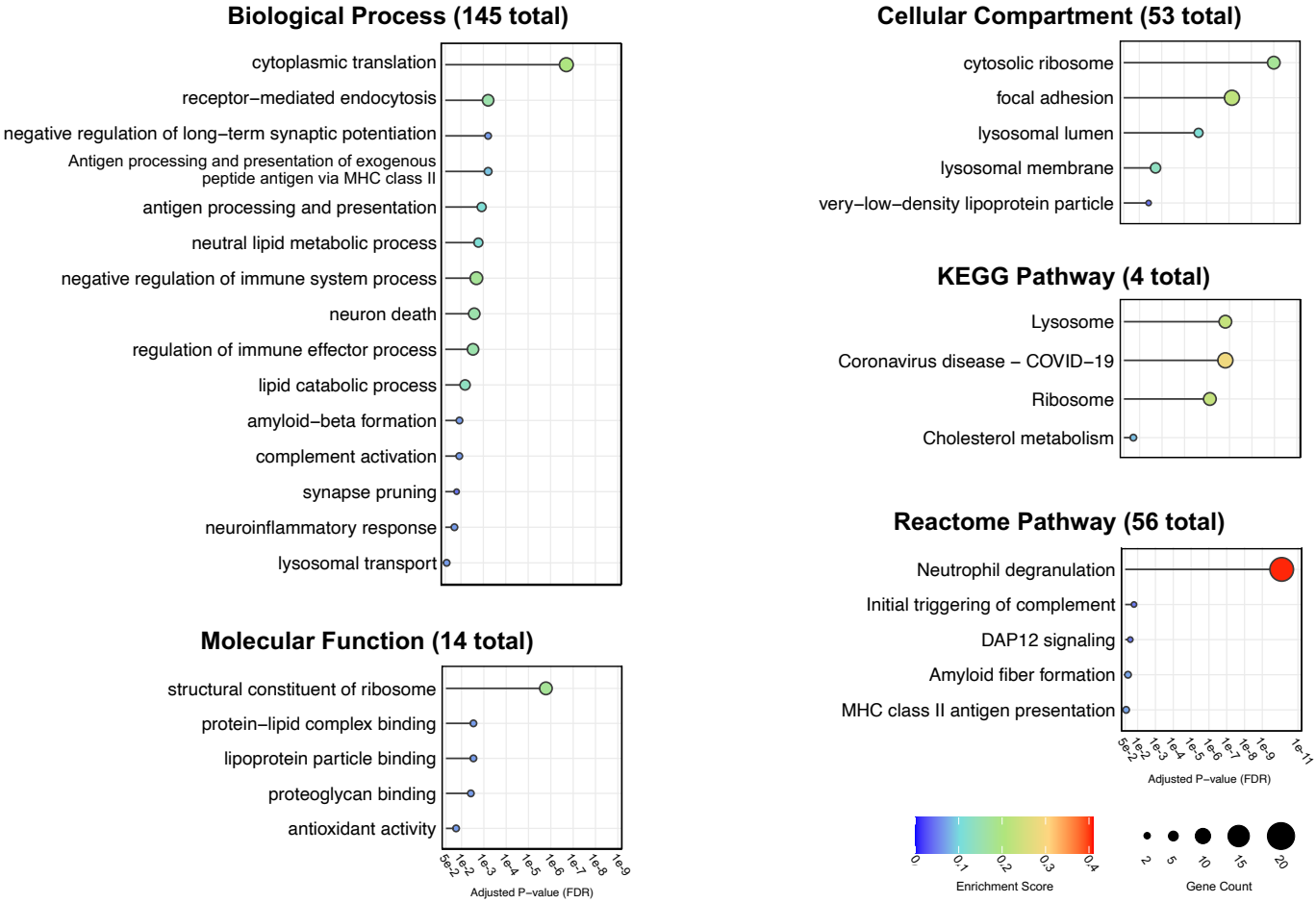

Figure 4.4 Genes upregulated exclusively by plaque contact are involved in lipid homeostasis and immune response
Gene ontology analysis of genes upregulated specifically in microglia upon plaque contact, highlighting selected enriched terms from: (A) Biological Process, (B) Molecular Function, (C) Cellular Component, (D) KEGG Pathways, and (E) Reactome Pathways. The total number of significant terms identified in each database is indicated in brackets. P values adjusted for multiple comparisons using Benjamini-Hochberg false discovery rate (FDR) method.

4.2.5 Genes upregulated gradually towards plaques are involved in microglial activation, chemotaxis, and phagocytosis

Ontology enrichment analysis was conducted on the 308 upregulated graded response genes, which exhibited a progressive increase in expression from away regions to periplaque regions and finally to plaque-contacting regions (Figure 4.5).

A common trend was terms enriched with microglial activation and phagocytosis-associated genes. Ontology terms here included: positive regulation of immune effector process (BP), phagocytosis (BP), microglial cell activation (BP), immunological synapse (CC), and neutrophil degranulation (reactome). Genes enriching these terms were the complement

factor *C1QA*, cytokine *IL4*, chemokines *CCL21* and *CCL13*, immune regulating kinase *PTPRC*, microglial ATP receptor *P2RX7*, and importantly, the microglial activation hub gene and AD-associated *TREM2*.

Similarly to the upregulated plaque response genes, the graded response genes also play important lipid-associated roles, with terms including: Lipid storage (BP), protein-lipid complex binding (MF), and apolipoprotein binding (MF). Example genes enriching these terms are lipid droplet-associated protein encoded by *PLIN2*, cholesterol transporter *NPC2*, glycolipid transport protein *GM2A*, lipid storage protein *FITM2*, and cholesterol regulation protein *SOAT1*.

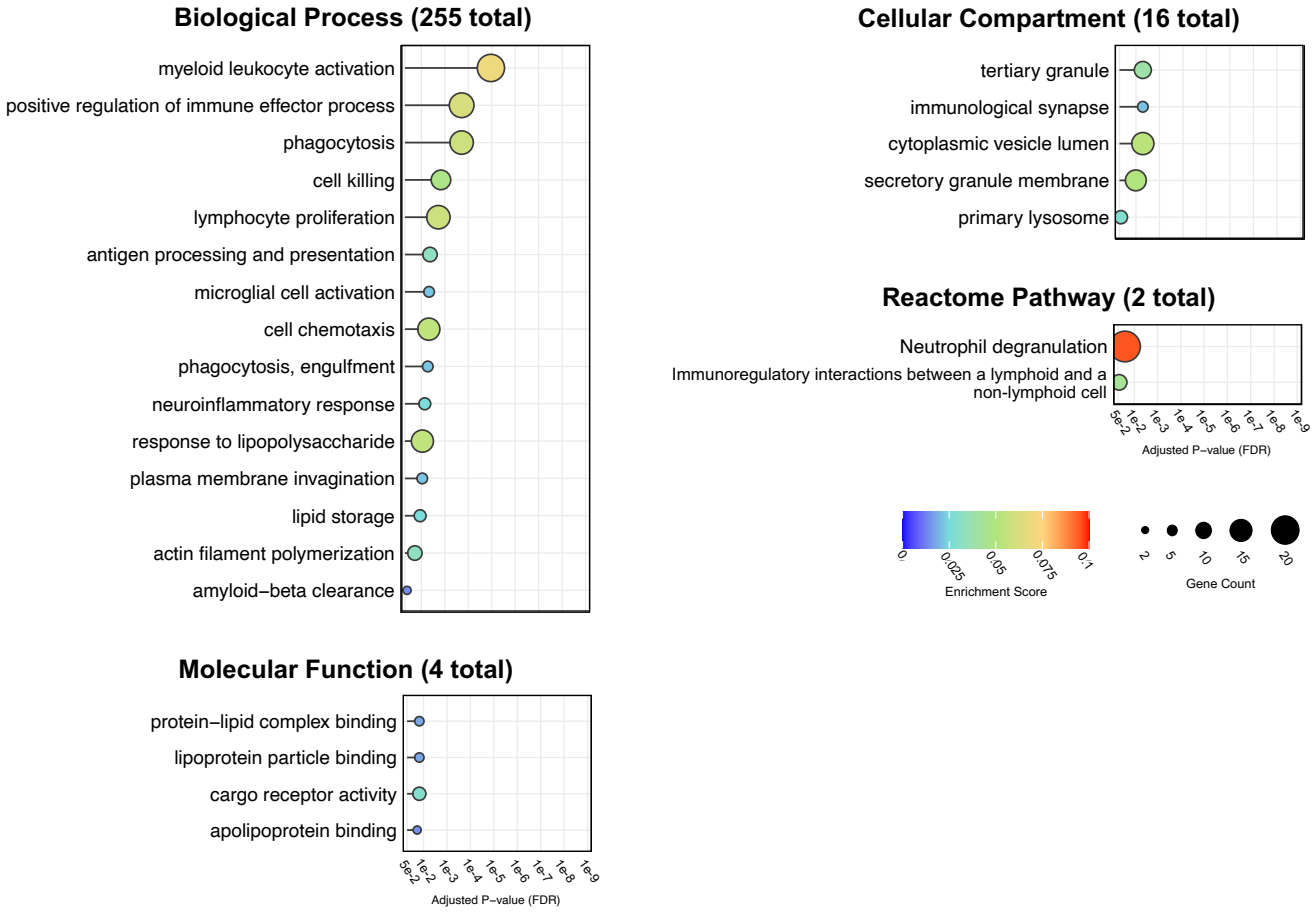

Figure 4.5 Genes upregulated gradually towards plaques are involved in microglial activation, chemotaxis, and phagocytosis
Gene ontology analysis of genes upregulated in microglia gradually towards plaques, highlighting selected enriched terms from: (A) Biological Process, (B) Molecular Function, (C) Cellular Component, and (D) Reactome Pathways. The total number of significant terms identified in each database is indicated in brackets. P values adjusted for multiple comparisons using Benjamini-Hochberg false discovery rate (FDR) method.

4.2.6 Genes downregulated exclusively by plaque contact are involved in metal ion response and cellular development

Although genes that are upregulated in microglia in response to plaque provide valuable insights into the roles microglia adopt due to Aβ plaque pathology, genes that are downregulated can be equally important. They help to assess which roles microglia may be sacrificing, reveal potential dysfunctions, and may also be involved in the adoption of new roles. Therefore, ontology enrichment analysis was performed on the 20 downregulated plaque response genes, which showed decreased expression exclusively in microglia directly contacting plaques (Figure 4.6).

Surprisingly, many of the enriched ontology terms indicate that these genes are involved in the response to metal ions. Key ontology terms here include cellular response to metal ion (BP), response to copper, zinc and cadmium ions (BP), and metallothioneins bind metals (reactome). Genes enriching these terms are mainly the heavy metal binding proteins encoded by *MT2A*, *MT3*, *MT1M*, and *MT1E*.

Downregulated plaque-responsive genes also appear to be involved in cell development, as indicated by the enriched terms: regulation of cell size (BP), cell growth (BP) and glial cell projection (CC). Genes here include gap junction protein *GJA1*, microtubule-associated tau protein MAPT, along with the metallothioneins listed above.

Finally, the KEGG pathway labelled Alzheimer's disease was a significant and heavily enriched KEGG pathway for genes belonging to the downregulated plaque response category. Genes contributing to this term are MHC peptide processor PSMD8, microtubule subunits *TUBB4B* and *TUBB2B*, and *MAPT*.

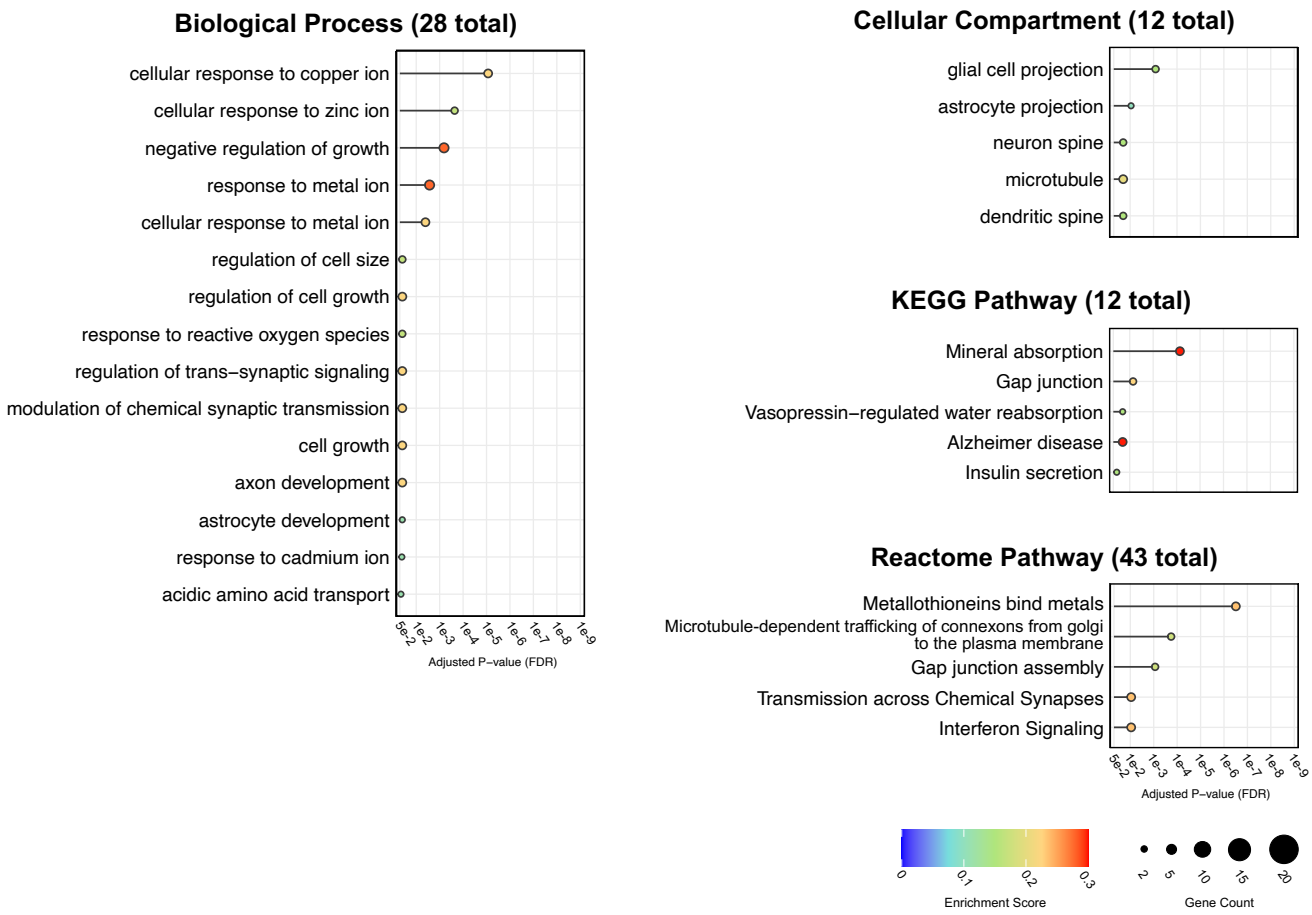

Figure 4.6 Genes downregulated exclusively by plaque contact are involved in metal ion response and cellular development
Gene ontology analysis of genes downregulated specifically in microglia upon plaque contact, highlighting selected enriched terms from: (A) Biological Process, (B) Molecular Function, (C) Cellular Component, and (D) Reactome Pathways. The total number of significant terms identified in each database is indicated in brackets. P values adjusted for multiple comparisons using Benjamini-Hochberg false discovery rate (FDR) method.

4.2.7 Genes downregulated gradually towards plaques are involved in glial and neuronal development

Ontology enrichment analysis was performed on the 145 downregulated graded response genes (Figure 4.7). A trend throughout the enrichment analysis was myelination-associated terms, including ensheathment of neurons (BP), myelination (BP), structural constituent of myelin sheath (MF), and myelin sheath (CC). Genes enriching these terms mainly encode oligodendrocyte-specific myelin structural proteins encoded by *MBP*, *PLP1*, *MAG*, and *MOBP* and myelin regulatory proteins encoded by *MYRF*, *FA2H* and *TPPP*.

Similarly to the downregulated plaque response genes, terms relating to cell dynamics and development, including glial cell development (BP), axon development (BP), regulation of cell size (BP), and microtubule polymerisation and depolymerisation (BP), were enriched

with genes in the downregulated graded response category. Many genes enriching these terms included the above oligodendrocytic genes as well as microglial chromatin assembly factor *SUN2*, microtubule tracking protein encoding *SLAIN1*, and microtubule destabilising protein encoding *STMN1*.

Finally, and surprisingly, amyloid fibril formation (BP) is significantly enriched among the downregulated plaque response genes, in part due to the plaque-specific decrease in *APP* and the APP processing gamma-secretase subunit *PSEN1*.

Ontology enrichment analysis was also performed on genes within the periplaque-responsive and plaque- and periplaque-responsive categories; however, no significantly enriched terms were identified.

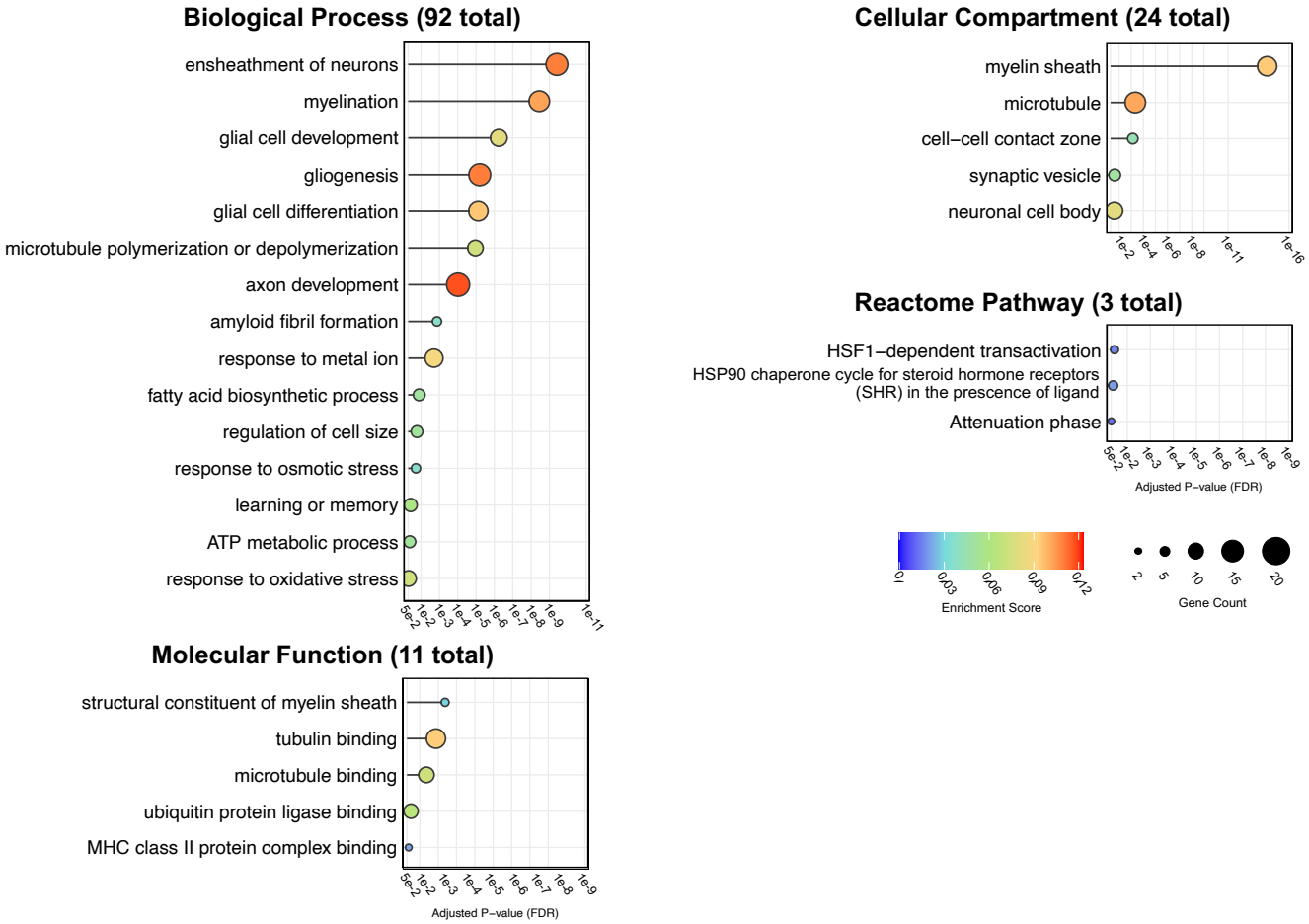

Figure 4.7 Genes downregulated gradually towards plaques are involved in glial and neuronal development

Gene ontology analysis of genes downregulated in microglia gradually towards plaques, highlighting selected enriched terms from: (A) Biological Process, (B) Molecular Function, (C) Cellular Component, and (D) Reactome Pathways. The total number of significant terms identified in each database is indicated in brackets. P values adjusted for multiple comparisons using Benjamini-Hochberg false discovery rate (FDR) method.

4.3 Chapter Summary

The major finding of this chapter is that the spatial regulation of microglial gene expression by Aβ plaque proximity, previously observed in the NLF mouse model (Chapter 3), is conserved in human AD tissue. In both species, physical contact between microglia and Aβ plaques was necessary for many AD-associated transcriptional changes.

Gene expression patterns varied in their spatial dynamics, but could, as in the mouse study, be broadly categorised. Microglia directly contacting plaques showed upregulation of immune-, lysosomal-, and lipid-associated genes, including *C1QB/C*, *CD68*, *TYROBP*, and *GRN*. Genes that increased progressively towards plaques were enriched in similar pathways but included a greater number of cell communication and migration genes, such as *IL4*, *CCL21*, and *CCL13*.

Unlike the targeted PIG analysis in mice, the unbiased whole-transcriptome approach in human tissue enabled the identification of genes that decreased in expression toward plaques. Although many of these likely represent transcripts from non-microglial cells due to the 3D capture of GeoMx barcodes, meaningful ontologies emerged. Genes specifically downregulated at plaques were unexpectedly enriched for metal ion binding functions, particularly metallothioneins. Gradually downregulated genes were strongly associated with oligodendrocyte and neuronal functions, including myelination and synapse-associated transcripts, suggesting a loss or dysfunction of these cells in the plaque niche.

Some species differences were noted, such as the plaque-specific upregulation of *Trem2* in NLF mice versus its graded increase in human tissue. Nevertheless, across both models, spatial microglial responses to plaques involved shared pathways including phagocytosis, lysosomal degradation, and lipid homeostasis. Notably, these included genes carrying AD risk variants such as *TREM2*, *APOE*, and *GRN*, underlining the relevance of spatial context in understanding microglial dysfunction in AD.

CHAPTER 5

Aβ PLAQUE DYNAMICS: AGEING AND STRUCTURAL MATURATION

5.1 Introduction

A central, unresolved question in AD research is why Aβ plaque pathology, despite being hypothesised as the initial trigger of neurodegeneration, correlates poorly with cognitive decline (Morris et al., 2014). To better understand this discrepancy, research has focused on investigating the impact of Aβ pathology on the surrounding tissue. In mouse models of AD, this is frequently evaluated across chronological ageing due to the relatively consistent progression in severity (Benitez et al., 2021). Similarly, in human AD, this impact is commonly assessed in relation to Braak or Thal staging. However, these approaches, along with commonly used plaque detection methods that rely on a single staining approach, tend to group all plaques into a homogenous category. As a result, they overlook the substantial heterogeneity in structure and maturation that exists among individual Aβ plaques.

When plaque heterogeneity is considered, it is typically approached from two directions. The first is structural morphology, in which plaques are categorised as diffuse, fibrillar, or cored, with increasing aggregation density, respectively (Dickson and Vickers, 2001; Rohr et al., 2020). The second is based on their impact on surrounding neurites, classifying plaques as either neuritic (damaging) or non-neuritic. These classifications are not mutually exclusive; for instance, diffuse, fibrillar, and cored plaques have all been shown to exhibit neuritic influence (Dickson and Vickers, 2001). The term neuritic plaque is commonly used in the neuropathological assessments of human tissue and refers to plaques that stain positive for hyperphosphorylated tau, autophagic stress, ubiquitin positivity, or the presence of neurofilament proteins (Hyman et al., 2012). This classification is therefore a diagnostic construct based on a combination of associated pathological features. In contrast, structural classifications are plaque-centric and are not restricted to a defined set of surrounding proteins, allowing for the investigation of any protein of interest in relation to distinct plaque types.

Clinical observations highlight the importance of understanding plaque heterogeneity. For example, some individuals remain cognitively normal despite extensive Aβ deposition observed at post-mortem examination (Murray and Dickson, 2014; Serrano-Pozo et al., 2011). Notably, these individuals' brains are predominantly populated by diffuse plaques, which are thought to represent immature, relatively non-toxic forms of Aβ aggregates. Conversely, a higher prevalence of highly aggregated cored plaques has been consistently

associated with progressive cognitive impairment (Liu et al., 2022; Rijal Upadhaya et al., 2014; Serrano-Pozo et al., 2016). Such findings may explain why Aβ deposition can occur decades before the onset of symptomatic AD. It is therefore critical to understand the maturation of Aβ depositions over time; the contribution of early deposited Aβ from that deposited at much later stages.

Efforts to track plaque development over time have often relied on *in vivo* imaging approaches, using cranial windows on transgenic models of AD, to visualise the de novo appearance and radial growth of Aβ plaques labelled with fluorescent dyes. These studies have revealed that plaques can form rapidly, with a subsequent slowing in their radial expansion as they mature (Burgold et al., 2011; Hefendehl et al., 2011; Meyer-Luehmann et al., 2008; Yan et al., 2009). However, this technique typically captures only short time windows, has a restricted field of view, and is limited to imaging superficial cortical plaques near the cranial window. Moreover, the amyloid dyes used in these methods bind only to already structurally aggregated forms of Aβ, preventing the visualisation of diffuse plaques. Critically, such imaging cannot track how plaques, as they evolve with age, impact surrounding tissue.

A technique developed to overcome the issue of temporal tracking involves using mass spectrometry imaging (MALDI-MSI) on tissue metabolically labelled with stable isotopes such as ^{15}N and ^{14}N nitrogen, originally developed to monitor protein turnover in human patients through following stable isotope labelling kinetics (SILK; Bateman et al., 2006; McClatchy et al., 2007). While having the same chemical properties, the ^{15}N isotope is heavier than the naturally abundant ^{14}N due to the inclusion of an extra neutron. In the SILK paradigm, mice are fed a standard diet naturally abundant in ^{14}N; however, for a 'pulse' period they are given a diet rich in ^{15}N. Thus, amino acids and peptides produced during the pulse period will be labelled with the heavy ^{15}N isotope. Using MALDI-MSI on SILK tissue, one can visualise Aβ produced during the pulse period, as these peptides will be detected as a shift towards a heavier mass. Recently, this SILK imaging approach (iSILK) has been employed in AD mouse models (the NLGF model) with two contrasting pulse schemes: during and after the initial deposition of Aβ. This labelling paradigm separated early from late deposited Aβ, discovering the importance of Aβ42 in forming the initial plaque core (Michno et al., 2021). The spatial and temporal pattern of Aβ deposition, enabled by MALDI-MSI, has provided valuable information delineating plaque heterogeneity in AD. However, it remains unknown how these plaques differ in their impact on their surrounding environment. In this chapter, I apply the iSILK technique to temporally track plaque formation using MALDI-MSI to measure plaque age based on the abundance of ^{15}N-labelled Aβ42. To assess the

functional impact of plaque age, I pair this technique with GeoMx spatial transcriptomics to capture gene expression changes in the tissue surrounding individual plaques. This combined approach enables the identification of gene expression patterns that evolve independently of the age of the mouse.

A consistent finding in structurally classified plaque types is that fibrillated plaques induce high levels of microglial clustering, synaptic loss, dystrophic neurites, and a host of other toxicity-associated proteins (Bittner et al., 2012; Condello et al., 2015; Spires et al., 2005). However, the majority of these studies define plaques either with a structural dye alone, hence disregarding diffuse plaques, or pair a structural dye with an Aβ antibody. This method still does not differentiate fibrillar plaques from cored plaques. Recent advances in structural derivatives of thioflavin have produced a range of dyes capable of selectively binding to distinct amyloid structural conformations (Klingstedt et al., 2011; Nystrom et al., 2013). In this chapter, in addition to ^{15}N isotope labelling, I employ a combination of two such thioflavin-derived amyloid structural dyes alongside an Aβ antibody to rapidly and accurately classify plaques into diffuse, fibrillar, or cored types. This high-throughput plaque classification approach was then used to investigate the differential toxicity associated with each plaque subtype. Furthermore, findings in AD mouse models with *Trem2* deficiency reveal important functions of Trem2 in controlling microglial plaque compaction and possible seeding (Wang et al., 2015; Yuan et al., 2016). Therefore, in this chapter, I also investigate the impact of the *Trem2*^{R47H} mutation on plaque type pathology and consequent toxicity,

The results presented in this chapter on NLF mice have been accepted for publication following peer review at Nature Communications. A preprint is available on bioRxiv (Wood et al., 2024).

5.2 Isotope-encoded spatial transcriptomics detects plaque-age-related gene expression changes

5.2.1 SILK x MALDI-MSI delineates plaque age

In NLF mice, plaques begin to deposit in the hippocampus at approximately 9 months of age, with plaque load starting to plateau at around 18 months (Benitez et al., 2021). Unlike other Alzheimer's disease mouse models such as NLGF mice, NLF mice produce humanised Aβ without altering its amino acid sequence. This is because the NL and F mutations flank the Aβ coding region, rather than modifying it directly. In contrast, NLGF mice carry the Arctic mutation, which lies within the Aβ sequence itself and alters its amino acid composition. (Saito et al., 2014). As a result, the dynamics of Aβ aggregation and

plaque maturation, combined with the late onset and slow deposition of plaques in NLF mice, may more closely resemble those observed in human AD compared to other mouse models. In human AD, the dynamics of plaque aggregation lead to a variety of plaque types, which may reflect different stages of maturation (Dickson and Vickers, 2001; Koutarapu et al., 2024; Rohr et al., 2020). To assess plaque heterogeneity in NLF mice, a pulse-chase SILK metabolic labelling approach was employed. A diet enriched with the heavy ^{15}N isotope of nitrogen was administered between 6 and 10 months of age, flanking the initial phase of amyloid plaque deposition, which begins around 9 months (Figure 5.1A and 5.1B). Pulse-chase labelling was initiated at 6 months to ensure that no unlabelled plaques were present prior to the pulse. A prolonged labelling period was necessary due to the slow and gradual plaque development characteristic of the NLF model; even by the end of the pulse at 10 months, only a limited number of plaques have formed (Benitez et al., 2021; Saito et al., 2014). This contrasts with more aggressive models, such as transgenic lines or NLGF mice, where plaque development occurs earlier and more extensively. The temporal and regional progression of Aβ pathology in NLF and NLGF mice is described in detail by Saito et al. (2014). A chase period followed, whereby mice were moved off the ^{15}N isotope diet and fed standard chow naturally abundant in the light ^{14}N isotope of nitrogen. Amino acids and peptides produced during and shortly after the pulse phase will be enriched in ^{15}N (Figure 5.1C). As the pulse period coincides with the onset of plaque deposition (at ~ 9 months of age), all newly formed plaques will be heavily enriched in ^{15}N, with this enrichment decreasing from the onset of the chase period at 10 months to the experimental endpoint of 18 months (Figure 5.1C). In short, plaques that are older, having formed during or near the pulse phase, will contain the heavier ^{15}N isotope, while plaques that are younger, deposited near the experimental endpoint, will be enriched in the lighter ^{14}N isotope (Figure 5.1D).

MALDI-MSI is an imaging system that uses a laser to ionise and desorb molecules from tissue sections in a defined raster (Figure 5.1E). The desorbed molecules are accelerated into a time-of-flight mass spectrometer, which measures the mass-to-charge ratio (m/z) of each molecular species by their respective flight time, where the m/z is proportional to the square of the flight time. The pixel-by-pixel nature of this technique enables the creation of molecular ion-specific images. These single-ion images are generated by selecting the species-specific molecular weight and mapping the intensity of each detected species across the pre-defined acquisition raster. This method has proven invaluable in AD research, particularly in assessing the contribution of different forms of Aβ at the single plaque scale (Michno et al., 2021; Michno et al., 2019; Michno et al., 2018). As Aβ42 is the primary constituent of plaques in NLF mice, this species was the focus of this experiment (Figure 5.1F). By using MALDI-MSI to detect the mass of Aβ42 within the SILK paradigm, the age of

a plaque becomes a correlate of the shift in average mass of the Aβ42 mass peak within the targeted pixel. The earliest seeded plaques, and thus oldest, will show higher ^{15}N enrichment and, as a result, will be heavier compared to the recently seeded, younger plaques with little ^{15}N incorporation. The measurement of ^{15}N incorporation is known as the “Nitrogen Index”, a calculation of the shift in Aβ42 peptide mass from the standard non-labelled species (Figure 5.1G).

Validation of the SILK method to detect plaque age in these mice was performed by other members of the Hanrieder x Edwards Lab collaboration and was published in preprint, Wood et al. (2024). The data showed greater ^{15}N enrichment at the centre of the plaque compared to the periphery, suggesting that the precipitation of new Aβ42 species occurs around the plaque's outer edges. Further validation revealed that the cortex, which experiences plaque deposition before the hippocampus, had higher ^{15}N enrichment compared to the hippocampus, again confirming the ^{15}N enrichment in earlier deposited Aβ42 species.

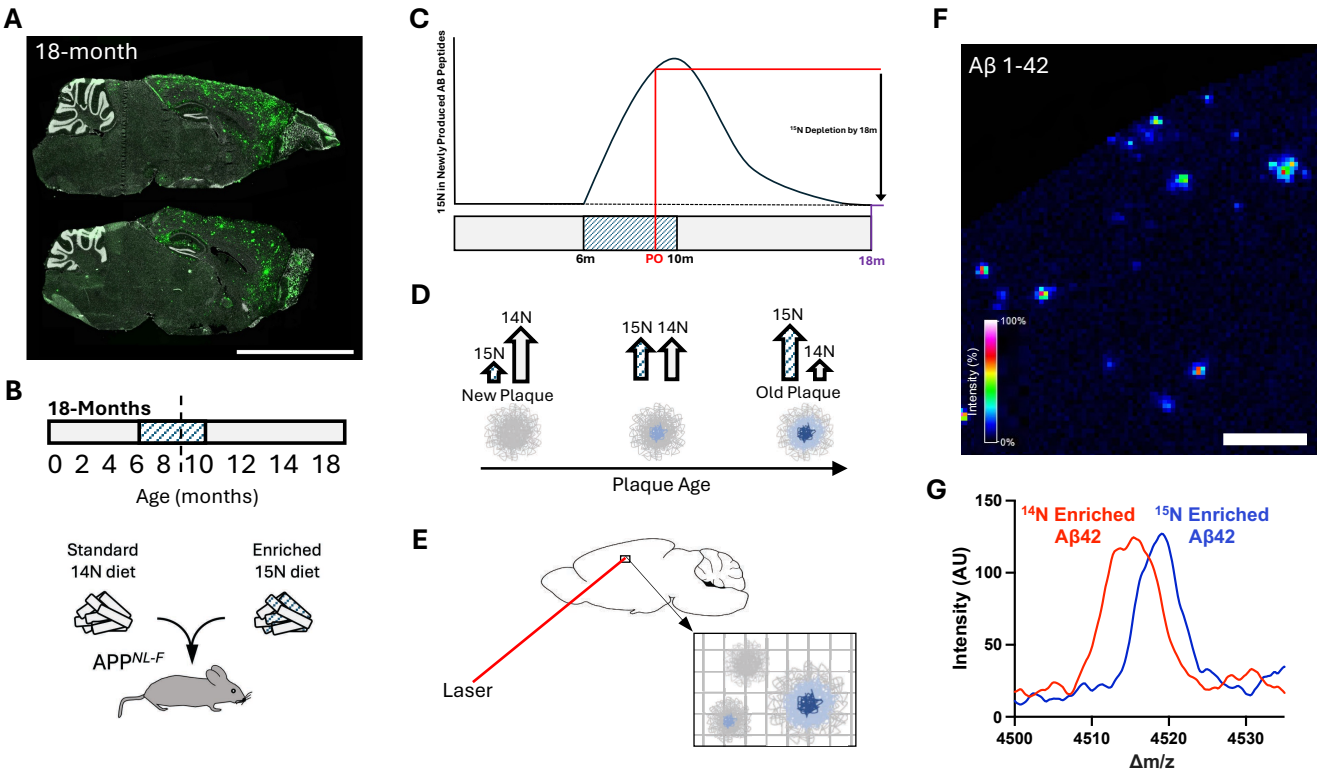

Figure 5.1 SILK x MALDI MSI delineates plaque age
(A) Representative whole sagittal sections of 18-month-old NLF mice, showing Aβ plaques (Aβ40/42, green) and nuclei (SYTO83, white). Scale bar: 5000 µm. (B) Pulse-chase feeding paradigm, ^{15}N-enriched diet was administered between 6–10 months (pulse period), flanking the plaque onset (dotted line, 9 months).^{14}N standard diet was provided before 6 months and after 10 months (chase period). (C) Predicted ^{15}N enrichment within plaques over the experimental time course, showing peak enrichment at the end of the pulse period. PO: plaque onset (D) Diagram depicting ^{15}N incorporation in newly deposited vs. older plaques.

(E) MALDI MSI workflow illustrating plaque detection through laser-desorbed Aβ signals in a defined raster. (F) Representative MALDI-MSI image displaying Aβ42 species detected in NLF cortical tissue. Scale bar: 200 µm. (G) Example MALDI MSI mass spectra showing distinct ^{14}N and ^{15}N-enriched Aβ42 peaks. All figures are adapted from figures presented in Wood et al. (2024).

5.2.2 MALDI MSI-detected plaques map to GeoMx IHC detected plaques

After determining a measure of plaque ageing, I aimed to assess its impact on the response of the surrounding tissue. To do this, I employed GeoMx spatial transcriptomics to evaluate how individual plaques influence gene expression in the surrounding tissue. As MALDI-MSI and GeoMx are not compatible for use on the same tissue section, neighbouring sections were used, whereby plaques traversing both sections were selected as ROIs for GeoMx collection (Figure 5.2A). As single plaques were being analysed, the collection area was not large enough to enrich for specific cell types; instead, a circle centred around the plaque's centre, with a radius three times that of the associated plaque, were captured regardless of cell type. An antibody capable of detecting both Aβ40 & Aβ42 was used to detect plaques, while the microglial-specific protein TMEM119 was used to stain microglia, alongside the SYTO13 dye to counterstain nuclei (Figure 5.2B). Neither the microglial nor the nuclei staining guided ROI selection or analysis; their purpose was solely to assess tissue and protein quality. For each of the selected plaques, the shift in Aβ42 mass was measured from MALDI-MSI, along with the associated gene expression counts from GeoMx spatial transcriptomics (Figure 5.2B).

As the analysis was non-hypothesis driven, counts over the whole transcriptome were analysed. The simplicity of the samples and the breadth of analysis determine the complexity of the count normalisation method. Similar to the NLF microglial-enriched spatial transcriptomics, the genetics, age, and environment of the mice were controlled. However, as with human microglial-enriched spatial transcriptomics, analysing counts across the entire transcriptome would introduce too much variability if housekeeping normalization were used. Therefore, to minimise large variability between regions of interest (ROIs) while maintaining simplicity in normalisation, all genes within an ROI were quantile normalised.

To examine the impact of plaque ageing on surrounding tissue gene expression, plaque age, as measured by the shift in Aβ42 weight, was correlated against the gene expression count of each gene. All genes and their relation to plaque age can be searched in this custom application - https://hanriederlab.shinyapps.io/PlaqueAgeTranscriptomics/. However, as ROIs were centred on plaques without cell-type-specific enrichment or segmentation, the resulting gene expression profiles represent mixed-cell populations. As a result, it is not

possible to determine whether observed changes reflect shifts in gene expression within specific cell types or changes in cell-type composition. A key limitation of applying the correction, such as the commonly used Benjamini-Hochberg method, for multiple comparisons in genome-wide correlation analyses rather than simple pairwise comparisons (across 19,963 genes) is that the threshold for statistical significance becomes extremely stringent. Specifically, only near-perfect correlations ($r \approx 0.9$) will survive correction. To address this, I instead passed gene-level correlation statistics into a gene ontology enrichment analysis, allowing correction for multiple comparisons to be applied at the pathway level (FDR < 0.05). Gene enrichment within biological process (BP), cellular compartment (CC), molecular function (MF), KEGG pathway (KEGG) and Reactome pathway (Reactome) databases was analysed. Additional limitations of this dataset should also be considered.

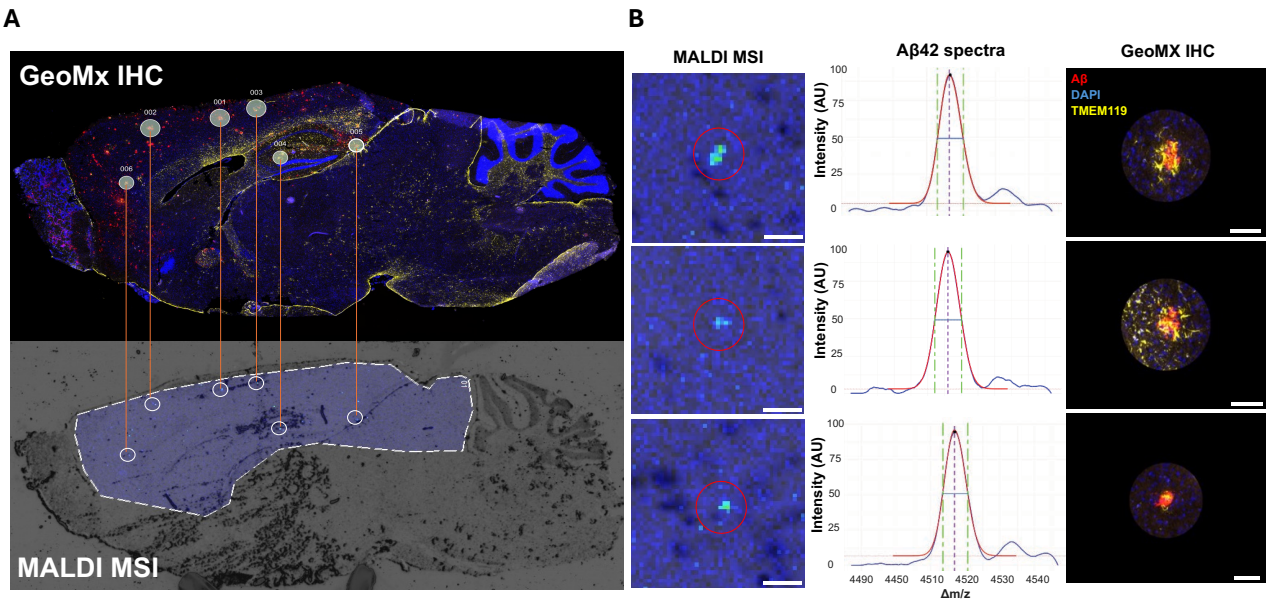

Figure 5.2 MALDI MSI-detected plaques map to GeoMx IHC detected plaques
(A) Matching plaques across consecutive mirrored sections: the upper section was used for GeoMx spatial transcriptomics, with plaque detection by immunohistochemistry (IHC), while the lower section was analysed using MALDI MSI. (B) Individual plaque comparisons showing plaque detection by MALDI MSI alongside the corresponding mass spectra of the detected Aβ42 species and the far-right panels showing GeoMx immunohistochemistry images of plaques (Aβ, red), microglia (TMEM119, yellow), and nuclei (SYTO83, blue). Scale bar: 100 μm. Figures adapted from figures presented in Wood et al. (2024).

5.2.3 Expression of genes involved in metabolism and channel activity increases with plaque age

Ontology enrichment analysis of genes that increase in expression with plaque age revealed a common trend of the associated terms linked to metabolic processes. These included terms such as glycolytic process through glucose-6-phosphate (BP), monosaccharide catabolic process (BP), ATP hydrolysis activity (MF), and inositol triphosphate phosphatase activity (MF). Genes related to these functions include ATP synthase subunits *Atp5a1* and *Atp5k*, cytochrome c-associated *Cox7a2* and *Coa6*, and ubiquinone-synthesising *Coq7* (Figure 5.3).

Genes associated with neuronal homeostasis, and primarily those genes associated with channel activity, also appeared enriched in this dataset. Terms here included the regulation of membrane potential (BP), transmission of nerve impulse (BP), channel activity (MF) and distal axon (CC). Genes contributing to these ontology terms include the potassium channel encoding genes *Kcnj2* and *Kcna2,* voltage-gated sodium channel subunits *Scn1a* and *Scn2b*, and AMPA receptor subunit *Gria3* (Figure 5.3).

No significant terms were enriched in either the KEGG pathway or the Reactome pathway databases.

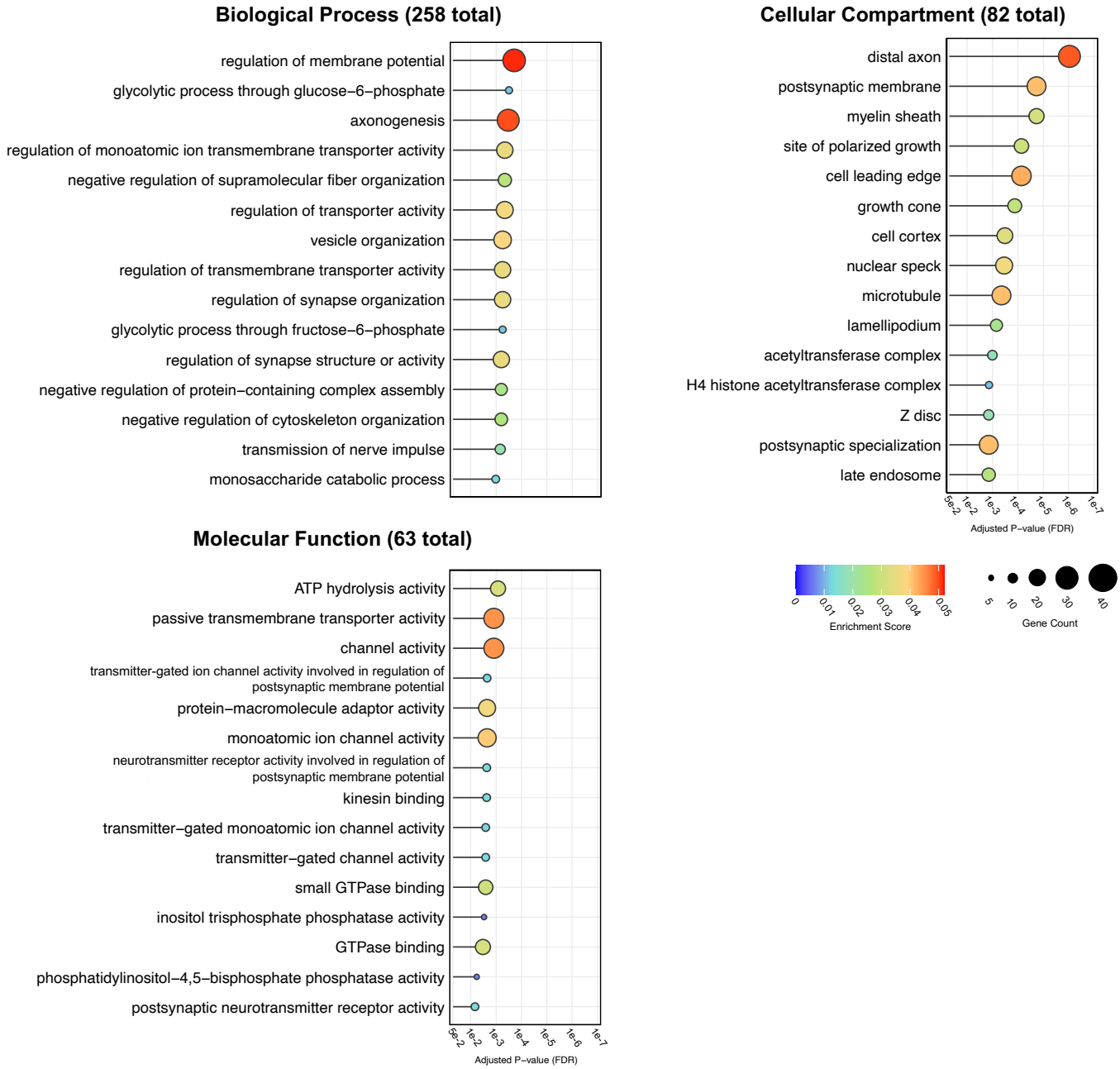

Figure 5.3 Expression of genes involved in metabolism and channel activity increases with plaque age

Gene ontology (GO) analysis of genes positively correlated with plaque age, showing the top 15 most significantly enriched: Biological processes, Cellular compartments, and Molecular functions. Multiple comparisons were corrected using Benjamini-Hochberg false discovery rate (FDR). NLF n=18 plaques over n=4 mice.

5.2.4 Expression of primarily synaptic genes decreases with plaque age

Ontology enrichment analysis of genes that decrease with increasing plaque age were primarily synapse-associated. Enriched synapse-associated terms comprised regulation of neurotransmitter receptor activity (BP), regulation of neuronal synaptic plasticity (BP), structural constituent of postsynapse (MF), dendritic spine (CC), long-term potentiation (KEGG) and protein-protein interactions at synapses (Reactome). Acetylcholine receptor encoding *Chrna7*, dopamine receptor *Drd1,* and neuronal pentraxin *Nptx2* (Figure 5.4).

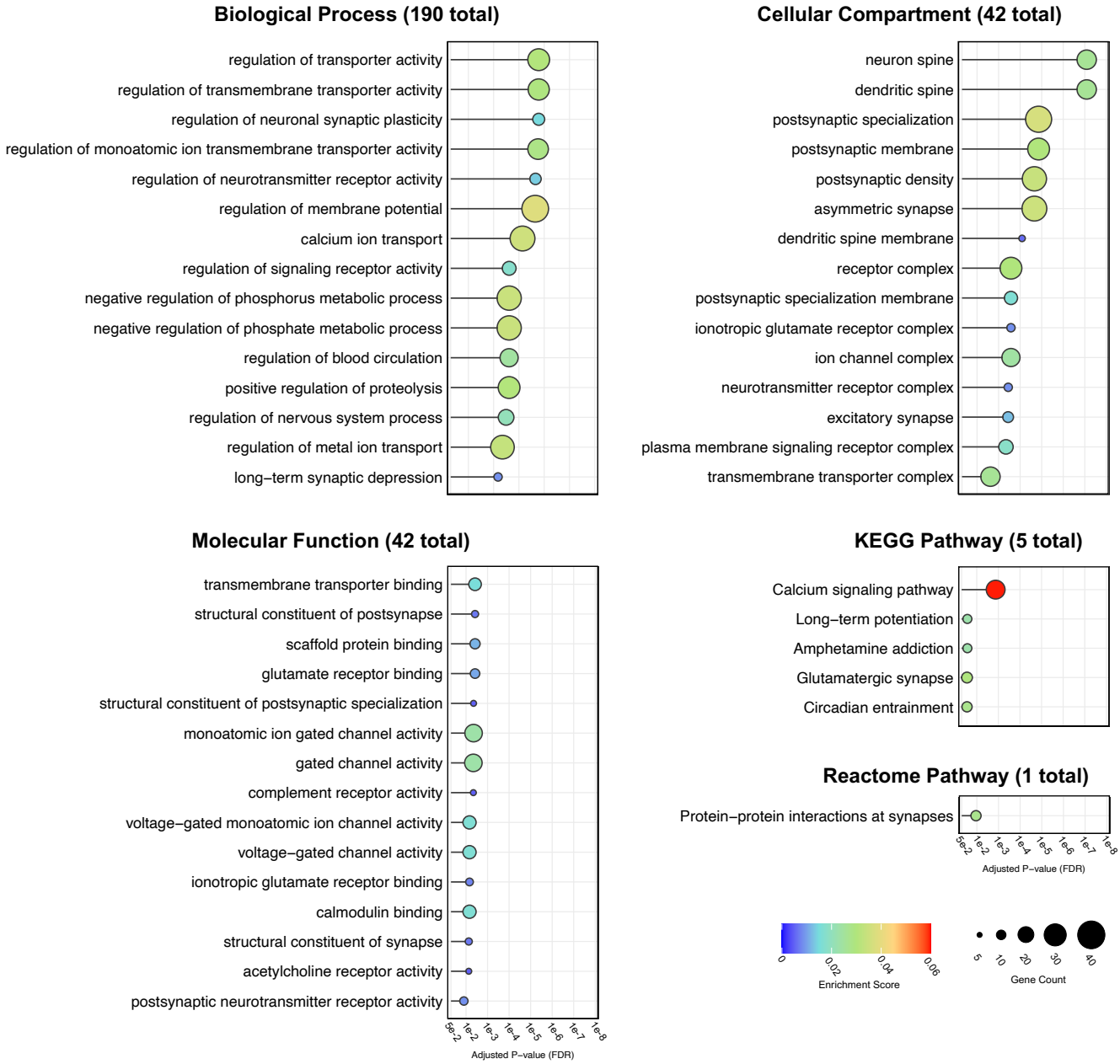

Figure 5.4 Expression of synaptic genes decrease with plaque age

Gene ontology analysis of genes positively correlated with plaque age, showing the top 15 most significantly enriched: Biological processes, Cellular compartments, Molecular functions, KEGG pathway and Reactome pathway databases. Multiple comparisons were

corrected using Benjamini-Hochberg false discovery rate (FDR) method. NLF n=18 plaques over n=4 mice.

5.3 Plaque structural morphologies and associated impacts

5.3.1 qFTAA and hFTAA dyes reveal distinct plaque structural morphologies

In Chapter 3, the Amytracker520 dye was used to target and stain the β-pleated sheet structure of aggregated Aβ. Along with Congo Red and Thioflavin T dyes, Amytrackers contain a chain of thiophene aromatic rings that interact with hydrophobic pockets along the long axis of amyloid fibrils (Frieg et al., 2020). The structural specificity of such dyes can be altered through editing their hydrophobic side chains along with the length of the thiophene chain (Aslund et al., 2007; Aslund et al., 2009; Klingstedt et al., 2011). Two such derivatives are qFTAA and hFTAA LCO dyes, which bind to tightly aggregated β-pleated sheets and both tightly and moderately aggregated β-pleated sheets, respectively (Nystrom et al., 2013). They have previously been used in tandem to assess the degree of Aβ plaque aggregation in human AD and mouse models (Nystrom et al., 2013; Parvin et al., 2024; Rasmussen et al., 2017).

These dyes have spectrally different yet overlapping emission spectra. qFTAA exhibits a blue-shifted emission, whereas hFTAA has a red-shifted emission. Using a standard confocal photon detector, these two dyes cannot be spectrally distinguished (Figure 5.5A). However, a hyperspectral detector, capable of distinguishing small ranges of emission wavelengths, has been used to identify the blue or red shifts in emission, corresponding to greater qFTAA binding compared to hFTAA binding, respectively. The Hanrieder x Edwards lab collaboration, using this hyperspectral qFTAA-hFTAA imaging paradigm, established that as SILK-determined plaque age increases, plaques exhibit a more blue-shifted emission, indicating stronger qFTAA binding (Wood et al., 2024). In short, this shows that as plaques age, they become more aggregated.

A different approach to hyperspectral imaging is the use of linear unmixing that uses reference spectra from qFTAA and hFTAA to separate the two LCOs into separate channels (Figure 5.5A). Interestingly, in NLF mice, qFTAA positivity in hFTAA-positive plaques appears almost binary, suggesting that tightly aggregated β-pleated sheet structures are either present or absent in the plaques. Similarly, when using these dyes in conjunction with an anti-Aβ42 antibody (see Key Resources table), hFTAA positivity in Aβ42-positive plaques also appears to be either present or absent. This suggests that many Aβ42-positive plaques have either not formed a β-pleated sheet structure, or the β-pleated sheets present are too

immature for hFTAA to bind. This categorical relationship of plaque staining divides all plaques into three categories based on the positivity of the anti-Aβ42 antibody (Aβ), hFTAA LCO dye (h), and qFTAA LCO dye (q): Aβ+h+q+ plaques, Aβ+h+q- plaques, and Aβ+h-q- plaques, listed in descending order of β-pleated sheet tightness (Figure 5.5B). These plaque types likely reflect cored plaques (Aβ+h+q+), fibrillar plaques (Aβ+h+q-) and diffuse plaques (Aβ+h-q), respectively.

I set out to characterise these three plaque types in the hippocampus of 18-month-old NLF mice. Interestingly, the average size of Aβ+h-q- plaques was very small (~50 μm^2), compared to the more aggregated Aβ+h+q+ plaques, which were significantly larger (~700 μm^2, Figure 5.5C). However, when assessing the density of plaques across various size bins, Aβ+h-q- plaques were present in all size bins, with the very small plaques (<100 μm^2) vastly outnumbering the larger plaques (Figure 5.5D). All plaque types were present in each of the size bins. Interestingly, as a percentage of the total plaque count, Aβ+h-q- plaques accounted for about ~80% of the plaques in the hippocampus, compared to around ~10% each for Aβ+h+q+ and Aβ+h+q- plaques. Although Aβ+h-q- plaques are by far the most abundant plaque type, their smaller average size means that their contribution to the total Aβ+ area is non-significant when compared to Aβ+h+q+ and Aβ+h+q- plaques (Figure 5.5F). This trend was observed across these plaque types, with Aβ+h-q- plaques showing the lowest Aβ42 fluorescence intensity, which increased to Aβ+h+q- plaques and further to Aβ+h+q+ plaques (Figure 5.5G and 5.5H). Together, the data show hippocampi of 18-month-old NLF mice have an abundance of small, possibly non-pleated plaques with a minority population of moderately and tightly aggregated larger plaques.

Unlike morphology-defined plaque classifications, this staining-based categorisation enables high-throughput image analysis of all plaques across the hippocampus, covering three hippocampal sections per mouse, totalling thousands of analysed plaques. Such large-scale analysis would not have been feasible using traditional, manually defined morphological classifications.

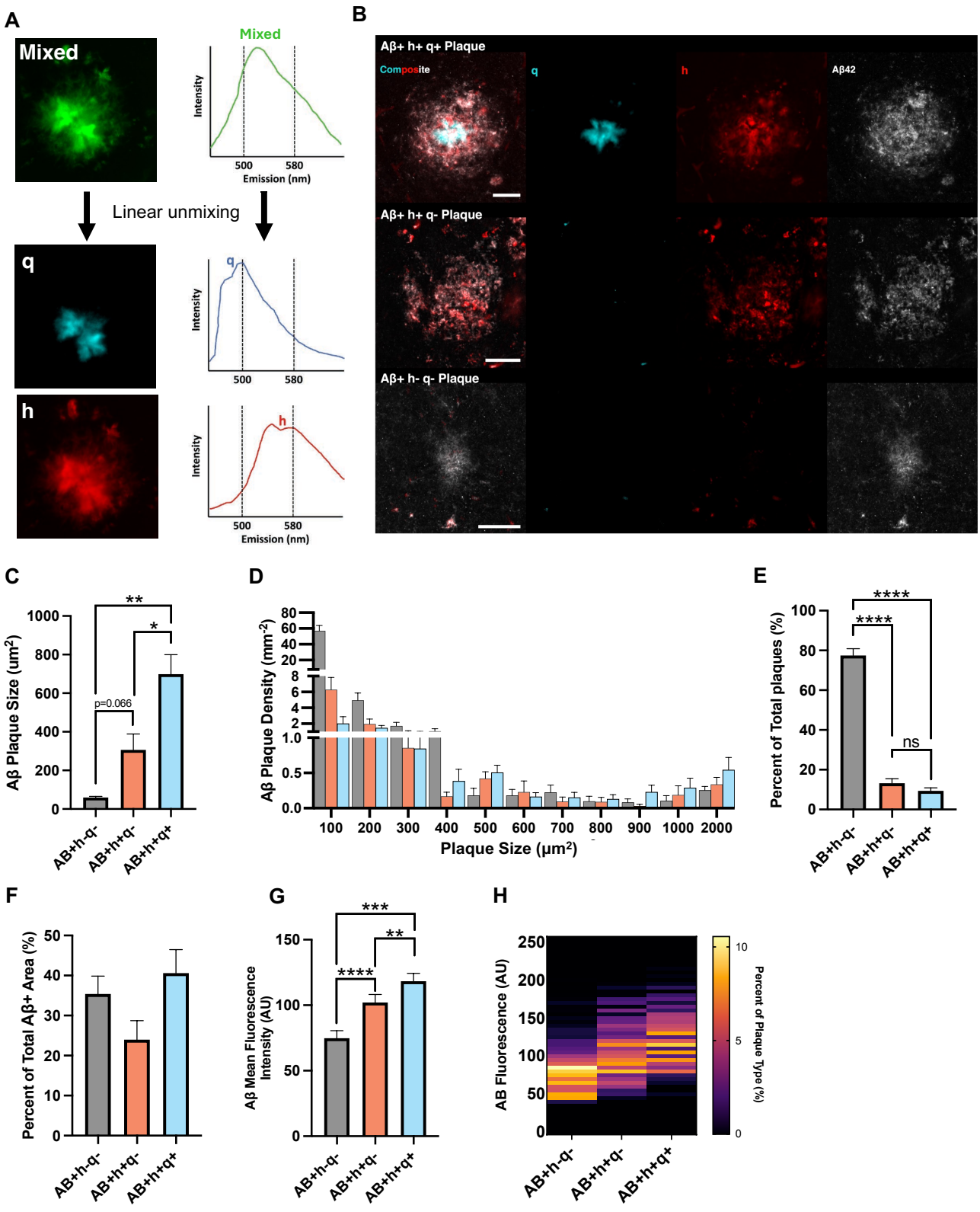

Figure 5.5 qFTAA and hFTAA dyes reveal distinct plaque structural morphologies
(A) Overlapping emission spectra of mixed qFTAA (q) and hFTAA (h) signal can be delineated into distinct channels with hyperspectral confocal imaging followed by linear unmixing. (B) Representative images of Aβ+h+q+ (top), Aβ+h+q- (middle), and Aβ+h-q- (bottom) plaque types defined by the positivity of Aβ42 antibody signal (white), hFTAA dye

(red), and qFTAA dye (cyan). Scale bar: 20 μm. (C) Average area of individual plaques for each plaque type. (D) Histogram showing the relationship between plaque area and plaque density at defined sizes for each plaque type. (E) Proportion of each plaque type as a percentage of the total plaque count. (F) Proportion of each plaque type as a percentage of the total plaque area. (G) Average Aβ42 fluorescence intensity for each plaque type. (H) Heatmap of Aβ42 fluorescence intensity for each plaque type. Analysis performed on projected z-stacked confocal images. Statistical analysis: (C, E, F, & G) One-way paired ANOVA followed by Tukeys correction for multiple comparisons, shown on graphs. ****P<0.0001; ***P<0.001; **P<0.01; *P<0.05. NLF 18m n= 6. Data plotted as mean + SEM. A, B, C, D, F, & G are also presented in in Wood et al. (2024).

5.3.2 Structurally defined plaque types develop over mouse chronological age

Three plaque types were characterised in 9-, 14-, and 18-month-old mice, incorporating the previous data from the 18-month-old mice (Figure 5.5). Surprisingly, in 9-month-old NLF mice, which is around the age of initial plaque deposition in NLF mice, ~85% of plaques are Aβ+h+q+ or Aβ+h+q-, with a minority of around 15% being non-pleated Aβ+h-q- plaques (Figure 5.6A). This result, which contrasts with that of 18-month-old mice, could suggest that initial deposition of already moderately or tightly aggregated Aβ could occur. The proportion of Aβ+h-q- plaques, compared to the LCO+ plaques, increases with mouse age, reaching ~50% at 14 months and, as previously stated, around 80% at 18 months (Figure 5.6A). In short, the percentage of Aβ+h-q- plaques of the total plaque population increases over mouse age. Next, I assessed how the densities of these plaque types change over age. As expected, all three plaque types increased in density over age, with the biggest increase seen in Aβ+h-q- plaques (Figure 5.6B). Although the density of Aβ+h-q- plaques was increasing with chronological age, their average size did not change (Figure 5.6C). In contrast, the average size of both Aβ+h+q- and Aβ+h+q+ plaques increased over age (Figure 5.6C). The changes in density and size of the plaque types resulted in small differences in the contribution of each plaque type to the total Aβ+ area over age, with the contribution of Aβ+h-q- plaque steadily increasing over age (Figure 5.6D). Finally, and unsurprisingly, the percentage area of the hippocampus covered with plaques also increased for each plaque type over age (Figure 5.6E). Altogether, Aβ+h+q- and Aβ+h+q+ plaques are the predominant plaque types during initial deposition, steadily increasing in both density and size with age. In contrast, Aβ+h-q- plaques are sparse at the time of initial deposition but rapidly increase in density over time.

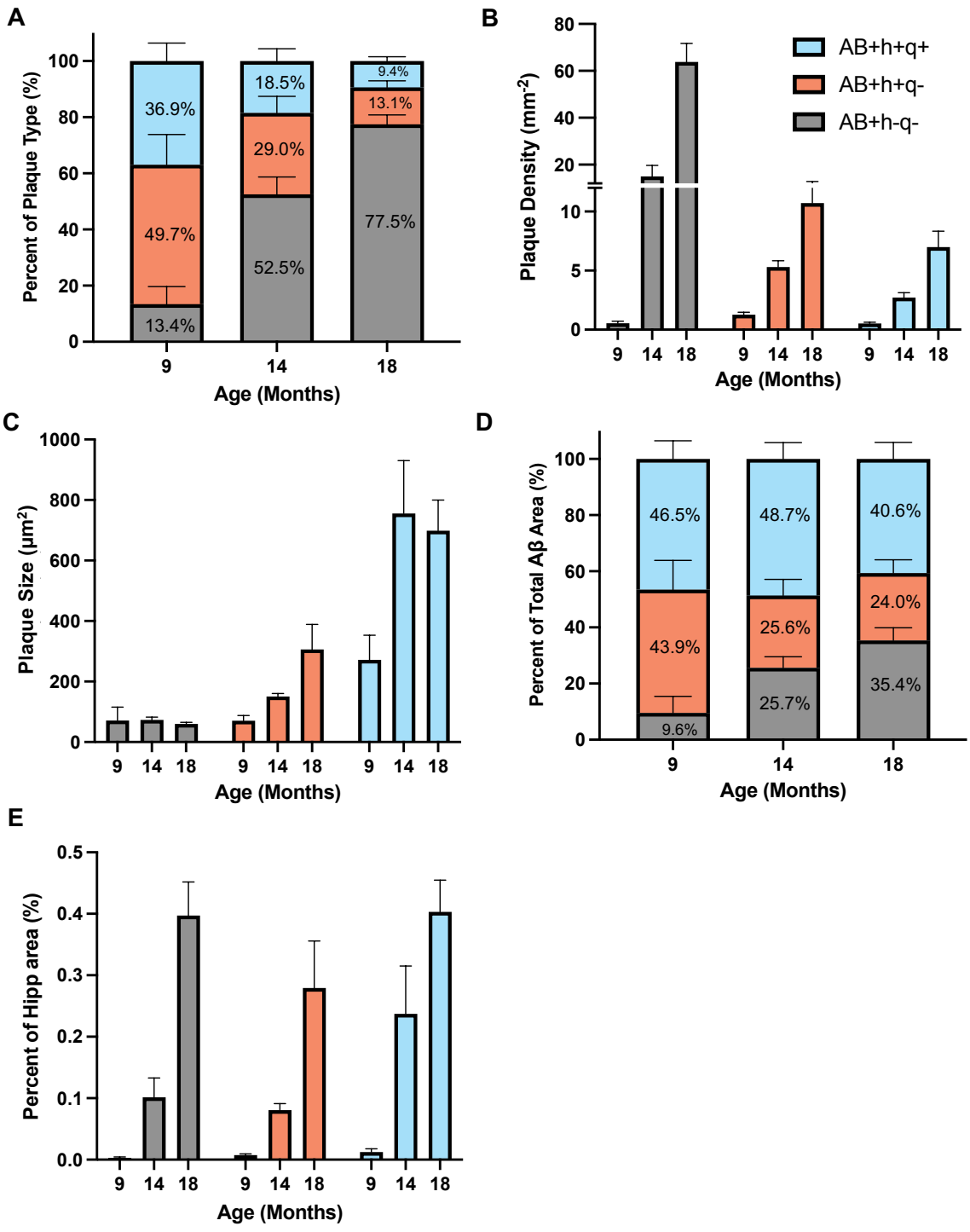

Figure 5.6 Structurally defined plaque types develop over mouse chronological age
(A) Proportion of each plaque type as a percentage of the total plaque count over mouse age. (B) Density of each plaque type over mouse age. (C) Average size of individual plaques for each plaque type over time. (D) Proportion of each plaque type as a percentage of the total plaque area over mouse age. (E) Percent coverage of hippocampal area by each plaque type over age. Analysis performed on projected z-stacked confocal images. NLF 9m n=7, NLF 14m n=5, NLF 18m n= 6. Data plotted as mean + SEM. Figure also in supplementary of Wood et al. (2024).

5.3.3 Density of small plaques increases with the *Trem2*^{R47H} mutation regardless of plaque type

As seen with Amytracker520 LCO staining, the density of small plaques is increased with the addition of the *Trem2*^{R47H} mutation, suggesting a potential role for TREM2 in moderating plaque dynamics, including seeding and maturation (Figure 3.11). To investigate this further, I evaluated the impact of introducing the *Trem2*^{R47H} mutation into NLF mice on the characterisation of the three structurally defined plaque types (Figure 5.5B). While there was a clear main effect of plaque type, with Aβ+h-q- having a much greater density than Aβ+h+q- and Aβ+h+q+ plaques, there was also a trend towards a main effect of genotype (P=0.06), with NLFTrem2^{R47H} mice showing a tendency for increased overall plaque density (Figure 5.7A). Similarly, when looking at the percent coverage of each plaque type, there was a significant main effect of genotype (P<0.05), with plaques in NLFTrem2^{R47H} mice covering a greater relative hippocampal area than NLF mice. Finally, I investigated whether the increase in small plaques, observed previously with Amytracker520 staining, was also present with any of the three plaque types. Interestingly, across each of Aβ+h-q- (Figure 5.7Ci), Aβ+h+q- (Figure 5.7Cii), and Aβ+h+q+ plaques (Figure 5.7Ciii), there was a significant increase in the density of small plaques (<100 μm^2) in NLFTrem2^{R47H} mice compared to NLF mice.

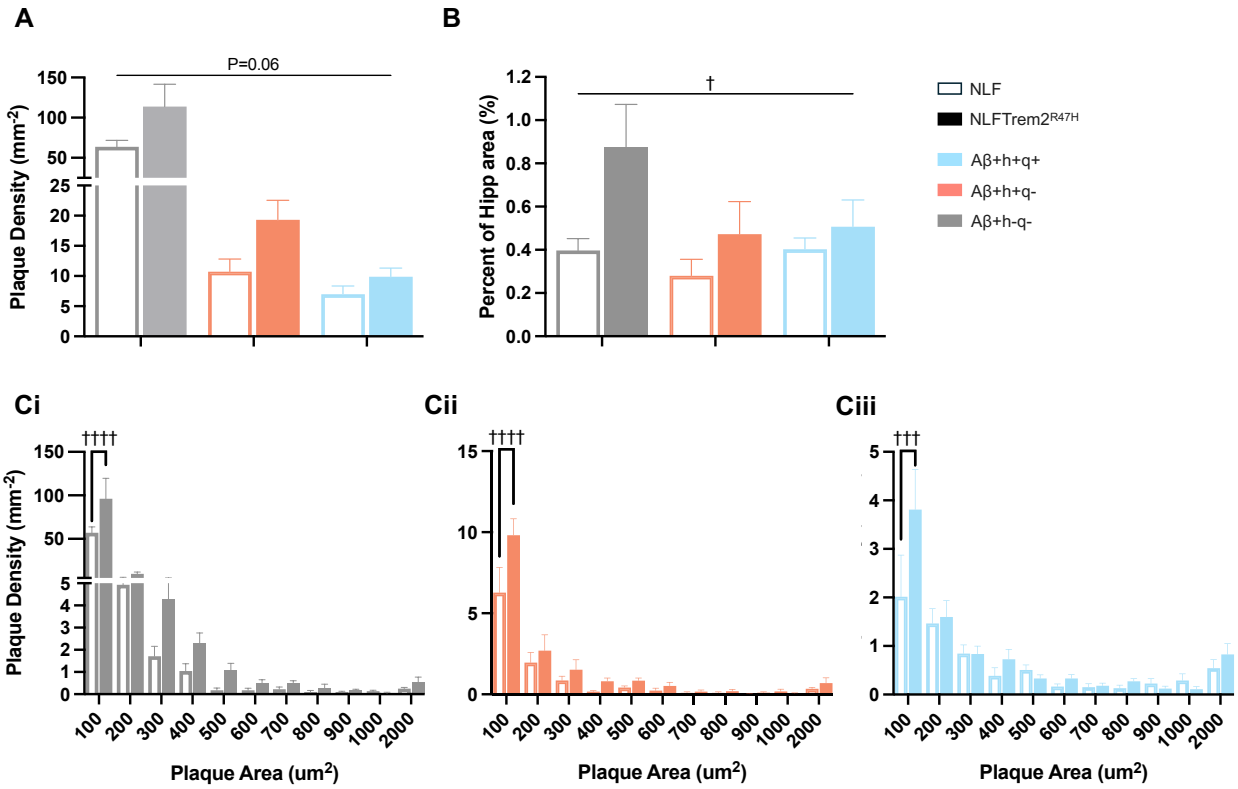

Figure 5.7 Density of small plaques increases with the *Trem2*^{R47H} mutation regardless of plaque type
(A) Comparison of plaque density between 18-month-old NLF and NLFTrem2^{R47H} mice for different plaque types. (Main effects: plaque type P<0.0001; genotype P=0.06; interaction P>0.1). (B) Comparison of the percent coverage of the hippocampal area between 18-month-old NLF and NLFTrem2^{R47H} mice for different plaque types. (Main effects: plaque type P>0.1; genotype P<0.05; interaction P>0.1). (C) Histogram showing the relationship between plaque area and plaque density at defined sizes in 18-month-old NLF and NLFTrem2^{R47H} mice for different plaque types: (Ci) Aβ+h+q+ (Main effects: plaque size P<0.0001; genotype P>0.1; interaction P<0.05), (Cii) Aβ+h+q+ (Main effects: plaque size P<0.0001; genotype P>0.1; interaction P<0.05), and (Ciii) Aβ+h+q+ (Main effects: plaque size P<0.0001; genotype P>0.1; interaction P=0.053). Analysis performed on projected z-stacked confocal images. Statistical analysis: (A & B) Two-way ANOVA between plaque type and genotype. (C) Two-way ANOVA between plaque size and genotype, followed by Sidak correction for multiple comparisons, shown on graphs. ††††P<0.0001; †††P<0.001; ††P<0.01; †P<0.05. †-between genotype significance. NLF n=6, NLFTrem2^{R47H} n=7. Data plotted as mean + SEM.

5.3.4 Spine loss is more pronounced in highly aggregated plaques

I have found that a combination of qFTAA, hFTAA, and Aβ42 staining can categorise plaques into three distinct, structurally defined categories (Figure 5.5). Additionally, each plaque type is influenced by both mouse chronological age (Figure 5.6) and the *Trem2*^{R47H} mutation (Figure 5.7). However, how each plaque type differs in its impact on the surrounding environment remains unknown. A distinct feature of AD is the profound loss of neuronal matter that correlates with cognitive decline (Fox et al., 1999; Sze et al., 1997). A possible contributor to this loss is the synaptic loss around plaques that is commonly observed in both human AD and mouse models (Bittner et al., 2012; Spires et al., 2005; Spires-Jones et al., 2007). Interestingly, different plaque types defined by either thioflavin-positivity or morphological assessment exhibit differential synapse loss (Koffie et al., 2009; Schmidt et al., 1995). This finding is further supported by the previous figure, which shows a correlation between the decrease in synapse-associated genes and increasing plaque age (Figure 5.4), with plaque age also correlating with increasing plaque aggregation (Wood et al., 2024). This elimination of synapses associated with Aβ-induced toxicity has been hypothesised as a key role of microglia, with TREM2 playing an important role in regulating this process (Hong et al., 2016; Rueda-Carrasco et al., 2023; Spangenberg et al., 2016).

I investigated the loss of the postsynaptic-specific protein HOMER1 and the influence of both plaque type and the *Trem2*^{R47H} mutation. To accommodate the high-throughput analysis, fold-change in HOMER1 fluorescence intensity was measured rather than counting HOMER1-defined postsynaptic puncta. This approach was necessary due to the large-scale analysis, which included all plaques within the hippocampus across multiple sections and

many animals. Interestingly, no loss of HOMER1 was seen in Aβ+h-q- plaques at any distance from plaques, including on the plaque area itself (Figure 5.8A and 5.8B). In NLF mice, the loss of HOMER1 was more pronounced with increased plaque aggregation, showing the most severe loss within the plaque area in Aβ+h+q+ plaques; however, there was still significant loss in Aβ+h+q- plaques (Figure 5.8A and 5.8Bi). The loss of HOMER1 remained in Aβ+h+q+ plaques at a distance of 10 μm from the plaque surface. This finding was not seen around Aβ+h+q- plaques. The pattern of increasing HOMER1 loss with increasing plaque aggregation was also seen in NLFTrem2^{R47H} mice (Figure 5.8Bii). To directly compare HOMER1 loss between NLF and NLFTrem2^{R47H} mice, the loss of HOMER1 within the plaque area was compared. Surprisingly, the introduction of the *Trem2^{R47H}* mutation caused no change in HOMER1 loss for each plaque type (Figure 5.8C).

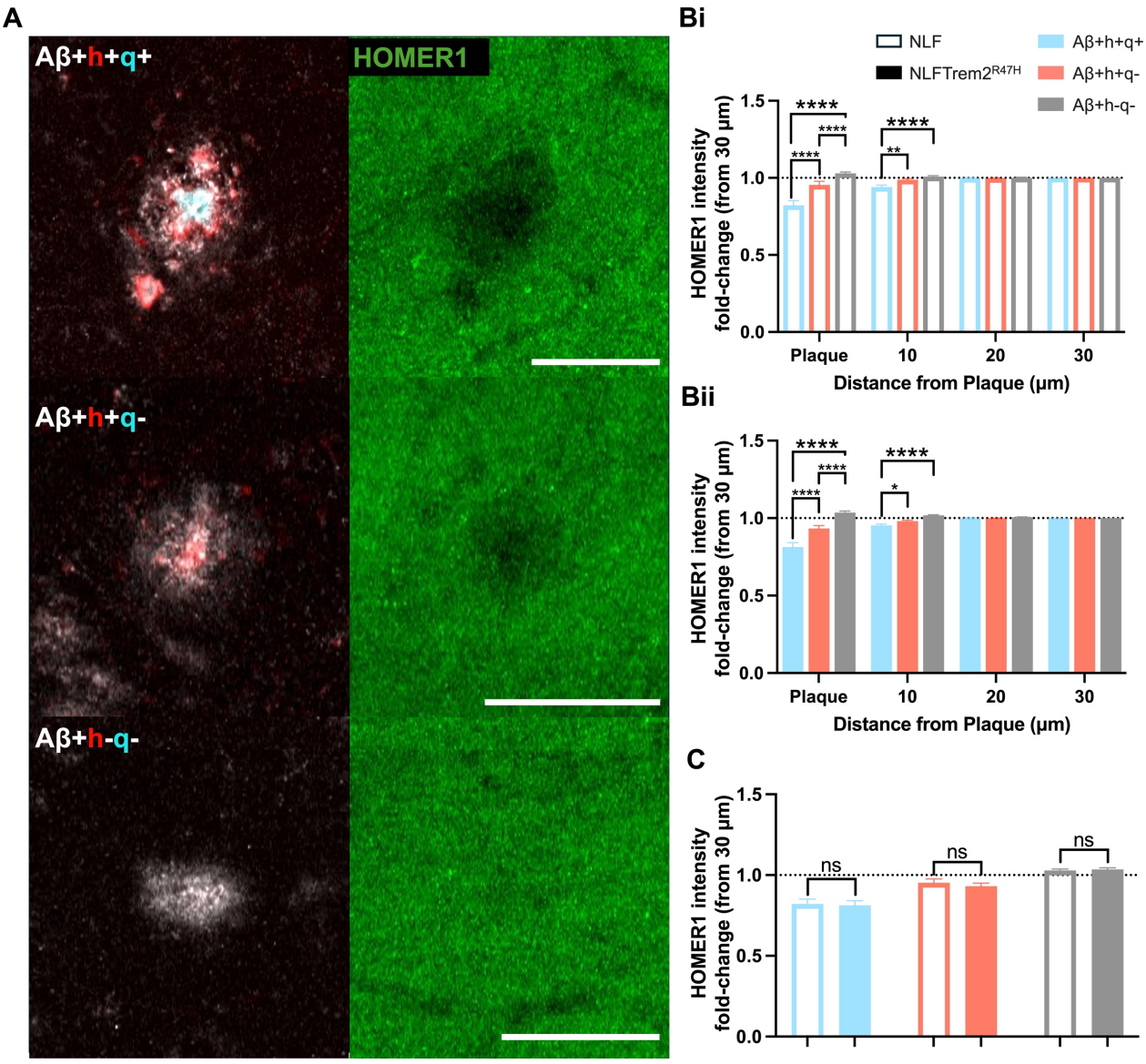

Figure 5.8 Spine loss is more pronounced in highly aggregated plaques
(A) Representative confocal images of Aβ+h+q+ (top), Aβ+h+q- (middle), and Aβ+h-q- (bottom) plaques with corresponding images of dendritic spines labelled with HOMER1 (green). Scale bar: 50 μm. (B) Quantification of HOMER1 protein levels, measured as fold change in fluorescence intensity from 30 μm for each plaque type in: (Bi) 18-month-old NLF mice (main effects: plaque type P<0.0001; distance to plaque P<0.0001; interaction P<0.001). (Bii) 18-month-old NLFTrem2^{R47H} mice (main effects: plaque type P<0.0001; distance to plaque P<0.0001; interaction P<0.0001). (C) Comparison of synapse loss at plaques between NLF and NLFTrem2^{R47H} mice. Analysis performed on projected z-stacked confocal images. Statistical analysis: (Bi & Bii) Two-way repeated measures ANOVA between plaque type and distance from plaque, followed by Tukey's post hoc correction for multiple comparisons, shown on the graph. (C) Individual T-tests were used to assess the main effect of genotype for each plaque type, as shown on the graph. ***P<0.001; *P<0.01; P<0.05. NLF n=6, NLFTrem2^{R47H} n=7. Data plotted as mean + SEM. Bi adapted from figure presented in in Wood et al. (2024).

5.3.5 Highly aggregated plaques are more toxic

The greater loss of synaptic puncta observed with increased plaque aggregation suggests that more highly aggregated plaques may be more toxic. To test this, I measured the expression of two toxicity markers surrounding the different plaque types in 18-month-old NLF and NLFTrem2^{R47H} mice. Firstly, I stained for the lysosomal protein LAMP1. As a highly expressed lysosomal membrane protein, LAMP1 labels the lysosomal enlargements present in dystrophic neurites surrounding plaques (Figure 5.9A). The degree of LAMP1 staining has previously been used as a correlate of plaque toxicity, reflecting the amount of autophagic stress placed on surrounding neurites (Condello et al., 2011; Condello et al., 2015). For this experiment, I first distinguished between fibrillised and non-cored plaques using an Aβ antibody and the broad-spectrum LCO Amytracker520, which combines properties of both h and q LCOs (Figures 5.9B and 5.9E). I then went on to test whether the aggregation density between cored and fibrilised plaques affected the results by staining with hFTAA and qFTAA LCOs separately (Figures 5.9C, 5.9D, 5.9F, and 5.9G).

Amytracker520 defined plaques exhibited a greater increase in LAMP1 fluorescence compared to Aβ+AMY- plaques in both NLF and NLFTrem2^{R47H} mice (Figures 5.9Bi and 5.9Bii). This suggests that the non-fibrillated Aβ+AMY- plaques are potentially less toxic, which correlates well with the lack of synaptic loss observed in the previous figure (Figure 5.8). The pattern of increasing toxicity with higher aggregation is further supported by qFTAA and hFTAA staining, which show a significant increase in LAMP1 staining around h+q+ plaques compared to h+q- plaques in both NLF and NLFTrem2^{R47H} mice (Figures 5.9Ci and 5.9Cii). Together, these findings reveal that plaques with increased aggregation induce greater autophagic stress on the surrounding tissue. Next, I compared plaque-induced

autophagic stress between NLF and NLFTrem2^{R47H} mice. No significant differences were seen in LAMP1 staining over the three plaque types between NLF and NLFTrem2^{R47H} mice ($P>0.05$, Figure 5.9D).

Next, I stained for the neuronal pentraxin NPTX2. Interestingly, CSF levels of NPTX2 appear to decrease with AD progression and cognitive decline (Libiger et al., 2021; Xiao et al., 2017), which aligns well with the decrease of *Nptx2* expression seen with increasing plaque age (Figure 5.4). In contrast, NPTX2, along with other members of the pentraxin family, is seen to be increased in dystrophic neurites surrounding plaques (Figure 4.9A, Cummings et al., 2017). The synaptic specificity of NPTX2 and its increased presence around plaques presents a potential new approach for staining dystrophy, offering an alternative to the assessment of the typically stained enlarged lysosomes (Abad et al., 2006; Cummings et al., 2017).

NPTX2 had a significantly larger increase in expression at AMY+ plaques compared to Aβ+AMY- plaques in both NLF and NLFTrem2^{R47H} mice (Figures 5.9Ei and 5.9Eii). This is further delineated in hFTAA- and qFTAA-defined plaques showing an increase in NPTX2 in h+q+ plaques compared to h+q- plaques in both NLF and NLFTrem2^{R47H} mice (Figures 5.9Fi and 5.9Fii). Next, NLF and NLFTrem2^{R47H} mice were compared to test for the effect that the *Trem2*^{R47H} mutation has on plaque-induced synaptic dystrophy. Surprisingly, NLF mice had significantly heightened NPTX2 expression on Aβ+h+q+ plaques compared to NLFTrem2^{R47H} mice (Figure 5.9G).

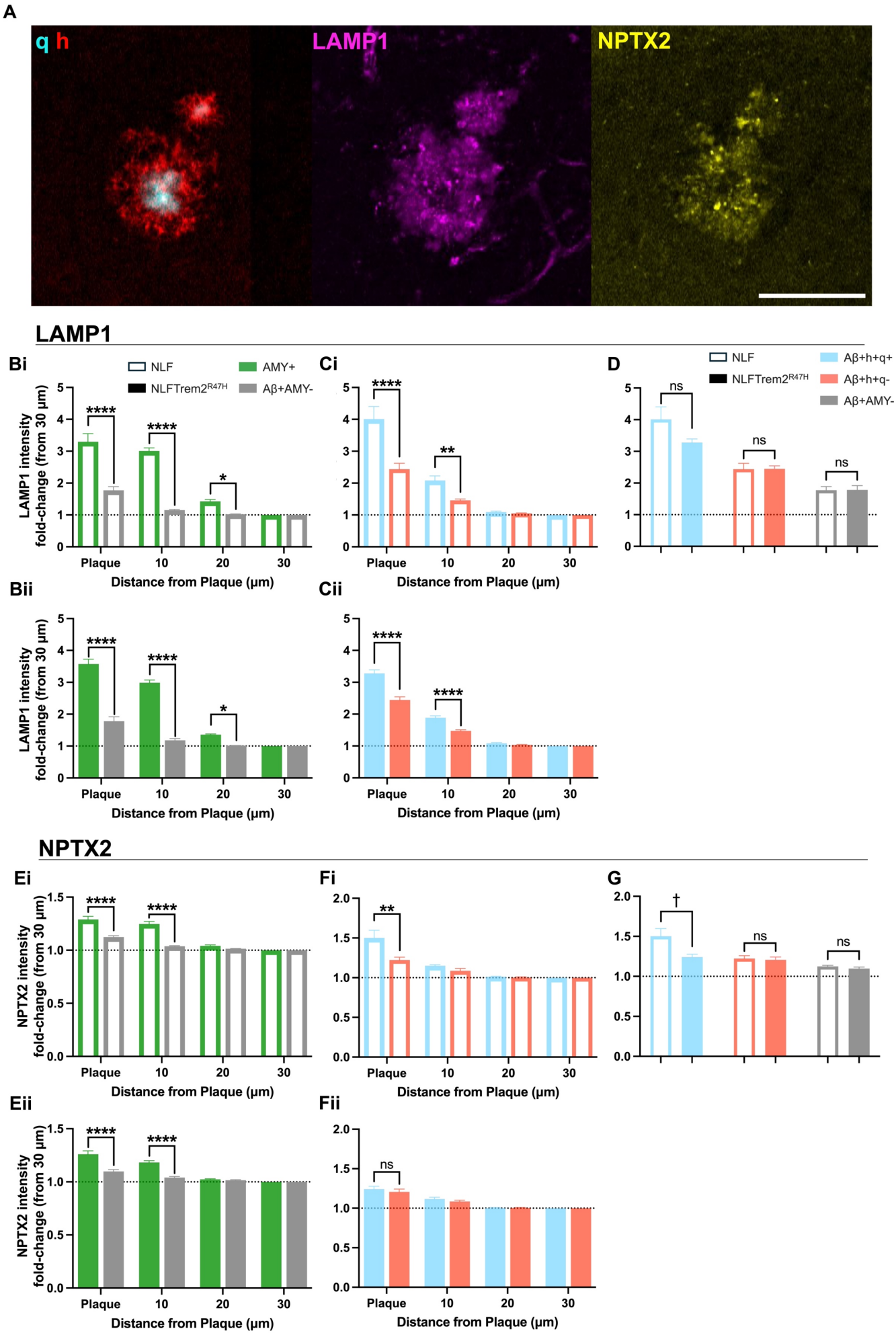
A
q h
LAMP1
NPTX2
LAMP1
Bi
NLF
NLFTrem2R47H
AMY+
Aβ+AMY-
LAMP1 intensity fold-change (from 30 µm)
Plaque
10
20
30
Distance from Plaque (µm)
Ci
D
Aβ+h+q+
Aβ+h+q-
Aβ+AMY-
ns
Bii
Cii
NPTX2
Ei
NPTX2 intensity fold-change (from 30 µm)
Fi
G
†
Eii
Fii

Figure 5.9 Highly aggregated plaques are more toxic
(A) Representative confocal images of an Aβ+h+q+ plaque with corresponding images of LAMP1 (purple) and NPTX2 (yellow) staining. Scale bar: 50 μm. (B) Quantification of LAMP1 protein measured by fold change in fluorescence intensity from 30 μm at varying distances from the plaque between Amytracker+ (AMY+) and Aβ+h-q- plaques in 18-month-old NLF and NLFTrem2^{R47H} mice. (Bi) NLF mice (main effects: plaque type P<0.0001; distance to plaque P<0.0001; interaction P<0.0001). (Bii) NLFTrem2^{R47H} mice (main effects: plaque type P<0.0001; distance to plaque P<0.0001; interaction P<0.0001). (C) Quantification of LAMP1 protein at varying distances from the plaque between Aβ+h+q+ and Aβ+h+q- plaques in NLF and NLFTrem2^{R47H} mice. (Ci) NLF mice (main effects: plaque type P<0.05; distance to plaque P<0.0001; interaction P<0.0001). (Cii) NLFTrem2^{R47H} mice (main effects: plaque type P<0.001; distance to plaque P<0.0001; interaction P<0.0001). (D) Comparison of LAMP1 protein on plaque between NLF and NLFTrem2^{R47H} mice. (E) Quantification of NPTX2 protein at varying distances from the plaque between AMY+ and Aβ+h-q- plaques in 18m NLF and NLFTrem2^{R47H} mice. (Ei) NLF mice (main effects: plaque type P<0.0001; distance to plaque P<0.0001; interaction P<0.0001). (Eii) NLFTrem2^{R47H} mice (main effects: plaque type P<0.0001; distance to plaque P<0.0001; interaction P<0.0001). (F) Quantification of NPTX2 protein at varying distances from the plaque between Aβ+h+q+ and Aβ+h+q- plaques in NLF and NLFTrem2^{R47H} mice. (Fi) NLF mice (main effects: plaque type P>0.1; distance to plaque P<0.0001; interaction P<0.05). (Fii) NLFTrem2^{R47H} mice (main effects: plaque type P>0.1; distance to plaque P<0.0001; interaction P>0.1). (G) Comparison of NPTX2 protein on plaque between NLF and NLFTrem2^{R47H} mice. Analysis performed on projected z-stacked confocal images. Statistical analysis: (B, C, E, & F) Two-way repeated measures ANOVA between plaque type and distance from plaque, followed by Tukey's post hoc correction for multiple comparisons, shown on graph. (D, G) Individual T-tests to assess the main effect of genotype for each plaque type, statistics shown on graph. ****P<0.0001; ***P<0.001; **P<0.01; */†P<0.05. *-within genotype significance, †-between genotype significance. AMY experiments: NLF n=7, NLFTrem2^{R47H} n=8. q and h experiments: NLF n=4, NLFTrem2^{R47H} n=5. Data plotted as mean + SEM. Bi & Ci adapted from figures presented in in Wood et al. (2024).

5.4 Chapter summary

The major finding of this chapter is that Aβ plaque heterogeneity, investigated through both plaque age and structural morphology, is a critical determinant of the plaque-associated effects on surrounding tissue in NLF mice.

This chapter presents a novel method of estimating plaque age using a stable isotope labelling scheme that uses an enrichment of ^{15}N to time stamp the period of initial plaque deposition. Mass spectrometry imaging was then used to measure the mass of Aβ species within individual plaques, with a shift toward higher molecular weight indicating greater ^{15}N incorporation and thus the plaque was deposited earlier in the disease progression. To assess how plaque age influences local tissue responses, single-plaque GeoMx spatial transcriptomics was employed to quantify whole-transcriptome gene expression in the

immediate plaque microenvironment. This enabled a direct correlation between plaque age and changes in gene expression. Interestingly, increasing plaque age was associated with a decline in the expression of synapse-associated genes, while genes related to metabolic processes and neuronal homeostasis showed a positive correlation, increasing with plaque age.

This chapter introduces a new approach to categorising structural plaque morphologies using hyperspectral imaging of hFTAA and qFTAA structural amyloid dyes in combination with an Aβ antibody. This resulted in three plaque types, Aβ+h+q+, Aβ+h+q-, and Aβ+h-q-, which likely correspond to cored, fibrillar, and diffuse plaque types, respectively. Surprisingly, at 9 months of age, the age of initial plaque deposition, the vast majority of plaques were already fibrillar or cored (Aβ+h+q- or Aβ+h+q+, respectively), with very few diffuse (Aβ+h-q-) plaques observed. As mice aged, the proportion of diffuse plaques increased relative to fibrillar and cored plaques, ultimately comprising ~80% of all plaques by 18 months of age. Notably, most diffuse plaques were very small (<100 μm^2), and average plaque size increased with aggregation density, with cored plaques being the largest on average.

This high-throughput method of plaque categorisation enabled a comprehensive assessment of the toxicity associated with each distinct plaque type. In this chapter, I demonstrated that the most highly aggregated plaques (Aβ+h+q+) are associated with significantly greater toxicity compared to less aggregated plaque types, as evidenced by pronounced dendritic spine loss (HOMER1), elevated levels of dystrophic neurites (LAMP1), and increased accumulation of damaged synapses (NPTX2). However, the introduction of the *Trem2*^{R47H} mutation into NLF mice only influenced a significant reduction in NPTX2 staining around Aβ+h+q+ plaques. Finally, in the previous chapter, I demonstrated that the *Trem2*^{R47H} mutation leads to an increase in small Amytracker-defined plaques. Building on this, with the added structural distinction between Aβ+h+q+, Aβ+h+q-, and Aβ+h-q- plaque types, I revealed that the increase in small plaques is consistent across all three plaque types.

CHAPTER 6

DISCUSSION

The amyloid hypothesis of AD proposes that the accumulation of Aβ, particularly the more aggregation-prone Aβ42, is the primary initiating event in a cascade of pathological and clinical changes. This cascade includes the development of tau pathology, neuroinflammation, neuronal loss, and ultimately cognitive decline (Long and Holtzman, 2019). However, several inconsistencies challenge the importance of Aβ in AD pathogenesis. These include the substantial temporal gap between Aβ deposition and the onset of downstream pathological and clinical changes, the weak correlation between Aβ plaque burden and cognitive impairment, and the failure of AD mouse models to show Aβ-induced tau pathology or overt cognitive deficits. Furthermore, while Aβ-targeting immunotherapies can effectively reduce plaque load, they have demonstrated only modest and often clinically insignificant benefits (Behl, 2024; Morris et al., 2014). The aim of this thesis was to investigate the relationship between Aβ plaques and their effects on the local tissue environment. This was explored across three chapters: the first examined the microglial response to Aβ plaques in a mouse model of AD, the second extended this analysis to human AD brain tissue, and the third focused on how plaque heterogeneity also influences surrounding tissue.

6.1 The *Trem2*^{R47H} mutation reduces Trem2 expression

The *TREM2*^{R47H} mutation increases the risk of developing AD by 3- to 5-fold, a risk attributed to a loss of function of TREM2 as opposed to a reduction in total *TREM2* expression (Guerreiro et al., 2013). However, in multiple mouse models harbouring the *Trem2*^{R47H} mutation, an aberrant splicing event of *Trem2* mRNA frequently occurs, reducing the expression of *Trem2* by ~50-60% (Liu et al., 2020; Xiang et al., 2018). I show that in qPCR performed on whole hippocampus, Trem2^{R47H} mice have a 63% reduction in *Trem2* expression compared to WT mice. Surprisingly, however, in the immunohistochemistry and spatial transcriptomics analysis, I presented a ~20-25% reduction of *Trem2* expression. A reasonable explanation could be the use of dorsal hippocampal sections in the immunohistochemical and spatial transcriptomic methods compared to the whole hippocampus used in RNAseq and qPCR. This is supported by the substantial molecular differences reported along this hippocampal axis (Vogel et al., 2020). Another consideration is the reliance of both immunohistochemistry and spatial transcriptomics on antibody or probe binding efficiency. Probe-based methods are not fully quantitative, as their accuracy depends on the binding efficacy and specificity of the probes, which may vary between

targets and conditions. In immunohistochemistry, fluorescence intensity does not always scale linearly with protein expression levels, and discrepancies between RNA and protein expression due to post-transcriptional regulation can further complicate interpretation. Additionally, non-specific binding of probes and antibodies may obscure true biological differences by introducing a background signal. Supporting this, a study using Western blotting, which mitigates background signal from tissue autofluorescence, reported an approximate 50% reduction in TREM2 protein levels in whole hemisphere extraction from $Trem2^{R47H}$ mice (Kotredes et al., 2021). Nonetheless, study of the *Trem2*^{R47H} harbouring mice provides insights into due to a combined loss of expression and loss of function.

6.2 Plaque contact is required for the microglial response to Aβ plaques in NLF mice

The use of the NLF model in AD research has been unpopular due to the late onset and slow rise of Aβ plaque pathology. The necessity to age NLFs is costly but much more appropriate to AD as advanced age is the largest risk factor (Guerreiro and Bras, 2015; Kukull et al., 2002; Stam et al., 1986). Until now, analysing changes in the NLF model using standard transcriptomic analysis such as qPCR and RNAseq has come to little avail, as even at older ages, the majority of brain tissue remains non-plaque-associated and hence dilutes any plaque-induced effects (Figure 3.1; Benitez et al., 2021; Saito et al., 2014). The commonly used transgenic or aggressive knock-in models overcome this problem of non-plaque associated tissue by overexpressing *App* or increasing its aggregation properties to massively increase plaque load. However, the early onset of plaques and overexpression artefacts of transgenesis in these models sacrifice their similitude to human AD (Sasaguri et al., 2017). This study overcomes these problems using the spatial transcriptomic technique on NLF tissue to analyse RNA expression in microglia directly contacting plaques, microglia in periplaque regions, and microglia away from plaques. Here, the spatial sensitivity enables the measurement of plaque-induced change without the diluting effect of bulk analysis.

I focused on the recently reported plaque-induced genes (PIGs), a set of genes defined through spatial transcriptomics that show increased expression with rising plaque density within defined tissue regions (Chen et al., 2020). In this thesis, I found that 70% of PIGs significantly increased in expression in relation to plaque (Chen et al., 2020). The lack of significance of the remaining 17 genes is most likely due to the difference in the model used, with Chen et al. (2020) having employed the aggressive NLGF model that harbours a mutation in the Aβ sequence that drives a pathology of compact and early depositing plaques (Lord et al., 2011; Saito et al., 2014). Since age is the strongest risk factor for AD, and young microglia are known to function differently from aged microglia (Daria et al., 2017), these factors may influence microglial gene expression. Furthermore, In the present

study, plaques were grouped together, and therefore, the range of plaque types seen in NLF mice may have diluted any unique influences of cored plaques seen in NLGF mice. Moreover, unlike Chen et al. (2020), this study focused on genes enriched in microglia. Therefore, this loss of significant genes may have also been due to their association with other cell types. Indeed, the 30% of the PIGs that did not come out in the present analysis as being differentially expressed in relation to distance from plaque had been previously identified as genes highly expressed in other cell types such as oligodendrocytes, epithelial cells, or astrocytes (Ximerakis et al., 2019; Zhang et al., 2014). Finally, the question asked by the presented spatial transcriptomic experiment was different from that of Chen et al. (2020). PIGs were identified as genes whose expression increases with rising plaque density within a fixed region, whereas in the present study, the focus was on genes that change in expression spatially towards plaques. Therefore, the two approaches capture overlapping but distinct sets of plaque-associated transcriptional changes.

An important distinction between this project and previous transcriptomic studies is the high spatial resolution of the reported plaque-induced expression. This enabled the separation of the 38 significant PIGs into three distinct groups. The plaque response group was of particular interest, as these genes were only upregulated upon direct contact of microglia with plaques. Numerous roles have previously been proposed for microglia in direct contact with plaques, primarily based on findings from in vivo and in vitro imaging studies. These include phagocytosis of plaques and synapses (Tzioras et al., 2023), formation of a protective barrier around plaques (Condello et al., 2015), compaction of plaques into more aggregated structures (Spangenberg et al., 2019), potential involvement in plaque seeding (Baik et al., 2016), and regulation of lipid metabolism and storage (Prakash et al., 2024). For the first time, I demonstrate that these functional roles are congruent with the specific transcriptional profile of plaque-associated microglia. This includes an upregulation of *Npc2*, *Grn*, and a range of cathepsins (*Ctsd*, *Ctsz*, *Ctss*, *Ctsb*, *Ctsl*) associated with lipid and lysosomal processes, likely reflecting responses to internalised material. Notably, all three components of the C1q complement complex were selectively upregulated in plaque-contacting microglia, consistent with a role in synaptic pruning and potential Aβ uptake (Carpanini et al., 2022; Hong et al., 2016). Importantly, *Trem2* and its adaptor *Tyrobp*, both well-established hub genes, were also upregulated exclusively in microglia at the plaque interface and are known to regulate many of the aforementioned processes. For example, loss of Trem2 function has been shown to impair phagocytosis (Takahashi et al., 2005), reduce the number of plaque-surrounding microglia (Wang et al., 2016; Wood et al., 2022), lead to less compacted plaques and altered plaque burden (Yuan et al., 2016), and disrupts lipid droplet metabolism (Claes et al., 2021).

The second category, graded response, represented genes that increased gradually towards plaque; this is likely induced by molecules that exist at the plaque periphery as well as the plaque itself, such as cytokines, soluble Aβ, and other messenger molecules. This is exemplified by the increase in Csf1r, a receptor involved in signalling microglial proliferation (Menassa and Gomez-Nicola, 2018), and *B2m*, a subunit of the MHC1 complex important in alerting the immune system to potential harm (Smith et al., 2015). Finally, the third category, plaque and periplaque response, comprises only four genes, all of which are predominantly expressed by astrocytes. This group includes *Apoe* and *Clu*, both of which encode lipid chaperone proteins that also play roles in controlling inflammatory processes. Notably, variants in both genes are associated with an increased risk of developing AD (DeMattos et al., 2004). Their significant upregulation in periplaque regions is likely due to the increase in astrocytic area around plaques that exist at further distances compared to the tight microglial clustering (Wood et al., 2022). Additionally, astrocytic processes are generally longer than those of microglia, which means that a signal detected 30 µm from a plaque could originate from an astrocyte that is in contact with the plaque. Although these genes are typically associated with astrocytes under homeostatic conditions, *Apoe* has been shown to have increased expression within microglia in the context of Aβ plaque pathology (Wang et al., 2021). This is further supported in the presented immunohistochemical analysis, which revealed a significant increase in microglial APOE protein expression as microglia approach plaques. Therefore, it remains unclear whether other significant PIG genes classically expressed in astrocytes, such as *Igfbp5*, *Clu*, *Prdx6*, and *Gfap*, are also expressed by plaque-associated microglia. This uncertainty is due to the limitation of the GeoMx technique, whereby microglia-enriched regions can be contaminated with gene expression of other cell types.

6.3 Unimpaired Trem2 is required for the microglial response to Aβ plaques

To assess the *Trem2*-dependence of plaque-associated gene expression, the *Trem2*^{R47H} mutation was introduced to impair *Trem2* function. This revealed that nine genes, each belonging to the plaque response only category, were no longer upregulated in microglia at plaques. The *Trem2*-dependent module falling within the plaque response only category is consistent with the finding that *Trem2* itself is also classified within this group. I also translated this finding to the protein level, showing that while TREM2 is significantly increased in microglia surrounding plaques, its expression is significantly impaired by the *Trem2*^{R47H} mutation. This observation suggests the presence of a plaque-specific TREM2 ligand that initiates this transcriptional programme. Its specificity to plaques suggests that the ligand is likely lipophilic or otherwise restricted to the plaque environment, such as

plaque- associated damaged synapses. Several known TREM2 ligands are enriched at plaques, including PtdSer (Huang et al., 2021; Scott-Hewitt et al., 2020), apolipoprotein E (Atagi et al., 2015), and lipoproteins such as low-density lipoprotein (LDL) and clusterin (Hamerman et al., 2006; Yeh et al., 2016). Furthermore, the exposure of TREM2 ligands such as PtdSer at damaged synapses and dystrophic neurites, as well as plaques, could suggest that rather than being plaque responsive, this gene module could also be damage responsive (Rueda-Carrasco et al., 2023; Sapar et al., 2018).

This TREM2-dependent gene module encodes complement components *C1qa* & *C1qc*; cathepsins *Ctsz*, *Ctss*, *Ctsd*, & *Ctsb*; the cholesterol transporter *Npc2*, the lysosomal regulator *Grn*, and the phagosome-associated *Plek*.

Complement components: C1qa, C1qc

The observed *Trem2*-dependence of *C1qa* and *C1qc*, which encode components of the classical complement cascade, aligns with findings from aged *Trem2*-knockout mice, where reduced expression of these genes was accompanied by increased synaptic and neuronal density and decreased expression of phagocytosis-associated markers (Linnartz-Gerlach et al., 2019). Moreover, PtdSer, a damage-associated marker exposed on plaques, damaged synapses, and degenerating neurons, has been shown to bind C1q (Rueda-Carrasco et al., 2023; Scott-Hewitt et al., 2020). On top of this, C1q has been shown to bind directly to TREM2 (Greven et al., 2025). These findings support a model in which functional TREM2 activation in plaque-contacting microglia induces the expression and extracellular release of C1q. This complement protein then opsonises plaques and damaged neurites, perhaps via PtdSer exposure, enabling their recognition by TREM2, which initiates subsequent phagocytic clearance. Alternatively, the complement system may cascade further, leading to the presentation of iC3b via C1q-dependent cleavage events, in which case the microglial receptor CR3 would mediate phagocytosis, a process still ultimately dependent on plaque contact-driven TREM2 activation (Carpanini et al., 2022; Nimmo et al., 2024).

A recently published study, however, proposes an opposing relationship between TREM2 and the complement system (Zhong et al., 2023). While showing that TREM2 binds with high affinity to C1q subunits, the authors suggest that this interaction inhibits, rather than facilitates, C1q activity. In *Trem2* haploinsufficient mice, they report increased activation of C1q via C3-opsonised synapses, which contributed to a corresponding loss of postsynaptic densities and an increase in microglial engulfment of postsynapses. Although the notion that TREM2 induces C1q expression but simultaneously inhibits its activity may appear contradictory, the study also demonstrates that soluble TREM2 (sTREM2), a sheddase-

derived product that retains the C1q-binding ectodomain, can also sequester C1q. Therefore, the enhanced C1q activity observed in Trem2 haploinsufficient mice may stem from the loss of sTREM2- rather than TREM2-mediated inhibition. While the authors interpret this inhibition as a protective mechanism that prevents excessive C1q-driven synaptic elimination (Monroe and Lewcock, 2023; Zhong et al., 2023), it may alternatively represent an aberrant process in which accumulated sTREM2 suppresses the necessary removal of damaged synapses. This failure to clear dysfunctional synapses could allow local damage to propagate and cause larger network damage (Edwards, 2019). Ultimately, further research is needed to clarify the relationship between TREM2, sTREM2, and the complement system in AD.

Cathepsins: Ctsz, Ctss, Ctsd, Ctsb

Cathepsins constitute four of the nine *Trem2*-dependent genes. They encode lysosomal peptidases that target aspartic acid, cysteine, or serine, depending on the residues in their active sites. Interestingly, CTSB, CTSD, and CTSL have been shown to degrade Aβ, with their deficiency leading to an increase in Aβ deposition in various mouse models of AD (Cermak et al., 2016; Mueller-Steiner et al., 2006; Suire et al., 2020). Many sequencing experiments have shown large increases in plaque-induced cathepsin expression within microglia (Chen et al., 2020; Keren-Shaul et al., 2017; Matarin et al., 2015; Olah et al., 2020). The original characterisation of disease-associated microglia (DAM) in 5xFAD mice revealed marked upregulation of multiple lysosomal cathepsins, including *Ctsz*, *Ctsd*, *Ctsl*, *Ctsa*, *Ctss*, and *Ctsb*, in response to Aβ pathology (Keren-Shaul et al., 2017). Notably, the expression of many of these cathepsins was significantly reduced in *Trem2*-knockout mice. The present study extends this observation by demonstrating that the *Trem2*-dependence of *Ctsz*, *Ctss*, *Ctsd*, and *Ctsb* is specific to microglia in direct contact with plaques.

An obvious reason for the *Trem2*-dependent increase in microglial cathepsin expression is the phagocytosis of plaque-associated damage and Aβ itself, which necessitates an increase in lysosomal function and associated proteases (Cho et al., 2014). An alternative explanation could relate to the known ability of microglia to secrete high volumes of cathepsins through lysosomal exocytosis, where, under homeostatic conditions, their protease activity contributes to plasma membrane repair and extracellular matrix remodelling (Castro-Gomes et al., 2016; Vidak et al., 2019; Vizovisek et al., 2019). In the context of AD, the extracellular release of cathepsins is believed to play a role in the degradation of Aβ plaques (Jacquet et al., 2024). Notably, CTSB is being explored as a potential therapeutic target to enhance the digestive exophagy of plaques (Sulatsky et al., 2025; Theodoropoulou et al., 2024). Interestingly, a recent study in *Ctsd*-knockout mice revealed not only

substantial increases in intracellular Aβ but also elevated accumulation of phosphorylated tau, with some neurons even exhibiting tangle positivity in silver staining (Terron et al., 2024). The exact mechanism by which *Ctsd*-knockout leads to tau phosphorylation remains unclear. However, it does propose an interesting hypothesis connecting Aβ accumulation, tau pathology, and the presented *Trem2*-dependence on cathepsin expression. Here, the accumulation of plaques and the decrease in *Trem2* function will result in the inhibition of activity and a decrease in the expression of CTSD (and possibly other cathepsins). This persistent inhibition and altered CTSD expression, much like the CTSD-knockout mouse, will lead to the development of hyperphosphorylated tau, which may begin to spread and form tangles.

Cholesterol transporter Npc2

Npc2 encodes the lysosomal protein NPC2 that, together with NPC1, mediates the egress of cholesterol from late endosomes and lysosomes to other intracellular compartments (Storch and Xu, 2009). Both proteins are essential for maintaining intracellular cholesterol homeostasis, and loss-of-function mutations in these genes cause Niemann-Pick disease type C (NPC), a lysosomal storage disorder characterised by the accumulation of cholesterol within lysosomes. While NPC is caused by homozygous mutations in *Npc1* or *Npc2*, recent evidence suggests that heterozygous variants may increase the risk of AD (Sorrentino et al., 2021). Cholesterol homeostasis is increasingly recognised to be disrupted in the pathogenesis of AD. For example, cholesterol has been shown to accumulate at Aβ plaques (Burns et al., 2003), and potentially seed plaques by co-aggregating with Aβ (Banerjee et al., 2021; Habchi et al., 2018). Furthermore, high cholesterol levels seem to drive the amyloidogenic APP processing pathway to produce higher Aβ levels through inhibition of α-secretase activity (Bodovitz and Klein, 1996; Cole et al., 2005).

In microglia surrounding plaques, an aberrant increase in intracellular cholesterol leads to its esterification and subsequent storage within intracellular organelles known as lipid droplets (Marschallinger et al., 2020; Prakash et al., 2024). These lipid droplet-rich microglia have lower phagocytic ability and show signs of cellular senescence (Marschallinger et al., 2020). Notably, NPC2 is a regulator of lipid droplet formation in microglia, as knockdown of *Npc2* in cultured microglia significantly inhibited lipid droplet accumulation (Marschallinger et al., 2020). Therefore, the presented increase in plaque-contacting microglial *Npc2* expression may reflect a response to elevated microglial cholesterol uptake from plaques, where NPC2 is facilitating its trafficking into lipid droplets.

Consistent with the findings of this thesis, in a demyelination model of cholesterol stress, *Npc2* expression was significantly reduced in *Trem2*-deficient microglia (Nugent et al., 2020). While this was associated with increased lipid droplet accumulation, other demyelination studies have reported the opposite effect, showing reduced lipid droplet formation in *Trem2* knockout mice (Gouna et al., 2021). Similarly, in AD mouse models, microglia surrounding plaques harbouring the *Trem2*^{R47H} risk mutation also display reduced lipid droplet accumulation (Claes et al., 2021). These findings align with the role of *Npc2* as a positive regulator of lipid droplet formation. Therefore, the reduced *Npc2* expression observed in plaque-associated microglia of NLFTrem2^{R47H} mice may contribute to impaired lipid droplet formation in this context.

Cathepsins also play important roles in NPC2-related lysosomal function, as loss of cathepsin B and L causes cholesterol accumulation and upregulation of NPC1/2, mimicking the lysosomal storage pathology in NPC disease (Cermak et al., 2016). Similarly, in AD mouse models with *Npc1*-knockout, cathepsins B and D are significantly upregulated, potentially suggesting a compensatory response to lysosomal stress (Maulik et al., 2013). Finally, NPC, like AD, is one of the only other neurodegenerative diseases to form NFT pathology without mutations in *MAPT* (Nixon, 2004). This suggests that cholesterol trafficking defects, such as those resulting from *Npc2* knockdown, may promote tau pathology (Nixon, 2004). Moreover, the presence of tau pathology in NPC due to *Npc2* mutations, as well as in models of Cathepsin D knockout (Terron et al., 2024), points to a potential mechanistic link between TREM2 signalling, Aβ plaques, and NFTs.

Although a significant reduction in plaque-induced *Npc2* expression was seen in NLFTrem2^{R47H} mice, immunohistochemical analysis of NPC2 protein revealed no plaque-induced change of protein expression between NLF and NLFTrem2^{R47H} mice. This suggests the presence of compensatory post-translational mechanisms that preserve NPC2 protein expression in microglia despite reduced transcript levels. However, overall, I did observe a significant increase in NPC2 protein towards plaques, supporting the notion that the cholesterol transport function is reflected at the protein level surrounding plaques. The lack of significant increase in *Npc2* expression observed in the periplaque region, as measured by spatial transcriptomics, contrasts with the significant increase in NPC2 protein found at 10 µm from the plaque. The difference in results is likely due to the higher spatial resolution of the immunohistochemistry analysis, which samples NPC2 at 10 µm increments. In contrast, the spatial transcriptomics method uses larger 30 µm increments, which may dilute any increases that occur within the 10 µm range.

Lysosomal regulator Grn

Like the cathepsins and *Npc2*, *Grn* encodes a lysosome-associated protein, progranulin, a large glycoprotein composed of 7.5 tandem repeats of the GRN protein. Varying degrees of progranulin loss-of-function are associated with distinct neurological diseases. Full loss of progranulin function is linked to lysosomal storage diseases, haploinsufficiency is associated with frontotemporal dementia, and an SNP reducing progranulin function to around ~80% is connected to an increased risk of AD (Baker et al., 2006; Bellenguez et al., 2022; Huin et al., 2020; Sheng et al., 2014; Smith et al., 2012).

Although its exact role remains unclear, insights from *Grn*-deficient mice suggest that PGRN regulates several cellular processes. Here, *Grn* deficiency has been associated with increased lipofuscin accumulation, enhanced lysosomal staining in both microglia and neurons, associated lysosomal dysfunction, heightened microglial activation, neuronal loss, and a significant reduction in synapse density, which appears to be dependent on the complement system (Ahmed et al., 2010; Lui et al., 2016; Petkau et al., 2017; Root et al., 2024). Moreover, in the same paper implicating *Npc2* as a positive controller of lipid droplet formation, *Grn* deficiency had opposite effects, leading to increased lipid droplet formation in microglia (Marschallinger et al., 2020).

Progranulin is also known to be cleaved into individual granulin proteins within lysosomes by cathepsins (Cenik et al., 2012). A recent study has demonstrated that expression of individual granulin peptides in *Grn*-knockout mice substantially rescues lysosomal dysfunction and reverses the associated pro-inflammatory phenotype (Root et al., 2024). This suggests that the significant anti-inflammatory effects may not be due to the full-length progranulin molecule itself, but rather to the lysosome-mediated production of individual granulins.

Grn consistently shows increased gene expression in both neurons and microglia in response to Aβ plaque pathology (Chen et al., 2020; Keren-Shaul et al., 2017; Petkau et al., 2010; Satoh et al., 2014). Interestingly, a study directly comparing *Grn*- and *Trem2*-knockout microglia revealed opposing regulation of microglial transcriptional states. While *Trem2*-deficient microglia showed an increased homeostatic-like signature, *Grn*-deficient microglia showed a shift toward the DAM transcriptional state (Gotzl et al., 2019). This suggests that, under pathological conditions, an equilibrium may exist between *Trem2*- and *Grn*-driven transcriptional programs. Supporting this, in double *Grn*-*Trem2*-knockout mice, the DAM-like transcriptional phenotype induced by *Grn*-deficiency was attenuated by the absence of *Trem2*, indicating that the two genes converge on the same regulatory pathways

(Reifschneider et al., 2022). Together, these findings implicate *Grn*, *Npc2*, and cathepsin expression within the same process of lysosomal function, particularly in lipid homeostasis and the formation of lipid droplets. Furthermore, *Grn* may have functions beyond the lysosome in modulating the transcriptional states controlled by *Trem2*.

Phagosome-associated Plek

Of the *Trem2*-dependent genes, pleckstrin (*Plek*) is the least well-researched. In macrophages, pleckstrin localises to phagosomal membranes following the ingestion of opsonised particles, where it may coordinate phagosome formation (Brumell et al., 1999). In the context of AD, beyond its categorisation as a PIG gene (Chen et al., 2020), *Plek* expression has been shown to be upregulated in transgenic AD models, potentially driven by reduced levels of the regulatory microRNA miR-409-5p (Guo et al., 2019; Papazoglou et al., 2024). It is therefore likely that in plaque-contacting microglia, pleckstrin participates in a *Trem2*-dependent formation of the microglial phagosome after the phagocytosis of plaque-associated material.

Overall, the TREM2-dependent gene module activated in plaque-contacting microglia exerts coordinated control over phagocytic and lysosomal processes. This includes the opsonisation of targets for phagocytosis, the formation and maturation of the phagosome, degradation of ingested material within the lysosome, and the trafficking of lipids and cholesterol into lipid droplets (Figure 6.1). The increased AD risk associated with the $TREM2^{R47H}$ mutation may therefore result from disruption of this module, impairing microglial clearance, lipid homeostasis, and degradation.

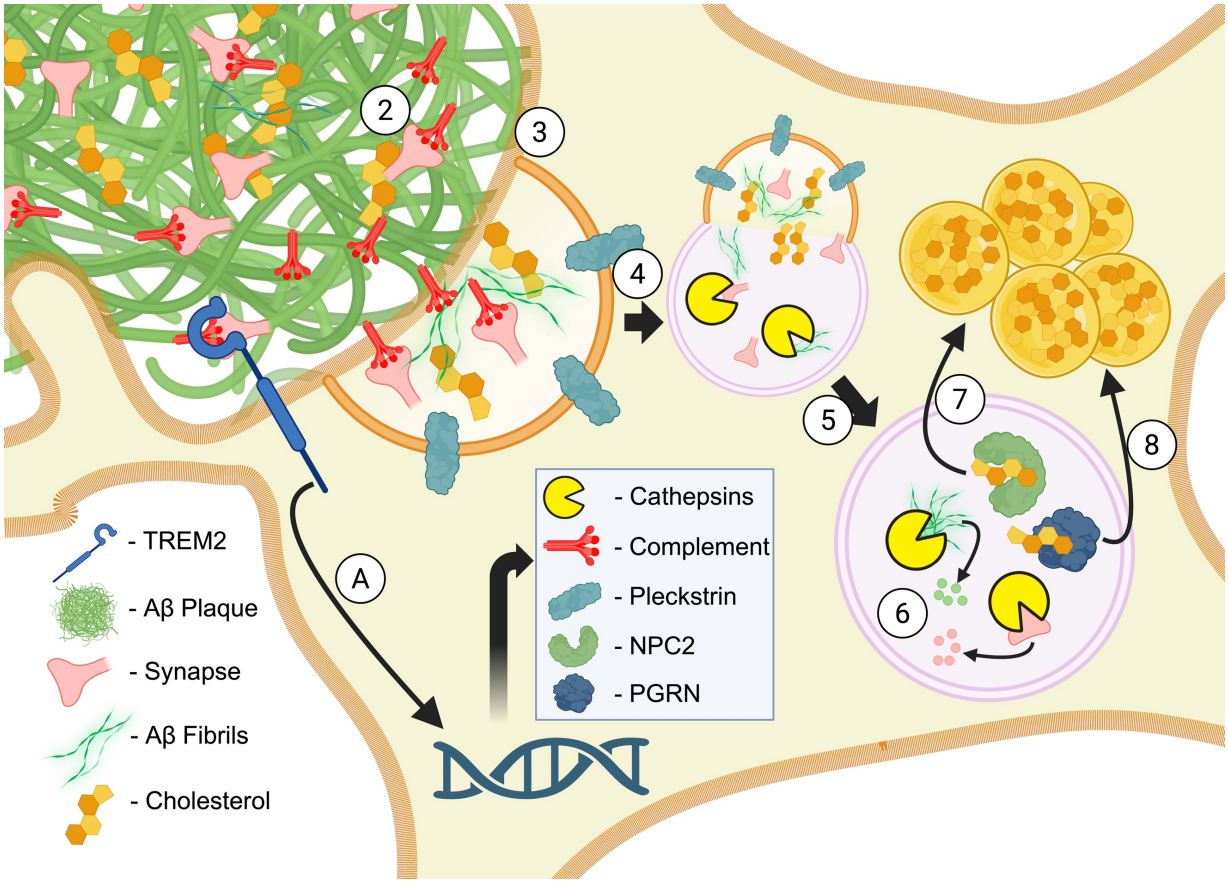

Figure 6.1 Proposed *Trem2*-dependent module functioning
(1) Activation of TREM2 by plaque-associated ligand results in increased gene expression of complement components *C1qa* & *C1qc*; cathepsins *Ctsz*, *Ctss*, *Ctsd*, & *Ctsb*; the cholesterol transporter *Npc2*, the lysosomal regulator *Grn*, and the phagosome-associated *Plek*. (2) Complement proteins opsonise Aβ aggregates and damaged synapses, marking them for phagocytosis. (3) Opsonised material, including Aβ fibrils and synapses, are internalised into a phagosome, with pleckstrin contributing to membrane and cytoskeletal remodelling. (4) The phagosome fuses with a lysosome to form a phagolysosome. (5) The mature lysosome contains cathepsins for proteolysis, as well as NPC2 and PGRN to support lipid metabolism and lysosomal homeostasis. (6) Cathepsins degrade engulfed Aβ fibrils and synaptic proteins. (7, 8) NPC2 and PGRN regulate the trafficking and sequestration of cholesterol into lipid droplets. Original diagram, Biorender.

6.4 APOE but not *Apoe* expression is disrupted by the *Trem2*^{R47H} mutation

Although microglial *Apoe* expression, in the NLF spatial transcriptomics analysis, increases progressively towards plaques, no significant difference was observed between the response of NLF and NLFTrem2^{R47H} mice. However, Apoe and Trem2 are frequently implicated in the same AD-associated mechanisms. For example, the *Trem2*-dependent gene module above is strongly enriched for genes involved in lipid metabolism and storage, which is a main function of APOE as both a lipid transporter and regulator of lipid droplet dynamics (Haney et al., 2024; Nugent et al., 2020). Furthermore, like *TREM2, APOE* genetic variants are linked to increased AD risk, with the APOE4 allele being the strongest genetic

risk factor for late-onset AD disease (Raulin et al., 2022). Moreover, APOE is a known ligand of TREM2, promoting intracellular processes including phagocytosis. The *Trem2*^{R47H} mutation has also been shown to reduce TREM2's binding affinity to APOE (Atagi et al., 2015). These converging lines of evidence suggest that impaired *Trem2,* via the *Trem2*^{R47H} mutation, may have implications on APOE beyond transcriptional regulation. In agreement with this, I showed that in NLF mice, there is a significant increase in plaque-associated APOE compared to NLFTrem2^{R47H} mice. Thus, functional *Trem2* promotes either APOE translation or inhibits its mRNA or protein breakdown. This result has also been similarly shown in human AD samples harbouring loss-of-function *TREM2* mutations, including the *R47H* mutation*,* presenting reduced plaque-associated APOE levels (Parhizkar et al., 2019). It should be noted that the immunohistochemical analysis of APOE had a larger sample size (n=~8) compared to the spatial transcriptomics analysis (n=~5). Consequently, the *Trem2*-dependent changes in plaque-associated *Apoe* expression may not be observed due to the smaller sample size in the spatial transcriptomics analysis.

This increase in APOE with functional *Trem2* may be associated with the highly studied role of Trem2 in plaque compaction (Yuan et al., 2016), as APOE has likewise been shown to facilitate both the initial seeding of Aβ plaques and their subsequent aggregation (Kaji et al., 2024; Ulrich et al., 2018). Therefore, TREM2- and APOE-dependent plaque compaction may work through a shared pathway. This idea of a common pathway is also supported by the known role of *Apoe* in the genetic regulation of similar pathways to *Trem2,* such as governing the shift from homeostatic to disease-associated microglia (Krasemann et al., 2017). Although the exact mechanisms remain unclear, it is likely that the overlapping pathways by which TREM2 and APOE regulate the microglial response to plaques further promote the expression of APOE. This finding also points to a limitation of the presented spatial transcriptomic experiment, whereby *Trem2*-dependent influence over microglial processes may extend beyond transcriptional regulation. Therefore, extensive proteomics with a similar experimental design in testing microglia contacting plaques is a future perspective.

6.5 Aβ pathology modulates the impact of *Trem2*^{R47H} on synaptic signalling

At an interstimulus interval of 25 ms, there was a significant interaction between Aβ pathology due to the *App* genotype (*NL* and *F* mutations) and the *Trem2*^{R47H} mutation. Here, post-hoc analysis revealed that NLFTrem2^{R47H} mice had a significantly greater paired pulse ratio than NLF and Trem2^{R47H} mice. Thus, the *Trem2*^{R47H} mutation in the presence of Aβ plaque pathology likely reduces the probability of glutamate release (Zucker and Regehr, 2002). This suggests a possible presynaptic dysfunction whereby microglia are inefficiently

removing plaque-induced damaged synapses due to the known reduced phagocytic capacity of *Trem2*^{R47H} harbouring microglia (Takahashi et al., 2005). This could then result in an accumulation of dysfunctional presynaptic terminals with reduced capacity to release neurotransmitter.

There was a similar trend (P<0.06) for an *App* and *Trem2*^{R47H} genotype interaction after LTP conditioning, whereby the direction of change compared to WT was for reduced LTP in Trem2^{R47H} and NLF mice; however, in NLFTrem2^{R47H} mice, there was no change. In NLFTrem2^{R47H} mice, there is likely a shift toward pro-inflammatory microglial signalling accompanied by reduced phagocytic activity (Keren-Shaul et al., 2017; Takahashi et al., 2005). This is also supported by the presented deficits in phagosomal and lysosomal pathway-associated genes in microglia surrounding plaques. While this may lead to an accumulation of aberrant synapses, the overall synaptic density may be more similar to that of wild-type mice, which could support preserved LTP. This finding is similar to the results from Hong et al. (2016), which demonstrated that C1q inhibition rescues oligomeric Aβ-induced LTP deficits, restoring LTP to control levels. Thus, the presented reduced plaque-associated expression of *C1qa* and *C1qc* in NLFTrem2^{R47H} mice may reflect impaired complement-mediated synaptic pruning, ultimately preserving synapses that would otherwise be lost through C1q-dependent mechanisms. Although this result may suggest a protective mechanism of the *Trem2*^{R47H} mutation when in the presence of Aβ pathology, the potential buildup of aberrant synapses may eventually result in larger network disturbances (Edwards, 2019).

Paired pulse ratios were also measured throughout the time course of the LTP experiment and revealed that, after LTP conditioning, again, there was a trend (P<0.06) for an *App* and *Trem2*^{R47H} genotype interaction. Similarly, the direction of change compared to WT was for an increase in release probability in Trem2^{R47H} and NLF mice after LTP; however, in NLFTrem2^{R47H} mice, there was no change. A tendency for increased probability of release after LTP conditioning has previously been observed in old NLF mice, whereby it is suggested that while LTP seems to enhance presynaptic mechanisms, disruption of postsynaptic mechanisms counterbalances this effect, resulting in no change in LTP (Benitez et al., 2021). Thus, with the addition of the *Trem2*^{R47H} mutation, the change in LTP expression towards enhanced presynaptic mechanisms and reduced postsynaptic mechanisms is disrupted. Given the risk associated with the *Trem2*^{R47H} mutation, the change towards LTP expression at the presynapse in NLF mice may therefore represent a microglial-mediated protective mechanism.

6.6 The *Trem2*^{R47H} mutation increases the density of small plaques

This thesis presented a consistent increase in the density of small plaques (<100 μm^2) with the introduction of the *Trem2*^{R47H} mutation in the hippocampus of 18-month-old NLF mice. Not only was this finding present in the initial Amytracker-defined plaques, but also in each of the plaque types: diffuse (Aβ+h-q-), fibrillar (Aβ+h+q-), and cored plaques (Aβ+h+q+). This is largely in agreement with the findings of the *Trem2*-dependent gene module, whereby the reduction of phagocytosis- and lysosomal-associated genes may prevent the ingestion and degradation of small plaques irrespective of plaque type. This finding also parallels studies showing a reduction of internalised fibrillar Aβ in *Trem2*-knockout microglia surrounding plaques (Wang et al., 2016). However, it seems once the plaques grow past about 100 μm^2, microglia are no longer effective in their clearance, potentially due to an inability to completely clear a large volume of Aβ. Here, the large accumulation of internalised Aβ may induce autophagic stress, ultimately driving microglial dysfunction, senescence, or cell death (Baik et al., 2016; Friedrich et al., 2010; Paresce et al., 1996).

This concept of autophagic stress also supports an alternative hypothesis for the observed increase in small plaques associated with the *Trem2*^{R47H} mutation, in which it promotes *de novo* seeding of Aβ plaques. In this hypothesis, the *Trem2*^{R47H}-induced disruption of lysosomal function, such as reduced cathepsin expression, impairs the degradation of internalised Aβ fibrils. The accumulation of Aβ within the acidic lysosomal lumen may facilitate fibril aggregation into Aβ seeds, which are then exocytosed back into the extracellular space (Friedrich et al., 2010; Paresce et al., 1996; Su and Chang, 2001). Alternatively, progressive lysosomal disruption in *Trem2*^{R47H} mutants could lead to microglial cell death, releasing undigested Aβ aggregates into the surrounding tissue, thereby contributing to further plaque formation (Baik et al., 2016). Therefore, the increase in small Aβ plaques could represent microglial deposited Aβ seeds.

Other studies attempting to delineate the impact of impaired *Trem2* on Aβ plaque load have found mixed results depending on the age of testing and the model used. Increases in plaque burden have been found at earlier time points (Meilandt et al., 2020; Wang et al., 2015b), while reductions in plaque load have been reported in older mice (Meilandt et al., 2020). In contrast to the current study, these investigations used models with transgenic overexpression of APP, which do not capture the gradual, age-dependent progression of Aβ pathology (Jankowsky and Zheng, 2017; Saito et al., 2016). Moreover, the level of plaque deposition in aged NLF mice, as in this study, is comparable to that seen in much younger transgenic models (Saito et al., 2014). Thus, when comparing animals at equivalent stages of plaque severity, the observed increase in plaque density due to *Trem2* impairment is

consistent across models. It is possible that if NLF mice were aged beyond 18 months, a similar shift toward reduced plaque burden might also be seen.

Several studies have reported that TREM2 influences plaque compaction, with *Trem2* deficiency leading to a shift towards more diffuse plaque morphology (Meilandt et al., 2020; Wang et al., 2015b; Yuan et al., 2016). In contrast, the present findings indicate that the *Trem2*^{R47H} mutation exerted a comparable effect across all plaque types, with no clear shift towards increased diffuse plaque types. While this discrepancy may reflect differences in the AD mouse models used or the age at testing, it is more likely attributable to methodological differences. Specifically, previous results assessing plaque 'diffuseness' typically analysed individual plaque morphology rather than categorising plaques. Therefore, it remains possible that the *Trem2*^{R47H} mutation in this study increased the diffuse Aβ halo surrounding fibrillar or cored plaques, which would not be captured by plaque classification analysis.

6.7 Plaque contact is required for the microglial response to Aβ plaques in human AD

In the NLF mouse model, I conducted a hypothesis-driven analysis using a previously defined gene set showing increased expression with increasing plaque density in NLGF mice (Chen et al., 2020). While this approach did not identify novel genes, it provided enhanced spatial resolution, demonstrating that the expression of PIGs in microglia is dependent on the distance to plaques and plaque contact. In contrast, for the human experiment, there have been many studies suggesting a lack of translation from mouse to human experiments, especially in the microglial DAM transcriptional state (Mathys et al., 2019; Srinivasan et al., 2020). Moreover, spatial transcriptomic analyses of plaque-associated gene expression in human AD tissue are still lacking, and as such, a gene set for validation does not currently exist.

Of the 38 PIGs identified as significantly upregulated in NLF mice, 18 were also significantly increased in plaque-contacting microglia compared to away microglia in the human spatial transcriptomics dataset (Figure 6.2). These genes were *B2M, C1QA, C1QB, C1QC, CTSS, FCER1G, GRN, LAPTM5, LGMN, LY86, APOE, CTSB, CTSD, CTSZ, HEXA, NPC2, TREM2,* and *TYROBP*. Thus, this group of genes show consistent upregulation in NLGF mice with increasing plaque load (Chen et al., 2020) and in microglia located towards plaques in both NLF mice and human AD tissue. Consequently, they likely represent critical microglial genes that are important in the response to plaques. Only one PIG gene, *CTSH*, was significant in the human analysis and not in the NLF analysis (Figure 6.2).

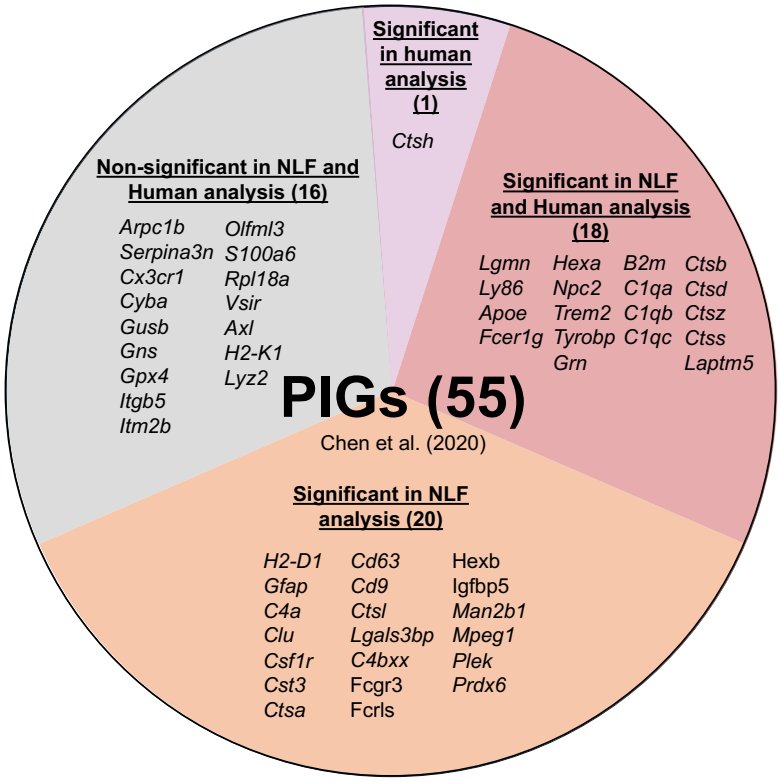

Figure 6.2 PIG genes in the NLF and human tissue analysis

The 55 plaque-induced genes (PIGs) split based on their statistical significance in the microglial-enriched- NLF mouse spatial transcriptomic data (Chapter 3) and human AD spatial transcriptomic data (Chapter 4).

Notably, this set of 18 genes included all genes from the previously described *Trem2*-dependent module described in the NLF experiment, except for pleckstrin (*PLEK*). This suggests that the TREM2-dependent gene module is active in plaque-associated microglia in human AD. However, as the human dataset lacked samples carrying the $TREM2^{R47H}$ variant, it remains unclear whether the activation of this module is similarly *TREM2*-dependent in the context of human AD.

As in the NLF experiment, genes that varied with distance from plaques could be categorised based on their spatial expression pattern. These categories were: plaque response, graded response, periplaque response, and combined plaque and periplaque response. All of these genes could be split between genes that were upregulated or downregulated towards plaques. The ligands driving these spatial responses are therefore likely to differ in their distribution relative to plaques. As with the interpretation of the NLF findings, plaque-specific responses may be triggered by ligands concentrated within plaques such as lipid species, damage-associated molecules like phosphatidylserine, or plaque-

associated proteins such as APOE (Atagi et al., 2015; Huang et al., 2021; Wang et al., 2015b). In contrast, genes displaying a graded response toward plaques may reflect activation by diffusible factors forming concentration gradients, such as cytokines and chemokines potentially released by plaque-associated microglia or otherwise diffusing from the plaque itself (Wang et al., 2015a).

Within the plaque-only response category, there was an enrichment of genes that play similar roles to those in the *Trem2*-dependent module from the NLF experiment. These genes were associated with ontology terms related to phagocytosis, lysosomal function, and lipid metabolism. Examples included complement components *C1QB* and *C1QC*, the TREM2 signalling adaptor *TYROBP*, lipid transporters such as *APOE* and *APOC1*, and lysosomal regulators including *GRN*, *LAPTM5*, *CD68*, and the lysosomal lipase *LIPA*. These findings suggest that plaque-contacting microglia play key roles in the ingestion, degradation, and storage of plaque-associated material, particularly lipids. A similar enrichment of lipid metabolism and phagocytic pathways was observed among genes that gradually increased in expression towards the plaque. This included genes involved in lipid droplet regulation, such as *NPC2*, *PLIN2*, *FITM2*, and *SOAT1*, further supporting the idea that microglial lipid processes play an important role in plaque-associated responses. An increased phagocytic response at plaques has been widely observed, with synapses and Aβ identified as main targets (Condello et al., 2015; D'Andrea et al., 2004; Tzioras et al., 2023). In addition to the gene expression findings presented in this thesis, other studies have also reported a corresponding upregulation of phagocytosis-related genes in association with Aβ plaque pathology (Das et al., 2024). As well as Aβ and associated damage, plaques are also enriched in lipid species, particularly cholesterol (Burns et al., 2003; Michno et al., 2024), and lipid uptake and storage into lipid droplets have been shown in plaque-associated microglia (Wu et al., 2025). Consistently, lipid-processing genes have also been shown to be upregulated in microglia in response to Aβ pathology (Das et al., 2024).

It is important to note that, unlike in the mouse experiment, the human study employed a dye specific to fibrillar Aβ plaques, as Aβ antibodies were ineffective on human tissue following protein digestion required by the GeoMx protocol. As a result, a halo of non-fibrillar Aβ likely surrounds the fibrillar core identified by the dye (Koffie et al., 2009). Consequently, the periplaque regions in the human samples may contain higher concentrations of Aβ than the periplaque regions in the mouse experiment, where both fibrillar and non-fibrillar forms were detected. This methodological difference likely contributed to the observed discrepancies in plaque-associated gene expression between the two species. For example, in the mouse experiment, *Trem2* expression was elevated specifically in plaque-contacting microglia,

whereas in human tissue, *TREM2* expression increased gradually towards plaques. These findings suggest that Trem2 expression in microglia may be responsive to the Aβ halo surrounding plaques, rather than exclusively to fibrillar Aβ. Alternatively, the pattern may reflect species-specific regulation of TREM2 expression in response to Aβ plaque pathology.

The human spatial transcriptomics dataset provides unique insight into tissue that harbours tau pathology developed from Aβ pathology, which cannot currently be modelled in mice with AD-associated genetic changes. Therefore, investigating the gene expression changes towards plaques may provide important clues about potential mechanisms of Aβ plaque-induced tau pathology.

As well as being implicated in Aβ pathogenesis, elevated cholesterol, particularly the stored esterified form of cholesterol in lipid droplets, has been linked to increased tau phosphorylation, with these effects mitigated by cholesteryl ester-lowering treatments (van der Kant et al., 2019). Consequently, the upregulation of genes associated with phagosomal, lysosomal, and lipid droplet pathways, such as *NPC2*, *PLIN2*, *FITM2*, *SOAT1*, *GRN*, *LAPTM5*, *CD68*, *APOE*, and *APOC1*, may point to a potential role for these processes in tau pathogenesis. In line with this, a recent study investigating *Grn*-deficiency in tau transgenic mice showed an increase in tau phosphorylation (Takahashi et al., 2024). Likewise, the upregulation of lysosomal cathepsins, particularly CTSD, as discussed in the context of plaque-induced genes in NLF mice, is notable, given that *Ctsd*-deficient mice exhibit marked increases in tau phosphorylation and the development of tau tangles (Terron et al., 2024). An additional relevant gene that increases at plaque in the human tissue analysis is *P2RX7.* This gene encodes the P2RX7 protein, a microglial ATP-gated receptor resulting in the activation of the NLRP3 inflammasome. Here, *P2RX7* expression has been shown to positively correlate with increasing Braak stage in human AD and increasing age in transgenic tau mouse models. Furthermore, *P2RX7* mRNA has been shown in other studies to increase around plaques in microglia. In support of a pathological role, pharmacological Inhibition of *P2rx7* in organotypic slices of tau transgenic mice resulted in decreased levels of insoluble tau (Beltran-Lobo et al., 2023).

Genes that are downregulated near Aβ plaques may also offer important insights into tau-related mechanisms. Notably, this includes *AQP4* and *AQP1*, both are water-selective transporters critical to the function of the glymphatic system, which facilitates waste clearance. A decline in AQP4/1 near plaques may therefore impair the removal of phosphorylated tau and Aβ, contributing to pathological accumulation. This is supported by studies demonstrating that pharmacological inhibition or genetic knockout of *Aqp4* reduces

tau clearance and increases Aβ plaque burden (Harrison et al., 2020; Pedersen et al., 2023). Interestingly, AQP4-dependent processes are also sensitive to lipid disruption, as mice receiving a high-fat diet show reduced glymphatic Aβ clearance that is rescued through pharmacological activation of AQP4 (Peng et al., 2024). Therefore, the lipid-rich plaque environment and dysregulation of lipid processes by plaque-contacting microglia may influence efficient glymphatic clearance. Although AQP4 is predominantly expressed on astrocytic endfeet, and while it is therefore unlikely to be microglial-associated in this study, its altered expression has important implications for AD pathogenesis. Interestingly, spatial transcriptomic data from the astrocyte-enriched regions of the NLF mouse model show increased *Aqp4* expression at plaques (Wood et al., 2022), which contrasts with the decrease observed in human AD tissue. This species difference may help explain why Aβ-induced tau pathology is not present in Aβ plaque-bearing mice due to more effective glymphatic clearance.

It is worth noting that expression of *PSEN1* (γ-secretase subunit), *APP* (amyloid precursor protein), and *MAPT* (encoding tau) all decrease towards Aβ plaques in the human spatial transcriptomic analysis. While this reduction could suggest a protective downregulation of genes involved in the AD pathogenic processes, as these genes are primarily neuronal, their loss likely reflects the loss of neurites around plaques (Shah et al., 2010). Similarly, the downregulation of myelin-associated genes, including *MBP*, *MAG*, and *MOBP*, may indicate a selective vulnerability of myelin to plaque-associated pathology compared to a broader loss of axons. Therefore, additional imaging studies are needed to distinguish between selective vulnerabilities and total neurite loss around plaques.

6.8 Plaque age is an important determinant of local gene expression

The staging of AD pathology reveals a delay between the initial deposition of Aβ plaques and the onset of NFTs and cognitive decline (Josephs et al., 2008; Morris et al., 2014). Traditionally, Aβ plaque pathology is assessed by overall plaque density, with the possibility that once plaque load reaches a certain threshold, widespread toxicity eventually drives NFT formation and cognitive symptoms. An alternative hypothesis suggests that this delay reflects the maturation of individual plaques over time. In this model, newly formed plaques are relatively inert but gradually become more toxic, suggesting that their pathological impact depends on their age rather than their collective density. To delineate the impact of plaque age, I employed a ^{15}N stable isotope diet to timestamp the early deposited plaques; the diet was reversed back to a ^{14}N diet in older ages. The relative abundance of ^{15}N in the Aβ42 peptide, quantified by weight via mass spectrometry, served as a timestamp, with higher ^{15}N content indicating older plaques. This stable isotope labelling approach has

previously been used in AD mouse models to temporally assess Aβ species at individual plaques (Michno et al., 2021) and to examine proteome turnover in whole-brain tissue across different AD models (Hark et al., 2021). However, the specific impact of plaque age on the surrounding tissue microenvironment remained unexplored.

Correlating plaque age with gene expression revealed that genes involved in metabolic processes and ion channel activity increase in expression as plaques age. This includes ATP synthase subunits (*Atp5a1* and *Atp5*) as well as Complex IV-related genes such as the assembly factor *Coa6* and the structural subunit *Cox7a2*. Mitochondrial dysfunction is a hallmark of AD pathology, with multiple studies implicating disruptions in neuroinflammatory signalling (Lautrup et al., 2019), oxidative stress (Andersen, 2004; Gan et al., 2014), and, similarly, respiratory chain activity (Maynard et al., 2015). Overall, this results in hypometabolism and reduced ATP levels in AD brains (Cha et al., 2015; Mosconi et al., 2008; Zhang et al., 2015). Furthermore, even before the development of pathology, mitochondrial-associated genes, including those associated with complex IV, show reduced expression in the hippocampus of AD mouse models (Navarro et al., 2020). This is in contrast to the observed upregulation of respiratory chain genes around older plaques. This, therefore, may reflect increased local metabolic demand, potentially driven by plaque-associated cell types such as microglia and astrocytes. Supporting this, while ATP5A1 expression is reduced in bulk AD tissue (Cha et al., 2015), the protein is seen to accumulate at Aβ plaques (Yue et al., 2021). Beyond its canonical role in ATP synthesis, ATP5A1 has also been shown to exert anti-inflammatory effects by directly binding to and neutralising LPS, an inflammatory molecule found within plaques (Yue et al., 2021).

I also present an increase in expression with plaque ageing of the potassium channel genes *Kcnj2* and *Kcna*. Although the loss of neurites surrounding plaques might suggest a reduction in neuronal potassium channel expression, the upregulation of these genes may instead reflect microglial changes. *Kcnj2*, which encodes the inwardly rectifying potassium channel Kir2.1, is notably upregulated in DAM, a microglial activation state that is responsive to Aβ pathology (Keren-Shaul et al., 2017). This is consistent with the roles of Kir2.1 and *Kcna* encoding Kv1.1 in regulating microglial membrane potential, a key modulator of the inflammatory response (Laprell et al., 2021). Kir2.1 expression has been shown to increase following stimulation with the anti-inflammatory cytokine IL-4 (Nguyen et al., 2017), while Kv1.1 is upregulated in response to damaging stimuli such as hypoxia and LPS exposure (Wu et al., 2009). Together, these findings suggest that increased *Kcnj2* and *Kcna* expression may represent a disease-associated microglial response that becomes more prominent as plaques age and mature.

Genes negatively correlated with plaque age were predominantly associated with neuronal compartments and dendritic spines. Notably, this included *Chrna9* and *Chrna7*, which encode subunits of the acetylcholine receptor critical for cholinergic transmission. The progressive degeneration of cholinergic afferents is a well-established feature of AD pathology (Davies and Maloney, 1976), and cholinesterase inhibitors remain a key component of symptomatic treatment (Dubois et al., 2015; Hampel et al., 2018; Summers et al., 1986). More recently, the loss of cholinergic projections has been directly linked to their proximity to Aβ plaques (Lee and Chen, 2024). Beyond cholinergic systems, markers of synaptic transmission consistently decline in AD models, particularly in the regions immediately surrounding plaques (Bittner et al., 2012; Spires et al., 2005). This is consistent with the hypothesis that microglia actively phagocytose dystrophic neurites near plaques (Tzioras et al., 2023). The plaque age-associated decline in synaptic gene expression also aligns with SILK proteomic studies showing impaired turnover of synaptic proteins from plaque extracts (Hark et al., 2021). Importantly, this gradual loss of synaptic gene expression may help to explain the gap between plaque deposition and the development of NFTs, where cumulative synaptic damage could drive network dysfunction and downstream tau pathology (Edwards, 2019). It should be emphasised that this experiment was not a study of the genetic changes caused by plaque presence alone, as all ROIs analysed contained plaques. Instead, what distinguishes the current study is the insight that changes in synaptic and metabolic gene expression reflect the maturation of the plaques over age.

6.9 Plaque type development over chronological age

The widely referenced diffuse, fibrillar, and cored plaque types have traditionally been categorised based on their morphological appearance (Dickson and Vickers, 2001). Such classifications rely on subjective visual assessment, making the process time-consuming and often lacking in quantification. Here, I present an advancement in plaque categorisation methods using a combined staining approach of an Aβ antibody, a fibrillar Aβ-specific dye (hFTAA), and a plaque core-specific dye (qFTAA). Based on the presence or absence of these three markers, plaques were categorised into three types: Aβ+h+q+, Aβ+h+q-, and Aβ+h-q-, which likely correspond to the morphologically defined dense-cored, fibrillar, and diffuse plaques, respectively. This allowed the analysis of all plaques within the hippocampus over many sections, resulting in thousands of analysed plaques per group.

A surprising finding was that in 9-month-old NLF mice, which represents the age of initial hippocampal plaque deposition, ~80% of plaques (by number) were fibrillised (cored or fibrillar plaques) with just under half of these already having qFTAA positivity, indicative of a

core. We have seen similar results in a previous stable isotope labelling study on the NLGF model, suggesting that plaques initially precipitate as small, dense deposits(Michno et al., 2021). Unexpectedly, however, the proportion of diffuse plaques increased with chronological age. By 18 months, ~80% of plaques were diffuse, suggesting that many of the later-formed plaques do not follow the trajectory of initial core formation. These findings contrast with the commonly proposed sequence whereby diffuse plaques are deposited first, followed by more compact, fibrillar structures (Thal et al., 2006). One possible explanation is that young NLF mice have the capacity to rapidly aggregate the overexpressed Aβ42 into compact plaque seeds. In contrast, older mice may experience a saturation of this Aβ seeding and compaction mechanism due to persistently high Aβ42 levels. This discrepancy may be explained by microglial involvement in plaque compaction. In younger animals, lower levels of Aβ42 may be efficiently sequestered by microglia, aggregated within acidic lysosomes, and redeposited into the extracellular space as compact plaques (Baik et al., 2016; Huang et al., 2021). In older mice, however, the sheer volume of Aβ42 likely overwhelms microglial capacity, leading to incomplete aggregation and increased deposition of diffuse plaques. Additionally, prolonged Aβ42 sequestration may induce autophagic stress, contributing to microglial dysfunction and senescence at older ages (Baik et al., 2016). This hypothesis is supported by several studies showing that microglial phagocytic capacity declines with age and inflammation. For example, microglia from younger mice exhibit greater phagocytic ability than those from older animals (Daria et al., 2017; Hellwig et al., 2015), and in the absence of microglia altogether, Aβ plaques tend to be less compact (Kiani Shabestari et al., 2022).

The presence of all three plaque types among the earliest deposited plaques supports the notion that plaque morphology is determined by the characteristics of the initial Aβ seed, with each type developing independently rather than through a shared progression. One study similarly demonstrated that plaque seeds from mice predominantly forming cored plaques give rise to cored plaques when introduced into other mouse models, and similarly, seeds from mice producing mainly diffuse plaques induce diffuse plaques (Xu et al., 2022). Furthermore, in familial forms of AD, plaque morphology is seemingly genetically determined; for example, individuals with PSEN1 mutations typically develop diffuse plaques that do not progress into other plaque types (Miki et al., 2019). In contrast, recent results from the Hanrieder lab suggest that the SILK-determined plaque age positively correlates with increasing qFTAA fluorescence compared to hFTAA, suggesting that plaques progress to a more aggregated state at the centre of a plaque over age (Figure 6.3, Wood et al., 2024). This progression of aggregation may indicate a potential for fibrillar plaques to slowly aggregate over time. However, as this measurement of aggregation is based solely on

hFTAA and qFTAA fluorescence and does not account for overall Aβ intensity, the development of diffuse plaques remains unknown and may still develop independently of fibrillar and cored plaques.

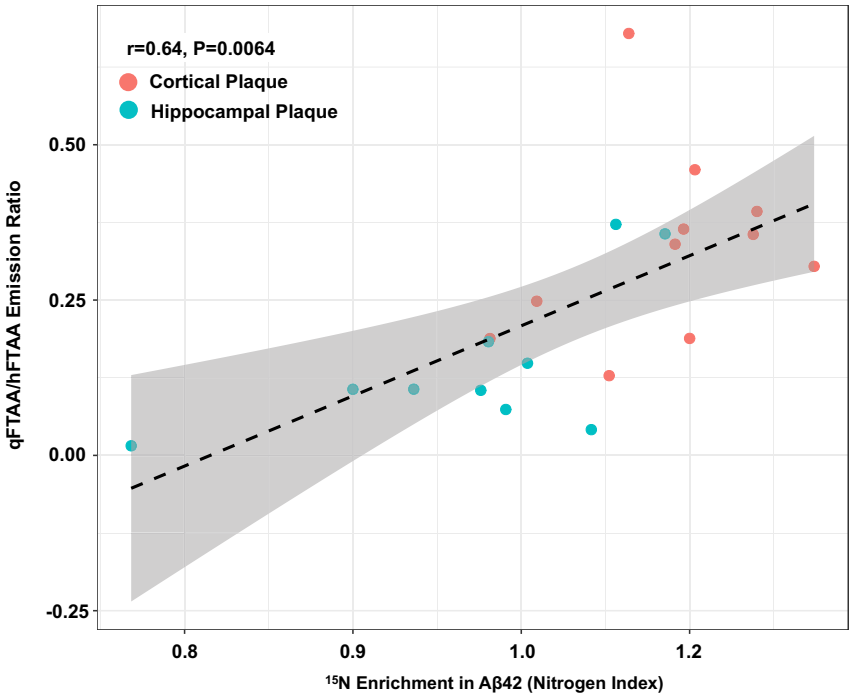

Figure 6.3 Plaques aggregate over age
Unpublished data from the Hanrieder Lab demonstrating a positive correlation between plaque age, quantified by ^{15}N enrichment, and plaque aggregation, measured by the emission intensity ratio of qFTAA to hFTAA. Combined data points from n=3 18-month-old NLF mice.

In addition to changes in the relative proportions of plaque types across chronological age, all plaque types exhibit increased density over time. Both Aβ+h+q+ (cored) and Aβ+h+q- (fibrillar) plaques also show a progressive increase in average size with age. In contrast, Aβ+h-q- (diffuse) plaques appear not to grow substantially. However, this likely reflects a marked increase in the density of very small deposits, which masks any size increase among a minority of larger Aβ+h-q- (diffuse) plaques. This pattern is exemplified in the histogram of 18-month-old NLFs, where large Aβ+h-q- deposits are present but are vastly outnumbered by small deposits. These findings suggest that, despite shifts in plaque type distribution, plaque formation and plaque growth continue throughout ageing.

6.10 Plaque type is a key determinant of local toxicity and synapse loss

The findings of this thesis demonstrate that as plaques age, there is a progressive decline in the expression of synapse-associated genes. Furthermore, as individual plaques are associated with progressive aggregation as they age (Figure 6.3), I set out to test the

influence of plaque type, as defined through aggregation state, on surrounding tissue. Cored plaques have been consistently associated with local synapse loss (Spires et al., 2005; Spires-Jones et al., 2007; Tsai et al., 2004). In contrast, while the idea of a lack of synapse loss around diffuse plaques is frequently cited, the supporting evidence remains limited, as most studies rely on amyloid-binding dyes that do not distinguish diffuse plaques. I conducted a comprehensive analysis of postsynaptic loss, using HOMER1 as a marker, which revealed that higher plaque aggregation is associated with greater local synapse loss. Notably, diffuse plaques showed no detectable loss of postsynapses. This relationship between increasing structural aggregation and synaptotoxicity is consistent with previous studies of thioflavin-defined plaques (Koffie et al., 2009; Masliah et al., 1990; Spires et al., 2005).

This synapse loss is likely due to the presented increase in local toxicity associated with higher plaque aggregation, with cored plaques exhibiting the highest levels of autophagic stress, as indicated by elevated LAMP1 levels, and the greatest accumulation of dystrophic synapses, as measured by increased NPTX2 levels. These findings align with observations in cognitively unimpaired individuals with CU-AP, where diffuse plaques are associated with minimal neurotoxicity and no measurable cognitive decline (Dickson et al., 1992; Malek-Ahmadi et al., 2016). Furthermore, the finding of increased neurotoxicity with increasing aggregation is also consistent with studies showing that a higher propensity for Aβ aggregation and the presence of dense cored plaques are associated with increased progression of clinical dementia (Liu et al., 2022; Murray and Dickson, 2014; Rijal Upadhaya et al., 2014; Serrano-Pozo et al., 2016). In line with this, Aβ-induced toxicity has been shown to trigger microglial-mediated synapse removal through engulfment (Hong et al., 2016). An alternative explanation for synapse loss around more aggregated plaques is steric hindrance, the physical displacement of neuronal processes by plaques. This has been visualised as dendrites bending around plaques (Spires et al., 2005). More highly aggregated, and therefore denser, plaques may exert greater structural interference, contributing to more pronounced synaptic displacement or loss. However, I did not observe an increase in HOMER1 density in the periplaque regions, which might have been expected if synapses were being displaced rather than lost.

In contrast to the observed increase in NPTX2 towards plaques, CSF levels of NPTX2 are known to decline in several neurodegenerative and psychiatric conditions, including schizophrenia (Xiao et al., 2021) and AD (Libiger et al., 2021; Xiao et al., 2017), but also throughout normal ageing (Soldan et al., 2019). The exact cause of NPTX2 decline with AD progression remains unclear, but given that NPTX2 primarily functions at pyramidal-to-PV

interneuron synapses, Aβ-induced disruption of this pathway likely contributes to its reduction (Ali et al., 2019; Xiao et al., 2017), with NPTX2 overexpression shown to rescue this impairment in AD models (Papanikolaou et al., 2025). Conversely to the AD-associated loss, NPTX2 has also been observed to increase in dystrophic neurites surrounding plaques (Abad et al., 2006; Cummings et al., 2017). Moreover, in NPTX2-deficient mice, plaque-induced synapse loss is more severe, with an increase in synaptic puncta seen engulfed within microglia (Zhou et al., 2023). This protective function of NPTX2 appears to be dependent on a functioning complement system, and given that neuronal pentraxins are known to bind complement proteins, NPTX2 is likely acting as an inhibitor of complement-mediated synaptic engulfment by microglia (Nauta et al., 2003; Zhou et al., 2023). Therefore, the increase in NPTX2 surrounding plaques is likely to be a protective mechanism preventing the inadvertent elimination of synapses.

The increase in NPTX2 staining around cored plaques was significantly reduced in NLFTrem2^{R47H} compared to NLF mice. Reflecting a potential loss of the NPTX2-dependent synapse-protective mechanism, potentially rendering synapses more vulnerable to degeneration with the *Trem2^{R47H}* mutation. However, no corresponding increase in synaptic loss or local autophagic stress was detected in NLFTrem2^{R47H} mice. An alternative explanation is that, since NPTX2 inhibits complement-mediated synapse removal (Zhou et al., 2023), the reduced expression of complement genes in NLFTrem2^{R47H} mice may diminish the need for compensatory NPTX2 expression at synapses. In contrast to the increase in NPTX2 levels observed at plaques, I found a significant negative correlation between *Nptx2* expression and plaque age in the SILK spatial transcriptomic experiment. This decline in *Nptx2* transcription likely reflects progressive synapse loss over time, reducing local synaptic gene expression. However, the remaining synapses appear to be preserved and maintain NPTX2 positivity, consistent with its proposed protective role against C1q-dependent synaptic engulfment.

Recent work from the Edwards Lab analysing the same structurally defined plaque types revealed a significant increase in phosphorylated tau around cored plaques compared to diffuse plaques (Desai et al., 2024). This finding likely reflects the increased toxicity associated with cored plaques, as demonstrated in this thesis. This finding offers a potential explanation for the step between Aβ plaque deposition and the onset of tau pathology. Specifically, it suggests that plaques must reach a structurally mature, cored morphology before triggering the next step of the amyloid cascade of tau phosphorylation and tangle formation.

While this thesis assesses plaque-induced toxicity through multiple complementary measures, including autophagic stress (LAMP1), synaptic damage (NPTX2), and synaptic loss (HOMER1), these remain indirect proxies of toxicity. More direct markers of dystrophic neurites may provide clearer insights into the mechanisms of neuronal injury. For example, as previously discussed, staining for hyperphosphorylated tau offers a measure of downstream tau pathology that could help bridge the link between Aβ deposition and tangle formation (Desai et al., 2024). In addition to tau hyperphosphorylation, other markers of neuritic pathology, such as neurofilament light chain and ubiquitin, have been used to characterise axonal injury and neuritic plaques, and may serve as valuable complementary indicators of toxicity (Hyman et al., 2012). Taken together, integrating synapse-focused measures with these broader measures of neuritic pathology would, in future studies, provide a more comprehensive understanding of how different plaque types exert toxicity on the surrounding neural tissue.

The specific properties that explain the varying levels of synapse loss and toxicity among different plaque types remain poorly understood. A possibility raised by this thesis is that plaque-associated toxicity may take time to develop, with prolonged aggregation contributing to the differences seen between plaque types. Although Aβ42 is considered the most synaptotoxic Aβ species (Kuperstein et al., 2010), the diffuse plaques analysed here, which are primarily composed of Aβ42 (Iwatsubo et al., 1996), did not show detectable synapse loss. In contrast, cored plaques, which exhibited greater synaptotoxicity, are known to contain relatively higher levels of Aβ40 (Iwatsubo et al., 1994). This suggests that Aβ species alone may not determine toxicity. Lipidomic profiling has revealed that specific ceramide and ganglioside species are enriched in cored plaques (Enzlein et al., 2024; Ge et al., 2023). However, it remains unclear whether these lipids accumulate as a result of amyloid aggregation or actively contribute to plaque maturation. The functional impact of distinct lipid species on surrounding tissue is also not well defined, though certain ceramides have been implicated in metabolic disruption (Kalkman and Smigielski, 2025), and gangliosides have been linked to synapse loss (Herzer et al., 2018). Finally, Aβ oligomers are widely regarded as the most neurotoxic form of Aβ, capable of inducing synapse loss (Hong et al., 2016), impairing neuronal signalling, and triggering cell death (Hughes et al., 2020). Plaques have been hypothesised to act as reservoirs for toxic oligomers and consequently release them into the surrounding tissue (Bigi et al., 2022), with the toxicity of Aβ oligomers being conformation-dependent (Ashe, 2020). Nevertheless, there remains a lack of data investigating oligomer composition and conformation across different plaque types.

6.11 Conclusion

Overall, this work provides an in-depth spatially resolved understanding of the impact of Aβ plaques on surrounding tissue. Through spatial transcriptomic analyses in both an aged NLF mouse model and human AD tissue, I show that direct contact with plaques is essential for the expression of many AD-associated genes. In NLF mice, this response includes a *Trem2*-dependent module involved in phagosomal, lysosomal, and lipid-associated genes, which is disrupted by the *Trem2*^{R47H} AD-risk mutation. This highlights the importance of intact TREM2 signalling in the microglial response to plaques and potentially explains the AD risk associated with the *TREM2*^{R47H} mutation. Furthermore, despite the aberrant reduction in *Trem2* expression in Trem2^{R47H} mice, this model remains important in investigating the consequences of *Trem2* impairment. A similar microglial transcriptomic response to Aβ plaques was seen in human AD tissue, highlighting the NLF's ability to model plaque-induced changes despite the absence of overt cognitive decline or tau pathology (Saito et al., 2014). I further show that plaque age, not chronological age, is a key determinant of surrounding gene expression, with older plaques associated with increased metabolic gene expression and decreased synapse-associated genes. This may help to explain the gap between initial Aβ deposition and downstream events such as cognitive decline and tau pathology. In short, Aβ plaques may need time to become toxic. In support of this, plaque type, defined by aggregation state, is a significant determinant of the impact on surrounding tissue. Here, cored plaques, the most aggregate plaque type analysed, were associated with the greatest synapse loss and highest levels of surrounding toxicity. In contrast, diffuse plaques did not exhibit detectable synapse loss. These findings emphasise that plaque heterogeneity is an important factor in disease progression.

6.12 Future perspectives

While the spatial transcriptomic study in NLF mice offered important insights into the plaque-dependent regulation of known plaque-induced genes (PIGs) in microglia, it did not identify any novel gene candidates beyond this predefined set. Ongoing work in the Edwards Lab is investigating whole-transcriptome spatial data of microglial gene expression changes in relation to plaques. This approach may reveal novel genes involved in the microglial plaque response and allow for a more robust comparison with the genes emerging from the human AD spatial transcriptomic dataset.

A key finding across the spatial transcriptomic analyses of both NLF mice and human AD tissue is the consistent upregulation of lipid-associated genes in microglia in direct contact with plaques. This lipid-related transcriptional signature is further supported by the *Trem2*-dependent gene module, which highlights a gene set dependent on functional TREM2 for

the expression of genes involved in lipid processing. Therefore, as part of the Hanrieder x Edwards Lab collaboration, I have previously employed MALDI imaging to map the spatial distribution of many lipid species within the hippocampus and cortex of NLF and NLFTrem2^{R47H} mice. Ongoing analysis of this data may identify lipid species whose localisation or abundance depends on functional TREM2. Moreover, by overlaying this data with histochemical staining of Aβ, hFTAA, and qFTAA, I will be able to distinguish lipids across the three structurally defined plaque types. This approach may uncover specific lipid species that contribute to the differential toxicity associated with plaque type.

Similarly, further research is needed to evaluate how different plaque types influence the surrounding glial response. I am currently supervising a student project investigating microglial density and lipid droplet accumulation around the three structurally defined plaque types in NLF mice, both with and without the *Trem2^{R47H}* mutation. This work will generate data on the relative toxicity of cored versus diffuse plaques by assessing microgliosis and microglial dysfunction linked to lipid load. To build on this, and in keeping with the approach of this thesis, using microglial-enriched spatial transcriptomic analysis surrounding each plaque type would provide insights into the gene expression changes and mechanisms associated with the presented toxicity.

Finally, further investigation of the human AD spatial transcriptomics dataset is essential. While this thesis has revealed microglia-associated gene expression changes in relation to plaque proximity, the available samples can also be stratified by *APOE* genotype (*APOE3* vs *APOE4*) and sex (male vs female). Given that both APOE status and sex are well-established risk factors of AD, analysing differentially expressed genes between these groups could produce insights into the molecular mechanisms underlying the associated risk. Furthermore, the human spatial transcriptomics experiment lacks *TREM2^{R47H}* mutation carriers due to a limited number of available samples. Therefore, assessing the translation of the *Trem2*-dependent gene module from the NLF model to human samples will provide insight into the risk associated with the *TREM2^{R47H}* mutation.

6.13 Contribution statement:

- GeoMx slide preparation and readout for the NLF microglial enriched spatial transcriptomics, and NLF plaque age spatial transcriptomic analysis was processed by the Nanostring Technology Access Programme (Seattle, WA, USA).
- RNA sequencing was processed by Eurofins Genomics (Eurofins Genomics Europe Sequencing GmbH, Germany).
- GeoMx Barcode sequencing of the human tissue spatial transcriptomics was performed by UCL genomics (London, United Kingdom).
- Tissue sectioning for the NLF microglial enriched spatial transcriptomics and the human spatial transcriptomics was performed by UCL IQPath (London, United Kingdom).
- Heavy isotope diet administration was carried out in collaboration with Dr Katie Stringer, a previous PhD student of the Edwards lab.
- Mass spectrometry Imaging data collection was carried out alongside PhD student Junyue Ge at the Hanrieder Lab, Gothenburg University.
- ^{15}N enrichment score (Nitrogen Index) was calculated in collaboration with Maciej Dulewicz, a postdoc in the Hanrieder lab, Gothenburg University.
- Immunohistochemistry against TREM2 was carried out in a single batch and therefore shared with Eugenia Wong, a previous master's student in the lab.
- Immunohistochemistry against NPC2 and APOE was performed by two master's students, Eugenia Wong and Ridwaan Joghee, respectively, under my supervision.
- For the field electrophysiology experiments, a small subset of recordings was performed by Sneha Desai, a PhD student in the Edwards Lab, and Damian Cummings, a postdoctoral researcher in the lab at the time.
- The decapitation and vibratome slice preparation for field electrophysiology was performed by Karina Vitanova, a previous PhD student and Damian Cummings, a postdoctoral researcher in the lab at the time.
- Mouse decapitation and tissue collection were performed by a range of Edwards Lab members, including myself.

REFERENCES

Abad, M.A., Enguita, M., DeGregorio-Rocasolano, N., Ferrer, I., and Trullas, R. (2006). Neuronal pentraxin 1 contributes to the neuronal damage evoked by amyloid-beta and is overexpressed in dystrophic neurites in Alzheimer's brain. J Neurosci 26, 12735-12747.

Abramov, E., Dolev, I., Fogel, H., Ciccotosto, G.D., Ruff, E., and Slutsky, I. (2009). Amyloid-beta as a positive endogenous regulator of release probability at hippocampal synapses. Nat Neurosci 12, 1567-1576.

Afagh, A., Cummings, B.J., Cribbs, D.H., Cotman, C.W., and Tenner, A.J. (1996). Localization and cell association of C1q in Alzheimer's disease brain. Exp Neurol 138, 22-32.

Ahmed, Z., Sheng, H., Xu, Y.F., Lin, W.L., Innes, A.E., Gass, J., Yu, X., Wuertzer, C.A., Hou, H., Chiba, S.*, et al.* (2010). Accelerated lipofuscinosis and ubiquitination in granulin knockout mice suggest a role for progranulin in successful aging. The American journal of pathology 177, 311-324.

Ali, F., Baringer, S.L., Neal, A., Choi, E.Y., and Kwan, A.C. (2019). Parvalbumin-Positive Neuron Loss and Amyloid-beta Deposits in the Frontal Cortex of Alzheimer's Disease-Related Mice. J Alzheimers Dis 72, 1323-1339.

Allsop, D., Landon, M., and Kidd, M. (1983). The isolation and amino acid composition of senile plaque core protein. Brain Res 259, 348-352.

Alzheimer, A. (1907). About a peculiar disease of the cerebral cortex. (Translation by L. Jarvik and H. Greenson in 1987). Alzheimer Dis Assoc Disord 1, 3-8.

Alzheimer's Association (2024). 2024 Alzheimer's disease facts and figures. In Alzheimers Dement, pp. 3708-3821.

Alzheimer's Disease International, Sara Evans-Lacko, Elisa Aguzzoli, Sanna Read, Adelina Comas-Herrera, and Farina, N. (2024). World Alzheimer Report 2024.

Amin, E., Elgammal, Y.M., Zahran, M.A., and Abdelsalam, M.M. (2023). Alzheimer's disease: new insight in assessing of amyloid plaques morphologies using multifractal geometry based on Naive Bayes optimized by random forest algorithm. Sci Rep 13, 18568.

Andersen, J.K. (2004). Oxidative stress in neurodegeneration: cause or consequence? Nat Med 10 Suppl, S18-25.

Andoh, M., Shinoda, N., Taira, Y., Araki, T., Kasahara, Y., Takeuchi, H., Miura, M., Ikegaya, Y., and Koyama, R. (2025). Nonapoptotic caspase-3 guides C1q-dependent synaptic phagocytosis by microglia. Nat Commun 16, 918.

Araya, K., Watson, R., Khanipov, K., Golovko, G., and Taglialatela, G. (2025). Increased risk of dementia associated with herpes simplex virus infections: Evidence from a retrospective cohort study using U.S. electronic health records. J Alzheimers Dis 104, 393-402.

Arbaizar-Rovirosa, M., Pedragosa, J., Lozano, J.J., Casal, C., Pol, A., Gallizioli, M., and Planas, A.M. (2023). Aged lipid-laden microglia display impaired responses to stroke. EMBO Mol Med 15, e17175.

Armstrong, R.A. (1998). Beta-amyloid plaques: stages in life history or independent origin? Dement Geriatr Cogn Disord 9, 227-238.

Asano, K., Miwa, M., Miwa, K., Hanayama, R., Nagase, H., Nagata, S., and Tanaka, M. (2004). Masking of phosphatidylserine inhibits apoptotic cell engulfment and induces autoantibody production in mice. J Exp Med 200, 459-467.

Ashe, K.H. (2020). The biogenesis and biology of amyloid beta oligomers in the brain. Alzheimers Dement 16, 1561-1567.

Aslund, A., Herland, A., Hammarstrom, P., Nilsson, K.P., Jonsson, B.H., Inganas, O., and Konradsson, P. (2007). Studies of luminescent conjugated polythiophene derivatives: enhanced spectral discrimination of protein conformational states. Bioconjug Chem 18, 1860-1868.

Aslund, A., Sigurdson, C.J., Klingstedt, T., Grathwohl, S., Bolmont, T., Dickstein, D.L., Glimsdal, E., Prokop, S., Lindgren, M., Konradsson, P.*, et al.* (2009). Novel pentameric thiophene derivatives for in vitro and in vivo optical imaging of a plethora of protein aggregates in cerebral amyloidoses. Acs Chem Biol 4, 673-684.

Atagi, Y., Liu, C.C., Painter, M.M., Chen, X.F., Verbeeck, C., Zheng, H., Li, X., Rademakers, R., Kang, S.S., Xu, H.*, et al.* (2015). Apolipoprotein E Is a Ligand for Triggering Receptor Expressed on Myeloid Cells 2 (TREM2). The Journal of biological chemistry 290, 26043-26050.

Baik, S.H., Kang, S., Son, S.M., and Mook-Jung, I. (2016). Microglia contributes to plaque growth by cell death due to uptake of amyloid beta in the brain of Alzheimer's disease mouse model. Glia 64, 2274-2290.

Baker, M., Mackenzie, I.R., Pickering-Brown, S.M., Gass, J., Rademakers, R., Lindholm, C., Snowden, J., Adamson, J., Sadovnick, A.D., Rollinson, S.*, et al.* (2006). Mutations in progranulin cause tau-negative frontotemporal dementia linked to chromosome 17. Nature 442, 916-919.

Balin, B.J., Gerard, H.C., Arking, E.J., Appelt, D.M., Branigan, P.J., Abrams, J.T., Whittum-Hudson, J.A., and Hudson, A.P. (1998). Identification and localization of Chlamydia pneumoniae in the Alzheimer's brain. Med Microbiol Immunol 187, 23-42.

Bamberger, M.E., Harris, M.E., McDonald, D.R., Husemann, J., and Landreth, G.E. (2003). A cell surface receptor complex for fibrillar beta-amyloid mediates microglial activation. J Neurosci 23, 2665-2674.

Banerjee, S., Hashemi, M., Zagorski, K., and Lyubchenko, Y.L. (2021). Cholesterol in Membranes Facilitates Aggregation of Amyloid beta Protein at Physiologically Relevant Concentrations. ACS Chem Neurosci 12, 506-516.

Bao, H., and Shen, Y. (2023). Unmasking BACE1 in aging and age-related diseases. Trends Mol Med 29, 99-111.

Bard, F., Cannon, C., Barbour, R., Burke, R.L., Games, D., Grajeda, H., Guido, T., Hu, K., Huang, J., Johnson-Wood, K.*, et al.* (2000). Peripherally administered antibodies against amyloid beta-peptide enter the central nervous system and reduce pathology in a mouse model of Alzheimer disease. Nat Med 6, 916-919.

Bateman, R.J., Munsell, L.Y., Morris, J.C., Swarm, R., Yarasheski, K.E., and Holtzman, D.M. (2006). Human amyloid-beta synthesis and clearance rates as measured in cerebrospinal fluid in vivo. Nat Med 12, 856-861.

Bayer, T.A. (2022). Pyroglutamate Abeta cascade as drug target in Alzheimer's disease. Mol Psychiatry 27, 1880-1885.

Behl, C. (2024). In 2024, the amyloid-cascade-hypothesis still remains a working hypothesis, no less but certainly no more. Front Aging Neurosci 16, 1459224.

Bellenguez, C., Kucukali, F., Jansen, I.E., Kleineidam, L., Moreno-Grau, S., Amin, N., Naj, A.C., Campos-Martin, R., Grenier-Boley, B., Andrade, V.*, et al.* (2022). New insights into the genetic etiology of Alzheimer's disease and related dementias. Nature genetics 54, 412-436.

Beltran-Lobo, P., Hughes, M.M., Troakes, C., Croft, C.L., Rupawala, H., Jutzi, D., Ruepp, M.D., Jimenez-Sanchez, M., Perkinton, M.S., Kassiou, M.*, et al.* (2023). P2X(7)R influences tau aggregate burden in human tauopathies and shows distinct signalling in microglia and astrocytes. Brain Behav Immun 114, 414-429.

Benitez, D.P., Jiang, S., Wood, J., Wang, R., Hall, C.M., Peerboom, C., Wong, N., Stringer, K.M., Vitanova, K.S., Smith, V.C.*, et al.* (2021). Knock-in models related to Alzheimer's disease: synaptic transmission, plaques and the role of microglia. Mol Neurodegener 16, 47.

Bennett, M.L., Bennett, F.C., Liddelow, S.A., Ajami, B., Zamanian, J.L., Fernhoff, N.B., Mulinyawe, S.B., Bohlen, C.J., Adil, A., Tucker, A.*, et al.* (2016). New tools for studying microglia in the mouse and human CNS. P Natl Acad Sci USA 113, E1738-1746.

Bigi, A., Cascella, R., Chiti, F., and Cecchi, C. (2022). Amyloid fibrils act as a reservoir of soluble oligomers, the main culprits in protein deposition diseases. Bioessays 44, e2200086.

Birge, R.B., Boeltz, S., Kumar, S., Carlson, J., Wanderley, J., Calianese, D., Barcinski, M., Brekken, R.A., Huang, X., Hutchins, J.T.*, et al.* (2016). Phosphatidylserine is a global immunosuppressive signal in efferocytosis, infectious disease, and cancer. Cell Death Differ 23, 962-978.

Bittner, T., Burgold, S., Dorostkar, M.M., Fuhrmann, M., Wegenast-Braun, B.M., Schmidt, B., Kretzschmar, H., and Herms, J. (2012). Amyloid plaque formation precedes dendritic spine loss. Acta Neuropathol 124, 797-807.

Blatow, M., Caputi, A., Burnashev, N., Monyer, H., and Rozov, A. (2003). Ca2+ buffer saturation underlies paired pulse facilitation in calbindin-D28k-containing terminals. Neuron 38, 79-88.

Bliss, T.V., and Lømo, T. (1973). Long-lasting potentiation of synaptic transmission in the dentate area of the anaesthetized rabbit following stimulation of the perforant path. jphysiol 232, 331-356.

Boche, D., Donald, J., Love, S., Harris, S., Neal, J.W., Holmes, C., and Nicoll, J.A. (2010). Reduction of aggregated Tau in neuronal processes but not in the cell bodies after Abeta42 immunisation in Alzheimer's disease. Acta Neuropathol 120, 13-20.

Bodovitz, S., and Klein, W.L. (1996). Cholesterol modulates alpha-secretase cleavage of amyloid precursor protein. The Journal of biological chemistry 271, 4436-4440.

Bolos, M., Llorens-Martin, M., Jurado-Arjona, J., Hernandez, F., Rabano, A., and Avila, J. (2016). Direct Evidence of Internalization of Tau by Microglia In Vitro and In Vivo. J Alzheimers Dis 50, 77-87.

Bolos, M., Llorens-Martin, M., Perea, J.R., Jurado-Arjona, J., Rabano, A., Hernandez, F., and Avila, J. (2017). Absence of CX3CR1 impairs the internalization of Tau by microglia. Mol Neurodegener 12, 59.

Boon, B.D.C., Bulk, M., Jonker, A.J., Morrema, T.H.J., van den Berg, E., Popovic, M., Walter, J., Kumar, S., van der Lee, S.J., Holstege, H.*, et al.* (2020). The coarse-grained plaque: a divergent Abeta plaque-type in early-onset Alzheimer's disease. Acta Neuropathol 140, 811-830.

Borst, K., Dumas, A.A., and Prinz, M. (2021). Microglia: Immune and non-immune functions. Immunity 54, 2194-2208.

Brelstaff, J., Tolkovsky, A.M., Ghetti, B., Goedert, M., and Spillantini, M.G. (2018). Living Neurons with Tau Filaments Aberrantly Expose Phosphatidylserine and Are Phagocytosed by Microglia. Cell Rep 24, 1939-1948 e1934.

Brumell, J.H., Howard, J.C., Craig, K., Grinstein, S., Schreiber, A.D., and Tyers, M. (1999). Expression of the protein kinase C substrate pleckstrin in macrophages: association with phagosomal membranes. J Immunol 163, 3388-3395.

Budd Haeberlein, S., Aisen, P.S., Barkhof, F., Chalkias, S., Chen, T., Cohen, S., Dent, G., Hansson, O., Harrison, K., von Hehn, C.*, et al.* (2022). Two Randomized Phase 3 Studies of Aducanumab in Early Alzheimer's Disease. J Prev Alzheimers Dis 9, 197-210.

Burgold, S., Bittner, T., Dorostkar, M.M., Kieser, D., Fuhrmann, M., Mitteregger, G., Kretzschmar, H., Schmidt, B., and Herms, J. (2011). In vivo multiphoton imaging reveals gradual growth of newborn amyloid plaques over weeks. Acta Neuropathol 121, 327-335.

Burns, M.P., Noble, W.J., Olm, V., Gaynor, K., Casey, E., LaFrancois, J., Wang, L., and Duff, K. (2003). Co-localization of cholesterol, apolipoprotein E and fibrillar Aβ in amyloid plaques. Mol Brain Res 110, 119-125.

Campion, D., Dumanchin, C., Hannequin, D., Dubois, B., Belliard, S., Puel, M., Thomas-Anterion, C., Michon, A., Martin, C., Charbonnier, F.*, et al.* (1999). Early-onset autosomal dominant Alzheimer disease: prevalence, genetic heterogeneity, and mutation spectrum. American journal of human genetics 65, 664-670.

Carpanini, S.M., Torvell, M., Bevan, R.J., Byrne, R.A.J., Daskoulidou, N., Saito, T., Saido, T.C., Taylor, P.R., Hughes, T.R., Zelek, W.M., and Morgan, B.P. (2022). Terminal complement pathway activation drives synaptic loss in Alzheimer's disease models. Acta Neuropathol Commun 10, 99.

Casali, B.T., MacPherson, K.P., Reed-Geaghan, E.G., and Landreth, G.E. (2020). Microglia depletion rapidly and reversibly alters amyloid pathology by modification of plaque compaction and morphologies. Neurobiol Dis 142, 104956.

Castro-Gomes, T., Corrotte, M., Tam, C., and Andrews, N.W. (2016). Plasma Membrane Repair Is Regulated Extracellularly by Proteases Released from Lysosomes. Plos One 11, e0152583.

Cataldo, A.M., and Nixon, R.A. (1990). Enzymatically active lysosomal proteases are associated with amyloid deposits in Alzheimer brain. P Natl Acad Sci USA 87, 3861-3865.

Cenik, B., Sephton, C.F., Kutluk Cenik, B., Herz, J., and Yu, G. (2012). Progranulin: a proteolytically processed protein at the crossroads of inflammation and neurodegeneration. The Journal of biological chemistry 287, 32298-32306.

Cermak, S., Kosicek, M., Mladenovic-Djordjevic, A., Smiljanic, K., Kanazir, S., and Hecimovic, S. (2016). Loss of Cathepsin B and L Leads to Lysosomal Dysfunction, NPC-Like Cholesterol Sequestration and Accumulation of the Key Alzheimer's Proteins. Plos One 11, e0167428-e0167428.

Cha, M.Y., Cho, H.J., Kim, C., Jung, Y.O., Kang, M.J., Murray, M.E., Hong, H.S., Choi, Y.J., Choi, H., Kim, D.K.*, et al.* (2015). Mitochondrial ATP synthase activity is impaired by suppressed O-GlcNAcylation in Alzheimer's disease. Human Molecular Genetics 24, 6492-6504.

Chen, W.T., Lu, A., Craessaerts, K., Pavie, B., Sala Frigerio, C., Corthout, N., Qian, X., Lalakova, J., Kuhnemund, M., Voytyuk, I.*, et al.* (2020). Spatial Transcriptomics and In Situ Sequencing to Study Alzheimer's Disease. Cell 182, 976-991 e919.

Cheng-Hathaway, P.J., Reed-Geaghan, E.G., Jay, T.R., Casali, B.T., Bemiller, S.M., Puntambekar, S.S., von Saucken, V.E., Williams, R.Y., Karlo, J.C., Moutinho, M.*, et al.* (2018). The Trem2 R47H variant confers loss-of-function-like phenotypes in Alzheimer's disease. Mol Neurodegener 13, 29.

Cho, M.H., Cho, K., Kang, H.J., Jeon, E.Y., Kim, H.S., Kwon, H.J., Kim, H.M., Kim, D.H., and Yoon, S.Y. (2014). Autophagy in microglia degrades extracellular beta-amyloid fibrils and regulates the NLRP3 inflammasome. Autophagy 10, 1761-1775.

Claes, C., Danhash, E.P., Hasselmann, J., Chadarevian, J.P., Shabestari, S.K., England, W.E., Lim, T.E., Hidalgo, J.L.S., Spitale, R.C., Davtyan, H., and Blurton-Jones, M. (2021). Plaque-associated human microglia accumulate lipid droplets in a chimeric model of Alzheimer's disease. Mol Neurodegener 16, 50.

Clements, J.D., Lester, R.A., Tong, G., Jahr, C.E., and Westbrook, G.L. (1992). The time course of glutamate in the synaptic cleft. Science 258, 1498-1501.

Cole, S.L., Grudzien, A., Manhart, I.O., Kelly, B.L., Oakley, H., and Vassar, R. (2005). Statins cause intracellular accumulation of amyloid precursor protein, beta-secretase-cleaved fragments, and amyloid beta-peptide via an isoprenoid-dependent mechanism. The Journal of biological chemistry 280, 18755-18770.

Condello, C., Schain, A., and Grutzendler, J. (2011). Multicolor time-stamp reveals the dynamics and toxicity of amyloid deposition. Sci Rep 1, 19.

Condello, C., Yuan, P., Schain, A., and Grutzendler, J. (2015). Microglia constitute a barrier that prevents neurotoxic protofibrillar Abeta42 hotspots around plaques. Nat Commun 6, 6176.

Cornell, J., Salinas, S., Huang, H.Y., and Zhou, M. (2022). Microglia regulation of synaptic plasticity and learning and memory. Neural Regen Res 17, 705-716.

Cummings, D.M., Benway, T.A., Ho, H., Tedoldi, A., Fernandes Freitas, M.M., Shahab, L., Murray, C.E., Richard-Loendt, A., Brandner, S., Lashley, T.*, et al.* (2017). Neuronal and

Peripheral Pentraxins Modify Glutamate Release and may Interact in Blood-Brain Barrier Failure. Cerebral cortex (New York, NY : 1991) 27, 3437-3448.

Cummings, D.M., Liu, W., Portelius, E., Bayram, S., Yasvoina, M., Ho, S.H., Smits, H., Ali, S.S., Steinberg, R., Pegasiou, C.M.*, et al.* (2015). First effects of rising amyloid-beta in transgenic mouse brain: synaptic transmission and gene expression. Brain 138, 1992-2004.

D'Andrea, M.R., Cole, G.M., and Ard, M.D. (2004). The microglial phagocytic role with specific plaque types in the Alzheimer disease brain. Neurobiol Aging 25, 675-683.

Daria, A., Colombo, A., Llovera, G., Hampel, H., Willem, M., Liesz, A., Haass, C., and Tahirovic, S. (2017). Young microglia restore amyloid plaque clearance of aged microglia. The EMBO journal 36, 583-603.

Das, S., Li, Z., Wachter, A., Alla, S., Noori, A., Abdourahman, A., Tamm, J.A., Woodbury, M.E., Talanian, R.V., Biber, K.*, et al.* (2024). Distinct transcriptomic responses to Abeta plaques, neurofibrillary tangles, and APOE in Alzheimer's disease. Alzheimers Dement 20, 74-90.

Davalos, D., Grutzendler, J., Yang, G., Kim, J.V., Zuo, Y., Jung, S., Littman, D.R., Dustin, M.L., and Gan, W.B. (2005). ATP mediates rapid microglial response to local brain injury in vivo. Nat Neurosci 8, 752-758.

Davies, D.S., Ma, J., Jegathees, T., and Goldsbury, C. (2017). Microglia show altered morphology and reduced arborization in human brain during aging and Alzheimer's disease. Brain Pathol 27, 795-808.

Davies, P., and Maloney, A.J. (1976). Selective loss of central cholinergic neurons in Alzheimer's disease. Lancet 2, 1403.

De Felice, F.G., Wu, D., Lambert, M.P., Fernandez, S.J., Velasco, P.T., Lacor, P.N., Bigio, E.H., Jerecic, J., Acton, P.J., Shughrue, P.J.*, et al.* (2008). Alzheimer's disease-type neuronal tau hyperphosphorylation induced by A beta oligomers. Neurobiol Aging 29, 1334-1347.

De Schepper, S., Ge, J.Z., Crowley, G., Ferreira, L.S.S., Garceau, D., Toomey, C.E., Sokolova, D., Rueda-Carrasco, J., Shin, S.H., Kim, J.S.*, et al.* (2023). Perivascular cells induce microglial phagocytic states and synaptic engulfment via SPP1 in mouse models of Alzheimer's disease. Nat Neurosci 26, 406-415.

DeMattos, R.B., Cirrito, J.R., Parsadanian, M., May, P.C., O'Dell, M.A., Taylor, J.W., Harmony, J.A., Aronow, B.J., Bales, K.R., Paul, S.M., and Holtzman, D.M. (2004). ApoE and clusterin cooperatively suppress Abeta levels and deposition: evidence that ApoE regulates extracellular Abeta metabolism in vivo. Neuron 41, 193-202.

Desai, S., Camporesi, E., Brinkmalm, G., Alatza, A., Wood, J.I., Tripathi, T., Bez, S., Stasyuk, N., Hajar, H.B., Saito, T.*, et al.* (2024). Age- and amyloid-β-dependent initiation of neurofibrillary tau tangles: an improved mouse model of Alzheimer’s disease without mutations in MAPT. BioRXiv.

DeTure, M.A., and Dickson, D.W. (2019). The neuropathological diagnosis of Alzheimer's disease. Mol Neurodegener 14, 32.

Dickson, D.W., Crystal, H.A., Mattiace, L.A., Masur, D.M., Blau, A.D., Davies, P., Yen, S.H., and Aronson, M.K. (1992). Identification of normal and pathological aging in prospectively studied nondemented elderly humans. Neurobiol Aging 13, 179-189.

Dickson, T.C., and Vickers, J.C. (2001). The morphological phenotype of beta-amyloid plaques and associated neuritic changes in Alzheimer's disease. Neuroscience 105, 99-107.

Drummond, E., and Wisniewski, T. (2017). Alzheimer's disease: experimental models and reality. Acta Neuropathol 133, 155-175.

Dubois, B., Chupin, M., Hampel, H., Lista, S., Cavedo, E., Croisile, B., Louis Tisserand, G., Touchon, J., Bonafe, A., Ousset, P.J.*, et al.* (2015). Donepezil decreases annual rate of hippocampal atrophy in suspected prodromal Alzheimer's disease. Alzheimers Dement 11, 1041-1049.

Dubois, B., Feldman, H.H., Jacova, C., Dekosky, S.T., Barberger-Gateau, P., Cummings, J., Delacourte, A., Galasko, D., Gauthier, S., Jicha, G.*, et al.* (2007). Research criteria for the diagnosis of Alzheimer's disease: revising the NINCDS-ADRDA criteria. Lancet Neurol 6, 734-746.

Eanes, E.D., and Glenner, G.G. (1968). X-ray diffraction studies on amyloid filaments. J Histochem Cytochem 16, 673-677.

Edwards, F.A. (1995). Patch clamp recording in brain slices. In Brain slices in basic and clinical research, A. Schurr, and B.M. Rigor, eds. (CRC Press, Inc).

Edwards, F.A. (2019). A Unifying Hypothesis for Alzheimer's Disease: From Plaques to Neurodegeneration. Trends Neurosci 42, 310-322.

Edwards, F.A., and Konnerth, A. (1992). Patch-clamping cells in sliced tissue preparations. Methods in enzymology 207, 208-222.

Enzlein, T., Lashley, T., Sammour, D.A., Hopf, C., and Chavez-Gutierrez, L. (2024). Integrative Single-Plaque Analysis Reveals Signature Abeta and Lipid Profiles in the Alzheimer's Brain. Anal Chem 96, 9799-9807.

Epis, R., Marcello, E., Gardoni, F., Vastagh, C., Malinverno, M., Balducci, C., Colombo, A., Borroni, B., Vara, H., Dell'Agli, M.*, et al.* (2010). Blocking ADAM10 synaptic trafficking generates a model of sporadic Alzheimer's disease. Brain 133, 3323-3335.

Escartin, C., Galea, E., Lakatos, A., O'Callaghan, J.P., Petzold, G.C., Serrano-Pozo, A., Steinhauser, C., Volterra, A., Carmignoto, G., Agarwal, A.*, et al.* (2021). Reactive astrocyte nomenclature, definitions, and future directions. Nat Neurosci 24, 312-325.

Evers, B.M., Rodriguez-Navas, C., Tesla, R.J., Prange-Kiel, J., Wasser, C.R., Yoo, K.S., McDonald, J., Cenik, B., Ravenscroft, T.A., Plattner, F.*, et al.* (2017). Lipidomic and Transcriptomic Basis of Lysosomal Dysfunction in Progranulin Deficiency. Cell Rep 20, 2565-2574.

Fertan, E., Lam, J.Y.L., Albertini, G., Dewilde, M., Wu, Y., Akingbade, O.E.S., Böken, D., English, E.A., De Strooper, B., and Klenerman, D. (2024). Single-molecule characterisation of soluble beta-amyloid aggregate binding by Aducanumab, Lecanemab, Gantenerumab, and Donanemab. bioRxiv, 2024.2010.2011.617910.

Filipello, F., Morini, R., Corradini, I., Zerbi, V., Canzi, A., Michalski, B., Erreni, M., Markicevic, M., Starvaggi-Cucuzza, C., Otero, K.*, et al.* (2018). The Microglial Innate Immune Receptor TREM2 Is Required for Synapse Elimination and Normal Brain Connectivity. Immunity 48, 979-991 e978.

Floden, A.M., and Combs, C.K. (2006). Beta-amyloid stimulates murine postnatal and adult microglia cultures in a unique manner. J Neurosci 26, 4644-4648.

Fodor, S.P., Read, J.L., Pirrung, M.C., Stryer, L., Lu, A.T., and Solas, D. (1991). Light-directed, spatially addressable parallel chemical synthesis. Science 251, 767-773.

Folick, A., Cheang, R.T., Valdearcos, M., and Koliwad, S.K. (2022). Metabolic factors in the regulation of hypothalamic innate immune responses in obesity. Exp Mol Med 54, 393-402.

Fonseca, M.I., Chu, S.H., Hernandez, M.X., Fang, M.J., Modarresi, L., Selvan, P., MacGregor, G.R., and Tenner, A.J. (2017). Cell-specific deletion of C1qa identifies microglia as the dominant source of C1q in mouse brain. J Neuroinflamm 14, 48.

Fox, N., Scahill, R., and Rossor, M. (1999). Correlation between rates of brain atrophy and cognitive decline in AD. Neurology 52.

Fox, N.C., and Schott, J.M. (2004). Imaging cerebral atrophy: normal ageing to Alzheimer's disease. Lancet 363, 392-394.

Frackowiak, J., Wisniewski, H.M., Wegiel, J., Merz, G.S., Iqbal, K., and Wang, K.C. (1992). Ultrastructure of the microglia that phagocytose amyloid and the microglia that produce beta-amyloid fibrils. Acta Neuropathol 84, 225-233.

Frade, J.M., and Barde, Y.A. (1998). Microglia-derived nerve growth factor causes cell death in the developing retina. Neuron 20, 35-41.

Friedrich, R.P., Tepper, K., Ronicke, R., Soom, M., Westermann, M., Reymann, K., Kaether, C., and Fandrich, M. (2010). Mechanism of amyloid plaque formation suggests an intracellular basis of Abeta pathogenicity. P Natl Acad Sci USA 107, 1942-1947.

Frieg, B., Gremer, L., Heise, H., Willbold, D., and Gohlke, H. (2020). Binding modes of thioflavin T and Congo red to the fibril structure of amyloid-beta(1-42). Chem Commun (Camb) 56, 7589-7592.

Gan, X., Huang, S., Wu, L., Wang, Y., Hu, G., Li, G., Zhang, H., Yu, H., Swerdlow, R.H., Chen, J.X., and Yan, S.S. (2014). Inhibition of ERK-DLP1 signaling and mitochondrial division alleviates mitochondrial dysfunction in Alzheimer's disease cybrid cell. Biochim Biophys Acta 1842, 220-231.

Garcia-Reitboeck, P., Phillips, A., Piers, T.M., Villegas-Llerena, C., Butler, M., Mallach, A., Rodrigues, C., Arber, C.E., Heslegrave, A., Zetterberg, H.*, et al.* (2018). Human Induced Pluripotent Stem Cell-Derived Microglia-Like Cells Harboring TREM2 Missense Mutations Show Specific Deficits in Phagocytosis. Cell Rep 24, 2300-2311.

Ge, J., Koutarapu, S., Jha, D., Dulewicz, M., Zetterberg, H., Blennow, K., and Hanrieder, J. (2023). Tetramodal Chemical Imaging Delineates the Lipid-Amyloid Peptide Interplay at Single Plaques in Transgenic Alzheimer's Disease Models. Anal Chem 95, 4692-4702.

Ginhoux, F., Greter, M., Leboeuf, M., Nandi, S., See, P., Gokhan, S., Mehler, M.F., Conway, S.J., Ng, L.G., Stanley, E.R.*, et al.* (2010). Fate mapping analysis reveals that adult microglia derive from primitive macrophages. Science 330, 841-845.

Glenner, G.G., Wong, C.W., Quaranta, V., and Eanes, E.D. (1984). The amyloid deposits in Alzheimer's disease: their nature and pathogenesis. Appl Pathol 2, 357-369.

Gogesch, P., Dudek, S., van Zandbergen, G., Waibler, Z., and Anzaghe, M. (2021). The Role of Fc Receptors on the Effectiveness of Therapeutic Monoclonal Antibodies. Int J Mol Sci 22.

Gotkiewicz, M., Capra, J., Miettinen, P.O., Natunen, T., and Tanila, H. (2025). Three-dimensional view of microglia-amyloid plaque interactions. Glia 73, 196-209.

Gotzl, J.K., Brendel, M., Werner, G., Parhizkar, S., Sebastian Monasor, L., Kleinberger, G., Colombo, A.V., Deussing, M., Wagner, M., Winkelmann, J.*, et al.* (2019). Opposite microglial activation stages upon loss of PGRN or TREM2 result in reduced cerebral glucose metabolism. EMBO Mol Med 11.

Gouna, G., Klose, C., Bosch-Queralt, M., Liu, L., Gokce, O., Schifferer, M., Cantuti-Castelvetri, L., and Simons, M. (2021). TREM2-dependent lipid droplet biogenesis in phagocytes is required for remyelination. J Exp Med 218.

Greven, J.A., Wydra, J.R., Greer, R.A., Zhi, C., Price, D.A., Svoboda, J.D., Camitta, C.L.M., Washington, M., Leung, D.W., Song, Y.*, et al.* (2025). Biophysical mapping of TREM2-ligand interactions reveals shared surfaces for engagement of multiple Alzheimer's disease ligands. Mol Neurodegener 20, 3.

Grubman, A., Choo, X.Y., Chew, G., Ouyang, J.F., Sun, G., Croft, N.P., Rossello, F.J., Simmons, R., Buckberry, S., Landin, D.V.*, et al.* (2021). Transcriptional signature in microglia associated with Abeta plaque phagocytosis. Nat Commun 12, 3015.

Grupe, A., Abraham, R., Li, Y., Rowland, C., Hollingworth, P., Morgan, A., Jehu, L., Segurado, R., Stone, D., Schadt, E.*, et al.* (2007). Evidence for novel susceptibility genes for late-onset Alzheimer's disease from a genome-wide association study of putative functional variants. Hum Mol Genet 16, 865-873.

Guerreiro, R., and Bras, J. (2015). The age factor in Alzheimer's disease. Genome Med 7, 106.

Guerreiro, R., Wojtas, A., Bras, J., Carrasquillo, M., Rogaeva, E., Majounie, E., Cruchaga, C., Sassi, C., Kauwe, J.S.K., Younkin, S.*, et al.* (2013). TREM2 variants in Alzheimer's disease. The New England journal of medicine 368, 117-127.

Guo, J., Cai, Y., Ye, X., Ma, N., Wang, Y., Yu, B., and Wan, J. (2019). MiR-409-5p as a Regulator of Neurite Growth Is Down Regulated in APP/PS1 Murine Model of Alzheimer's Disease. Front Neurosci 13, 1264.

Gyorffy, B.A., Kun, J., Torok, G., Bulyaki, E., Borhegyi, Z., Gulyassy, P., Kis, V., Szocsics, P., Micsonai, A., Matko, J.*, et al.* (2018). Local apoptotic-like mechanisms underlie complement-mediated synaptic pruning. P Natl Acad Sci USA 115, 6303-6308.

Habchi, J., Chia, S., Galvagnion, C., Michaels, T.C.T., Bellaiche, M.M.J., Ruggeri, F.S., Sanguanini, M., Idini, I., Kumita, J.R., Sparr, E.*, et al.* (2018). Cholesterol catalyses Abeta42

aggregation through a heterogeneous nucleation pathway in the presence of lipid membranes. Nat Chem 10, 673-683.

Habib, N., McCabe, C., Medina, S., Varshavsky, M., Kitsberg, D., Dvir-Szternfeld, R., Green, G., Dionne, D., Nguyen, L., Marshall, J.L.*, et al.* (2020). Disease-associated astrocytes in Alzheimer's disease and aging. Nat Neurosci 23, 701-706.

Haga, S., Akai, K., and Ishii, T. (1989). Demonstration of microglial cells in and around senile (neuritic) plaques in the Alzheimer brain. An immunohistochemical study using a novel monoclonal antibody. Acta Neuropathol 77, 569-575.

Halle, A., Hornung, V., Petzold, G.C., Stewart, C.R., Monks, B.G., Reinheckel, T., Fitzgerald, K.A., Latz, E., Moore, K.J., and Golenbock, D.T. (2008). The NALP3 inflammasome is involved in the innate immune response to amyloid-beta. Nature immunology 9, 857-865.

Halle, M., Tribout-Jover, P., Lanteigne, A.M., Boulais, J., St-Jean, J.R., Jodoin, R., Girouard, M.P., Constantin, F., Migneault, A., Renaud, F.*, et al.* (2015). Methods to monitor monocytes-mediated amyloid-beta uptake and phagocytosis in the context of adjuvanted immunotherapies. J Immunol Methods 424, 64-79.

Hamerman, J.A., Jarjoura, J.R., Humphrey, M.B., Nakamura, M.C., Seaman, W.E., and Lanier, L.L. (2006). Cutting edge: inhibition of TLR and FcR responses in macrophages by triggering receptor expressed on myeloid cells (TREM)-2 and DAP12. J Immunol 177, 2051-2055.

Hammarstrom, P., Simon, R., Nystrom, S., Konradsson, P., Aslund, A., and Nilsson, K.P. (2010). A fluorescent pentameric thiophene derivative detects in vitro-formed prefibrillar protein aggregates. Biochemistry 49, 6838-6845.

Hampel, H., Hardy, J., Blennow, K., Chen, C., Perry, G., Kim, S.H., Villemagne, V.L., Aisen, P., Vendruscolo, M., Iwatsubo, T.*, et al.* (2021). The Amyloid-beta Pathway in Alzheimer's Disease. Mol Psychiatry 26, 5481-5503.

Hampel, H., Mesulam, M.M., Cuello, A.C., Farlow, M.R., Giacobini, E., Grossberg, G.T., Khachaturian, A.S., Vergallo, A., Cavedo, E., Snyder, P.J., and Khachaturian, Z.S. (2018). The cholinergic system in the pathophysiology and treatment of Alzheimer's disease. Brain 141, 1917-1933.

Haney, M.S., Pálovics, R., Munson, C.N., Long, C., Johansson, P.K., Yip, O., Dong, W., Rawat, E., West, E., Schlachetzki, J.C.M.*, et al.* (2024). APOE4/4 is linked to damaging lipid droplets in Alzheimer's disease microglia. Nature 628, 154-161.

Hardy, J.A., and Higgins, G.A. (1992). Alzheimer's disease: the amyloid cascade hypothesis. Science 256, 184-185.

Hark, T.J., Rao, N.R., Castillon, C., Basta, T., Smukowski, S., Bao, H., Upadhyay, A., Bomba-Warczak, E., Nomura, T., O'Toole, E.T.*, et al.* (2021). Pulse-Chase Proteomics of the App Knockin Mouse Models of Alzheimer's Disease Reveals that Synaptic Dysfunction Originates in Presynaptic Terminals. Cell Syst 12, 141-158 e149.

Harold, D., Abraham, R., Hollingworth, P., Sims, R., Gerrish, A., Hamshere, M.L., Pahwa, J.S., Moskvina, V., Dowzell, K., Williams, A.*, et al.* (2009). Genome-wide association study identifies variants at CLU and PICALM associated with Alzheimer's disease. Nature genetics 41, 1088-1093.

Harrison, I.F., Ismail, O., Machhada, A., Colgan, N., Ohene, Y., Nahavandi, P., Ahmed, Z., Fisher, A., Meftah, S., Murray, T.K.*, et al.* (2020). Impaired glymphatic function and clearance of tau in an Alzheimer's disease model. Brain 143, 2576-2593.

He, S., Xu, Z., and Han, X. (2025). Lipidome disruption in Alzheimer's disease brain: detection, pathological mechanisms, and therapeutic implications. Mol Neurodegener 20, 11.

Hefendehl, J.K., Wegenast-Braun, B.M., Liebig, C., Eicke, D., Milford, D., Calhoun, M.E., Kohsaka, S., Eichner, M., and Jucker, M. (2011). Long-term in vivo imaging of beta-amyloid plaque appearance and growth in a mouse model of cerebral beta-amyloidosis. J Neurosci 31, 624-629.

Hellwig, S., Masuch, A., Nestel, S., Katzmarski, N., Meyer-Luehmann, M., and Biber, K. (2015). Forebrain microglia from wild-type but not adult 5xFAD mice prevent amyloid-β plaque formation in organotypic hippocampal slice cultures. Scientific Reports 5, 14624.

Heneka, M.T., Sastre, M., Dumitrescu-Ozimek, L., Hanke, A., Dewachter, I., Kuiperi, C., O'Banion, K., Klockgether, T., Van Leuven, F., and Landreth, G.E. (2005). Acute treatment with the PPARgamma agonist pioglitazone and ibuprofen reduces glial inflammation and Abeta1-42 levels in APPV717I transgenic mice. Brain 128, 1442-1453.

Henry, C.J., Huang, Y., Wynne, A.M., and Godbout, J.P. (2009). Peripheral lipopolysaccharide (LPS) challenge promotes microglial hyperactivity in aged mice that is associated with exaggerated induction of both pro-inflammatory IL-1beta and anti-inflammatory IL-10 cytokines. Brain Behav Immun 23, 309-317.

Herzer, S., Hagan, C., von Gerichten, J., Dieterle, V., Munteanu, B., Sandhoff, R., Hopf, C., and Nordstrom, V. (2018). Deletion of Specific Sphingolipids in Distinct Neurons Improves Spatial Memory in a Mouse Model of Alzheimer's Disease. Front Mol Neurosci 11, 206.

Hollingworth, P., Harold, D., Sims, R., Gerrish, A., Lambert, J.C., Carrasquillo, M.M., Abraham, R., Hamshere, M.L., Pahwa, J.S., Moskvina, V.*, et al.* (2011). Common variants at ABCA7, MS4A6A/MS4A4E, EPHA1, CD33 and CD2AP are associated with Alzheimer's disease. Nature genetics 43, 429-435.

Hong, S., Beja-Glasser, V.F., Nfonoyim, B.M., Frouin, A., Li, S., Ramakrishnan, S., Merry, K.M., Shi, Q., Rosenthal, A., Barres, B.A.*, et al.* (2016a). Complement and microglia mediate early synapse loss in Alzheimer mouse models. Science 352, 712-716.

Hong, S., Dissing-Olesen, L., and Stevens, B. (2016b). New insights on the role of microglia in synaptic pruning in health and disease. Curr Opin Neurobiol 36, 128-134.

Hong, S., and Stevens, B. (2016). Microglia: Phagocytosing to Clear, Sculpt, and Eliminate. Dev Cell 38, 126-128.

Hook, V.Y., Kindy, M., Reinheckel, T., Peters, C., and Hook, G. (2009). Genetic cathepsin B deficiency reduces beta-amyloid in transgenic mice expressing human wild-type amyloid precursor protein. Biochem Bioph Res Co 386, 284-288.

Hoshiko, M., Arnoux, I., Avignone, E., Yamamoto, N., and Audinat, E. (2012). Deficiency of the microglial receptor CX3CR1 impairs postnatal functional development of thalamocortical synapses in the barrel cortex. J Neurosci 32, 15106-15111.

Hristovska, I., Robert, M., Combet, K., Honnorat, J., Comte, J.C., and Pascual, O. (2022). Sleep decreases neuronal activity control of microglial dynamics in mice. Nat Commun 13, 6273.

Hsieh, C.L., Koike, M., Spusta, S.C., Niemi, E.C., Yenari, M., Nakamura, M.C., and Seaman, W.E. (2009). A role for TREM2 ligands in the phagocytosis of apoptotic neuronal cells by microglia. J Neurochem 109, 1144-1156.

Huang, Y., Happonen, K.E., Burrola, P.G., O'Connor, C., Hah, N., Huang, L., Nimmerjahn, A., and Lemke, G. (2021). Microglia use TAM receptors to detect and engulf amyloid beta plaques. Nature immunology 22, 586-594.

Hughes, C., Choi, M.L., Yi, J.H., Kim, S.C., Drews, A., George-Hyslop, P.S., Bryant, C., Gandhi, S., Cho, K., and Klenerman, D. (2020). Beta amyloid aggregates induce sensitised TLR4 signalling causing long-term potentiation deficit and rat neuronal cell death. Commun Biol 3, 79.

Huin, V., Barbier, M., Bottani, A., Lobrinus, J.A., Clot, F., Lamari, F., Chat, L., Rucheton, B., Fluchere, F., Auvin, S*., et al.* (2020). Homozygous GRN mutations: new phenotypes and new insights into pathological and molecular mechanisms. Brain 143, 303-319.

Humphries, C.E., Kohli, M.A., Nathanson, L., Whitehead, P., Beecham, G., Martin, E., Mash, D.C., Pericak-Vance, M.A., and Gilbert, J. (2015). Integrated whole transcriptome and DNA methylation analysis identifies gene networks specific to late-onset Alzheimer's disease. J Alzheimers Dis 44, 977-987.

Hyman, B.T., Phelps, C.H., Beach, T.G., Bigio, E.H., Cairns, N.J., Carrillo, M.C., Dickson, D.W., Duyckaerts, C., Frosch, M.P., Masliah, E*., et al.* (2012). National Institute on Aging-Alzheimer's Association guidelines for the neuropathologic assessment of Alzheimer's disease. Alzheimers Dement 8, 1-13.

Ichimata, S., Martinez-Valbuena, I., Forrest, S.L., and Kovacs, G.G. (2022). Expanding the spectrum of amyloid-beta plaque pathology: the Down syndrome associated 'bird-nest plaque'. Acta Neuropathol 144, 1171-1174.

Ikeda, K., Haga, C., and Kosaka, K. (1990). Light and electron microscopic examination of amyloid-rich primitive plaques: comparison with diffuse plaques. J Neurol 237, 88-93.

Ishii, T., and Haga, S. (1984). Immuno-electron-microscopic localization of complements in amyloid fibrils of senile plaques. Acta Neuropathol 63, 296-300.

Islam, S., Kjallquist, U., Moliner, A., Zajac, P., Fan, J.B., Lonnerberg, P., and Linnarsson, S. (2011). Characterization of the single-cell transcriptional landscape by highly multiplex RNA-seq. Genome Res 21, 1160-1167.

Itagaki, S., McGeer, P.L., Akiyama, H., Zhu, S., and Selkoe, D. (1989). Relationship of microglia and astrocytes to amyloid deposits of Alzheimer disease. Journal of neuroimmunology 24, 173-182.

Ito, S., Yagi, R., Ogata, S., Masuda, T., Saito, T., Saido, T., and Ohtsuki, S. (2023). Proteomic alterations in the brain and blood-brain barrier during brain Abeta accumulation in an APP knock-in mouse model of Alzheimer's disease. Fluids Barriers CNS 20, 66.

Iwatsubo, T., Odaka, A., Suzuki, N., Mizusawa, H., Nukina, N., and Ihara, Y. (1994). Visualization of A beta 42(43) and A beta 40 in senile plaques with end-specific A beta

monoclonals: evidence that an initially deposited species is A beta 42(43). Neuron 13, 45-53.

Iwatsubo, T., Saido, T.C., Mann, D.M., Lee, V.M., and Trojanowski, J.Q. (1996). Full-length amyloid-beta (1-42(43)) and amino-terminally modified and truncated amyloid-beta 42(43) deposit in diffuse plaques. The American journal of pathology 149, 1823-1830.

Jacquet, R.G., Gonzalez Ibanez, F., Picard, K., Funes, L., Khakpour, M., Gouras, G.K., Tremblay, M.E., Maxfield, F.R., and Sole-Domenech, S. (2024). Microglia degrade Alzheimer's amyloid-beta deposits extracellularly via digestive exophagy. Cell Rep 43, 115052.

Jadhav, V.S., Lin, P.B.C., Pennington, T., Di Prisco, G.V., Jannu, A.J., Xu, G., Moutinho, M., Zhang, J., Atwood, B.K., Puntambekar, S.S*., et al.* (2020). Trem2 Y38C mutation and loss of Trem2 impairs neuronal synapses in adult mice. Molecular neurodegeneration 15, 62-62.

Jankowsky, J.L., and Zheng, H. (2017). Practical considerations for choosing a mouse model of Alzheimer's disease. Mol Neurodegener 12, 89.

Janus, C., Pearson, J., McLaurin, J., Mathews, P.M., Jiang, Y., Schmidt, S.D., Chishti, M.A., Horne, P., Heslin, D., French, J*., et al.* (2000). A beta peptide immunization reduces behavioural impairment and plaques in a model of Alzheimer's disease. Nature 408, 979-982.

Jay, T.R., Miller, C.M., Cheng, P.J., Graham, L.C., Bemiller, S., Broihier, M.L., Xu, G., Margevicius, D., Karlo, J.C., Sousa, G.L*., et al.* (2015). TREM2 deficiency eliminates TREM2+ inflammatory macrophages and ameliorates pathology in Alzheimer's disease mouse models. J Exp Med 212, 287-295.

Jiang, T., Wan, Y., Zhang, Y.D., Zhou, J.S., Gao, Q., Zhu, X.C., Shi, J.Q., Lu, H., Tan, L., and Yu, J.T. (2017). TREM2 Overexpression has No Improvement on Neuropathology and Cognitive Impairment in Aging APPswe/PS1dE9 Mice. Mol Neurobiol 54, 855-865.

Jiwaji, Z., Tiwari, S.S., Aviles-Reyes, R.X., Hooley, M., Hampton, D., Torvell, M., Johnson, D.A., McQueen, J., Baxter, P., Sabari-Sankar, K*., et al.* (2022). Reactive astrocytes acquire neuroprotective as well as deleterious signatures in response to Tau and Ass pathology. Nat Commun 13, 135.

Jonsson, T., Atwal, J.K., Steinberg, S., Snaedal, J., Jonsson, P.V., Bjornsson, S., Stefansson, H., Sulem, P., Gudbjartsson, D., Maloney, J*., et al.* (2012). A mutation in APP protects against Alzheimer's disease and age-related cognitive decline. Nature 488, 96-99.

Jonsson, T., Stefansson, H., Steinberg, S., Jonsdottir, I., Jonsson, P.V., Snaedal, J., Bjornsson, S., Huttenlocher, J., Levey, A.I., Lah, J.J*., et al.* (2013). Variant of TREM2 associated with the risk of Alzheimer's disease. N Engl J Med 368, 107-116.

Josephs, K.A., Whitwell, J.L., Ahmed, Z., Shiung, M.M., Weigand, S.D., Knopman, D., Boeve, B., Parisi, J.E., Petersen, R.C., Dickson, D., and Jack, C. (2008). β-Amyloid Burden Is Not Associated withRates of Brain Atrophy. Annals of Neurology 63, 204-212.

Kaji, S., Berghoff, S.A., Spieth, L., Schlaphoff, L., Sasmita, A.O., Vitale, S., Buschgens, L., Kedia, S., Zirngibl, M., Nazarenko, T*., et al.* (2024). Apolipoprotein E aggregation in microglia initiates Alzheimer's disease pathology by seeding beta-amyloidosis. Immunity.

Kalkman, H.O., and Smigielski, L. (2025). Ceramides may Play a Central Role in the Pathogenesis of Alzheimer's Disease: a Review of Evidence and Horizons for Discovery. Mol Neurobiol.

Kang, J., Lemaire, H.G., Unterbeck, A., Salbaum, J.M., Masters, C.L., Grzeschik, K.H., Multhaup, G., Beyreuther, K., and Muller-Hill, B. (1987). The precursor of Alzheimer's disease amyloid A4 protein resembles a cell-surface receptor. Nature 325, 733-736.

Katz, B., and Miledi, R. (1968). The role of calcium in neuromuscular facilitation. jphysiol 195, 481-492.

Kawabori, M., Kacimi, R., Kauppinen, T., Calosing, C., Kim, J.Y., Hsieh, C.L., Nakamura, M.C., and Yenari, M.A. (2015). Triggering Receptor Expressed on Myeloid Cells 2 (TREM2) Deficiency Attenuates Phagocytic Activities of Microglia and Exacerbates Ischemic Damage in Experimental Stroke. J Neurosci 35, 3384-3396.

Keren-Shaul, H., Spinrad, A., Weiner, A., Matcovitch-Natan, O., Dvir-Szternfeld, R., Ulland, T.K., David, E., Baruch, K., Lara-Astaiso, D., Toth, B.*, et al.* (2017). A Unique Microglia Type Associated with Restricting Development of Alzheimer's Disease. Cell 169, 1276-1290 e1217.

Kiani Shabestari, S., Morabito, S., Danhash, E.P., McQuade, A., Sanchez, J.R., Miyoshi, E., Chadarevian, J.P., Claes, C., Coburn, M.A., Hasselmann, J.*, et al.* (2022). Absence of microglia promotes diverse pathologies and early lethality in Alzheimer's disease mice. Cell Rep 39, 110961.

Kierdorf, K., Erny, D., Goldmann, T., Sander, V., Schulz, C., Perdiguero, E.G., Wieghofer, P., Heinrich, A., Riemke, P., Holscher, C.*, et al.* (2013). Microglia emerge from erythromyeloid precursors via Pu.1- and Irf8-dependent pathways. Nat Neurosci 16, 273-280.

Kim, C.K., Lee, Y.R., Ong, L., Gold, M., Kalali, A., and Sarkar, J. (2022). Alzheimer's Disease: Key Insights from Two Decades of Clinical Trial Failures. J Alzheimers Dis 87, 83-100.

Kim, M., Suh, J., Romano, D., Truong, M.H., Mullin, K., Hooli, B., Norton, D., Tesco, G., Elliott, K., Wagner, S.L.*, et al.* (2009). Potential late-onset Alzheimer's disease-associated mutations in the ADAM10 gene attenuate {alpha}-secretase activity. Hum Mol Genet 18, 3987-3996.

Kim, S.M., Mun, B.R., Lee, S.J., Joh, Y., Lee, H.Y., Ji, K.Y., Choi, H.R., Lee, E.H., Kim, E.M., Jang, J.H.*, et al.* (2017). TREM2 promotes Abeta phagocytosis by upregulating C/EBPalpha-dependent CD36 expression in microglia. Sci Rep 7, 11118.

Kim, W., and Hecht, M.H. (2005). Sequence determinants of enhanced amyloidogenicity of Alzheimer Abeta42 peptide relative to Abeta40. The Journal of biological chemistry 280, 35069-35076.

Kimberly, W.T., LaVoie, M.J., Ostaszewski, B.L., Ye, W., Wolfe, M.S., and Selkoe, D.J. (2003). Gamma-secretase is a membrane protein complex comprised of presenilin, nicastrin, Aph-1, and Pen-2. P Natl Acad Sci USA 100, 6382-6387.

Kiskis, J., Fink, H., Nyberg, L., Thyr, J., Li, J.-Y., and Enejder, A. (2015). Plaque-associated lipids in Alzheimer’s diseased brain tissue visualized by nonlinear microscopy. Scientific Reports 5, 13489.

Kitazawa, M., Medeiros, R., and Laferla, F.M. (2012). Transgenic mouse models of Alzheimer disease: developing a better model as a tool for therapeutic interventions. Curr Pharm Des 18, 1131-1147.

Klingstedt, T., Aslund, A., Simon, R.A., Johansson, L.B., Mason, J.J., Nystrom, S., Hammarstrom, P., and Nilsson, K.P. (2011). Synthesis of a library of oligothiophenes and their utilization as fluorescent ligands for spectral assignment of protein aggregates. Org Biomol Chem 9, 8356-8370.

Klingstedt, T., Blechschmidt, C., Nogalska, A., Prokop, S., Haggqvist, B., Danielsson, O., Engel, W.K., Askanas, V., Heppner, F.L., and Nilsson, K.P. (2013). Luminescent conjugated oligothiophenes for sensitive fluorescent assignment of protein inclusion bodies. Chembiochem 14, 607-616.

Koenigsknecht, J., and Landreth, G. (2004). Microglial phagocytosis of fibrillar beta-amyloid through a beta1 integrin-dependent mechanism. J Neurosci 24, 9838-9846.

Koenigsknecht-Talboo, J., and Landreth, G.E. (2005). Microglial phagocytosis induced by fibrillar beta-amyloid and IgGs are differentially regulated by proinflammatory cytokines. J Neurosci 25, 8240-8249.

Koffie, R.M., Meyer-Luehmann, M., Hashimoto, T., Adams, K.W., Mielke, M.L., Garcia-Alloza, M., Micheva, K.D., Smith, S.J., Kim, M.L., Lee, V.M.*, et al.* (2009). Oligomeric amyloid beta associates with postsynaptic densities and correlates with excitatory synapse loss near senile plaques. P Natl Acad Sci USA 106, 4012-4017.

Kontush, A., Berndt, C., Weber, W., Akopyan, V., Arlt, S., Schippling, S., and Beisiegel, U. (2001). Amyloid-beta is an antioxidant for lipoproteins in cerebrospinal fluid and plasma. Free Radic Biol Med 30, 119-128.

Kotredes, K.P., Oblak, A., Pandey, R.S., Lin, P.B., Garceau, D., Williams, H., Uyar, A., O'Rourke, R., O'Rourke, S., Ingraham, C.*, et al.* (2021). Uncovering Disease Mechanisms in a Novel Mouse Model Expressing Humanized APOEepsilon4 and Trem2*R47H. Front Aging Neurosci 13, 735524.

Koutarapu, S., Ge, J., Dulewicz, M., Srikrishna, M., Szadziewska, A., Wood, J., Blennow, K., Zetterberg, H., Michno, W., Ryan, N.S.*, et al.* (2024). Chemical signatures delineate heterogeneous amyloid plaque populations across the Alzheimer's disease spectrum. bioRxiv.

Koutarapu, S., Ge, J., Dulewicz, M., Srikrishna, M., Szadziewska, A., Wood, J., Blennow, K., Zetterberg, H., Michno, W., Ryan, N.S.*, et al.* (2025). Chemical imaging delineates Abeta plaque polymorphism across the Alzheimer's disease spectrum. Nat Commun 16, 3889.

Krahling, S., Callahan, M.K., Williamson, P., and Schlegel, R.A. (1999). Exposure of phosphatidylserine is a general feature in the phagocytosis of apoptotic lymphocytes by macrophages. Cell Death Differ 6, 183-189.

Krasemann, S., Madore, C., Cialic, R., Baufeld, C., Calcagno, N., El Fatimy, R., Beckers, L., O'Loughlin, E., Xu, Y., Fanek, Z.*, et al.* (2017). The TREM2-APOE Pathway Drives the Transcriptional Phenotype of Dysfunctional Microglia in Neurodegenerative Diseases. Immunity 47, 566-581 e569.

Kuhn, P.H., Wang, H., Dislich, B., Colombo, A., Zeitschel, U., Ellwart, J.W., Kremmer, E., Rossner, S., and Lichtenthaler, S.F. (2010). ADAM10 is the physiologically relevant,

constitutive alpha-secretase of the amyloid precursor protein in primary neurons. The EMBO journal 29, 3020-3032.

Kukull, W.A., Higdon, R., Bowen, J.D., McCormick, W.C., Teri, L., Schellenberg, G.D., van Belle, G., Jolley, L., and Larson, E.B. (2002). Dementia and Alzheimer disease incidence: a prospective cohort study. Arch Neurol 59, 1737-1746.

Kunkle, B.W., Grenier-Boley, B., Sims, R., Bis, J.C., Damotte, V., Naj, A.C., Boland, A., Vronskaya, M., van der Lee, S.J., Amlie-Wolf, A.*, et al.* (2019). Genetic meta-analysis of diagnosed Alzheimer's disease identifies new risk loci and implicates Abeta, tau, immunity and lipid processing. Nature genetics 51, 414-430.

Kuperstein, I., Broersen, K., Benilova, I., Rozenski, J., Jonckheere, W., Debulpaep, M., Vandersteen, A., Segers-Nolten, I., Van Der Werf, K., Subramaniam, V.*, et al.* (2010). Neurotoxicity of Alzheimer's disease Abeta peptides is induced by small changes in the Abeta42 to Abeta40 ratio. The EMBO journal 29, 3408-3420.

Lammich, S., Kojro, E., Postina, R., Gilbert, S., Pfeiffer, R., Jasionowski, M., Haass, C., and Fahrenholz, F. (1999). Constitutive and regulated alpha-secretase cleavage of Alzheimer's amyloid precursor protein by a disintegrin metalloprotease. P Natl Acad Sci USA 96, 3922-3927.

Laprell, L., Schulze, C., Brehme, M.L., and Oertner, T.G. (2021). The role of microglia membrane potential in chemotaxis. J Neuroinflamm 18, 21.

Lautrup, S., Lou, G., Aman, Y., Nilsen, H., Tao, J., and Fang, E.F. (2019). Microglial mitophagy mitigates neuroinflammation in Alzheimer's disease. Neurochem Int 129, 104469.

Lee, M., Bard, F., Johnson-Wood, K., Lee, C., Hu, K., Griffith, S.G., Black, R.S., Schenk, D., and Seubert, P. (2005). Abeta42 immunization in Alzheimer's disease generates Abeta N-terminal antibodies. Ann Neurol 58, 430-435.

Lee, M.K., and Chen, G. (2024). Loss of Cholinergic and Monoaminergic Afferents in APPswe/PS1DeltaE9 Transgenic Mouse Model of Cerebral Amyloidosis Preferentially Occurs Near Amyloid Plaques. Int J Mol Sci 25.

Lemere, C.A., Blusztajn, J.K., Yamaguchi, H., Wisniewski, T., Saido, T.C., and Selkoe, D.J. (1996). Sequence of deposition of heterogeneous amyloid beta-peptides and APO E in Down syndrome: implications for initial events in amyloid plaque formation. Neurobiol Dis 3, 16-32.

Lemke, G., and Huang, Y. (2022). The dense-core plaques of Alzheimer's disease are granulomas. J Exp Med 219.

Levy, E., Carman, M.D., Fernandez-Madrid, I.J., Power, M.D., Lieberburg, I., van Duinen, S.G., Bots, G.T., Luyendijk, W., and Frangione, B. (1990). Mutation of the Alzheimer's disease amyloid gene in hereditary cerebral hemorrhage, Dutch type. Science 248, 1124-1126.

Lewis, J., Dickson, D.W., Lin, W.L., Chisholm, L., Corral, A., Jones, G., Yen, S.H., Sahara, N., Skipper, L., Yager, D.*, et al.* (2001). Enhanced neurofibrillary degeneration in transgenic mice expressing mutant tau and APP. Science 293, 1487-1491.

Leyns, C.E.G., Gratuze, M., Narasimhan, S., Jain, N., Koscal, L.J., Jiang, H., Manis, M., Colonna, M., Lee, V.M.Y., Ulrich, J.D., and Holtzman, D.M. (2019). TREM2 function impedes tau seeding in neuritic plaques. Nat Neurosci 22, 1217-1222.

Leyns, C.E.G., Ulrich, J.D., Finn, M.B., Stewart, F.R., Koscal, L.J., Remolina Serrano, J., Robinson, G.O., Anderson, E., Colonna, M., and Holtzman, D.M. (2017). TREM2 deficiency attenuates neuroinflammation and protects against neurodegeneration in a mouse model of tauopathy. P Natl Acad Sci USA 114, 11524-11529.

Liao, F., Li, A., Xiong, M., Bien-Ly, N., Jiang, H., Zhang, Y., Finn, M.B., Hoyle, R., Keyser, J., Lefton, K.B*., et al.* (2018). Targeting of nonlipidated, aggregated apoE with antibodies inhibits amyloid accumulation. J Clin Invest 128, 2144-2155.

Libiger, O., Shaw, L.M., Watson, M.H., Nairn, A.C., Umana, K.L., Biarnes, M.C., Canet-Aviles, R.M., Jack, C.R., Jr., Breton, Y.A., Cortes, L*., et al.* (2021). Longitudinal CSF proteomics identifies NPTX2 as a prognostic biomarker of Alzheimer's disease. Alzheimers Dement 17, 1976-1987.

Linnartz-Gerlach, B., Bodea, L.G., Klaus, C., Ginolhac, A., Halder, R., Sinkkonen, L., Walter, J., Colonna, M., and Neumann, H. (2019). TREM2 triggers microglial density and age-related neuronal loss. Glia 67, 539-550.

Little, C.S., Hammond, C.J., MacIntyre, A., Balin, B.J., and Appelt, D.M. (2004). Chlamydia pneumoniae induces Alzheimer-like amyloid plaques in brains of BALB/c mice. Neurobiol Aging 25, 419-429.

Liu, F., Sun, J., Wang, X., Jin, S., Sun, F., Wang, T., Yuan, B., Qiu, W., and Ma, C. (2022). Focal-type, but not Diffuse-type, Amyloid Beta Plaques are Correlated with Alzheimer's Neuropathology, Cognitive Dysfunction, and Neuroinflammation in the Human Hippocampus. Neurosci Bull 38, 1125-1138.

Liu, K., and Czaja, M.J. (2013). Regulation of lipid stores and metabolism by lipophagy. Cell Death Differ 20, 3-11.

Liu, W., Taso, O., Wang, R., Bayram, S., Graham, A.C., Garcia-Reitboeck, P., Mallach, A., Andrews, W.D., Piers, T.M., Botia, J.A*., et al.* (2020). Trem2 promotes anti-inflammatory responses in microglia and is suppressed under pro-inflammatory conditions. Hum Mol Genet 29, 3224-3248.

Logiacco, F., Xia, P., Georgiev, S.V., Franconi, C., Chang, Y.J., Ugursu, B., Sporbert, A., Kuhn, R., Kettenmann, H., and Semtner, M. (2021). Microglia sense neuronal activity via GABA in the early postnatal hippocampus. Cell Rep 37, 110128.

Logovinsky, V., Satlin, A., Lai, R., Swanson, C., Kaplow, J., Osswald, G., Basun, H., and Lannfelt, L. (2016). Safety and tolerability of BAN2401--a clinical study in Alzheimer's disease with a protofibril selective Abeta antibody. Alzheimers Res Ther 8, 14.

Long, J.M., and Holtzman, D.M. (2019). Alzheimer Disease: An Update on Pathobiology and Treatment Strategies. Cell 179, 312-339.

Lord, A., Philipson, O., Klingstedt, T., Westermark, G., Hammarstrom, P., Nilsson, K.P., and Nilsson, L.N. (2011). Observations in APP bitransgenic mice suggest that diffuse and compact plaques form via independent processes in Alzheimer's disease. The American journal of pathology 178, 2286-2298.

Lowe, S.L., Duggan Evans, C., Shcherbinin, S., Cheng, Y.J., Willis, B.A., Gueorguieva, I., Lo, A.C., Fleisher, A.S., Dage, J.L., Ardayfio, P.*, et al.* (2021). Donanemab (LY3002813) Phase 1b Study in Alzheimer's Disease: Rapid and Sustained Reduction of Brain Amyloid Measured by Florbetapir F18 Imaging. J Prev Alzheimers Dis 8, 414-424.

Lue, L.-F., and Rogers, J. (2010). Full Complement Activation Fails in Diffuse Plaques of the Alzheimer's Disease Cerebellum. Dementia 3, 308-313.

Lue, L.F., Walker, D.G., Brachova, L., Beach, T.G., Rogers, J., Schmidt, A.M., Stern, D.M., and Yan, S.D. (2001). Involvement of microglial receptor for advanced glycation endproducts (RAGE) in Alzheimer's disease: identification of a cellular activation mechanism. Exp Neurol 171, 29-45.

Lui, H., Zhang, J., Makinson, S.R., Cahill, M.K., Kelley, K.W., Huang, H.Y., Shang, Y., Oldham, M.C., Martens, L.H., Gao, F.*, et al.* (2016). Progranulin Deficiency Promotes Circuit-Specific Synaptic Pruning by Microglia via Complement Activation. Cell 165, 921-935.

Luo, W., Liu, W., Hu, X., Hanna, M., Caravaca, A., and Paul, S.M. (2015). Microglial internalization and degradation of pathological tau is enhanced by an anti-tau monoclonal antibody. Sci Rep 5, 11161.

Luo, Y., Bolon, B., Kahn, S., Bennett, B.D., Babu-Khan, S., Denis, P., Fan, W., Kha, H., Zhang, J., Gong, Y.*, et al.* (2001). Mice deficient in BACE1, the Alzheimer's beta-secretase, have normal phenotype and abolished beta-amyloid generation. Nat Neurosci 4, 231-232.

Mabrouk, R., Gotkiewicz, M., Rauramaa, T., and Tanila, H. (2022). DAPI (4',6-diamidino-2-phenylindole) Stains Compact Amyloid Plaques. J Alzheimers Dis 88, 949-955.

Maiti, P., Bowers, Z., Bourcier-Schultz, A., Morse, J., and Dunbar, G.L. (2021). Preservation of dendritic spine morphology and postsynaptic signaling markers after treatment with solid lipid curcumin particles in the 5xFAD mouse model of Alzheimer's amyloidosis. Alzheimers Res Ther 13, 37.

Maiti, P., Plemmons, A., Bowers, Z., Weaver, C., and Dunbar, G. (2019). Labeling and Imaging of Amyloid Plaques in Brain Tissue Using the Natural Polyphenol Curcumin. Jove-J Vis Exp.

Malek-Ahmadi, M., Perez, S.E., Chen, K., and Mufson, E.J. (2016). Neuritic and Diffuse Plaque Associations with Memory in Non-Cognitively Impaired Elderly. J Alzheimers Dis 53, 1641-1652.

Maphis, N., Xu, G., Kokiko-Cochran, O.N., Jiang, S., Cardona, A., Ransohoff, R.M., Lamb, B.T., and Bhaskar, K. (2015). Reactive microglia drive tau pathology and contribute to the spreading of pathological tau in the brain. Brain 138, 1738-1755.

Marin-Teva, J.L., Dusart, I., Colin, C., Gervais, A., van Rooijen, N., and Mallat, M. (2004). Microglia promote the death of developing Purkinje cells. Neuron 41, 535-547.

Marschallinger, J., Iram, T., Zardeneta, M., Lee, S.E., Lehallier, B., Haney, M.S., Pluvinage, J.V., Mathur, V., Hahn, O., Morgens, D.W.*, et al.* (2020). Lipid-droplet-accumulating microglia represent a dysfunctional and proinflammatory state in the aging brain. Nat Neurosci 23, 194-208.

Masliah, E., Terry, R.D., Mallory, M., Alford, M., and Hansen, L.A. (1990). Diffuse plaques do not accentuate synapse loss in Alzheimer's disease. The American journal of pathology 137, 1293-1297.

Masters, C.L., Multhaup, G., Simms, G., Pottgiesser, J., Martins, R.N., and Beyreuther, K. (1985a). Neuronal origin of a cerebral amyloid: neurofibrillary tangles of Alzheimer's disease contain the same protein as the amyloid of plaque cores and blood vessels. The EMBO journal 4, 2757-2763.

Masters, C.L., Simms, G., Weinman, N.A., Multhaup, G., McDonald, B.L., and Beyreuther, K. (1985b). Amyloid plaque core protein in Alzheimer disease and Down syndrome. P Natl Acad Sci USA 82, 4245-4249.

Matarin, M., Salih, D.A., Yasvoina, M., Cummings, D.M., Guelfi, S., Liu, W., Nahaboo Solim, M.A., Moens, T.G., Paublete, R.M., Ali, S.S*., et al.* (2015). A genome-wide gene-expression analysis and database in transgenic mice during development of amyloid or tau pathology. Cell Rep 10, 633-644.

Mathys, H., Davila-Velderrain, J., Peng, Z., Gao, F., Mohammadi, S., Young, J.Z., Menon, M., He, L., Abdurrob, F., Jiang, X*., et al.* (2019). Single-cell transcriptomic analysis of Alzheimer's disease. Nature 570, 332-337.

Mattson, M.P., Barger, S.W., Cheng, B., Lieberburg, I., Smith-Swintosky, V.L., and Rydel, R.E. (1993). beta-Amyloid precursor protein metabolites and loss of neuronal Ca2+ homeostasis in Alzheimer's disease. Trends Neurosci 16, 409-414.

Maulik, M., Thinakaran, G., and Kar, S. (2013). Alterations in gene expression in mutant amyloid precursor protein transgenic mice lacking Niemann-Pick type C1 protein. Plos One 8, e54605.

Maynard, S., Hejl, A.M., Dinh, T.S., Keijzers, G., Hansen, A.M., Desler, C., Moreno-Villanueva, M., Burkle, A., Rasmussen, L.J., Waldemar, G., and Bohr, V.A. (2015). Defective mitochondrial respiration, altered dNTP pools and reduced AP endonuclease 1 activity in peripheral blood mononuclear cells of Alzheimer's disease patients. Aging (Albany NY) 7, 793-815.

McClatchy, D.B., Dong, M.Q., Wu, C.C., Venable, J.D., and Yates, J.R., 3rd (2007). 15N metabolic labeling of mammalian tissue with slow protein turnover. J Proteome Res 6, 2005-2010.

McKhann, G., Drachman, D., Folstein, M., Katzman, R., Price, D., and Stadlan, E.M. (1984). Clinical diagnosis of Alzheimer's disease: report of the NINCDS-ADRDA Work Group under the auspices of Department of Health and Human Services Task Force on Alzheimer's Disease. Neurology 34, 939-944.

McLellan, M.E., Kajdasz, S.T., Hyman, B.T., and Bacskai, B.J. (2003). In vivo imaging of reactive oxygen species specifically associated with thioflavine S-positive amyloid plaques by multiphoton microscopy. J Neurosci 23, 2212-2217.

McNamara, N.B., Munro, D.A.D., Bestard-Cuche, N., Uyeda, A., Bogie, J.F.J., Hoffmann, A., Holloway, R.K., Molina-Gonzalez, I., Askew, K.E., Mitchell, S*., et al.* (2023). Microglia regulate central nervous system myelin growth and integrity. Nature 613, 120-129.

Medawar, E., Benway, T.A., Liu, W., Hanan, T.A., Haslehurst, P., James, O.T., Yap, K., Muessig, L., Moroni, F., Nahaboo Solim, M.A*., et al.* (2019). Effects of rising amyloidbeta

levels on hippocampal synaptic transmission, microglial response and cognition in APPSwe/PSEN1M146V transgenic mice. EBioMedicine 39, 422-435.

Meilandt, W.J., Ngu, H., Gogineni, A., Lalehzadeh, G., Lee, S.H., Srinivasan, K., Imperio, J., Wu, T., Weber, M., Kruse, A.J.*, et al.* (2020). Trem2 Deletion Reduces Late-Stage Amyloid Plaque Accumulation, Elevates the Abeta42:Abeta40 Ratio, and Exacerbates Axonal Dystrophy and Dendritic Spine Loss in the PS2APP Alzheimer's Mouse Model. J Neurosci 40, 1956-1974.

Menassa, D.A., and Gomez-Nicola, D. (2018). Microglial Dynamics During Human Brain Development. Front Immunol 9, 1014.

Meyer-Luehmann, M., Coomaraswamy, J., Bolmont, T., Kaeser, S., Schaefer, C., Kilger, E., Neuenschwander, A., Abramowski, D., Frey, P., Jaton, A.L.*, et al.* (2006). Exogenous induction of cerebral beta-amyloidogenesis is governed by agent and host. Science 313, 1781-1784.

Meyer-Luehmann, M., Spires-Jones, T.L., Prada, C., Garcia-Alloza, M., de Calignon, A., Rozkalne, A., Koenigsknecht-Talboo, J., Holtzman, D.M., Bacskai, B.J., and Hyman, B.T. (2008). Rapid appearance and local toxicity of amyloid-beta plaques in a mouse model of Alzheimer's disease. Nature 451, 720-724.

Michno, W., Bowman, A., Jha, D., Minta, K., Ge, J., Koutarapu, S., Zetterberg, H., Blennow, K., Lashley, T., Heeren, R.M.A., and Hanrieder, J. (2024). Spatial Neurolipidomics at the Single Amyloid-beta Plaque Level in Postmortem Human Alzheimer's Disease Brain. ACS Chem Neurosci 15, 877-888.

Michno, W., Nyström, S., Wehrli, P., Lashley, T., Brinkmalm, G., Guerard, L., Syvänen, S., Sehlin, D., Kaya, I., Brinet, D.*, et al.* (2019a). Pyroglutamation of amyloid-βx-42 (Aβx-42) followed by Aβ1–40 deposition underlies plaque polymorphism in progressing Alzheimer’s disease pathology. Journal of Biological Chemistry 294, 6719-6732.

Michno, W., Stringer, K.M., Enzlein, T., Passarelli, M.K., Escrig, S., Vitanova, K., Wood, J., Blennow, K., Zetterberg, H., Meibom, A.*, et al.* (2021). Following spatial Abeta aggregation dynamics in evolving Alzheimer's disease pathology by imaging stable isotope labeling kinetics. Sci Adv 7, eabg4855.

Michno, W., Wehrli, P., Meier, S., Sehlin, D., Syvanen, S., Zetterberg, H., Blennow, K., and Hanrieder, J. (2019b). Chemical Imaging of Evolving Amyloid Plaque Pathology and Associated Abeta Peptide Aggregation in a Transgenic Mouse Model of Alzheimer's Disease. J Neurochem.

Michno, W., Wehrli, P., Meier, S.R., Sehlin, D., Syvänen, S., Zetterberg, H., Blennow, K., and Hanrieder, J. (2020). Chemical imaging of evolving amyloid plaque pathology and associated Aβ peptide aggregation in a transgenic mouse model of Alzheimer's disease. J Neurochem 152, 602-616.

Michno, W., Wehrli, P.M., Blennow, K., Zetterberg, H., and Hanrieder, J. (2018). Molecular imaging mass spectrometry for probing protein dynamics in neurodegenerative disease pathology. J Neurochem.

Miki, T., Yokota, O., Haraguchi, T., Ikeuchi, T., Zhu, B., Takenoshita, S., Terada, S., and Yamada, N. (2019). Young adult-onset, very slowly progressive cognitive decline with spastic paraparesis in Alzheimer's disease with cotton wool plaques due to a novel presenilin1 G417S mutation. Acta Neuropathol Commun 7, 19.

Mirra, S.S., Heyman, A., McKeel, D., Sumi, S.M., Crain, B.J., Brownlee, L.M., Vogel, F.S., Hughes, J.P., van Belle, G., and Berg, L. (1991). The Consortium to Establish a Registry for Alzheimer's Disease (CERAD). Part II. Standardization of the neuropathologic assessment of Alzheimer's disease. Neurology 41, 479-486.

Monroe, K.M., and Lewcock, J.W. (2023). Cleaning crew: Soluble TREM2 mops up complement. Immunity 56, 1701-1703.

Morgan, D., Diamond, D.M., Gottschall, P.E., Ugen, K.E., Dickey, C., Hardy, J., Duff, K., Jantzen, P., DiCarlo, G., Wilcock, D*., et al.* (2000). A beta peptide vaccination prevents memory loss in an animal model of Alzheimer's disease. Nature 408, 982-985.

Morris, G.P., Clark, I.A., and Vissel, B. (2014). Inconsistencies and controversies surrounding the amyloid hypothesis of Alzheimer's disease. Acta Neuropathol Commun 2, 135.

Mortazavi, A., Williams, B.A., McCue, K., Schaeffer, L., and Wold, B. (2008). Mapping and quantifying mammalian transcriptomes by RNA-Seq. Nature methods 5, 621-628.

Mosconi, L., De Santi, S., Li, J., Tsui, W.H., Li, Y., Boppana, M., Laska, E., Rusinek, H., and de Leon, M.J. (2008). Hippocampal hypometabolism predicts cognitive decline from normal aging. Neurobiol Aging 29, 676-692.

Mueller-Steiner, S., Zhou, Y., Arai, H., Roberson, E.D., Sun, B., Chen, J., Wang, X., Yu, G., Esposito, L., Mucke, L., and Gan, L. (2006). Antiamyloidogenic and neuroprotective functions of cathepsin B: implications for Alzheimer's disease. Neuron 51, 703-714.

Mullan, M., Crawford, F., Axelman, K., Houlden, H., Lilius, L., Winblad, B., and Lannfelt, L. (1992). A pathogenic mutation for probable Alzheimer's disease in the APP gene at the N-terminus of beta-amyloid. Nature genetics 1, 345-347.

Murphy, M.P., and LeVine, H., 3rd (2010). Alzheimer's disease and the amyloid-beta peptide. J Alzheimers Dis 19, 311-323.

Murray, M.E., and Dickson, D.W. (2014). Is pathological aging a successful resistance against amyloid-beta or preclinical Alzheimer's disease? Alzheimers Res Ther 6, 24.

Nagata, S., Sakuragi, T., and Segawa, K. (2020). Flippase and scramblase for phosphatidylserine exposure. Curr Opin Immunol 62, 31-38.

Nagata, S., Suzuki, J., Segawa, K., and Fujii, T. (2016). Exposure of phosphatidylserine on the cell surface. Cell Death Differ 23, 952-961.

Naureckiene, S., Sleat, D.E., Lackland, H., Fensom, A., Vanier, M.T., Wattiaux, R., Jadot, M., and Lobel, P. (2000). Identification of HE1 as the second gene of Niemann-Pick C disease. Science 290, 2298-2301.

Nauta, A.J., Bottazzi, B., Mantovani, A., Salvatori, G., Kishore, U., Schwaeble, W.J., Gingras, A.R., Tzima, S., Vivanco, F., Egido, J*., et al.* (2003). Biochemical and functional characterization of the interaction between pentraxin 3 and C1q. European journal of immunology 33, 465-473.

Navarro, J.F., Croteau, D.L., Jurek, A., Andrusivova, Z., Yang, B., Wang, Y., Ogedegbe, B., Riaz, T., Stoen, M., Desler, C*., et al.* (2020). Spatial Transcriptomics Reveals Genes

Associated with Dysregulated Mitochondrial Functions and Stress Signaling in Alzheimer Disease. iScience 23, 101556.

Nedelec, T., Couvy-Duchesne, B., Monnet, F., Daly, T., Ansart, M., Gantzer, L., Lekens, B., Epelbaum, S., Dufouil, C., and Durrleman, S. (2022). Identifying health conditions associated with Alzheimer's disease up to 15 years before diagnosis: an agnostic study of French and British health records. Lancet Digit Health 4, e169-e178.

Nguyen, H.M., Grossinger, E.M., Horiuchi, M., Davis, K.W., Jin, L.W., Maezawa, I., and Wulff, H. (2017). Differential Kv1.3, KCa3.1, and Kir2.1 expression in "classically" and "alternatively" activated microglia. Glia 65, 106-121.

Nicoll, J.A., Wilkinson, D., Holmes, C., Steart, P., Markham, H., and Weller, R.O. (2003). Neuropathology of human Alzheimer disease after immunization with amyloid-beta peptide: a case report. Nat Med 9, 448-452.

Nimmerjahn, A., Kirchhoff, F., and Helmchen, F. (2005). Resting microglial cells are highly dynamic surveillants of brain parenchyma in vivo. Science 308, 1314-1318.

Nimmo, J., Byrne, R.A.J., Daskoulidou, N., Watkins, L.M., Carpanini, S.M., Zelek, W.M., and Morgan, B.P. (2024). The complement system in neurodegenerative diseases. Clin Sci (Lond) 138, 387-412.

Nixon, R.A. (2004). Niemann-Pick Type C disease and Alzheimer's disease: the APP-endosome connection fattens up. The American journal of pathology 164, 757-761.

Nugent, A.A., Lin, K., van Lengerich, B., Lianoglou, S., Przybyla, L., Davis, S.S., Llapashtica, C., Wang, J., Kim, D.J., Xia, D.*, et al.* (2020). TREM2 Regulates Microglial Cholesterol Metabolism upon Chronic Phagocytic Challenge. Neuron 105, 837-854 e839.

Nystrom, S., Psonka-Antonczyk, K.M., Ellingsen, P.G., Johansson, L.B., Reitan, N., Handrick, S., Prokop, S., Heppner, F.L., Wegenast-Braun, B.M., Jucker, M.*, et al.* (2013). Evidence for age-dependent in vivo conformational rearrangement within Abeta amyloid deposits. Acs Chem Biol 8, 1128-1133.

Oddo, S., Billings, L., Kesslak, J.P., Cribbs, D.H., and LaFerla, F.M. (2004). Abeta immunotherapy leads to clearance of early, but not late, hyperphosphorylated tau aggregates via the proteasome. Neuron 43, 321-332.

Ohno, M., Cole, S.L., Yasvoina, M., Zhao, J., Citron, M., Berry, R., Disterhoft, J.F., and Vassar, R. (2007). BACE1 gene deletion prevents neuron loss and memory deficits in 5XFAD APP/PS1 transgenic mice. Neurobiol Dis 26, 134-145.

Olah, M., Menon, V., Habib, N., Taga, M.F., Ma, Y., Yung, C.J., Cimpean, M., Khairallah, A., Coronas-Samano, G., Sankowski, R.*, et al.* (2020). Single cell RNA sequencing of human microglia uncovers a subset associated with Alzheimer's disease. Nat Commun 11, 6129.

Olney, K.C., Gibson, K.A., Cadiz, M.P., Rahimzadeh, N., Swarup, V., and Fryer, J.D. (2025). Postmortem Interval Leads to Loss of Disease-Specific Signatures in Brain Tissue. eNeuro 12.

Olson, J.K., and Miller, S.D. (2004). Microglia initiate central nervous system innate and adaptive immune responses through multiple TLRs. J Immunol 173, 3916-3924.

Olzmann, J.A., and Carvalho, P. (2019). Dynamics and functions of lipid droplets. Nat Rev Mol Cell Biol 20, 137-155.

Paasila, P.J., Aramideh, J.A., Sutherland, G.T., and Graeber, M.B. (2021). Synapses, Microglia, and Lipids in Alzheimer's Disease. Front Neurosci 15, 778822.

Paidassi, H., Tacnet-Delorme, P., Garlatti, V., Darnault, C., Ghebrehiwet, B., Gaboriaud, C., Arlaud, G.J., and Frachet, P. (2008). C1q binds phosphatidylserine and likely acts as a multiligand-bridging molecule in apoptotic cell recognition. J Immunol 180, 2329-2338.

Paolicelli, R.C., Bolasco, G., Pagani, F., Maggi, L., Scianni, M., Panzanelli, P., Giustetto, M., Ferreira, T.A., Guiducci, E., Dumas, L.*, et al.* (2011). Synaptic pruning by microglia is necessary for normal brain development. Science 333, 1456-1458.

Papanikolaou, A., Graykowski, D., Lee, B.I., Yang, M., Ellingford, R., Zunkler, J., Bond, S.A., Rowland, J.M., Rajani, R.M., Harris, S.S.*, et al.* (2025). Selectively vulnerable deep cortical layer 5/6 fast-spiking interneurons in Alzheimer's disease models in vivo. Neuron.

Papazoglou, A., Henseler, C., Weickhardt, S., Teipelke, J., Papazoglou, P., Daubner, J., Schiffer, T., Krings, D., Broich, K., Hescheler, J.*, et al.* (2024). Sex- and region-specific cortical and hippocampal whole genome transcriptome profiles from control and APP/PS1 Alzheimer's disease mice. Plos One 19, e0296959.

Paresce, D.M., Chung, H., and Maxfield, F.R. (1997). Slow degradation of aggregates of the Alzheimer's disease amyloid beta-protein by microglial cells. The Journal of biological chemistry 272, 29390-29397.

Paresce, D.M., Ghosh, R.N., and Maxfield, F.R. (1996). Microglial cells internalize aggregates of the Alzheimer's disease amyloid beta-protein via a scavenger receptor. Neuron 17, 553-565.

Parhizkar, S., Arzberger, T., Brendel, M., Kleinberger, G., Deussing, M., Focke, C., Nuscher, B., Xiong, M., Ghasemigharagoz, A., Katzmarski, N.*, et al.* (2019). Loss of TREM2 function increases amyloid seeding but reduces plaque-associated ApoE. Nat Neurosci 22, 191-204.

Park, J., Choi, Y., Jung, E., Lee, S.H., Sohn, J.W., and Chung, W.S. (2021). Microglial MERTK eliminates phosphatidylserine-displaying inhibitory post-synapses. The EMBO journal 40, e107121.

Park, J.C., Han, J.W., Lee, W., Kim, J., Lee, S.E., Lee, D., Choi, H., Han, J., Kang, Y.J., Diep, Y.N.*, et al.* (2024). Microglia Gravitate toward Amyloid Plaques Surrounded by Externalized Phosphatidylserine via TREM2. Adv Sci (Weinh) 11, e2400064.

Parvin, F., Haglund, S., Wegenast-Braun, B., Jucker, M., Saito, T., Saido, T.C., Nilsson, K.P.R., Nilsson, P., Nystrom, S., and Hammarstrom, P. (2024). Divergent Age-Dependent Conformational Rearrangement within Abeta Amyloid Deposits in APP23, APPPS1, and App(NL-F) Mice. ACS Chem Neurosci 15, 2058-2069.

Pedersen, T.J., Keil, S.A., Han, W., Wang, M.X., and Iliff, J.J. (2023). The effect of aquaporin-4 mis-localization on Abeta deposition in mice. Neurobiol Dis 181, 106100.

Peng, W., Yuan, Y., Lei, J., Zhao, Y., Li, Y., Qu, Q., and Wang, J. (2024). Long-Term High-Fat Diet Impairs AQP4-Mediated Glymphatic Clearance of Amyloid Beta. Mol Neurobiol.

Petkau, T.L., Kosior, N., de Asis, K., Connolly, C., and Leavitt, B.R. (2017). Selective depletion of microglial progranulin in mice is not sufficient to cause neuronal ceroid lipofuscinosis or neuroinflammation. J Neuroinflamm 14, 225.

Petkau, T.L., Neal, S.J., Orban, P.C., MacDonald, J.L., Hill, A.M., Lu, G., Feldman, H.H., Mackenzie, I.R., and Leavitt, B.R. (2010). Progranulin expression in the developing and adult murine brain. J Comp Neurol 518, 3931-3947.

Plant, L.D., Boyle, J.P., Smith, I.F., Peers, C., and Pearson, H.A. (2003). The production of amyloid beta peptide is a critical requirement for the viability of central neurons. J Neurosci 23, 5531-5535.

Postina, R., Schroeder, A., Dewachter, I., Bohl, J., Schmitt, U., Kojro, E., Prinzen, C., Endres, K., Hiemke, C., Blessing, M.*, et al.* (2004). A disintegrin-metalloproteinase prevents amyloid plaque formation and hippocampal defects in an Alzheimer disease mouse model. J Clin Invest 113, 1456-1464.

Prakash, P., Manchanda, P., Paouri, E., Bisht, K., Sharma, K., Rajpoot, J., Wendt, V., Hossain, A., Wijewardhane, P.R., Randolph, C.E.*, et al.* (2024). Amyloid beta Induces Lipid Droplet-Mediated Microglial Dysfunction in Alzheimer's Disease. bioRxiv.

Pretorius, E., Page, M.J., Hendricks, L., Nkosi, N.B., Benson, S.R., and Kell, D.B. (2018). Both lipopolysaccharide and lipoteichoic acids potently induce anomalous fibrin amyloid formation: assessment with novel Amytracker stains. J R Soc Interface 15.

Puzzo, D., Privitera, L., Fa, M., Staniszewski, A., Hashimoto, G., Aziz, F., Sakurai, M., Ribe, E.M., Troy, C.M., Mercken, M.*, et al.* (2011). Endogenous amyloid-beta is necessary for hippocampal synaptic plasticity and memory. Ann Neurol 69, 819-830.

Puzzo, D., Privitera, L., Leznik, E., Fa, M., Staniszewski, A., Palmeri, A., and Arancio, O. (2008). Picomolar amyloid-beta positively modulates synaptic plasticity and memory in hippocampus. J Neurosci 28, 14537-14545.

Qin, L., Wu, X., Block, M.L., Liu, Y., Breese, G.R., Hong, J.S., Knapp, D.J., and Crews, F.T. (2007). Systemic LPS causes chronic neuroinflammation and progressive neurodegeneration. Glia 55, 453-462.

Qu, Y., Hu, H.-Y., Ou, Y.-N., Shen, X.-N., Xu, W., Wang, Z.-T., Dong, Q., Tan, L., and Yu, J.-T. (2020). Association of body mass index with risk of cognitive impairment and dementia: A systematic review and meta-analysis of prospective studies. Neuroscience & Biobehavioral Reviews 115, 189-198.

Rasmussen, J., Mahler, J., Beschorner, N., Kaeser, S.A., Hasler, L.M., Baumann, F., Nystrom, S., Portelius, E., Blennow, K., Lashley, T.*, et al.* (2017). Amyloid polymorphisms constitute distinct clouds of conformational variants in different etiological subtypes of Alzheimer's disease. P Natl Acad Sci USA 114, 13018-13023.

Raulin, A.C., Doss, S.V., Trottier, Z.A., Ikezu, T.C., Bu, G., and Liu, C.C. (2022). ApoE in Alzheimer's disease: pathophysiology and therapeutic strategies. Mol Neurodegener 17, 72.

Reed-Geaghan, E.G., Savage, J.C., Hise, A.G., and Landreth, G.E. (2009). CD14 and toll-like receptors 2 and 4 are required for fibrillar A{beta}-stimulated microglial activation. J Neurosci 29, 11982-11992.

Reifschneider, A., Robinson, S., van Lengerich, B., Gnorich, J., Logan, T., Heindl, S., Vogt, M.A., Weidinger, E., Riedl, L., Wind, K.*, et al.* (2022). Loss of TREM2 rescues hyperactivation of microglia, but not lysosomal deficits and neurotoxicity in models of progranulin deficiency. The EMBO journal 41, e109108.

Rijal Upadhaya, A., Kosterin, I., Kumar, S., von Arnim, C.A., Yamaguchi, H., Fandrich, M., Walter, J., and Thal, D.R. (2014). Biochemical stages of amyloid-beta peptide aggregation and accumulation in the human brain and their association with symptomatic and pathologically preclinical Alzheimer's disease. Brain 137, 887-903.

Rohr, D., Boon, B.D.C., Schuler, M., Kremer, K., Hoozemans, J.J.M., Bouwman, F.H., El-Mashtoly, S.F., Nabers, A., Grosserueschkamp, F., Rozemuller, A.J.M., and Gerwert, K. (2020). Label-free vibrational imaging of different Abeta plaque types in Alzheimer's disease reveals sequential events in plaque development. Acta Neuropathol Commun 8, 222.

Root, J., Mendsaikhan, A., Taylor, G., Merino, P., Nandy, S., Wang, M., Araujo, L.T., Ryu, D., Holler, C., Thompson, B.M.*, et al.* (2024). Granulins rescue inflammation, lysosome dysfunction, lipofuscin, and neuropathology in a mouse model of progranulin deficiency. Cell Rep 43, 114985.

Rozemuller, J.M., Eikelenboom, P., Stam, F.C., Beyreuther, K., and Masters, C.L. (1989). A4 protein in Alzheimer's disease: primary and secondary cellular events in extracellular amyloid deposition. J Neuropathol Exp Neurol 48, 674-691.

Rueda-Carrasco, J., Sokolova, D., Lee, S.E., Childs, T., Jurcakova, N., Crowley, G., De Schepper, S., Ge, J.Z., Lachica, J.I., Toomey, C.E.*, et al.* (2023). Microglia-synapse engulfment via PtdSer-TREM2 ameliorates neuronal hyperactivity in Alzheimer's disease models. The EMBO journal, e113246.

Saito, T., Matsuba, Y., Mihira, N., Takano, J., Nilsson, P., Itohara, S., Iwata, N., and Saido, T.C. (2014). Single App knock-in mouse models of Alzheimer's disease. Nat Neurosci 17, 661-663.

Saito, T., Matsuba, Y., Yamazaki, N., Hashimoto, S., and Saido, T.C. (2016). Calpain Activation in Alzheimer's Model Mice Is an Artifact of APP and Presenilin Overexpression. J Neurosci 36, 9933-9936.

Salih, D.A., Bayram, S., Guelfi, S., Reynolds, R.H., Shoai, M., Ryten, M., Brenton, J.W., Zhang, D., Matarin, M., Botia, J.A.*, et al.* (2019). Genetic variability in response to amyloid beta deposition influences Alzheimer's disease risk. Brain Commun 1, fcz022.

Sapar, M.L., Ji, H., Wang, B., Poe, A.R., Dubey, K., Ren, X., Ni, J.Q., and Han, C. (2018). Phosphatidylserine Externalization Results from and Causes Neurite Degeneration in Drosophila. Cell Rep 24, 2273-2286.

Sasaguri, H., Nilsson, P., Hashimoto, S., Nagata, K., Saito, T., De Strooper, B., Hardy, J., Vassar, R., Winblad, B., and Saido, T.C. (2017). APP mouse models for Alzheimer's disease preclinical studies. The EMBO journal 36, 2473-2487.

Satoh, J., Kino, Y., Asahina, N., Takitani, M., Miyoshi, J., Ishida, T., and Saito, Y. (2016). TMEM119 marks a subset of microglia in the human brain. Neuropathology 36, 39-49.

Satoh, J., Kino, Y., Kawana, N., Yamamoto, Y., Ishida, T., Saito, Y., and Arima, K. (2014). TMEM106B expression is reduced in Alzheimer's disease brains. Alzheimers Res Ther 6, 17.

Schafer, D.P., Lehrman, E.K., Kautzman, A.G., Koyama, R., Mardinly, A.R., Yamasaki, R., Ransohoff, R.M., Greenberg, M.E., Barres, B.A., and Stevens, B. (2012). Microglia sculpt postnatal neural circuits in an activity and complement-dependent manner. Neuron 74, 691-705.

Schenk, D., Barbour, R., Dunn, W., Gordon, G., Grajeda, H., Guido, T., Hu, K., Huang, J., Johnson-Wood, K., Khan, K.*, et al.* (1999). Immunization with amyloid-beta attenuates Alzheimer-disease-like pathology in the PDAPP mouse. Nature 400, 173-177.

Schindelin, J., Arganda-Carreras, I., Frise, E., Kaynig, V., Longair, M., Pietzsch, T., Preibisch, S., Rueden, C., Saalfeld, S., Schmid, B.*, et al.* (2012). Fiji: an open-source platform for biological-image analysis. Nature methods 9, 676-682.

Schmidt, M.L., Robinson, K.A., Lee, V.M., and Trojanowski, J.Q. (1995). Chemical and immunological heterogeneity of fibrillar amyloid in plaques of Alzheimer's disease and Down's syndrome brains revealed by confocal microscopy. The American journal of pathology 147, 503-515.

Scott-Hewitt, N., Perrucci, F., Morini, R., Erreni, M., Mahoney, M., Witkowska, A., Carey, A., Faggiani, E., Schuetz, L.T., Mason, S.*, et al.* (2020). Local externalization of phosphatidylserine mediates developmental synaptic pruning by microglia. The EMBO journal 39, e105380.

Sekar, A., Bialas, A.R., de Rivera, H., Davis, A., Hammond, T.R., Kamitaki, N., Tooley, K., Presumey, J., Baum, M., Van Doren, V.*, et al.* (2016). Schizophrenia risk from complex variation of complement component 4. Nature 530, 177-183.

Serrano-Pozo, A., Betensky, R.A., Frosch, M.P., and Hyman, B.T. (2016). Plaque-Associated Local Toxicity Increases over the Clinical Course of Alzheimer Disease. The American journal of pathology 186, 375-384.

Serrano-Pozo, A., Frosch, M.P., Masliah, E., and Hyman, B.T. (2011a). Neuropathological alterations in Alzheimer disease. Cold Spring Harbor perspectives in medicine 1, a006189.

Serrano-Pozo, A., Mielke, M.L., Gomez-Isla, T., Betensky, R.A., Growdon, J.H., Frosch, M.P., and Hyman, B.T. (2011b). Reactive glia not only associates with plaques but also parallels tangles in Alzheimer's disease. The American journal of pathology 179, 1373-1384.

Sevigny, J., Chiao, P., Bussiere, T., Weinreb, P.H., Williams, L., Maier, M., Dunstan, R., Salloway, S., Chen, T., Ling, Y.*, et al.* (2016). The antibody aducanumab reduces Abeta plaques in Alzheimer's disease. Nature 537, 50-56.

Shah, P., Lal, N., Leung, E., Traul, D.E., Gonzalo-Ruiz, A., and Geula, C. (2010). Neuronal and axonal loss are selectively linked to fibrillar amyloid-{beta} within plaques of the aged primate cerebral cortex. The American journal of pathology 177, 325-333.

Sheng, J., Su, L., Xu, Z., and Chen, G. (2014). Progranulin polymorphism rs5848 is associated with increased risk of Alzheimer's disease. Gene 542, 141-145.

Sherrington, R., Rogaev, E.I., Liang, Y., Rogaeva, E.A., Levesque, G., Ikeda, M., Chi, H., Lin, C., Li, G., Holman, K.*, et al.* (1995). Cloning of a gene bearing missense mutations in early-onset familial Alzheimer's disease. Nature 375, 754-760.

Shi, Q., Chowdhury, S., Ma, R., Le, K.X., Hong, S., Caldarone, B.J., Stevens, B., and Lemere, C.A. (2017). Complement C3 deficiency protects against neurodegeneration in aged plaque-rich APP/PS1 mice. Sci Transl Med 9.

Sierra, A., Encinas, J.M., Deudero, J.J., Chancey, J.H., Enikolopov, G., Overstreet-Wadiche, L.S., Tsirka, S.E., and Maletic-Savatic, M. (2010). Microglia shape adult hippocampal neurogenesis through apoptosis-coupled phagocytosis. Cell Stem Cell 7, 483-495.

Sigurdson, C.J., Nilsson, K.P., Hornemann, S., Manco, G., Polymenidou, M., Schwarz, P., Leclerc, M., Hammarstrom, P., Wuthrich, K., and Aguzzi, A. (2007). Prion strain discrimination using luminescent conjugated polymers. Nature methods 4, 1023-1030.

Sims, J.R., Zimmer, J.A., Evans, C.D., Lu, M., Ardayfio, P., Sparks, J., Wessels, A.M., Shcherbinin, S., Wang, H., Monkul Nery, E.S.*, et al.* (2023). Donanemab in Early Symptomatic Alzheimer Disease: The TRAILBLAZER-ALZ 2 Randomized Clinical Trial. JAMA 330, 512-527.

Smith, K.R., Damiano, J., Franceschetti, S., Carpenter, S., Canafoglia, L., Morbin, M., Rossi, G., Pareyson, D., Mole, S.E., Staropoli, J.F.*, et al.* (2012). Strikingly different clinicopathological phenotypes determined by progranulin-mutation dosage. American journal of human genetics 90, 1102-1107.

Smith, L.K., He, Y., Park, J.S., Bieri, G., Snethlage, C.E., Lin, K., Gontier, G., Wabl, R., Plambeck, K.E., Udeochu, J.*, et al.* (2015). beta2-microglobulin is a systemic pro-aging factor that impairs cognitive function and neurogenesis. Nat Med 21, 932-937.

Snowden, S.G., Ebshiana, A.A., Hye, A., An, Y., Pletnikova, O., O'Brien, R., Troncoso, J., Legido-Quigley, C., and Thambisetty, M. (2017). Association between fatty acid metabolism in the brain and Alzheimer disease neuropathology and cognitive performance: A nontargeted metabolomic study. PLoS Med 14, e1002266.

Snyder, S.W., Wang, G.T., Barrett, L., Ladror, U.S., Casuto, D., Lee, C.M., Krafft, G.A., Holzman, R.B., and Holzman, T.F. (1994). Complement C1q does not bind monomeric beta-amyloid. Exp Neurol 128, 136-142.

Society, A.s. (2024). Alzheimer’s Society Report 2023/24.

Soldan, A., Moghekar, A., Walker, K.A., Pettigrew, C., Hou, X., Lu, H., Miller, M.I., Alfini, A., Albert, M., Xu, D.*, et al.* (2019). Resting-State Functional Connectivity Is Associated With Cerebrospinal Fluid Levels of the Synaptic Protein NPTX2 in Non-demented Older Adults. Front Aging Neurosci 11, 132.

Sorrentino, F., Arighi, A., Serpente, M., Arosio, B., Arcaro, M., Visconte, C., Rotondo, E., Vimercati, R., Ferri, E., Fumagalli, G.G.*, et al.* (2021). Niemann-Pick Type C 1 (NPC1) and NPC2 Gene Variability in Demented Patients with Evidence of Brain Amyloid Deposition. J Alzheimers Dis 83, 1313-1323.

Soscia, S.J., Kirby, J.E., Washicosky, K.J., Tucker, S.M., Ingelsson, M., Hyman, B., Burton, M.A., Goldstein, L.E., Duong, S., Tanzi, R.E., and Moir, R.D. (2010). The Alzheimer's disease-associated amyloid beta-protein is an antimicrobial peptide. Plos One 5, e9505.

Sousa, C., Golebiewska, A., Poovathingal, S.K., Kaoma, T., Pires-Afonso, Y., Martina, S., Coowar, D., Azuaje, F., Skupin, A., Balling, R.*, et al.* (2018). Single-cell transcriptomics reveals distinct inflammation-induced microglia signatures. EMBO Rep 19.

Spangenberg, E., Severson, P.L., Hohsfield, L.A., Crapser, J., Zhang, J., Burton, E.A., Zhang, Y., Spevak, W., Lin, J., Phan, N.Y.*, et al.* (2019). Sustained microglial depletion with CSF1R inhibitor impairs parenchymal plaque development in an Alzheimer's disease model. Nat Commun 10, 3758.

Spangenberg, E.E., Lee, R.J., Najafi, A.R., Rice, R.A., Elmore, M.R., Blurton-Jones, M., West, B.L., and Green, K.N. (2016). Eliminating microglia in Alzheimer's mice prevents neuronal loss without modulating amyloid-beta pathology. Brain 139, 1265-1281.

Spires, T.L., Grote, H.E., Garry, S., Cordery, P.M., Van Dellen, A., Blakemore, C., and Hannan, A.J. (2004). Dendritic spine pathology and deficits in experience-dependent dendritic plasticity in R6/1 Huntington's disease transgenic mice. Eur J Neurosci 19, 2799-2807.

Spires, T.L., Meyer-Luehmann, M., Stern, E.A., McLean, P.J., Skoch, J., Nguyen, P.T., Bacskai, B.J., and Hyman, B.T. (2005). Dendritic spine abnormalities in amyloid precursor protein transgenic mice demonstrated by gene transfer and intravital multiphoton microscopy. J Neurosci 25, 7278-7287.

Spires-Jones, T.L., Meyer-Luehmann, M., Osetek, J.D., Jones, P.B., Stern, E.A., Bacskai, B.J., and Hyman, B.T. (2007). Impaired spine stability underlies plaque-related spine loss in an Alzheimer's disease mouse model. The American journal of pathology 171, 1304-1311.

Squarzoni, P., Oller, G., Hoeffel, G., Pont-Lezica, L., Rostaing, P., Low, D., Bessis, A., Ginhoux, F., and Garel, S. (2014). Microglia modulate wiring of the embryonic forebrain. Cell Rep 8, 1271-1279.

Srinivasan, K., Friedman, B.A., Etxeberria, A., Huntley, M.A., van der Brug, M.P., Foreman, O., Paw, J.S., Modrusan, Z., Beach, T.G., Serrano, G.E., and Hansen, D.V. (2020). Alzheimer's Patient Microglia Exhibit Enhanced Aging and Unique Transcriptional Activation. Cell Rep 31, 107843.

Stahl, P.L., Salmen, F., Vickovic, S., Lundmark, A., Navarro, J.F., Magnusson, J., Giacomello, S., Asp, M., Westholm, J.O., Huss, M.*, et al.* (2016). Visualization and analysis of gene expression in tissue sections by spatial transcriptomics. Science 353, 78-82.

Stalder, M., Phinney, A., Probst, A., Sommer, B., Staufenbiel, M., and Jucker, M. (1999). Association of microglia with amyloid plaques in brains of APP23 transgenic mice. The American journal of pathology 154, 1673-1684.

Stam, F.C., Wigboldus, J.M., and Smeulders, A.W. (1986). Age incidence of senile brain amyloidosis. Pathol Res Pract 181, 558-562.

Stevens, B., Allen, N.J., Vazquez, L.E., Howell, G.R., Christopherson, K.S., Nouri, N., Micheva, K.D., Mehalow, A.K., Huberman, A.D., Stafford, B.*, et al.* (2007). The classical complement cascade mediates CNS synapse elimination. Cell 131, 1164-1178.

Storch, J., and Xu, Z. (2009). Niemann-Pick C2 (NPC2) and intracellular cholesterol trafficking. Biochim Biophys Acta 1791, 671-678.

Strittmatter, W.J., Saunders, A.M., Schmechel, D., Pericak-Vance, M., Enghild, J., Salvesen, G.S., and Roses, A.D. (1993). Apolipoprotein E: high-avidity binding to beta-amyloid and increased frequency of type 4 allele in late-onset familial Alzheimer disease. P Natl Acad Sci USA 90, 1977-1981.

Su, Y., and Chang, P.T. (2001). Acidic pH promotes the formation of toxic fibrils from beta-amyloid peptide. Brain Res 893, 287-291.

Suire, C.N., Abdul-Hay, S.O., Sahara, T., Kang, D., Brizuela, M.K., Saftig, P., Dickson, D.W., Rosenberry, T.L., and Leissring, M.A. (2020). Cathepsin D regulates cerebral Abeta42/40 ratios via differential degradation of Abeta42 and Abeta40. Alzheimers Res Ther 12, 80.

Sulatsky, M.I., Stepanenko, O.V., Stepanenko, O.V., Mikhailova, E.V., and Sulatskaya, A.I. (2025). From protective enzyme to facilitator of amyloid propagation: Cathepsin D-mediated amyloid fibril fragmentation. Int J Biol Macromol 304, 140971.

Summers, W.K., Majovski, L.V., Marsh, G.M., Tachiki, K., and Kling, A. (1986). Oral tetrahydroaminoacridine in long-term treatment of senile dementia, Alzheimer type. N Engl J Med 315, 1241-1245.

Sun, N., Akay, L.A., Murdock, M.H., Park, Y., Galiana-Melendez, F., Bubnys, A., Galani, K., Mathys, H., Jiang, X., Ng, A.P.*, et al.* (2023). Single-nucleus multiregion transcriptomic analysis of brain vasculature in Alzheimer's disease. Nat Neurosci 26, 970-982.

Swanson, C.J., Zhang, Y., Dhadda, S., Wang, J., Kaplow, J., Lai, R.Y.K., Lannfelt, L., Bradley, H., Rabe, M., Koyama, A.*, et al.* (2021). A randomized, double-blind, phase 2b proof-of-concept clinical trial in early Alzheimer's disease with lecanemab, an anti-Abeta protofibril antibody. Alzheimers Res Ther 13, 80.

Sze, C.I., Troncoso, J.C., Kawas, C., Mouton, P., Price, D.L., and Martin, L.J. (1997). Loss of the presynaptic vesicle protein synaptophysin in hippocampus correlates with cognitive decline in Alzheimer disease. J Neuropathol Exp Neurol 56, 933-944.

Tahara, K., Kim, H.D., Jin, J.J., Maxwell, J.A., Li, L., and Fukuchi, K. (2006). Role of toll-like receptor signalling in Abeta uptake and clearance. Brain 129, 3006-3019.

Takahashi, H., Bhagwagar, S., Nies, S.H., Ye, H., Han, X., Chiasseu, M.T., Wang, G., Mackenzie, I.R., and Strittmatter, S.M. (2024). Reduced progranulin increases tau and alpha-synuclein inclusions and alters mouse tauopathy phenotypes via glucocerebrosidase. Nat Commun 15, 1434.

Takahashi, K., Rochford, C.D., and Neumann, H. (2005). Clearance of apoptotic neurons without inflammation by microglial triggering receptor expressed on myeloid cells-2. J Exp Med 201, 647-657.

Tang, F., Barbacioru, C., Wang, Y., Nordman, E., Lee, C., Xu, N., Wang, X., Bodeau, J., Tuch, B.B., Siddiqui, A.*, et al.* (2009). mRNA-Seq whole-transcriptome analysis of a single cell. Nature methods 6, 377-382.

Tang, Z., Chuang, K.V., DeCarli, C., Jin, L.W., Beckett, L., Keiser, M.J., and Dugger, B.N. (2019). Interpretable classification of Alzheimer's disease pathologies with a convolutional neural network pipeline. Nat Commun 10, 2173.

Terron, H.M., Parikh, S.J., Abdul-Hay, S.O., Sahara, T., Kang, D., Dickson, D.W., Saftig, P., LaFerla, F.M., Lane, S., and Leissring, M.A. (2024). Prominent tauopathy and intracellular beta-amyloid accumulation triggered by genetic deletion of cathepsin D: implications for Alzheimer disease pathogenesis. Alzheimers Res Ther 16, 70.

Terwel, D., Steffensen, K.R., Verghese, P.B., Kummer, M.P., Gustafsson, J.A., Holtzman, D.M., and Heneka, M.T. (2011). Critical role of astroglial apolipoprotein E and liver X receptor-alpha expression for microglial Abeta phagocytosis. J Neurosci 31, 7049-7059.

Thal, D.R., Capetillo-Zarate, E., Del Tredici, K., and Braak, H. (2006). The development of amyloid beta protein deposits in the aged brain. Sci Aging Knowledge Environ 2006, re1.

Theodoropoulou, M.K., Vraila, K.D., Papandreou, N.C., Nasi, G.I., and Iconomidou, V.A. (2024). Co-Localized in Amyloid Plaques Cathepsin B as a Source of Peptide Analogs Potential Drug Candidates for Alzheimer's Disease. Biomolecules 15.

Timofeeva, Y., and Volynski, K.E. (2015). Calmodulin as a major calcium buffer shaping vesicular release and short-term synaptic plasticity: facilitation through buffer dislocation. Front Cell Neurosci 9, 239.

Tomita, H., Vawter, M.P., Walsh, D.M., Evans, S.J., Choudary, P.V., Li, J., Overman, K.M., Atz, M.E., Myers, R.M., Jones, E.G.*, et al.* (2004). Effect of agonal and postmortem factors on gene expression profile: quality control in microarray analyses of postmortem human brain. Biol Psychiatry 55, 346-352.

Tsai, J., Grutzendler, J., Duff, K., and Gan, W.B. (2004). Fibrillar amyloid deposition leads to local synaptic abnormalities and breakage of neuronal branches. Nat Neurosci 7, 1181-1183.

Tsering, W., de la Rosa, A., Ruan, I.Y., Philips, J.L., Bathe, T., Villareal, J.A., and Prokop, S. (2025). Preferential clustering of microglia and astrocytes around neuritic plaques during progression of Alzheimer's disease neuropathological changes. J Neurochem 169, e16275.

Tzioras, M., Daniels, M.J.D., Davies, C., Baxter, P., King, D., McKay, S., Varga, B., Popovic, K., Hernandez, M., Stevenson, A.J.*, et al.* (2023). Human astrocytes and microglia show augmented ingestion of synapses
in Alzheimer’s disease via MFG-E8. BioRXiv.

Ulland, T.K., Song, W.M., Huang, S.C., Ulrich, J.D., Sergushichev, A., Beatty, W.L., Loboda, A.A., Zhou, Y., Cairns, N.J., Kambal, A.*, et al.* (2017). TREM2 Maintains Microglial Metabolic Fitness in Alzheimer's Disease. Cell 170, 649-663 e613.

Ulrich, J.D., Ulland, T.K., Mahan, T.E., Nystrom, S., Nilsson, K.P., Song, W.M., Zhou, Y., Reinartz, M., Choi, S., Jiang, H.*, et al.* (2018). ApoE facilitates the microglial response to amyloid plaque pathology. J Exp Med 215, 1047-1058.

Umpierre, A.D., Bystrom, L.L., Ying, Y., Liu, Y.U., Worrell, G., and Wu, L.J. (2020). Microglial calcium signaling is attuned to neuronal activity in awake mice. Elife 9.

van der Kant, R., Langness, V.F., Herrera, C.M., Williams, D.A., Fong, L.K., Leestemaker, Y., Steenvoorden, E., Rynearson, K.D., Brouwers, J.F., Helms, J.B.*, et al.* (2019). Cholesterol Metabolism Is a Druggable Axis that Independently Regulates Tau and Amyloid-beta in iPSC-Derived Alzheimer's Disease Neurons. Cell Stem Cell 24, 363-375 e369.

van Dyck, C.H., Swanson, C.J., Aisen, P., Bateman, R.J., Chen, C., Gee, M., Kanekiyo, M., Li, D., Reyderman, L., Cohen, S.*, et al.* (2023). Lecanemab in Early Alzheimer's Disease. N Engl J Med 388, 9-21.

Vankriekelsvenne, E., Chrzanowski, U., Manzhula, K., Greiner, T., Wree, A., Hawlitschka, A., Llovera, G., Zhan, J., Joost, S., Schmitz, C.*, et al.* (2022). Transmembrane protein 119 is neither a specific nor a reliable marker for microglia. Glia 70, 1170-1190.

Varma, V.R., Busra Luleci, H., Oommen, A.M., Varma, S., Blackshear, C.T., Griswold, M.E., An, Y., Roberts, J.A., O'Brien, R., Pletnikova, O.*, et al.* (2021). Abnormal brain cholesterol homeostasis in Alzheimer's disease-a targeted metabolomic and transcriptomic study. NPJ Aging Mech Dis 7, 11.

Vassar, R., Bennett, B.D., Babu-Khan, S., Kahn, S., Mendiaz, E.A., Denis, P., Teplow, D.B., Ross, S., Amarante, P., Loeloff, R.*, et al.* (1999). Beta-secretase cleavage of Alzheimer's amyloid precursor protein by the transmembrane aspartic protease BACE. Science 286, 735-741.

Vellas, B., Black, R., Thal, L.J., Fox, N.C., Daniels, M., McLennan, G., Tompkins, C., Leibman, C., Pomfret, M., Grundman, M., and Team, A.N.S. (2009). Long-term follow-up of patients immunized with AN1792: reduced functional decline in antibody responders. Curr Alzheimer Res 6, 144-151.

Venegas, C., Kumar, S., Franklin, B.S., Dierkes, T., Brinkschulte, R., Tejera, D., Vieira-Saecker, A., Schwartz, S., Santarelli, F., Kummer, M.P.*, et al.* (2017). Microglia-derived ASC specks cross-seed amyloid-beta in Alzheimer's disease. Nature 552, 355-361.

Vidak, E., Javorsek, U., Vizovisek, M., and Turk, B. (2019). Cysteine Cathepsins and their Extracellular Roles: Shaping the Microenvironment. Cells 8.

Vizovisek, M., Fonovic, M., and Turk, B. (2019). Cysteine cathepsins in extracellular matrix remodeling: Extracellular matrix degradation and beyond. Matrix Biol 75-76, 141-159.

Vogel, J.W., La Joie, R., Grothe, M.J., Diaz-Papkovich, A., Doyle, A., Vachon-Presseau, E., Lepage, C., Vos de Wael, R., Thomas, R.A., Iturria-Medina, Y.*, et al.* (2020). A molecular gradient along the longitudinal axis of the human hippocampus informs large-scale behavioral systems. Nat Commun 11, 960.

Wakselman, S., Bechade, C., Roumier, A., Bernard, D., Triller, A., and Bessis, A. (2008). Developmental neuronal death in hippocampus requires the microglial CD11b integrin and DAP12 immunoreceptor. J Neurosci 28, 8138-8143.

Wang, C., Xiong, M., Gratuze, M., Bao, X., Shi, Y., Andhey, P.S., Manis, M., Schroeder, C., Yin, Z., Madore, C.*, et al.* (2021). Selective removal of astrocytic APOE4 strongly protects against tau-mediated neurodegeneration and decreases synaptic phagocytosis by microglia. Neuron 109, 1657-1674.e1657.

Wang, S., Sudan, R., Peng, V., Zhou, Y., Du, S., Yuede, C.M., Lei, T., Hou, J., Cai, Z., Cella, M.*, et al.* (2022). TREM2 drives microglia response to amyloid-beta via SYK-dependent and -independent pathways. Cell 185, 4153-4169 e4119.

Wang, W.Y., Tan, M.S., Yu, J.T., and Tan, L. (2015a). Role of pro-inflammatory cytokines released from microglia in Alzheimer's disease. Ann Transl Med 3, 136.

Wang, Y., Cella, M., Mallinson, K., Ulrich, J.D., Young, K.L., Robinette, M.L., Gilfillan, S., Krishnan, G.M., Sudhakar, S., Zinselmeyer, B.H.*, et al.* (2015b). TREM2 lipid sensing sustains the microglial response in an Alzheimer's disease model. Cell 160, 1061-1071.

Wang, Y., Ulland, T.K., Ulrich, J.D., Song, W., Tzaferis, J.A., Hole, J.T., Yuan, P., Mahan, T.E., Shi, Y., Gilfillan, S.*, et al.* (2016). TREM2-mediated early microglial response limits diffusion and toxicity of amyloid plaques. J Exp Med 213, 667-675.

Webster, S., Lue, L.F., Brachova, L., Tenner, A.J., McGeer, P.L., Terai, K., Walker, D.G., Bradt, B., Cooper, N.R., and Rogers, J. (1997). Molecular and cellular characterization of the membrane attack complex, C5b-9, in Alzheimer's disease. Neurobiol Aging 18, 415-421.

Weeraratna, A.T., Kalehua, A., Deleon, I., Bertak, D., Maher, G., Wade, M.S., Lustig, A., Becker, K.G., Wood, W., 3rd, Walker, D.G.*, et al.* (2007). Alterations in immunological and neurological gene expression patterns in Alzheimer's disease tissues. Exp Cell Res 313, 450-461.

Wightman, D.P., Jansen, I.E., Savage, J.E., Shadrin, A.A., Bahrami, S., Holland, D., Rongve, A., Borte, S., Winsvold, B.S., Drange, O.K.*, et al.* (2021). A genome-wide association study with 1,126,563 individuals identifies new risk loci for Alzheimer's disease. Nature genetics 53, 1276-1282.

Williams, J.B., Cao, Q., and Yan, Z. (2021). Transcriptomic analysis of human brains with Alzheimer's disease reveals the altered expression of synaptic genes linked to cognitive deficits. Brain Commun 3, fcab123.

Willumsen, N., Poole, T., Nicholas, J.M., Fox, N.C., Ryan, N.S., and Lashley, T. (2022). Variability in the type and layer distribution of cortical Abeta pathology in familial Alzheimer's disease. Brain Pathol 32, e13009.

Wisch, J.K., McKay, N.S., Boerwinkle, A.H., Kennedy, J., Flores, S., Handen, B.L., Christian, B.T., Head, E., Mapstone, M., Rafii, M.S.*, et al.* (2024). Comparison of tau spread in people with Down syndrome versus autosomal-dominant Alzheimer's disease: a cross-sectional study. Lancet Neurol 23, 500-510.

Wiśniewski, H.M., and Terry, R.D. (1973). Morphology of the aging brain, human and animal. Prog Brain Res 40, 167-186.

Wood, J.I., Dulewicz, M., Ge, J., Stringer, K., Szadziewska, A., Desai, S., Koutarapu, S., Hajar, H.B., Blennow, K., Zetterberg, H.*, et al.* (2024). Isotope Encoded chemical Imaging Identifies Amyloid Plaque Age Dependent Structural Maturation, Synaptic Loss, and Increased Toxicity. bioRxiv.

Wood, J.I., Wong, E., Joghee, R., Balbaa, A., Vitanova, K.S., Stringer, K.M., Vanshoiack, A., Phelan, S.J., Launchbury, F., Desai, S.*, et al.* (2022). Plaque contact and unimpaired Trem2 is required for the microglial response to amyloid pathology. Cell Rep 41, 111686.

Woollacott, I.O.C., Toomey, C.E., Strand, C., Courtney, R., Benson, B.C., Rohrer, J.D., and Lashley, T. (2020). Microglial burden, activation and dystrophy patterns in frontotemporal lobar degeneration. J Neuroinflamm 17, 234.

Wozniak, M.A., Mee, A.P., and Itzhaki, R.F. (2009). Herpes simplex virus type 1 DNA is located within Alzheimer's disease amyloid plaques. J Pathol 217, 131-138.

Wu, C.Y., Kaur, C., Sivakumar, V., Lu, J., and Ling, E.A. (2009). Kv1.1 expression in microglia regulates production and release of proinflammatory cytokines, endothelins and nitric oxide. Neuroscience 158, 1500-1508.

Wu, J., Anwyl, R., and Rowan, M.J. (1995). beta-Amyloid-(1-40) increases long-term potentiation in rat hippocampus in vitro. Eur J Pharmacol 284, R1-3.

Wu, X., Miller, J.A., Lee, B.T.K., Wang, Y., and Ruedl, C. (2025). Reducing microglial lipid load enhances beta amyloid phagocytosis in an Alzheimer's disease mouse model. Sci Adv 11, eadq6038.

Wyss-Coray, T., Yan, F., Lin, A.H., Lambris, J.D., Alexander, J.J., Quigg, R.J., and Masliah, E. (2002). Prominent neurodegeneration and increased plaque formation in complement-inhibited Alzheimer's mice. P Natl Acad Sci USA 99, 10837-10842.

Xiang, X., Piers, T.M., Wefers, B., Zhu, K., Mallach, A., Brunner, B., Kleinberger, G., Song, W., Colonna, M., Herms, J.*, et al.* (2018). The Trem2 R47H Alzheimer's risk variant impairs splicing and reduces Trem2 mRNA and protein in mice but not in humans. Mol Neurodegener 13, 49.

Xiao, M.F., Roh, S.E., Zhou, J., Chien, C.C., Lucey, B.P., Craig, M.T., Hayes, L.N., Coughlin, J.M., Leweke, F.M., Jia, M.*, et al.* (2021). A biomarker-authenticated model of schizophrenia implicating NPTX2 loss of function. Sci Adv 7, eabf6935.

Xiao, M.F., Xu, D., Craig, M.T., Pelkey, K.A., Chien, C.C., Shi, Y., Zhang, J., Resnick, S., Pletnikova, O., Salmon, D.*, et al.* (2017). NPTX2 and cognitive dysfunction in Alzheimer's Disease. Elife 6.

Xie, H., Guan, J., Borrelli, L.A., Xu, J., Serrano-Pozo, A., and Bacskai, B.J. (2013). Mitochondrial alterations near amyloid plaques in an Alzheimer's disease mouse model. J Neurosci 33, 17042-17051.

Ximerakis, M., Lipnick, S.L., Innes, B.T., Simmons, S.K., Adiconis, X., Dionne, D., Mayweather, B.A., Nguyen, L., Niziolek, Z., Ozek, C.*, et al.* (2019). Single-cell transcriptomic profiling of the aging mouse brain. Nat Neurosci 22, 1696-1708.

Xu, G., Fromholt, S., and Borchelt, D.R. (2022). Modeling the Competition between Misfolded Abeta Conformers That Produce Distinct Types of Amyloid Pathology in Alzheimer's Disease. Biomolecules 12.

Xu, G., Fromholt, S.E., Chakrabarty, P., Zhu, F., Liu, X., Pace, M.C., Koh, J., Golde, T.E., Levites, Y., Lewis, J., and Borchelt, D.R. (2020). Diversity in Abeta deposit morphology and secondary proteome insolubility across models of Alzheimer-type amyloidosis. Acta Neuropathol Commun 8, 43.

Xu, P.T., Li, Y.J., Qin, X.J., Scherzer, C.R., Xu, H., Schmechel, D.E., Hulette, C.M., Ervin, J., Gullans, S.R., Haines, J.*, et al.* (2006). Differences in apolipoprotein E3/3 and E4/4 allele-specific gene expression in hippocampus in Alzheimer disease. Neurobiol Dis 21, 256-275.

Xu, Y., Propson, N.E., Du, S., Xiong, W., and Zheng, H. (2021). Autophagy deficiency modulates microglial lipid homeostasis and aggravates tau pathology and spreading. P Natl Acad Sci USA 118.

Yamada, T., Kondo, A., Takamatsu, J., Tateishi, J., and Goto, I. (1995). Apolipoprotein E mRNA in the brains of patients with Alzheimer's disease. J Neurol Sci 129, 56-61.

Yamaguchi, H., Hirai, S., Morimatsu, M., Shoji, M., and Harigaya, Y. (1988). Diffuse type of senile plaques in the brains of Alzheimer-type dementia. Acta Neuropathol 77, 113-119.

Yan, P., Bero, A.W., Cirrito, J.R., Xiao, Q., Hu, X., Wang, Y., Gonzales, E., Holtzman, D.M., and Lee, J.M. (2009). Characterizing the appearance and growth of amyloid plaques in APP/PS1 mice. J Neurosci 29, 10706-10714.

Yeh, F.L., Wang, Y., Tom, I., Gonzalez, L.C., and Sheng, M. (2016). TREM2 Binds to Apolipoproteins, Including APOE and CLU/APOJ, and Thereby Facilitates Uptake of Amyloid-Beta by Microglia. Neuron 91, 328-340.

Yoshiyama, Y., Higuchi, M., Zhang, B., Huang, S.M., Iwata, N., Saido, T.C., Maeda, J., Suhara, T., Trojanowski, J.Q., and Lee, V.M. (2007). Synapse loss and microglial activation precede tangles in a P301S tauopathy mouse model. Neuron 53, 337-351.

Yuan, P., Condello, C., Keene, C.D., Wang, Y., Bird, T.D., Paul, S.M., Luo, W., Colonna, M., Baddeley, D., and Grutzendler, J. (2016). TREM2 Haplodeficiency in Mice and Humans Impairs the Microglia Barrier Function Leading to Decreased Amyloid Compaction and Severe Axonal Dystrophy. Neuron 90, 724-739.

Yue, L., Liu, P., Ma, N., Xu, Y., and Zhu, C. (2021). Interaction between extracellular ATP5A1 and LPS alleviates LPS-induced neuroinflammation in mice. Neurosci Lett 758, 136005.

Zelcer, N., Khanlou, N., Clare, R., Jiang, Q., Reed-Geaghan, E.G., Landreth, G.E., Vinters, H.V., and Tontonoz, P. (2007). Attenuation of neuroinflammation and Alzheimer's disease pathology by liver x receptors. P Natl Acad Sci USA 104, 10601-10606.

Zelek, W.M., Bevan, R.J., and Morgan, B.P. (2024). Targeting terminal pathway reduces brain complement activation, amyloid load and synapse loss, and improves cognition in a mouse model of dementia. Brain Behav Immun 118, 355-363.

Zhan, Y., Paolicelli, R.C., Sforazzini, F., Weinhard, L., Bolasco, G., Pagani, F., Vyssotski, A.L., Bifone, A., Gozzi, A., Ragozzino, D., and Gross, C.T. (2014). Deficient neuron-microglia signaling results in impaired functional brain connectivity and social behavior. Nat Neurosci 17, 400-406.

Zhang, C., Rissman, R.A., and Feng, J. (2015). Characterization of ATP alternations in an Alzheimer's disease transgenic mouse model. J Alzheimers Dis 44, 375-378.

Zhang, Y., Chen, K., Sloan, S.A., Bennett, M.L., Scholze, A.R., O'Keeffe, S., Phatnani, H.P., Guarnieri, P., Caneda, C., Ruderisch, N.*, et al.* (2014). An RNA-sequencing transcriptome and splicing database of glia, neurons, and vascular cells of the cerebral cortex. J Neurosci 34, 11929-11947.

Zhang, Y.W., Thompson, R., Zhang, H., and Xu, H. (2011). APP processing in Alzheimer's disease. Mol Brain 4, 3.

Zheng, Z., Zong, Y., Ma, Y., Tian, Y., Pang, Y., Zhang, C., and Gao, J. (2024). Glucagon-like peptide-1 receptor: mechanisms and advances in therapy. Signal Transduct Target Ther 9, 234.

Zhong, L., Sheng, X., Wang, W., Li, Y., Zhuo, R., Wang, K., Zhang, L., Hu, D.D., Hong, Y., Chen, L.*, et al.* (2023). TREM2 receptor protects against complement-mediated synaptic loss by binding to complement C1q during neurodegeneration. Immunity 56, 1794-1808 e1798.

Zhou, J., Wade, S.D., Graykowski, D., Xiao, M.F., Zhao, B., Giannini, L.A.A., Hanson, J.E., van Swieten, J.C., Sheng, M., Worley, P.F., and Dejanovic, B. (2023). The neuronal pentraxin Nptx2 regulates complement activity and restrains microglia-mediated synapse loss in neurodegeneration. Sci Transl Med 15, eadf0141.

Zhou, Y., Song, W.M., Andhey, P.S., Swain, A., Levy, T., Miller, K.R., Poliani, P.L., Cominelli, M., Grover, S., Gilfillan, S.*, et al.* (2020). Human and mouse single-nucleus transcriptomics reveal TREM2-dependent and TREM2-independent cellular responses in Alzheimer's disease. Nat Med 26, 131-142.

Zhu, X.C., Tan, L., Wang, H.F., Jiang, T., Cao, L., Wang, C., Wang, J., Tan, C.C., Meng, X.F., and Yu, J.T. (2015). Rate of early onset Alzheimer's disease: a systematic review and meta-analysis. Ann Transl Med 3, 38.

Zhu, Y., Wang, L., Yin, Y., and Yang, E. (2017). Systematic analysis of gene expression patterns associated with postmortem interval in human tissues. Sci Rep 7, 5435.

Zou, K., Gong, J.S., Yanagisawa, K., and Michikawa, M. (2002). A novel function of monomeric amyloid beta-protein serving as an antioxidant molecule against metal-induced oxidative damage. J Neurosci 22, 4833-4841.

Zucker, R.S., and Regehr, W.G. (2002). Short-term synaptic plasticity. Annu Rev Physiol 64, 355-405.

APPENDIX

Table A.1 Key resources table

REAGENT	SOURCE	IDENTIFIER	CONCENTRATION	USED IN
Primary Antibodies				
Rabbit anti-IBA1	FujiFilm Wako Chemicals (Osaka, Japan)	Cat # 019-19741	1:1000 (Mouse IHC) 1:300 (Human GeoMx)	Figures: 3.6, 3.9, & 4.1
Sheep anti-TREM2	R&D Systems (Minneapolis, MN, USA)	Cat # AF1729	1:500	Figure 3.6
Rabbit anti-TMEM119	SynapticSystems (Goettingen, Germany)	Cat # 400002	1:500	Figures: 3.1, 3.2, & 5.2
Goat anti-IBA1	Sigma-Aldrich (St. Louis, MO, USA)	Cat # 178479	1:300	Figures: 3.2, 3.8, & 3.9
Rabbit anti-NPC2	Abcam (Cambridge, UK)	Cat # AB218192	1:400	Figure 3.8
Goat anti-APOE	Sigma-Aldrich (St. Louis, MO, USA)	Cat # 178479	1:500	Figure 3.9
Rabbit anti-Aβ42	Thermo Fisher Scientific (Waltham, MA, USA)	Cat # 700254	1:500	Figures: 5.5, 5.8, & 5.9
Chicken anti-HOMER1	SynapticSystems (Goettingen, Germany)	Cat # 160001	1:200	Figure 5.8
Rat anti-LAMP1	Abcam (Cambridge, UK)	Cat # AB25245	1:500	Figure 5.9
Rabbit anti-NPTX2	Abcam (Cambridge, UK)	Cat # AB69858	1:200	Figure 5.9
Mouse anti-Aβ (6E10)	Biolegend (San Diego, CA, USA)	Cat # SIG-39320	1:500	Figure 5.9
Secondary Antibodies				
Donkey anti-rabbit Alexa Fluor 594	Thermo Fisher Scientific (Waltham, MA, USA)	Cat # A32	1:1000	Figures: 3.1, 3.2, 3.6, 3.8, 3.9, 5.2, 5.5, 5.8, & 5.9
Donkey anti-sheep Alexa Fluor 647	Abcam (Cambridge, UK)	Cat # AB150179	1:1000	Figure 3.6
Goat anti-rabbit Alexa Fluor 647	Thermo Fisher Scientific (Waltham, MA, USA)	Cat # A11037	1:1000	Figures: 4.1 & 5.9
Donkey anti-goat Alexa Fluor 647	Abcam (Cambridge, UK)	Cat # AB150135	1:1000	Figures: 3.2, 3.8, & 3.9

Goat anti-mouse Alexa Fluor 594	Thermo Fisher Scientific (Waltham, MA, USA)	Cat # A-11032	1:500	Figure 5.9
Goat anti-chicken AF647	Thermo Fisher Scientific (Waltham, MA, USA)	Cat # A-21449	1:500	Figure 5.8
Donkey anti-rat AF594	Thermo Fisher Scientific (Waltham, MA, USA)	Cat # A-21209	1:500	Figure 5.9
Conjugated Antibodies				
Mouse anti-Aβ40/42, Alexa Fluor 594	Nanostring Technologies (Seattle, WA, USA)	Cat # 121301306	1:25	Figures: 3.1 & 5.2
Mouse anti-GFAP, Alexa Fluor 488	Invitrogen, Thermo Fisher Scientific (Waltham, MA, USA)	Cat # 53-9892-82	1:25	Figure 3.2
Dyes				
4′,6-diamidino-2-phenylindole (DAPI)	Abcam (Cambridge, UK)	Cat # ab228549	1:10,000	Figures: 3.2, 3.6, 3.8, 3.9, & 5.1
Amytracker520	Ebba Biotech (Malmö, Sweden)	NA	1:1000	Figures: 3.2, 3.6, 3.8, 3.9, 3.11, 4.1, 5.1, & 5.9
SYTO 83	Invitrogen, Thermo Fisher Scientific (Waltham, MA, USA)	Cat # S11364	1:10	Figures: 3.1 & 5.2
qFTAA	Developed and gifted from P. Hammarström and P. Nilsson at Linköping University. (Klingstedt et al., 2011)	NA	3 μM	Figures: 5.5, 5.8, & 5.9
hFTAA	As with qFTAA	NA	1 μM	Figures: 5.5, 5.8, & 5.9
Blocking Serums				
Donkey serum	Sigma-Aldrich (St. Louis, MO, USA)	Cat # D9663	1:10	Figures: 3.2, 3.6, & 3.8
Goat serum	Thermo Fisher Scientific (Waltham, MA, USA)	Cat # PCN5000	3:100	Figures: 5.5, 5.8, & 5.9
Fish gelatine	Sigma-Aldrich (St. Louis, MO, USA)	Cat # G7041	2:100	Figure 3.8

PCR Primers		Sequence		
Actg1 Forward	Eurofins Genomics (Ebersberg, Germany)	TTTGAGCAAGAAATGGCTACTGC	10mM	Figure 3.3
Actg1 Reverse	Eurofins Genomics (Ebersberg, Germany)	TATTGGCATACAGGTCTTTGCGG	10mM	Figure 3.3
Aif1 Forward	Eurofins Genomics (Ebersberg, Germany)	GGAGACGTTCAGCTACTCTGAC	10mM	Figure 3.3
Aif1 Reverse	Eurofins Genomics (Ebersberg, Germany)	CATCCACCTCCAATCAGGGC	10mM	Figure 3.3
Trem2 Forward	Eurofins Genomics (Ebersberg, Germany)	GACCTCTCCACCAGTTTCTCC	10mM	Figure 3.3
Trem2 Reverse	Eurofins Genomics (Ebersberg, Germany)	TCAGAGTGATGGTGACGGTTC	10mM	Figure 3.3

Consumables			
Triton X-100	Sigma-Aldrich (St. Louis, MO, USA)	Cat # D9663	Histochemistry
Phosphate-buffered saline tablets	Sigma-Aldrich (St. Louis, MO, USA)	Cat # P4417	Histochemistry & GeoMx
Flouromount-G®	Southern Biotech (Birmingham, AL, USA)	Cat # 0100-01	Histochemistry
D(+)-Saccharose (sugar)	VWR (Radnor, PA, USA)	Cat # 27480.294	Histochemistry
Sodium azide	Sigma-Aldrich (St. Louis, MO, USA)	Cat # S2002	Histochemistry
Superfrost Plus microscope slides	Epredia (Chicago, IL, USA)	Cat # J1800AMNZ	Histochemistry & GeoMx
miRNeasy® Mini Kit	QIAGEN (Hilden, Germany)	Cat # 217004	RNA Extraction
QIAzol® Lysis Reagent	QIAGEN (Hilden, Germany)	Cat # 79306	RNA Extraction
RNaseOUT™	Thermo Fisher Scientific (Waltham, MA, USA)	Cat # 10777019	Reverse Transcription
DNase I, Amplification Grade	Thermo Fisher Scientific (Waltham, MA, USA)	Cat # 18068015	Reverse Transcription
SsoAdvancedTM Universal SYBR® Green Supermix	Bio-Rad (Hercules, CA, USA)	Cat # 1725274	RT-qPCR
High-Capacity cDNA Reverse Transcription Kit with RNase Inhibitor	Applied BiosciencesTM (Coventry, CA, USA)	Cat # 4374967	Reverse Transcription
RNase Free Water	QIAGEN (Hilden, Germany)	Cat # 1017979	RNA Extraction & Reverse Transcription & GeoMx Library Preparation
Chloroform	Sigma-Aldrich (St. Louis, MO, USA)	Cat # C2432	RNA Extraction
DEPC-Treated Water	Santa Cruz Biotechnology (Dallas, TX, USA)	Cat # 204391	GeoMx Slide Preparation
Tris Base	Fisher Scientific (Hampton, NH, USA)	Cat # 10103203	Histochemistry & GeoMx Slide Preparation
EDTA	Sigma-Aldrich (St. Louis, MO, USA)	Cat # E5134	Histochemistry & GeoMx Slide Preparation

Proteinase K	Thermo Fisher Scientific (Waltham, MA, USA)	Cat # AM2548	GeoMx Library Preparation
Molecular Biology Grade Ethanol	Sigma-Aldrich (St. Louis, MO, USA)	Cat # 51976	RNA Extraction & GeoMx protocol
RNase Away	Thermo Fisher Scientific (Waltham, MA, USA)	Cat # 7003PK	GeoMx preparation
Formaldehyde 4% stabilised, buffered	VWR (Radnor, PA, USA)	Cat # 9713.5000	Brain Fixation & GeoMx Slide Preparation
Deionised Formamide	VWR (Radnor, PA, USA)	Cat # 0606	GeoMx Library Preparation
20X SSC	Sigma-Aldrich (St. Louis, MO, USA)	Cat # S6639	GeoMx Slide Preparation
Glycine	Invitrogen, Thermo Fisher Scientific (Waltham, MA, USA)	15527-013	GeoMx Slide Preparation
Xylene	Fisher Chemicals (Pittsburgh, PA, USA)	Cat # Z/0200/17	GeoMx Slide Preparation
ImmEdge® Hydrophobic Pen	Vector Laboratories (Newark, CA, USA)	Cat # H-4000	GeoMx Slide Preparation
Agencourt AMPure XP	Beckman Coulter (Brea, CA, USA)	Cat # A63880	GeoMx Library Preparation
Elution Buffer	Teknova (Hollister, CA, USA)	Cat # T1485	GeoMx Library Preparation
D1000 TapeStation Screen Tape	Agilent (Santa Clara, CA, USA)	Cat # 5067-5582	GeoMx Library Preparation
D1000 TapeStation Ladder	Agilent (Santa Clara, CA, USA)	Cat # 5067-5586	GeoMx Library Preparation
D1000 TapeStation Sample Buffer	Agilent (Santa Clara, CA, USA)	Cat # 5067-5602	GeoMx Library Preparation
MouseExpress (15N, 98%) mouse feed kit (15N/14N)	Cambridge Isotope Laboratories (Andover, MA, USA)	Cat # MLK-SPIRULINA-N	SILK Diet
Teklad Global 18% Protein Rodent Diet	Inotiv (Indianapolis, IN, USA)	Cat # 2018C	Standard Mouse Chow
Acetone (Ac)	Fisher Scientific (Hampton, NH, USA)	Cat # A18-1	MALDI MSI
Acetonitrile (ACN)	Fisher Scientific (Hampton, NH, USA)	Cat # A998SK-1	MALDI MSI
Absolute ethanol	Fisher Scientific (Hampton, NH, USA)	Cat # 12498740	MALDI MSI
Paraformaldehyde (PFA)	Agar Scientific (Stansted, Essex, United Kingdom)	Cat # AGR1018	MALDI MSI
Formic acid (FA)	Honeywell Fluka (Seelze, Germany)	Cat # 56302	MALDI MSI
Trifluoroacetic acid (TFA)	Honeywell Fluka, (Seelze, Germany)	Cat # T6508	MALDI MSI
Methanol (MeOH)	Fisher Scientific (Hampton, NH, USA)	Cat # 10365710	MALDI MSI
2,5-Dihydroxyacetophenone (2,5-DHAP)	Sigma-Aldrich (St. Louis, MO, USA)	Cat # D107603	MALDI MSI
TissueTek optimal cutting temperature (OCT) compound	Sakura Finetek (AJ Alphen aan den Rijn, Netherlands)	Cat # 4583	MALDI MSI
Indium tin oxide (ITO)-coated conductive glass slides	Bruker Daltonics (Bremen, Germany)	Cat #1868957	MALDI MSI

Peptide calibration standard	Bruker Daltonics (Bremen, Germany)	Cat # 8206195	MALDI MSI
Loctite 406 Superglue	Loctite (Düsseldorf, Germany)	Cat # HECY50007	Field potential recording
Borosilicate glass capillaries	World Precision Instruments (Sarasota, FL, USA)	Cat # 1B150F-3	Field potential recording
Sodium Chloride (NaCl)	Fisher Chemical (Pittsburgh, PA, USA)	Cat # S/3161/60	ACSF, Field potential recording
Potassium Chloride (KCl)	MP Biomedicals (Santa Ana, CA, USA)	Cat # 151944	ACSF, Field potential recording
Sodium hydrogen carbonate ($NaHCO_3$)	VWR (Radnor, PA, USA)	Cat # 27778.293	ACSF, Field potential recording
Sodium phosphate monobasic (NaH_2PO_4)	Sigma-Aldrich (St. Louis, MO, USA)	Cat # 102552242	ACSF, Field potential recording
D-Glucose anhydrous	Fisher Chemical (Pittsburgh, PA, USA)	Cat # G/0500/53	ACSF, Field potential recording
Magnesium Chloride ($MgCl_2$)	Sigma-Aldrich (St. Louis, MO, USA)	Cat # M0250	ACSF, Field potential recording
Calcium chloride ($CaCl_2$)	Merck (Darmstadt, Germany)	Cat # 1.02383.1000	ACSF, Field potential recording
Proprietary GeoMx Reagents			
GeoMx Whole Transcriptome Probe Mix	Nanostring Technologies (Seattle, WA, USA)	NA	GeoMx Slide Preparation
Buffer W	Nanostring Technologies (Seattle, WA, USA)	NA	GeoMx Slide Preparation
Buffer R	Nanostring Technologies (Seattle, WA, USA)	NA	GeoMx Slide Preparation
Buffer S	Nanostring Technologies (Seattle, WA, USA)	NA	GeoMx Slide Preparation
Buffer H	Nanostring Technologies (Seattle, WA, USA)	NA	GeoMx Slide Preparation
Master Mix	Nanostring Technologies (Seattle, WA, USA)	NA	GeoMx Library Preparation
Seq Code Primer Plates A, B, C, & D	Nanostring Technologies (Seattle, WA, USA)	NA	GeoMx Library Preparation
Barcoded 96 well plates	Nanostring Technologies (Seattle, WA, USA)	NA	GeoMx Slide Preparation
Equipment			
Frozen sledge microtome	Leica (Wetzlar, Germany)	SM2010R	Histochemistry & GeoMx Slide
Cryostat	Leica (Wetzlar, Germany)	Model: CM1860	GeoMx Slide Preparation (MALDI GeoMx)
Rotary microtome	Leica (Wetzlar, Germany)	Model: RM2235	GeoMx FFPE Sectioning
EVOS® Fl Auto Cell imaging microscope	Thermo Fisher Scientific (Waltham, MA, USA)	Cat # AMAFD1000	Histochemistry Imaging
Hybrigene Slide Baking Oven	Techne (Minneapolis, MN, USA)	Cat # Z649570	GeoMx Slide Preparation
HybEZ™ II Hybridisation oven	ACDBio (Newark, CA, 2024)	Cat # 321720	GeoMx Slide Preparation
Water Bath	Grant Instruments (Royston, UK)	Model: JB1	Histochemistry & GeoMx Slide Preparation
Steamer	Tristar (Tilburg, UK)	Cat # VS-3914	GeoMx Slide Preparation

Tapestation	Agilent (Santa Clara, CA, USA)	Model 2200	GeoMx Library Preparation
Confocal	Zeiss (Oberkochen, Germany)	Model: LSM 880	Histochemistry Imaging
Water Purification System	Merck Millipore (Burlington, MA, USA)	Model: Milli-Q® Integral system	Histochemistry, GeoMx, & Field electrophysiology
MALDI-TOF Mass spectrometry imaging system	Bruker Daltonics (Bremen, Germany)	Model: rapifleX	MALDI-MSI
Matrix Sprayer	HTX Imaging (Chapel Hill, NC, USA)	Model: TM-Sprayer™	MALDI-MSI
Osmometer	Advanced Instruments (Norwood, MA, USA)	Model: 3300	Field electrophysiology
Vibratome	Campden Instruments (Loughborough, UK)	Model: Integraslice 7550MM	Field electrophysiology
Peristaltic Pump	Watson-Marlow Fluid Technology Solutions (Falmouth, UK)	Model: 505s	Field electrophysiology
aCSF Heater	Warner Intsruments (Holliston, MA, USA)	Model: Model TC-324B	Field electrophysiology
Electrode Puller	Narishige (Tokyo, Japan)	Model: PC-1000	Field electrophysiology
Stimulator	Grass Intrument Division, Astro-Med (Warwick, RI, USA)	Model: Grass SD8	Field electrophysiology
Headstage	Axon Instruments (Union City, CA, USA)	Model: HS-2	Field electrophysiology
Amplifier	Axon Instruments (Union City, CA, USA)	Model: Axoclamp 1B Amplifier	Field electrophysiology
Amplifier	Brownlee Precision, Neurophase (Santa Claram, CA, USA)	Model: 440 Amplifier	Field electrophysiology
50 hz Noise Eliminator	Quest Scientific, Digitimer (Welwyn Garden City, UK)	Model: Hum Bug	Field electrophysiology
Digitizer	Axon Instruments (Union City, CA, USA)	Model: Digidata 1322A	Field electrophysiology
RNA sequencer	Illumina (San Diego, CA, USA)	Model: NextSeq2000	GeoMx Sequencing & Bulk RNA Sequencing
Thermocycler	Biorad (Hercules, CA, USA)	Model: C1000	GeoMx Library Preparation
Thermocycler	MJ Research (St Bruno, QC, Canada)	Model: PTC-100	Reverse Transcription
GeoMx Spatial Transcriptomics	Nanostring Technologies (Seattle, WA, USA)	Model: GeoMx Digital Spatial Profiler	GeoMx Slide Preparation
Homogeniser	Kinemetica (Lucerne, Switzerland)	Model: Polytron PT 3000	RNA Extraction
Spectrophotometer	Thermo Fisher Scientific (Waltham, MA, USA)	Model: Nanodrop 2000	RNA Extraction
RT-qPCR Machine	Biorad (Hercules, CA, USA)	Model: CFX96	RT-qPCR

Experimental Models		
mouse: C57BL/6: C57BL/6NCrl	Charles River	Strain#027
mouse: *APP*$^{NL\text{-}F/NL\text{-}F}$: C57BL/6-App$^{tm2.1Tcs}$	Saito et al., (2014)	Available from the Saido lab
mouse: *Trem2*$^{R47H/R47H}$: C57BL/6J-Trem2$^{em1Adiuj/J}$	Jackson Laboratory	Strain#027918
mouse: APP$^{NL\text{-}F/NL\text{-}F}$*xTrem2*$^{R47H/R47H}$	Bred in-house	Wood et al., (2022)

Software	
FIJI	Schindelin et al. (2012)
Rstudio	RStudio Team (2020). RStudio: Integrated Development for R. RStudio, PBC, Boston, MA URL http://www.rstudio.com/.
WinWCP	University of Strathclyde (Glasgow, UK)
Graphpad Prism 10	GraphPad (La Jolla, CA, USA)
GeoMx NGS Pipeline GUI	Nanostring Technologies (Seattle, WA, USA)
FlexImaging 5.0	Bruker Daltonics (Bremen, Germany)
Origin v.8.1	OriginLab (Northampton, MA, USA)
Zen Black v2.3	Zeiss (Oberkochen, Germany)
CFX96 ManagerTM	Bio-Rad (Hercules, CA, USA)